

# Functionalization of polymer optical fibers for medical application

Présentée le 11 mai 2022

Faculté des sciences et techniques de l'ingénieur  
Laboratoire des fibres et matériaux photoniques  
Programme doctoral en science et génie des matériaux

pour l'obtention du grade de Docteur ès Sciences

par

**Jialuo LUO**

Acceptée sur proposition du jury

Prof. F. Nüesch, président du jury  
Prof. F. Sorin, Dr L. Fernandes Boesel, directeurs de thèse  
Prof. I. Herrmann, rapporteuse  
Prof. M. Wolf, rapporteur  
Prof. E. Amstad, rapporteuse

# Acknowledgements

After a few years of struggle comes finally the end of my Ph.D. It is indeed the most unforgettable journey with very complex emotions than any other period in my life. I swang between self-confidence and self-doubt yet I was accompanied, encouraged, supported by the people without whom I know I will not make it till here.

My deepest gratitude goes first to my supervisor Dr. Luciano Boesel who has a poker face and always is in green from head to feet. After such a long time working with him, I was deeply impressed by his uprightness, big heart, and a strong sense of responsibility towards work. I would thank him for offering me the chance to study on such an extraordinary platform as well as constantly guiding, supporting, and accompanying me over the tough journey. I would also thank him for never constraining me in research and forcing me as a "boss" but allowing me to explore myself and the meaning of work and life, as well as reach out to diverse possibilities in other fields. Thank him for listening patiently to my ideas, realistic and unrealistic ones. I will never forget the speechless but solid backup for me to recover when I fell into strong inner struggle in the middle of my Ph.D., including the advice for a gap year to take a breath. I give my appreciation to him for his patience towards my sentiment and emotional sensitivity.

My great appreciation also extends to my university supervisor Prof. Fabien Sorin, a talented scientist and a gentle tutor. He always gives illuminating advice to my research and kept encouraging me when I was stuck. I was still deeply impressed by his words in one group meeting in EPFL where he stated: His expectation to a Ph.D. student is that they have a clear understanding of the fundamentals while the paper is just a plus. It is worthy to do care about quality instead of quantity. His education philosophy is quite precious in a competitive atmosphere where many lost themselves in producing papers and forget about the original aspiration. For me, he is a real scientist.

I am greatly thankful to my colleagues for the joys, helps and encouragement they brought to me during these years. Thanks to my lovely labmates who always discuss with me and offer help when I came across problems in experiments, especially to Sebastian Ulrich, Michèle Clerc, and Sandipan Biswas for their sound and broad knowledge in chemical synthesis. Thanks to Nicolas Frommes for shocking me with plenty of IT tricks. Special thanks are given to Fei Pan for his always-fast response to my requests to use the advanced devices in his lab. For so many people who provided great help during my academic journey but whose name was not listed here, I am expressing here my sincere gratitude to you. Also, I want to express my thanks to Esther Zürcher for the patience, understanding, and solutions she offered when I was facing personal issues, visa administrative issues and conflicts.

My most enjoyable time during the Ph.D. is the time I spent with my friends. I have met so many fantastic people daily or in some "strange" circumstances with many of them I have built a lifelong friendship. Prominent among these are Yaping Cai, Qiuyun Huang, and Min Tuo. We have spent so much time together, traveling together all over the world, sharing happiness and sorrows, doing philosophy talking, and wandering in the forest of music and arts. Of course, I will not forget the Empa Chinese group, with whom I have spent most of my weekends together to do various activities, cooking, sports, games, etc.

I also feel lucky to meet a group of people sharing the same ideal with me. Thanks to my entrepreneurship partners for fighting together with me for one goal and helping me find out what I truly desire and care about. Thanks to my business case mock partners for bringing me to the fascinating business world and solving diverse business cases with me. The process is hard and exhausting, but I enjoy the sense of accomplishment to do something that has a grounding in reality and instant impacts on society, and I hope that one day we can again work together and shape the world in the way we like. Thanks to the professors and friends at University of St.Gallen for expanding my view in the field of economics, politics, and laws and refreshing my mind from scientific research.

Undoubtedly, I will give mountains of thanks to Empa, ETH, and EPFL for various resources for my personal development. I never get bored because there are always so many new things I could try and so many nice people I can learn from. I will never forget the time I spend in the big ETH community and I will continue my journey with the spiritual wealth endowed by it.

Thanks to the Ph.D. experience itself. I would have never known vividly how research is done if not do it in person. Even though it is not so smooth and pleasant for me, even a little bit painful, I feel grateful to have experienced it at a young age. It drives me to

## Acknowledgements

---

think deeply every day about life and the true desire and prepared me with a peaceful mind to face whatever could come in the future.

Last but not the least, this dissertation is for my significant other who I have no idea when I am going to meet in the future because you are the one that arouses my curiosity to see who you are which stops me from all dangerous thoughts when facing the hard time.

St.Gallen, 07 September 2021

# Abstract

The increasing challenges caused by the growing and aging population and the fast pace of life are calling for a change of our current medical care system towards being rapid, easy, and on-demand self-care. Empowerment with the self-caring components such as early diagnosis, treatment, and monitoring of individuals will sharply release the social burden. In this context, fibrous materials stand out for their small size, processing flexibility, designable functionalities, and the possibility to be further integrated into implants or wearable devices.

As we know, optical fiber is widely used in the biomedical field. For example, conventional silica optical fiber has mature applications such as light guides for surgery and catheter-based endoscopy while novel types of optical fiber (hydrogel, polymer, biomedical material, and elastomer) open the door to various new application scenarios like optogenetics, active monitoring, and continuous sensing, etc. While it remains a hot topic, the use of optical fibers for drug delivery is still in lack of exploration and suggests an ideal starting point for us. Optical fiber allows light propagation and thus gives the possibility to build up a light-responsive delivery system if combined with light-responsive drug carriers. Mesoporous silica nanoparticles (MSNP) were selected to host drug substances due to their high surface area, big pore volume, and versatility of functionalization and were coated on the fiber. Optical fiber will work as a light source to trigger the release from carriers. In this thesis, we constructed the hybrid system to give an optical fiber-based release system and elucidate the interaction between light from the optical fiber and drug-hosted particles with a further expectation to integrate with sensing or monitoring function to have an advanced delivery device.

The first part of the work involved the synthesis of mesoporous silica nanoparticles using non-surfactants as templating agents. For the first time, a systematic study has been carried out to unravel the morphogenetic mechanism of mesoporous silica nanoparticles by polyphenols. Our study has, on one side, suggested that the pKa value of the polyphenols is responsible for the particle size due to the effect on nucleation and particle growth process; on the other side, demonstrated that the formation of the supramolecular network contributes to the porous structure by serving as the skeleton for the silica precursors to polymerize around. The second part of the work is to establish a method to generate a particle-polymer optical fiber (POF) complex matrix. A robust and controlled strategy for the fabrication of particle-coated surfaces that applies to multiple genres of substrates and coating materials was proposed based on layer-by-layer (LbL) assembly. The approach enables a high drug loading as well as a low structural complexity endowed by a dense and homogenous monolayer coverage of particles on the substrates. The computer vision method was employed to quantitatively evaluate the particle coating, increasing dramatically the efficiency and accuracy of the coating evaluation. The final part of the work investigates the light-responsive release of photolabile coumarin-chlorambucil conjugates from optical fibers. To the best of our knowledge, it is the first study to explore the release of drugs from the side of optical fibers. Overall, this novel particle-optical fiber-based one-dimensional drug delivery system shows a great potential to be used for applications like implants, wearable devices, smart textiles, etc. with rapid, environment-independent, and on-demand releasing profiles.

## Keywords

Mesoporous silica nanoparticles, polymer optical fibers, surface modification, particle-fiber hybrid system, light-responsive drug delivery, photocleavable prodrug, implants, wearable device



# Résumé

Les défis émergents dû à une forte croissance et un vieillissement important de la population ainsi qu'un rythme de vie rapide nécessitent une adaptation de notre système de soins actuel afin qu'il soit rapide, facile et personnalisé. L'autonomisation à travers des matériaux intelligents du diagnostic précoce, du traitement et du suivi des individus allégera considérablement la charge sociale associée. Dans ce contexte, les fibres se distinguent de par leur petite taille, la flexibilité de leur fabrication, leurs fonctionnalités personnalisables et la possibilité d'être intégrées dans des implants ou des dispositifs portables.

La fibre optique est amplement utilisée dans le domaine biomédical. Par exemple, la fibre optique de silice conventionnelle a des applications comme guides lumineux pour la chirurgie et l'endoscopie par cathéter, tandis que de nouveaux types de fibres optiques (hydrogel, polymère, matériau biomédical et élastomère) ouvrent la voie à de nouvelles applications comme l'optogénétique, surveillance active, détection continue, etc. Bien qu'elle reste un sujet d'actualité, l'utilisation des fibres optiques pour l'administration de médicaments est encore peu explorée et apparaît comme un point de départ idéal. La fibre optique permet la propagation de la lumière donnant ainsi la possibilité de développer un système d'administration sensible à la lumière lorsqu'elle est combinée avec des vecteurs/transporteurs de médicaments répondant à la lumière. Des nanoparticules de silice mésoporeuses (MSNP) ont été sélectionnées pour contenir des substances médicamenteuses en raison de leur superficie élevée, de leur grand volume de pores ainsi que leur polyvalence à être fonctionnalisées et ont été déposées sur la fibre optique. La fibre optique fonctionnera comme une source lumineuse pour déclencher la libération des principes actifs. Dans cette thèse, nous avons développé un système hybride permettant la délivrance de principes actifs en utilisant les propriétés de la fibre optique. L'interaction entre la lumière de la fibre optique et les particules contenant le médicament a également été étudiée avec pour perspective d'intégrer la fonction de détection ou de surveillance pour avoir un système de délivrance de principes actifs avancé.

La première partie du travail a porté sur la synthèse de nanoparticules de silice mésoporeuses en utilisant des non-tensioactifs comme agents structurants. Pour la première fois, une étude systématique a été menée pour élucider le mécanisme morphogénétique des nanoparticules de silice mésoporeuses par les polyphénols. Notre étude a, d'une part, suggéré que la valeur du pKa des polyphénols est responsable de la taille des particules en raison de l'effet sur le processus de nucléation et de croissance; d'autre part, nous avons démontré que la formation du réseau supramoléculaire contribue à la structure poreuse en servant de squelette pour la polymérisation des précurseurs de silice. La deuxième partie de cette thèse consiste à établir une méthode pour générer une matrice complexe basée sur des fibres optiques polymères (POF). Une stratégie contrôlée pour la fabrication de surfaces décorées de particules applicable à plusieurs types de substrats et de matériaux de revêtement a été proposée sur la base de layer-by-layer assembly (LbL). L'approche permet une charge médicamenteuse élevée ainsi qu'une faible complexité structurale grâce à la déposition d'une monocouche dense et homogène de particules sur les substrats. Une méthode de détection par ordinateur a été utilisée pour évaluer quantitativement le revêtement de particules, augmentant considérablement l'efficacité et la précision de l'évaluation du revêtement. La dernière partie du travail étudie la libération sensible à la lumière de conjugués photolabiles coumarine-chlorambucil à partir de fibres optiques. À notre connaissance, il s'agit de la première étude à explorer la libération de médicaments le long de fibres optiques. Finalement, ce nouveau système d'administration de médicaments unidimensionnel à base de particules et de fibres optiques présente un grand potentiel pour des applications comme implants, dispositifs portables, textiles intelligents, etc. avec des profils de libération rapides, indépendants de l'environnement et à la demande.

## Mots-clés

Nanoparticules de silice mésoporeuses, fibres optiques polymères, modification de surface, système hybride particule-fibre, administration de médicament sensible à la lumière, promédicament photoclivable, implants, dispositif portable

# Contents

<b>Acknowledgements .....</b>	<b>v</b>
<b>Abstract.....</b>	<b>vii</b>
<b>Keywords.....</b>	<b>vii</b>
<b>Résumé.....</b>	<b>viii</b>
<b>Mots-clés .....</b>	<b>viii</b>
<b>List of Figures.....</b>	<b>xii</b>
<b>List of Tables.....</b>	<b>16</b>
<b>List of Equations .....</b>	<b>16</b>
<b>Chapter 1 Introduction of state of art.....</b>	<b>17</b>
1.1 Mesoporous silica materials for drug delivery use .....	17
1.1.1 Mesoporous silica nanoparticles (MSNPs) as drug carriers .....	17
1.1.2 Synthetic approaches of MSNPs .....	18
1.1.3 Surface modification of silica nanoparticles .....	18
1.2 Layer-by-Layer (LbL) approach for surface modification .....	21
1.2.1 The basic principle of LbL assembly .....	21
1.2.2 Building blocks for LbL approach .....	22
1.2.3 Parameter influencing the LbL process .....	22
1.2.4 Monitoring of the LbL assembly process.....	23
1.2.5 Application of LbL assembly .....	25
1.3 Polymer optical fiber (POF) for biomedical use.....	28
1.3.1 Basic concept of optical fibers .....	29
1.3.2 Materials and fabrication techniques of polymer optical fibers .....	30
1.3.3 Biomedical application of optical fibers .....	31
1.4 Light-responsive drug release.....	35
1.4.1 Controlled release via photoisomerization mechanism.....	35
1.4.2 Controlled release via the photocleavable mechanism .....	37
1.4.3 Controlled release via the photothermal mechanism .....	39
1.5 Objective of the PhD work.....	39
<b>Chapter 2 Polyphenol as morphogenetic agents for the controlled synthesis of mesoporous silica nanoparticles.....</b>	<b>41</b>

2.1	Introduction .....	41
2.2	Effect of tannic acid concentration on the morphology of MSNP .....	42
2.3	Investigation of tannic acid-related polyphenols as morphogenetic agents .....	49
2.3.1	Comparison of chemical structure of four phenol derivatives.....	49
2.3.2	Characterization of the phenol derivatives-templated silica nanoparticles .....	49
2.3.3	Study of influencing factors for size growth .....	51
2.3.4	Study of mechanism of pore formation .....	51
2.4	Conclusion .....	56
<b>Chapter 3</b>	<b>A robust and controlled strategy for surface modification with particles .....</b>	<b>57</b>
3.1	Introduction .....	57
3.2	Layer-by-layer approach for surface modification .....	57
3.2.1	Selection of coating approach.....	57
3.2.2	Plasma-assisted approach for surface treatment .....	59
3.2.3	Optimization of the layer-by-layer assembly via DoE .....	60
3.3	Study of the silanization approach .....	64
3.3.1	Selection of silanes.....	64
3.3.2	Characterization of the silanization on the substrate surface .....	65
3.4	Conclusion .....	68
<b>Chapter 4</b>	<b>Light-responsive drug release from flexible polymer optical fiber.....</b>	<b>69</b>
4.1	Introduction .....	69
4.2	Release of chlorambucil anticancer drug from isolated MSNPs and PDMS-nanoparticle hybrid films .....	70
4.2.1	Photolabile protecting groups (PPG) for controlled release .....	70
4.2.2	Characterization of coumarin-chlorambucil-anchored nanoparticles and films.....	70
4.2.3	Pre-release studies.....	72
4.3	Conclusion .....	78
<b>Chapter 5</b>	<b>Experimental.....</b>	<b>79</b>
5.1	Materials.....	79
5.2	Fabrication of PDMS fiber-based release system .....	79
5.2.1	Particle synthesis.....	79
5.2.2	Processing of PDMS fibers and PMMA substrates .....	79
5.2.3	Layer-by-Layer coating of nanoparticles to PDMS fibers and PMMA substrates.....	80
5.2.4	Silanization of particles .....	80
5.2.5	DoE and particle recognition.....	80
5.2.6	Synthesis of coumarin-chlorambucil conjugate .....	80
5.3	Characterization .....	89
5.4	Matlab code for qualitative analysis of particle coating.....	90
<b>Chapter 6</b>	<b>Conclusion and outlook.....</b>	<b>95</b>

6.1	Achieved results and future work.....	95
6.2	Simulation.....	96
6.2.1	3D simulation model .....	96
6.2.2	Light transmission and intensity simulation of the built-up model .....	96
6.2.3	Influence of PDDA layer on the light behavior .....	98
6.2.4	Influence of refractive index of medium on the light behavior .....	99
6.3	Outlook: Some potential applications of the complex delivery system .....	99
<b>References.....</b>		<b>101</b>
<b>Curriculum Vitae.....</b>		<b>108</b>

# List of Figures

Figure 1-1. Classes of nanoparticles that are used for drug delivery.[4] .....	17
Figure 1-2. Schema of synthesis of MSNPs by surfactants[22] .....	18
Figure 1-3. Functionalization of mesoporous silica by co-condensation and by post-synthetic treatment. A trialkoxysilane molecule bearing a functional moiety (red) is shown as an example of a precursor. The structure-directing agent (SDA) is represented by the blue micelles.[23].....	19
Figure 1-4. Left: Distribution of functional groups depending on the addition time of the organosilane component during synthesis.[28] .....	20
Figure 1-5. Left: CLSM images of SBA-15s (top panels) and ASNCs (hexagonal particles, also known as arrays of silica nanochannels, bottom panels) functionalized with APTES, BTESPA, or APTMEES. Three particles are shown for each silane/silica combination. In the case of the as-synthesized samples, the SDA was extracted before(a) and after(b) FITC labeling. Right: CLSM images of calcined ASNCs after functionalization with APTMEES in ethanol (a), acetone (b), THF (c), toluene (d), and subsequent FITC labeling.[29] .....	20
Figure 1-6. Principle of the LbL deposition technique.[32] .....	21
Figure 1-7. Fabrication of LbL film by spraying. [32] .....	22
Figure 1-8. LbL assembly of multilayer films by spin-assisted coating. [32] .....	22
Figure 1-9. The linear growth of film thickness monitored by ellipsometry. Left: (PEI/CNER) <sub>n</sub> film; Right: (magnetic NP/PAH) <sub>n</sub> film[62] .....	24
Figure 1-10. UV absorbance of growing films. Left: (PEI/CNER) <sub>n</sub> film; Right: (PSS/TiO <sub>2</sub> ) <sub>n</sub> film[63] .....	24
Figure 1-11. TEM image of TiO <sub>2</sub> particle coated with (PSS/PAH) <sub>n</sub> multilayer[64] .....	25
Figure 1-12. Photovoltaic cell composed of PPE and fullerene derivative[66] .....	25
Figure 1-13. Left: permeation principle of the system; Right: single pore lined with an Au nanolayer[73] .....	26
Figure 1-14. TEM(a) and SEM(b) images of the samples prepared using APTS-HMS as templates[77] .....	27
Figure 1-15. Au nanoparticle-embedded alumina porous matrix for catalyst use <sup>[79]</sup> .....	28
Figure 1-16. Concentration of urea, ammonia, and formate after 5 h of irradiation of TiO <sub>2</sub> suspension and TiO <sub>2</sub> -loaded polyelectrolyte capsules of 8.1, 4.2, and 2.2 μm diameter[80] .....	28
Figure 1-17. Light transmission in an optical fiber occurs by total internal reflection for which the transmitting fiber is coated with outer cladding material that has a lower refractive index than the inner core material.[100] α is defined as incident angle, ν is the refracted angle when light enters the optical fiber. ....	29
Figure 1-18. Overview about the different manufacturing techniques for POFs[100] .....	30
Figure 1-19. Design of the glucose-sensitive hydrogel optical fibers. a) Structural composition of the glucose-sensitive p(AM-co-PEGDA-co-3-APBA) fiber core cladded with Ca alginate. b) The hydrogel matrix is functionalized with 3-APBA. (1) PEG-crosslinked polyacrylamide hydrogel, (2) 3-APBA in charged tetrahedral state, (3) glucose. c) The PBA derivative binds cis diols of glucose molecules and changes the RI of the hydrogel fiber. d) The increase in the concentration of the glucose molecules can be quantified by measuring the variation in the intensity of the output light.[110] .....	32
Figure 1-20. a) Illustration of the optical loss in a sensing region containing absorption and scattering elements. As the fiber is stretched, the distribution of the loss elements is altered, resulting in loss increasing exponentially with the length of the sensing region. This relation offers a simple technique for strain sensing. b) Schematic of a fiber with three sensor regions doped with different dyes, respectively: RB: rose Bengal, MB: methylene blue, FL: fluorescein. c) Photos showing a dye-doped fiber on a glass slide, without (top) and with (bottom) excitation broadband light. d) Extracted absorption spectra of the three	

sensors when local strain was applied to each sensor at a time (RB as an example). e) The dye absorption as a function of strain, showing linear readout in terms of dB/strain and negligible crosstalk between sensors (RB as an example).[111]	32
Figure 1-21. Concept of the singlet oxygen fiber optic: (1) illuminator-to-fiber coupling, (2) compressed oxygen-to-fiber coupling via a flare T-valve to a borosilicate fiber optic consisting of a Teflon gas flow tube, (3) porous Vycor glass (PVG) cap-to-fiber coupling, (4) photocleavable sensitizer solid, (5) internally flowing light and oxygen, externally produced $^1\text{O}_2$ , [2 + 2] cycloaddition at the alkene site, (6) cleavage of sensitizer 3 free from the probe tip via the scission of dioxetane 2, and (7) production of cofragment 4 and hydrolysis byproduct.[112]	33
Figure 1-22. Schematic illustration describing the encapsulation of 5-FU into the UiO-66 thin film optical fiber and novel drug delivery system[113]	33
Figure 1-23. Silk waveguide guiding light in tissue. Light coupled from multimode glass fiber is confined within the silk film core of a 3.5 cm long waveguide. Inset shows the core of the waveguide glowing green after closure of the incisions.[114]	34
Figure 1-24. Potential medical applications of biomaterial waveguides. a) Continuous monitoring of biological analytes using an implanted optical fiber. b) Monitoring of the viability and function of a transplanted kidney using a mesh-type optical waveguide. c) Photodynamic therapy of skin tumors using an optical microneedle array. d) Minimally invasive photochemical crosslinking of the sclera using a flexible waveguide. e) Long-term optogenetic treatment of brain disorders using implanted optical waveguides. f) On-demand synthesis of therapeutic substances from optogenetic cells encapsulated in a light-guiding hydrogel implant. g) Photomodulation of wound healing using a wearable photonic bandage.[106]	34
Figure 1-25. Photoisomerization of 7-((3-triethoxysilyl) propoxy)coumarin under UV irradiation[137]	36
Figure 1-26. Drug release controlled by photoisomerization of AB derivatives[139]	36
Figure 1-27. Illustration of light-responsive micelle assembly and disassembly of spiropyran-hyperbranched-polyglycerol (SP-hb-PG)[140]	37
Figure 1-28. Illustration of the photocleavable release	37
Figure 1-29. a) Jablonski diagram for the DDS PHP-Benz-Cbl and photoproduct PHP-Benz-COOH. b) Emission spectra of the DDS as the irradiation time is gradually increased (0–15min)	38
Figure 2-1. Size distribution (by intensity, left panel) and raw correlation data (right panel) of TA-templated MSNP samples	42
Figure 2-2. SEM (left column) and TEM (right column) images of TA-templated silica nanoparticles prepared with increasing amounts of templating agent: a) TA64-MSNP, b) TA128-MSNP, c) TA256-MSNP, d) TA512-MSNP	43
Figure 2-3. MSNP templated with TA before and after detemplation	44
Figure 2-4. HRTEM images of tannic acid (TA) templated silica nanoparticles after removal of tannic acid. From up to down, the amount of tannic acid is 64mg, 128mg, 256mg, 512mg, respectively. Left column: MSNPs after piranha treatment, right column: MSNPs after TGA	44
Figure 2-5. a) Experimental and simulated scattering intensities versus scattering vector from silica particles synthesized without templating agent. The inset represents the 2D scattering pattern. b) the corresponding $p(r)$ obtained from IFT calculation.	45
Figure 2-6. a, c and e) The experimental scattering patterns and their relevant residual scattering obtained from subtraction of Porod line are shown together with the IFT evaluation of residual scattering. The insets represent the 2D scattering patterns. b, d and f) the pair-distance distribution function, $p(r)$ , obtained from IFT analysis of residual scattering from pores. The distribution reveals increase in pore size and pore volume by increasing templating agent concentration, in this case TA.	46
Figure 2-7. Radius of gyration ( $R_g$ ) of the pores and the Porod slope values obtained from TA-templated silica nanoparticles before and after piranha treatment.	47

Figure 2-8. Nitrogen adsorption-desorption isotherms of templated MSNPs after detemplation .....	48
Figure 2-9. Chemical structure and respective acidity constants of polyphenols used as morphogenetic agents .....	49
Figure 2-10. Size of particles out of various templating agents as a function of mass of templating agent .....	50
Figure 2-11. SEM images of particles synthesized by polyphenols as morphogenetic agents. For each morphogenetic agent, from left to right, the amount of morphogenetic agent is 64mg, 128mg, 256mg, and 512mg .....	50
Figure 2-12. SEM images of TA and GA frameworks before TEOS addition. a) TA512 supramolecular structure; b) GA512 cluster. Specimens were taken from the reaction solutions 20min after the beginning of the reaction .....	53
Figure 2-13. Schema of the formation mechanism of MSNPs using TA as templating agent .....	53
Figure 2-14. Comparison of particle surface. Left: SEM images of particles templated by GA (top) and EG (bottom). Center: AFM images of one GA512-MSN particle (rough) surrounded by smooth, non-templated SNP particles: amplitude scan (top), and phase scan (bottom). Right: AFM 3D representation of the same particles. ....	54
Figure 2-15. SEM image of particles templated by GA. TEOS was added 1h after the dissolution of GA. ....	54
Figure 3-1. Strategies to build amine-functionalized silica nanoparticle coating .....	58
Figure 3-2. Chemically bonded particle coating via glutaraldehyde .....	58
Figure 3-3. Morphology of particle coating on PMMA and PDMS surface .....	59
Figure 3-4. The density of particle coating when plasma-treated for different durations .....	60
Figure 3-5. Recognition of particles from images with distinguished brightness by Image J .....	61
Figure 3-6. Illustration of Delaunay triangulation .....	62
Figure 3-7. Particle recognition by Matlab. Left: original SEM image; Middle: particle recognition on the SEM image, identified red part will not be selected for the calculation of the adjacent distance to avoid a bias towards a higher value; Right: the network for calculation of the adjacent distance after removal of red part .....	62
Figure 3-8. Comparison of the particle recognition result for adherent particles .....	62
Figure 3-9. Analysis of the influence of each parameter on the density and homogeneity of the particle coating. Calculation was done based on the data in Table 3-2 .....	63
Figure 3-10. Determination of the prominent influencing factor .....	64
Figure 3-11. Surface morphology of PDMS substrate after one coating cycle(left) and three coating cycles(right).....	64
Figure 3-12. Chemical structure of APTMS, APTES and APDMES .....	65
Figure 3-13. SEM images of particles before and after silanization on PMMA substrates .....	65
Figure 3-14. XPS spectra of the particles with and without silane.....	66
Figure 3-15. a) Step to label the particle-coated substrates with FITC; b) The visualized FITC signal on the PDMA-coated PMMA substrate and particle-coated substrates with and without silanization (false colors, not real fluorescence); c) The fluorescence intensity of substrates with different coatings (Signal was calculated by ImageJ with saturated pixels fixed at 0.4% for contrast enhancement) .....	67
Figure 3-16. Contact angle measurement for PMMA and PDMS substrate .....	68
Figure 4-1. Illustration of photo-triggered release from optical fibers .....	69
Figure 4-2. The structure of coumarin-chlorambucil-prodrug and the releasing principle .....	70

Figure 4-3. Morphology of the MSNPs, AP-MSNPs, and coumarin-clb-MSNPs .....	71
Figure 4-4. SEM images of particle coating on PDMS fibers .....	71
Figure 4-5. SEM images of particle-PDMS substrates before and after the attachment of coumarin-chlorambucil conjugates .....	71
Figure 4-6. Fluorescence images of the MSNP-PDMS fibers (top left: before UV irradiation, bottom left: under UV irradiation) and MSNPs(right) decorated with coumarin-cbl-conjugates.....	72
Figure 4-7. Degree of swelling of PDMS in different solvents.[251] .....	73
Figure 4-8. Solvent influence on the distribution of FITC molecule.....	73
Figure 4-9. Influence of each layer of coating on the distribution of FITC.....	74
Figure 4-10. Setup for measurement of fluorescence excitation from the side of fiber .....	74
Figure 4-11. Fluorescent emission along PDMS fiber .....	75
Figure 4-12. Illustration of the steps for release study .....	75
Figure 4-13. LC-MS chromatogram & mass spectra of chlorambucil standard at 26.4 ng/μL .....	76
Figure 4-14. Mass spectra of released substances in dark condition, under direction irradiation and by through-fiber activation.....	78
Figure 5-1. HAMAMATSU L10290 light source .....	88
Figure 6-1. 3D simulation model of the particle-fiber delivery system .....	96
Figure 6-2.a) light transmission through the defined material (PDMS) with the incident angle changing from 0° to 90°; b) light transmission through the region when PDMS, PDDA, and solvent were properly defined with the incident angle changing from 0° to 90°; c) light transmission through the region when all materials were properly defined with the incident angle changing from 0° to 90°. Color bar: [-9E7, 9E7]. .....	97
Figure 6-3. Light intensity on PDMS fiber surface by simulation, color bar: [-9E8, 9E8] .....	98
Figure 6-4. Comparison of the light transmission on the side of optical fiber with (the same as Figure 5-2c) and without PDDA coating.....	98
Figure 6-5. Reflectance and transmittance of the light on the surface of optical fiber when PDDA and particles were introduced or missing.....	99
Figure 6-6. Reflectance and transmittance of the light on the surface of optical fiber in different releasing medium.....	99



## List of Tables

Table 2-1. Size information (obtained from DLS and SEM) of resulting particles templated with TA .	42
Table 2-2. Structural properties of TA-templated particles as determined by BET and SAXS .....	47
Table 2-3. DLS results of particles synthesized by different morphogenetic agents .....	51
Table 2-4. DLS results of reaction mixture without silica precursors.....	52
Table 2-5. Mass loss before and after calcination of particles prepared with different morphogenetic agents .....	55
Table 3-1. L9 orthogonal array table.....	60
Table 3-2. Distance between adjacent particles obtained by Matlab .....	63
Table 3-3. Zeta potential of different species of silica nanoparticles (after 4h of silanization) .....	65
Table 4-1. XPS element survey results (surface atomic%) .....	72
Table 4-2. High resolution scan for nitrogen and chlorine elements (surface atomic%) .....	72

## List of Equations

Equation 1-1. Numerical aperture (representation 1) .....	29
Equation 1-2. Numerical aperture (representation 2) .....	29
Equation 1-3. Fiber parameter.....	29
Equation 3-1. Wenzel equation .....	67

# Chapter 1 Introduction of state of art

## 1.1 Mesoporous silica materials for drug delivery use

### 1.1.1 Mesoporous silica nanoparticles (MSNPs) as drug carriers

Back to the very first drug delivery system in history made of starch and sugar, the design of delivery systems has evolved dramatically nowadays. Different ways of drug administration were developed in pursuit of an improvement in therapeutic safety and efficacy, from a simple pill to more advanced devices. Nanomaterials have shown a great potential for drug delivery that can significantly lower the side effects, elongate the circulation time and decrease the incidence of drug resistance. Thus, diverse types of nanoparticles were used to administrate active species[1-3] (e.g. drugs, enzymes, and genes), for example, the organic species including dendrimers, liposomes, polymer micelles, proteins, and inorganic hosts like metallic and silica-based nanoparticles[4] (Figure 1-1).

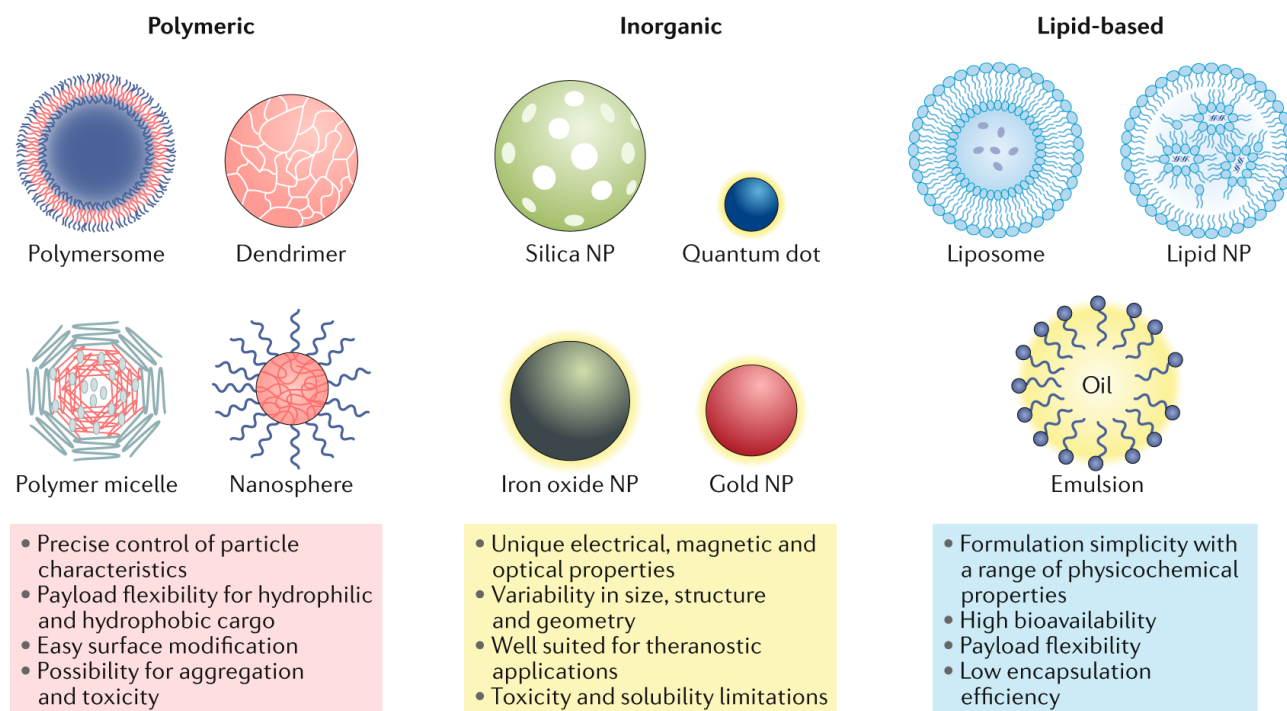


Figure 1-1. Classes of nanoparticles that are used for drug delivery.[4]

Among diverse nanomaterials, mesoporous silica nanoparticles (MSNPs) have been the subject of intense investigation for several reasons. 1) The size of particles can be tuned between dozens of nanometers to a few hundred nanometers and can be uptaken by cancer cells while no obvious cytotoxicity to healthy cells; 2) They possess ordered and stable morphology and higher resistance towards high temperature, pH, mechanical pressure and degradation compared to organic particles; 3) The pore size has a narrow distribution and can be tuned between 2 to 10nm to control the loading amount of drugs; 4) The surface area can reach around 1000m<sup>2</sup>/g to achieve an appreciable loading; 5) The inner surface and outer surface can be selectively functionalized with different functional groups that enable the use as multifunctional platforms. These properties make MSNPs highly attractive also for biomedical applications, especially for the development of multimodal imaging systems and for controlled delivery[5].

A good understanding and controlling of the transport properties at a nano-level is the basis for drug delivery use. Therefore, morphology, particle size, and dispersity of particles and pores should be well-defined[6]. Particle size affects the biodistribution in animal models, as well as the release rate. A larger size of particles and pores can contribute to a higher initial release and an over-

all release rate. The dispersity and morphology of both objects determine the smoothness of the release process. Pore opening size can also influence the loading and release rate because they can limit the transportation of cargo molecules through the pore opening. A large pore opening means a higher substance-exchanging rate, but it also increases the initial release and the risk for burst release. The chemical properties of the surface are very important to evaluate the performance of a drug carrier. The chemistry of the outer surface is responsible for the interaction with the external environment, influencing properties of targeting, dispersion, biodistribution, and so forth. The chemistry of the inner surface will account for the loading and release of cargo. Interactions between the inner surface and molecules of interest act as driving force[7] for the loading process, including hydrogen bonding, electrostatic interaction, Pi-Pi stacking, van der Waals forces, and hydrophobic interaction. Large pore size and stronger interaction between the matrix and the cargo molecules will contribute to a higher loading degree. However, it needs to be addressed that a stronger matrix-drug interaction may also result in a slower release.

### 1.1.2 Synthetic approaches of MSNPs

The synthesis of monodispersed silica nanoparticles can be performed via a sol-gel approach (Stöber method) involving the hydrolysis of tetraalkyl silicates in a mixture of alcohol and water with acid or base as a catalyst. The introduction of templating agents can result in the formation of porous structures and MSNPs. Generally used templating agents are classified into two categories, namely surfactants and non-surfactants. Surfactant-templating is the most widely used approach to obtain MSNPs (Figure 1-2). In 1992 it was reported that the spontaneous self-assembly of the surfactant (CTAB, short for cetyltrimethylammonium bromide) in presence of ammonium hydroxide can lead to the co-assembly of aqueous silica precursor to form an ordered mesoporous silica network[8]. Since then, a large variety of MSNPs such as SBA-[9], KIT-type[10] mesoporous silica was synthesized. These particles are of ordered pore arrangement, particularly suitable for drug delivery. However, the removal of the surfactants required very harsh treatments that prompted the development of synthesis methods via non-surfactants several years later. For example, Wei et al. showed how monolithic mesoporous silica could be produced using D-glucose, dibenzoyl-L-tartaric acid, and D-maltose[11, 12]. Subsequent studies indicated that other molecules, such as poly(propylene)imine dendrimers[13], organic hydroxy-carboxylic acids[14-17] (including citric acid, lactic acid, malic acid, and tartaric acid),  $\beta$ -cyclodextrin-urea complexes[18], fatty alcohols[19] and sugars[20] (including sucrose, maltose, and fructose) could be successfully used to generate mesoporous silica monoliths. Gao et al. proposed tannic acid[21] also as a non-surfactant for the synthesis of large-pore mesoporous silica nanoparticles. The synthesis route using non-surfactants as pore-forming reagents is regarded as a low-cost, environment-friendly, and easy-in-detemplation way to obtain MSNPs.

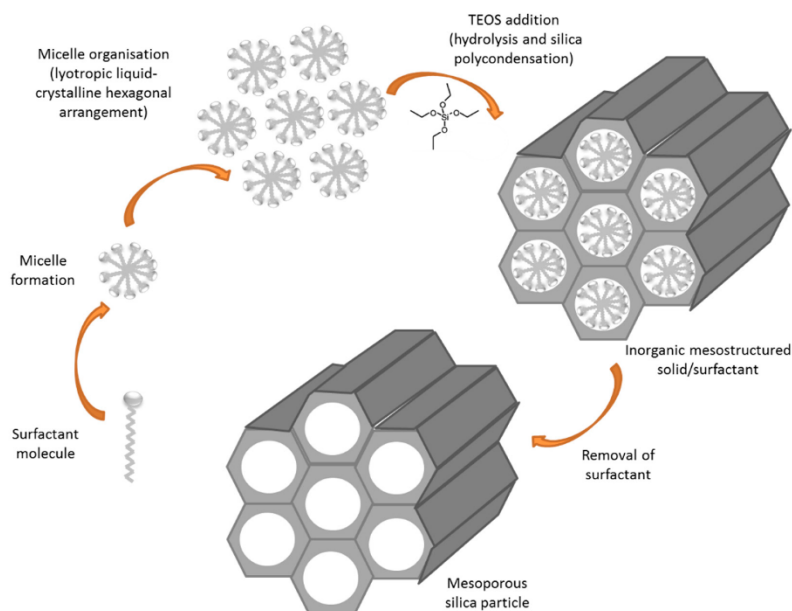


Figure 1-2. Schema of synthesis of MSNPs by surfactants[22]

### 1.1.3 Surface modification of silica nanoparticles

The surface of MSNPs can be modified with two approaches, summarized as co-condensation (one-pot modification) and post-synthesis method (grafting).[23]

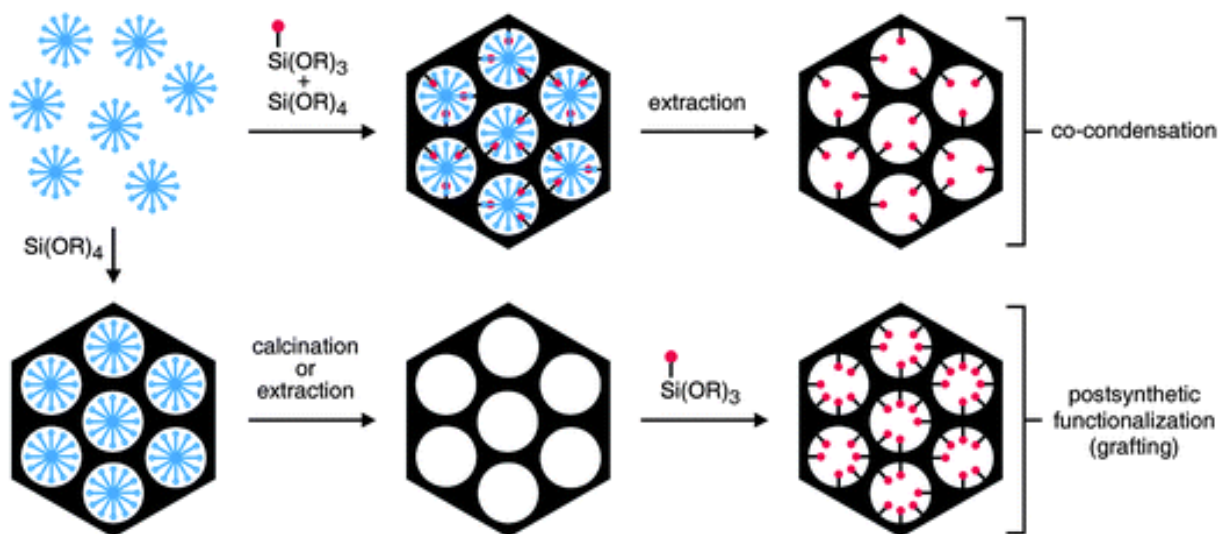


Figure 1-3. Functionalization of mesoporous silica by co-condensation and by post-synthetic treatment. A trialkoxysilane molecule bearing a functional moiety (red) is shown as an example of a precursor. The structure-directing agent (SDA) is represented by the blue micelles.[23]

Co-condensation method, as described by the name, is an approach to modify the surface during the formation of the MNSPs. It works for a large range of organosilanes and results in homogenous silane immobilization with a high density. However, studies showed the existence of silane reactants both on the surface and inside the walls of particles, which is useless for the sequential grafting of functional molecules. Post-synthesis method is conducted by silanization of the interfacial silanol groups either before or after the removal of templates. If a high grafting degree is expected, a high density of silanol groups is required, thus the preferential detemplation method will be a wet approach instead of calcination which leads to loss of reacting sites due to condensation of adjacent silanol groups. The grafting methods can maintain the structure of the silica matrix, yet the distribution of silanes on the surface is hard to control. Imprint coating[24, 25] has been applied with the grafting method to mesoporous silica to control the relative positioning of function groups. To give an example, a triangular template molecule was grafted to the pore surface as spacer. Then, the long-chain silanes reacted with the unoccupied pore surface. Later, the spacer molecules were removed to obtain desired cavities.[26]

Each route has certain advantages. The main advantage of co-condensation over post-synthesis grafting method is the resulting homogeneous distribution of silane molecules over the pore and wall surface, but the addition of silanes will have a pronounced effect on the pore structure and morphology of mesoporous material. High functionalization degrees can lead to decreasing mesoscopic order. Also, the templates can only be removed by extraction as calcination will destroy the grafted organic groups. Post-synthesis (grafting) method allows the removal of templates by both calcination and extraction. By changing the reaction condition, the distribution of the silanes can be controlled. A high functionalization degree can be achieved without destroying the mesoscopic order. However, the modification homogeneity is not as good as co-condensation method.

Density and distribution of the modification are crucial, especially for controlled delivery. The effectiveness of pore shielding and loading capacity is determined by the position and density of the silane chains. A too high density may lead to pore blocking, hindering the transportation of the cargo molecules while a too low density can cause failure in gated control. The position of grafted molecules can influence the loading capacity by changing the chemical properties and accessible pore volume. Selective functionalization, therefore, has been reported for either post-synthesis or co-condensation cases. For the grafting (post-synthesis) method, templating agents used for the formation of the pore structures remain after the generation of MNSPs to assist the selective functionalization of the inner and outer surface or even the separated functionalization of micropores and mesopores. An example is given by Yang et al. for the selective modification of micropores and mesopores in the SBA-15 matrix[27]. Poly(ethylene oxide)–poly(propylene oxide)–poly(ethylene oxide) ( $\text{EO}_n\text{PO}_m\text{EO}_n$ ) copolymers surfactants were selected as porogen. By partial cleavage of the P123 ( $\text{EO}_{20}\text{PO}_{70}\text{EO}_{20}$ ), the mesopore surface could be silanized with triethylchlorosilane while the micropores remained inaccessible until the complete removal of surfactants via calcination. The micropores were then functionalized with trivinylchlorosilane and reacted with a palladium complex to generate a final product with fully accessible mesopores and Pd nanoparticles located in the micropores. In the case of co-condensation[28], the site-selective functionalization of mesoporous nanoparticles can be achieved with a sequential co-condensation approach. The organosilanes were successfully dispersed inside the channels, concentrated in parts of mesopores, or exclusively placed on the external surface of MNSPs depending on the time of addition

of silanes (Figure 1-4). Compared to the grafting approach, it helps avoid the unwanted functionalization of the internal pore surface due to partial diffusion of the grafting reactants into the mesopores. Furthermore, the functional group density on the outer particle surface can be easily tuned by variation of the organosilane-to-silica precursor ratio.

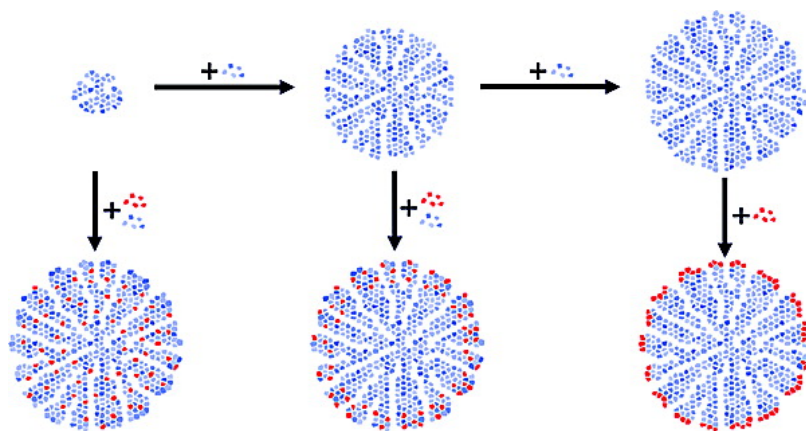


Figure 1-4. Left: Distribution of functional groups depending on the addition time of the organosilane component during synthesis.[28]

The type of silane species also influences the distribution of silanes. For instance, Gartmann et al. have studied the distribution of three silanes including frequently employed 3-aminopropyltriethoxysilane (APTES), 3-aminopropyltris(methoxyethoxyethoxy)silane (APTMEES), and bis(triethoxysilylpropyl)amine (BTESPA)[29]. Deposition of silanes from hexane at room temperature and curing at 80°C led to remarkably different distributions. The uniformity of the functional-group distribution decreases in the series APTES>BTESPA>APTMEES. This is because the distribution of silane is determined by its mobility on the mesoporous silica surface. The tendency is more pronounced when grafting to calcined hexagonal particles with narrower channels. The mobility is also proved to increase with the polarity of solvents. The deposition of APTMEES from toluene leads to excellent selectivity for the external surface of mesoporous silica.

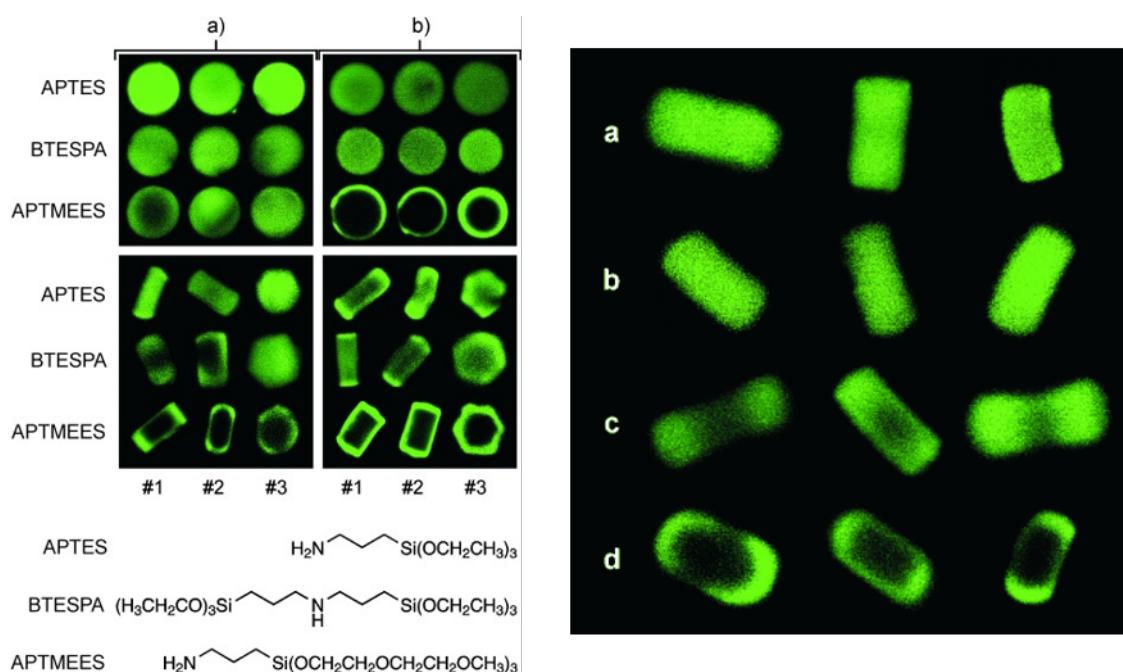


Figure 1-5. Left: CLSM images of SBA-15s (top panels) and ASNCs (hexagonal particles, also known as arrays of silica nanochannels, bottom panels) functionalized with APTES, BTESPA, or APTMEES. Three particles are shown for each silane/silica combination. In the case of the as-synthesized samples, the SDA was extracted before(a) and after(b) FITC labeling. Right: CLSM images of calcined ASNCs after functionalization with APTMEES in ethanol (a), acetone (b), THF (c), toluene (d), and subsequent FITC labeling.[29]



## 1.2 Layer-by-Layer (LbL) approach for surface modification

Layer-by-layer (LbL) assembly is a simple, versatile, and inexpensive approach by which nanocomponents of different groups can be combined to coat both macroscopically flat and non-planar (e.g., colloidal core-shell particles) surfaces. Compared with other available assembly methods, for instance, Langmuir-Blodgett (LB) technique and physical vapor deposition (PVD) and chemical vapor deposition (CVD), LbL assembly is simpler and more universal and allows more precise thickness control at the nanoscale. LbL can be used to combine a wide variety of species—including nanoparticles (NPs), nanosheets, and nanowires (NWs)—with polymers, thus merging the properties of each type of material. This versatility has led to recent exceptional growth in the use of LbL-generated nanocomposites.

### 1.2.1 The basic principle of LbL assembly

The layer-by-layer deposition is a versatile tool to fabricate the thin film. The first LbL research was reported by Iler that they have successfully assembled microparticles on glass slides.[30] The technique was then revitalized by the expansion of its application to a wide range of polyelectrolytes by Gero Decher.[31] A typical process of the building of multilayers requires two oppositely charged polyelectrolyte(PE) solutions and a charged surface as substrate. For example, a negatively charged substrate is dipped into a polycation solution, the polycation chains will stick to the substrate due to the ionic interaction. The substrate is then rinsed with pure water to remove the excess weakly attached chains. A new absorption of the negatively charged layer is obtained by dipping the substrate subsequently to the polyanion solution followed by the same rinsing step. One bilayer of polyelectrolytes is then obtained. The multilayer of polyelectrolyte complex thin film can be constructed by alternative deposition of positively and negatively charged layers(Figure 1-6).

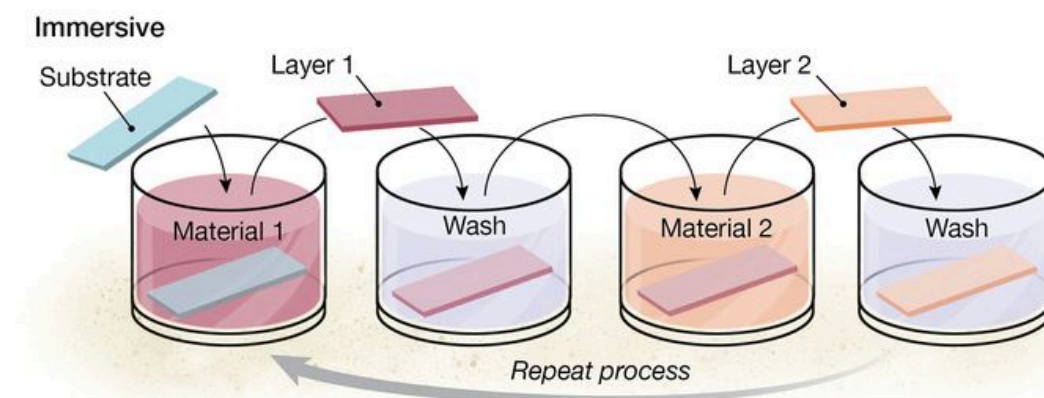


Figure 1-6. Principle of the LbL deposition technique.[32]

LbL assembly technique allows the building of thin films with a controlled structure and composition on almost any substrate. However, the process is somehow time-consuming. The assembly of a single layer normally takes a couple of minutes by dipping, and this has to be multiplied by the number of the deposition layers. To accelerate the process, the spraying process was introduced by Schlenoff in substitution of the dipping process.[33] The same sequence is repeated but the time for the deposition of a single layer is reduced dramatically from 10 minutes to 5 seconds. This is because, by dipping, the polyelectrolytes are absorbed on the surface due to the diffusion of the molecules, while by spraying, the polymers are forced to go faster to absorb on the surface. The thickness of the spray-induced film is thinner than that of dipping because there is a force to press the film during the film fabrication (Figure 1-7).

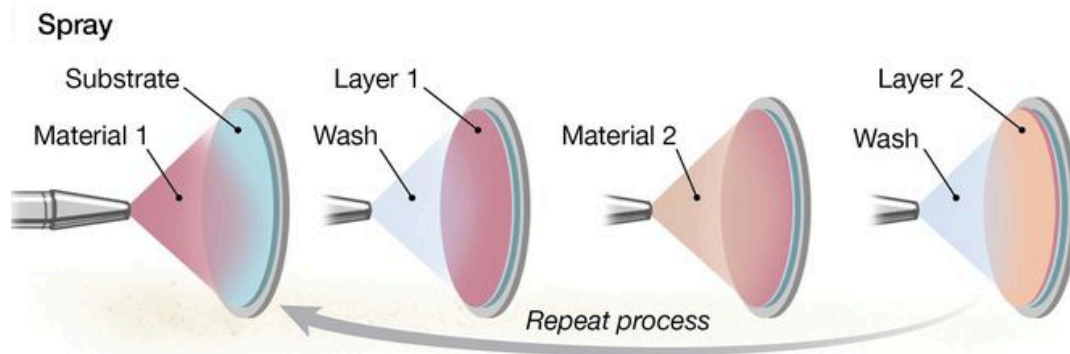


Figure 1-7. Fabrication of LbL film by spraying. [32]

Another fast approach for generating multilayer films by the LbL technique is spin-assisted LbL deposition (Figure 1-8). A drop of polyelectrolytes is placed on the center of the substrate, which is either spun at a low speed or stays in a static state. Then, a high speed of rotation is applied to the substrate, letting the spread of the coating material to the whole surface with centrifugal force. Rotation is continued while the fluid spins off the edges of the substrate until the desired thickness of the film is reached. Normally, volatile solvent is applied. The higher the angular speed of spinning is, the thinner the film is obtained. An interesting point that is worthy to mention here is that, for nanostructures with a high aspect ratio, the high rotation creates a centrifugal force to the material, which may lead to the alignment of the nanostructures in the radial direction.

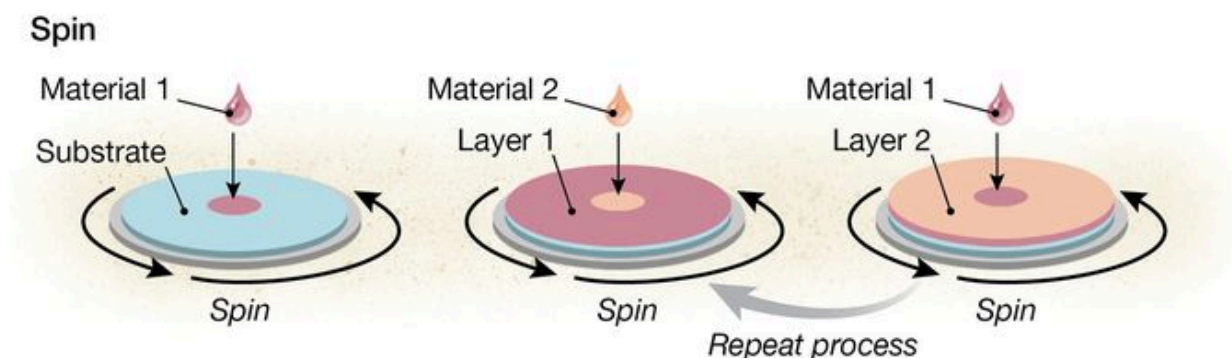


Figure 1-8. LbL assembly of multilayer films by spin-assisted coating. [32]

### 1.2.2 Building blocks for LbL approach

The assembly of LbL films initially involves only polyelectrolyte (PE) complex and nowadays expands to almost all categories of charged material. The most frequently used positively charged polyelectrolytes include polyallylamine hydrochloride (PAH), polyethylenimine (PEI), and poly(diallyldimethylammonium chloride)(PDAA), while the most applied negatively charged polyelectrolytes include polystyrene sulfonate (PSS), poly(acrylic acid)(PAA), and poly(vinyl sulfate). Polymers that are functionalized with ionic groups can also be utilized. Except for polymer, other charged materials including inorganic clusters, nanoparticles (silica, Au, TiO<sub>2</sub>, and magnetic particles), nanowires, nanosheet, organic dyes, dendrimers, polypeptides, DNA, and proteins are also used widely as a building material. Moreover, the bonding force of the building blocks is not limited to the ionic interaction, film assembly by hydrogen bonding[34], covalent attachment[35], biological recognition[36], host-guest interactions[37], and hydrophobic interactions[38] have also been intensively investigated.

### 1.2.3 Parameter influencing the LbL process

The LbL structure depends highly on the assembly conditions. Parameters such as pH, temperature, ionic strength electrolyte type, solvent, and properties of PEs including charge density, molecular weight, concentration, and architecture. To understand better the assembly process, we have discussed several factors that have a profound influence on the structure in this section.

Firstly, pH of a solution has a significant impact on the composition, structure, and cross-link density of LbL multilayer films as a result of the different ionization degrees of PEs under varied pH environment. Basically, strong PEs with substantial charges are fully charged independent of pH; however, weak PEs with carboxylic acid or amine functional groups are highly sensitive to the pH of the solution. Different pH of the solution can determine the ionized state of the polyelectrolytes either within the multilayer film or on the surface.[39, 40] The pH-responsive property of PEs brings opportunities to achieve direct control over the thickness, roughness, and internal structure of multilayer thin films or nanostructures using the LbL assembly technique. It is demonstrated that a tiny change in the pH of the solution for PAA and PAH can induce a pronounced change in the growth mechanism, thickness, and composition of the LbL films.[41-43] Also, a systematic study has been conducted to prove the possibility to tune the swelling behavior of LbL assembled structure.[44]

Temperature is also an important factor that can influence the thickness, structure, and stability of the LbL films.[45, 46] It is proven that multilayer films assembled at high temperatures were thicker than films assembled under ambient conditions due to the swelling of the films and increased interpenetration between layers.[47]

The effect of ionic strength on the stability, permeability, and growth of LbL multilayer systems has been explored by many researchers.[48, 49] The correlation of salt type and concentration with the thickness of multilayer films was also studied specifically. It was observed that the conformational transition of PE solution was switched from extended rod at a low salt concentration to globular coil at high salt concentration and thus give varied structures. An experiment was carried out on PDDA and PSS pairs to indicate how salt concentration influences the multilayer structure. When the salt concentration is below an optimum (around 0.3M), the thickness of assembled multilayer films increases with increasing salt concentration. As the concentration increases to around 0.6M, the bilayer disassembles completely due to the competition of PE pairs caused by external salt ions. It has been revealed that bilayer mass, stiffness, and swelling properties of the multilayer films were also dictated by ionic strength.[50-52]

The structure of PEs and the growth of multilayer thin films or nanostructures are closely related to the solvent environment. For example, Poptoshev et al. studied the effect of solvent quality on the growth and structure of PE multilayer thin films composed of PSS and PAH by varying the ethanol amount in the aqueous PE solutions.[53] The results suggested that decreasing the solvent quality through increasing the ethanol amount led to the increase of film thickness and mass loading, which could be attributed to the reduced solvating effect of aqueous solutions containing electrolyte ions. Thus, it is highly desirable to select a suitable solvent to prepare PE solutions for efficient LbL assembly buildup.

The charge density of PEs is also an important factor affecting the LbL assembly of multilayer systems. The influence of charge density of strong PEs on the growth of multilayer films was studied by Koetse's group using various cellulose derivatives.[54] The results revealed that film thickness increases with the decreasing charge density of PEs. The same trend was also observed in weak PEs such as PAA or PAH.[40]

The influence of molecular weight (MW) of PEs on the structure of PE multilayer films with mobile polymer chains was also evaluated.[55] It is found that an increase in polycation MW gave rise to an increase in the internal roughness of multilayer films. Meanwhile, the swelling and dissociation properties of multilayer films in response to pH could be precisely controlled by polyanion MW.[56] Besides, it is revealed that tunable control over MW of PEs could avoid the use of tedious post-treatment procedures to fabricate multilayer films, which would result in disassembly between internal deposition layers.[57, 58]

In addition, the architectures of PE chain including chain conformation and chain interpenetration can also affect the formation of PE multilayer thin films. As reported by Liu et al.[59, 60], chain conformation plays a pivotal role at a low salt concentration in the growth of multilayer films and chain interpenetration dictates the assembly of films when the multilayers are composed of flexible or semi-flexible PE chains.[61]

#### 1.2.4 Monitoring of the LbL assembly process

The architecture of the thin film is determined by the deposition condition as well as the component in any LbL process. It is essential to monitor the buildup process. For this purpose, ellipsometry is applied to conduct the measurement of the thickness of the fabricated layer. The thickness of the film is proportional to the number of the deposition cycle. When the thickness of the film grows linearly with the number of deposition cycles, the growth is called linear growth as illustrated in Figure 1-9.



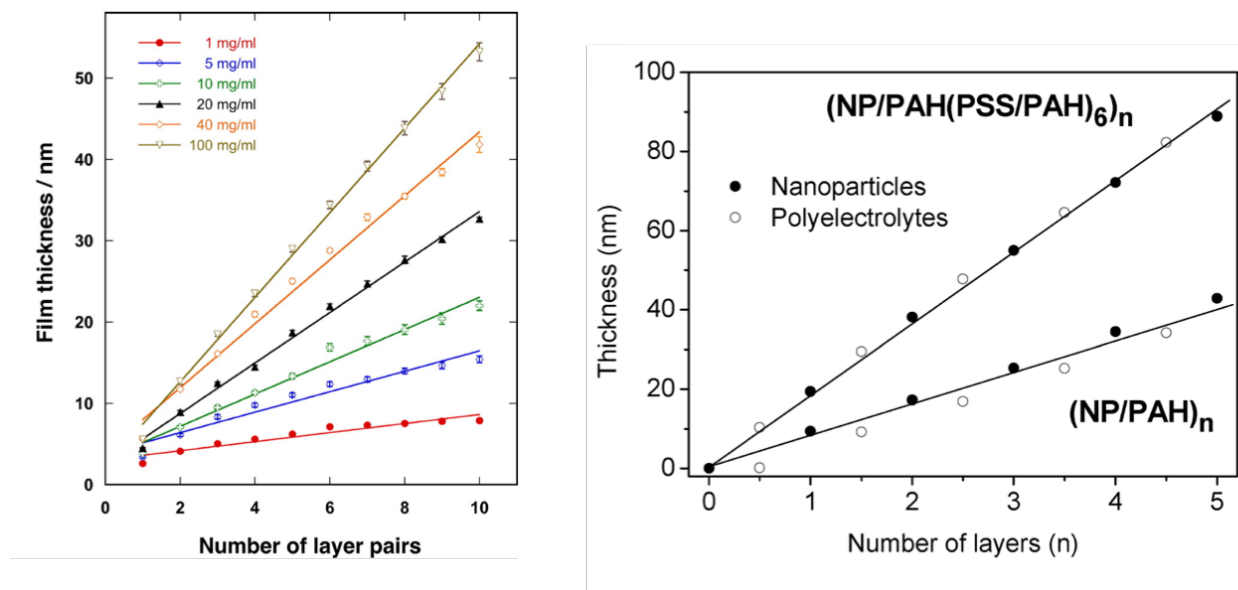


Figure 1-9. The linear growth of film thickness monitored by ellipsometry. Left: (PEI/CNER)<sub>n</sub> film; Right: (magnetic NP/PAH)<sub>n</sub> film[62]

Besides ellipsometry, UV-vis spectroscopy is also a useful tool to state the growth of the film (Figure 1-10). It can be used to characterize the layers on a plate substrate such as quartz slides or even on particles. The increment in absorbance per layer provides information on the film growth in terms of the amount of material absorbed on each layer as well as the structure information of film in terms of the peak position.

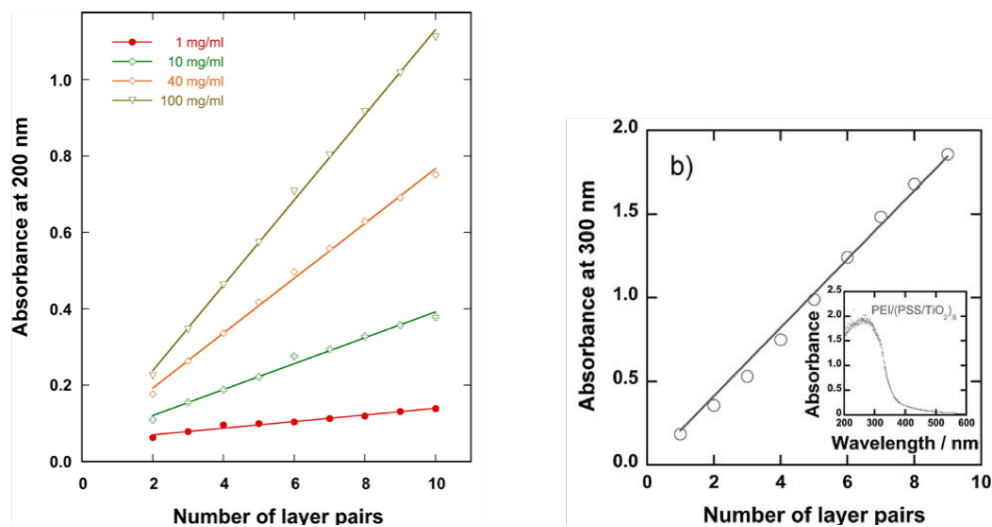


Figure 1-10. UV absorbance of growing films. Left: (PEI/CNER)<sub>n</sub> film; Right: (PSS/TiO<sub>2</sub>)<sub>n</sub> film[63]

For LbL assembly on colloidal particles, the thickness of the shell can be characterized by measuring the diameter of the particles before and after coating via electron microscopy and dynamic light scattering. Decher et. al[64] have monitored the LbL (PSS/PAH)<sub>n</sub> film built on gold nanoparticles with TEM(Figure 1-11).

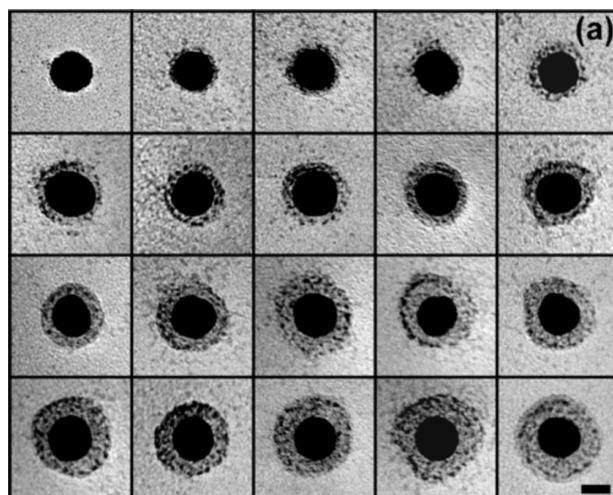


Figure 1-11. TEM image of  $\text{TiO}_2$  particle coated with  $(\text{PSS/PAH})_n$  multilayer[64]

## 1.2.5 Application of LbL assembly

The LbL method shows a great advantage in terms of that it does not require expensive and complicated experimental apparatus or special skills and can be applied to various materials. Thus, various applications were developed based on this simple method. In this section, we present some of the recent applications based on LbL techniques for physical and device uses and chemical and biological uses.

### 1.2.5.1 Physical and device application based on LbL assembly

The LbL method is attractive for the fabrication of photonic devices thanks to its precise control over thickness. Compared to the conventional spin coating method, it allows a coating in a nanometer scale that can bring more accuracy and complexity in structure and function. For example, Kotov and coworkers fabricated photoactive films from tellurium nanowire and polyelectrolyte that were found to be sensitive to light exposure.[65] A light-induced increased conductivity switched the LbL thin films between on and off states, giving an optical gating phenomenon. This light-on–light-off cycle was demonstrated to be very stable under ambient conditions for more than 100 repetitions without photodegradation.

LbL approach was also used to fabricate photovoltaic cells by building poly(p-phenylene ethynylene) (PPE)-based polyelectrolyte and a fullerene derivative multilayers.[66] This cell exhibited moderately efficient incident monochromatic photon to current conversion efficiency (IPCE) response under low-intensity monochromatic light illumination(Figure 1-12).

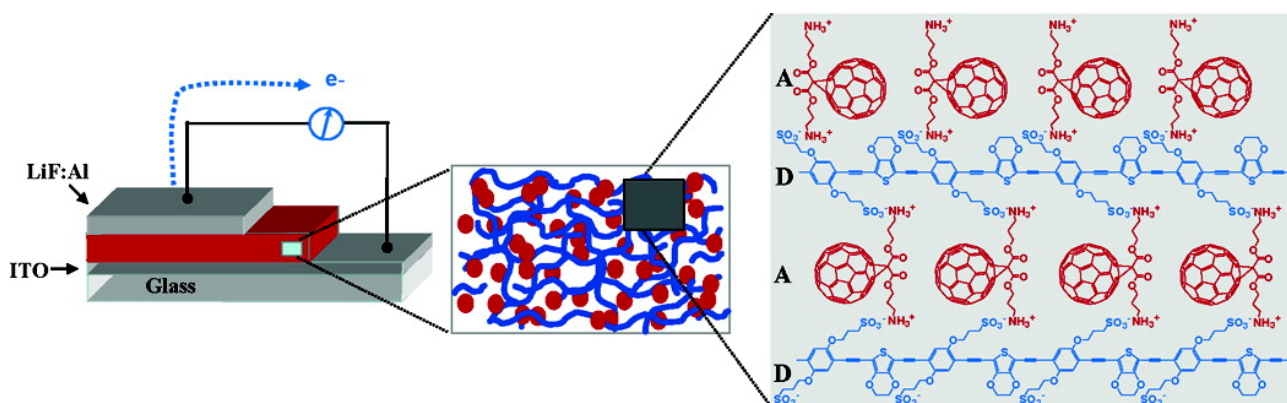


Figure 1-12. Photovoltaic cell composed of PPE and fullerene derivative[66]

LbL can also be used to build polymer-nanoparticle hybrid films. Wang et al. have constructed hybrid films of PPV and CdSe nanoparticles.[67] They have covalently crosslinked the PPV and CdSe particles, which provides a general route for preparing robust and uniform functional thin films. The multilayer films exhibit steady photocurrent responses with an overall optical-to-electrical power conversion efficiency of 0.71% upon illumination with white light at  $10 \text{ mW cm}^{-2}$ .

The fabrication of solar cells has been accomplished using the LbL technique. Agrios et al. fabricated dye-sensitized solar cells based on 50-cycle layers of  $\text{TiO}_2$  large particles on 50-cycle layers of  $\text{TiO}_2$  nanoparticles including photo-sensitive dye N719.[68] The upper scattering layer produced a current density of  $1.8 \text{ mA cm}^{-2}$ , accounting for 38% of the improvement due to the scattering layer over  $\text{TiO}_2$  nanoparticles.

Nolte et al. demonstrated the use of LbL approach and in-situ chemistry for creating multilayer nanocomposites.[69] They produced a special type of dielectric mirror through in situ growth of silver nanoparticles. The dielectric mirror possesses many thin layers that approximate a continuous, periodic refractive index profile to selectively increase the refractive index of precisely defined regions of the LbL film.

The LbL method is very suitable for surface modifications, and thus also be used to prepare superhydrophobic surfaces. Cho et al. has prepared organic-inorganic hybrid films by LbL deposition of PAH and  $\text{ZrO}_2$  nanoparticles that are coated with PAA with facile control of surface roughness and hydrophobicity.[70] The structure of films was controlled by the number of deposition cycles using PAA-coated  $\text{ZrO}_2$  nanoparticles and the pre-layer with PAH and PAA. Then hydrophilic silica nanoparticles were deposited on a 10-bilayer surface of PAH/PAA-coated  $\text{ZrO}_2$  followed by a simple fluorination. The yielding film exhibit superhydrophobic properties. Moreover, the chemical stability of the film was greatly increased by heat-induced cross-linking of the film.

Rubner et al. prepared hydrophilic patterns on superhydrophobic surfaces that can be used for water harvesting.[71] These were created using water/2-propanol solutions of a polyelectrolyte to produce surfaces with extreme hydrophobic contrast. Selective deposition of multilayer films onto the hydrophilic patterns introduces different properties to the area including super hydrophilicity. Multiple interesting properties like anti-reflective, antifogging, and self-cleaning properties can also be achieved by layer-by-layer deposition of  $\text{TiO}_2$  and  $\text{SiO}_2$  nanoparticles.[72] The presence of nanopores in the  $\text{TiO}_2/\text{SiO}_2$  coatings results in super hydrophilicity as well as anti-reflective properties. The super hydrophilicity of contaminated coatings could also be readily recovered and retained after ultraviolet irradiation.

#### 1.2.5.2 Chemical and biological application based on LbL assembly

The LbL technique has been applied in diverse biological fields like material separation, controlled permeation and release of target materials, reactor usages, and sensing to name a few.

Selective permeation and permeation blocking are fundamental properties of membranes. Hollman et al. have reported non-stoichiometric immobilization of charged LbL multilayers within a confined pore geometry, resulting in an enhanced volume density of ionizable groups in the membrane phase.[73] Such high density of the effective charge density permits permeation control upon Donnan exclusion of ionic species.

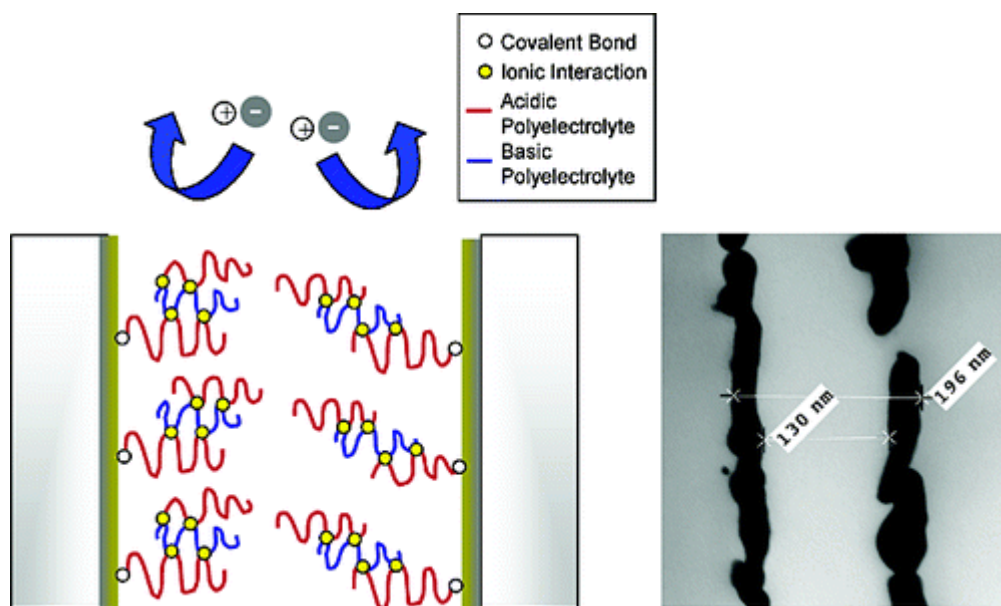


Figure 1-13. Left: permeation principle of the system; Right: single pore lined with an Au nanolayer[73]

Shiratori and coworkers have proposed a LbL film for the removal of environmentally unfriendly gasses.<sup>[74]</sup> They fabricated LbL films from PAH and PAA on a glass filter followed by thermal treatment. Basic odorants such as ammonia gas can be effectively trapped through electrostatic interaction with carboxyl groups, and aldehyde species can be trapped by amino groups in the film through Schiff's base formation. Rubner et al. also reported permeability control using LbL films.<sup>[75]</sup> They proposed pH-induced hysteretic gating of track-etched polycarbonate membranes that were filled with the LbL assembled polyelectrolyte multi-layers comprising PAH and PSS at high pH value. Swelling/deswelling properties of the multilayers lead to gating properties of material transport through the membrane. Such stimuli-responsive mechano-chemical valves can be used to gate the flow of water in microfluidic channels allowing either an open or closed state at a single pH condition.

Apart from the above-mentioned application, the LbL methods can also be employed to construct membranes and capsules for controlled release. Lynn et al. used a degradable polymer as a component of the LbL films to realize controlled DNA delivery.<sup>[76]</sup> Multi-layered films up to 100 nm thick containing a synthetic degradable cationic polymer and plasmid DNA coded with green fluorescent protein were fabricated onto the surfaces of planar silicon and quartz substrates. Degradation of the former components induced the release of the plasmid, which was confirmed by high levels of enhanced green fluorescent protein in the cell. Wang et al. synthesized nanoporous polymer-based spheres by sequentially depositing polyelectrolytes in mesoporous silica particles, followed by removal of the templates.<sup>[77]</sup> The resulting PAA/PAH nanoporous polymer spheres exhibited a high capacity for enzyme loading, with stimuli-responsive reversible loading and release of the protein triggered by changes in solution pH. The proposed systems, with nanoscale porosity and designed functionality, are envisaged to offer new opportunities for their application in biosensing, catalysis, and drug delivery.

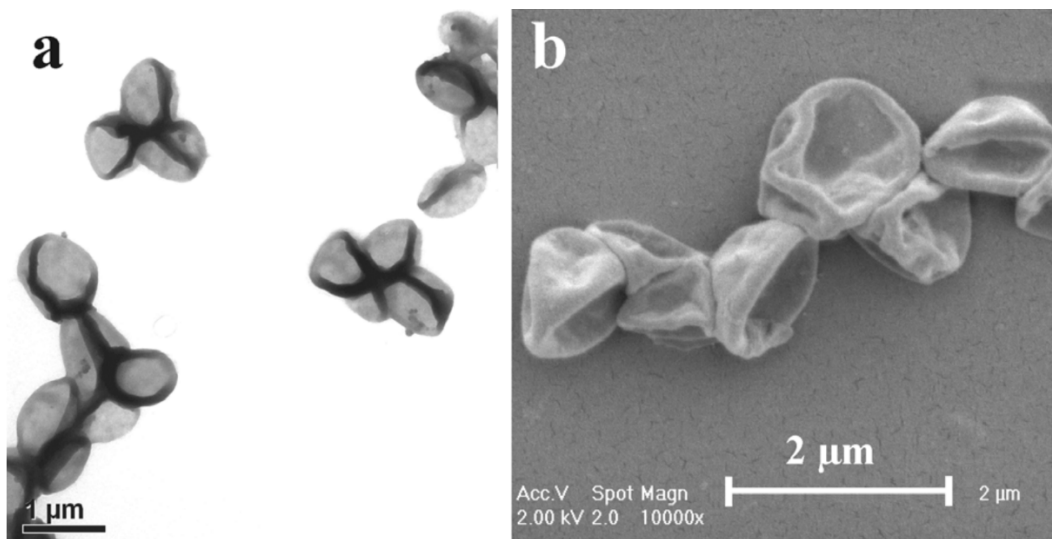


Figure 1-14. TEM(a) and SEM(b) images of the samples prepared using APTS-HMS as templates<sup>[77]</sup>

LbL approach is demonstrated to be suitable to build chemical reactors owing to its adaptability.<sup>[78]</sup> For example, Bruening et al. embedded gold nanoparticles within alumina porous matrix through LbL assembly to form catalytic membranes (Figure 1-15).<sup>[79]</sup> These colloid-modified membranes showed remarkable conversions of 4-nitrophenol to 4-aminophenol at high flow rates in the presence of the reducing reagent,  $\text{NaBH}_4$ . This system reduced >99% of 0.4 mM 4-nitrophenol at linear flow rates of  $0.98 \text{ cm s}^{-1}$ . Their results indicate a turnover number >1000 mol of 4-nitrophenol per mol of gold contained within the membrane.

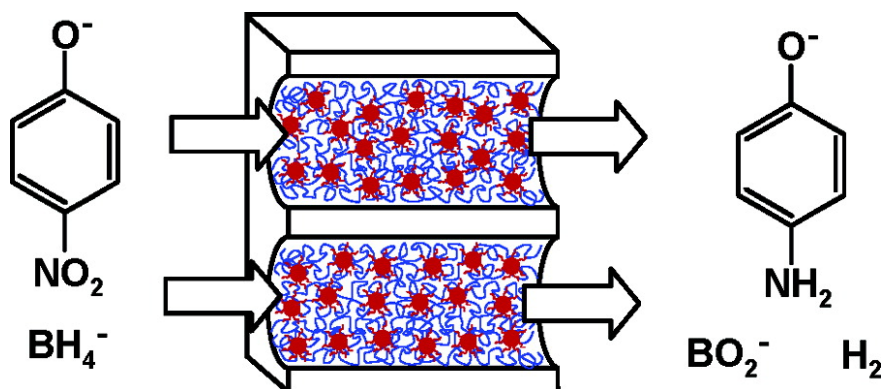


Figure 1-15. Au nanoparticle-embedded alumina porous matrix for catalyst use<sup>[79]</sup>

Shchukin et al. have prepared PSS/PAH LbL microcapsules containing  $\text{TiO}_2$  nanoparticles that catalyze photosynthesis of urea from inorganic precursors ( $\text{CO}_2$  and  $\text{NO}_3^-$ ) in aqueous solution (Figure 1-16).<sup>[80]</sup> In this work, poly(vinyl alcohol) was employed as an electron donor to facilitate the photosynthetic process. Decreasing the size of the confined microvolume of polyelectrolyte capsules accelerates the  $\text{NO}_3^-$  photoreduction, which is a limiting stage of the urea photosynthesis and, correspondingly, increases the efficiency of urea production. The highest yield of urea photosynthesis (37%) was achieved for Cu-modified  $\text{TiO}_2$  nanoparticles encapsulated inside 2.2  $\mu\text{m}$  poly(styrene sulfonate)/poly(allylamine hydrochloride) capsules.

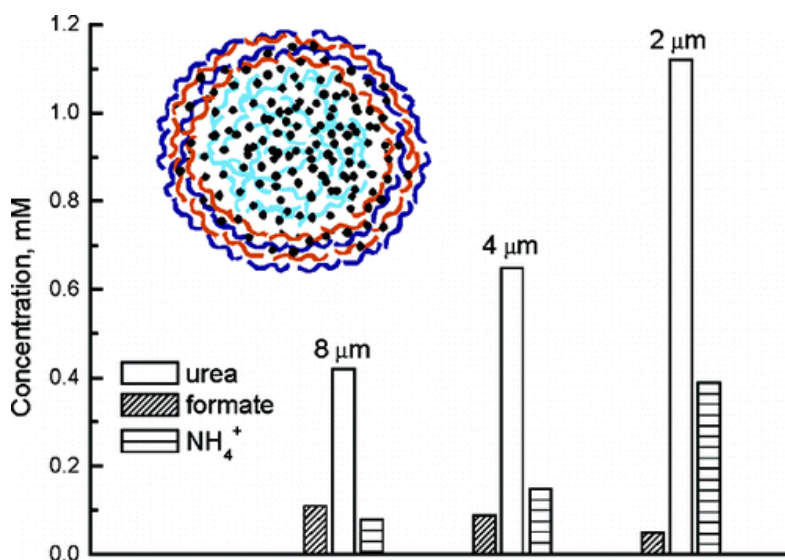


Figure 1-16. Concentration of urea, ammonia, and formate after 5 h of irradiation of  $\text{TiO}_2$  suspension and  $\text{TiO}_2$ -loaded polyelectrolyte capsules of 8.1, 4.2, and 2.2  $\mu\text{m}$  diameter<sup>[80]</sup>

Another application of LbL assembly is to fabricate films that is able to be used for bioprotective purposes. For example, Kotov and coworkers developed antimicrobial coating using LbL assembly of silver nanoparticles.<sup>[81]</sup> Silver is known to show effective antimicrobial activity. They constructed a nanostructured, hybrid, multifunctional composite containing clay layers implanted with starch-stabilized silver nanoparticles. The resulting composite showed excellent structural stability with no detectable levels of silver lost over 1 month. Moreover, almost complete growth inhibition of *E. coli* over an 18h period was observed. The amount of silver eluted from the LbL composite over 1 month was determined to be only 0.5–3.0  $\mu\text{g L}^{-1}$ , which did not prevent the growth of mammalian tissue cultures. This LbL composite was proved to show biocompatibility with a human osteoblast cell line.

Not limited to the theoretical research, LbL coating techniques have already been used in several practical applications including drug nano-encapsulation, biocompatible coating (eye lenses), and cellulose microfibril coating.<sup>[82-84]</sup>

### 1.3 Polymer optical fiber (POF) for biomedical use

Optical fibers with the ability to propagate and transfer data via optical signals have been used for decades in medicine. Biomaterials featuring the properties of softness, biocompatibility, and biodegradability enable the use of polymer optical fibers in biomedical

cal engineering applications such as medical implants and health monitoring systems. In this section, the basic principles and processing of optical fiber will be introduced following by a summary of the biomedical use of optical fibers.

### 1.3.1 Basic concept of optical fibers

Optical fibers are thin strands that can be used to transfer optical signals based on total internal reflection (TIR). It can be made of conventional silica glass, fluoraluminate, fluorozirconate, crystalline materials, and polymer. Optical fibers consist of two basic parts: core and cladding (Figure 1-17). The core part has a refractive index (RI) that is higher than that of the cladding material. By that, the light is constrained in the inner core region and cannot escape to the outer cladding. The structural design has a very low loss of intensity of light. Waveguiding properties are mainly determined by the difference of the two refractive indices at core and cladding. By controlling this difference, one can design the maximum acceptance angle of the fiber. To represent the difference of the different RI, the numerical aperture (NA) ( $A_N$ ) is defined as

$$A_N = \sqrt{n_{core}^2 - n_{cladding}^2}$$

Equation 1-1. Numerical aperture (representation 1)

NA reflects the fiber's maximum acceptance angle  $\alpha_{max}$  as shown below and in Figure 1-17. Typically, the value of the NA of step-index POFs is 0.5 with an acceptance angle of  $30^\circ$ . Those fibers are called standard-NA-POF.

$$A_N = \sin \alpha_{max}$$

Equation 1-2. Numerical aperture (representation 2)

Optical fibers are classified into two groups based on the diameter of the core and NA value: single-mode and multi-mode. Single-mode optical fibers have small cores that can only transmit light in one ray. Multi-mode optical fibers allow transmitting light in multiple rays. The larger the core diameter and NA are, the more modes are allowed in the optical fiber. The number of modes can be calculated by the following equation and V is defined as fiber parameter:

$$V = \frac{\pi D}{\lambda} A_N \quad (D \text{ is the core diameter})$$

Equation 1-3. Fiber parameter

The multimode fibers, based on the structure, include two types of step-index (SI, homogeneous core) and graded-index (GI, inhomogeneous core). [85] Applications in many different fields are carried out with optical fibers. To name a few, they are the emerging devices to be employed for telecommunications, [86, 87] sensors, [88, 89] endoscopes, [90, 91] interferometers, [92, 93] aerospace and geographical setups, [94] geotechnics and civil engineering, [95, 96] fiber lasers, [97] and healthcare applications. [98, 99]

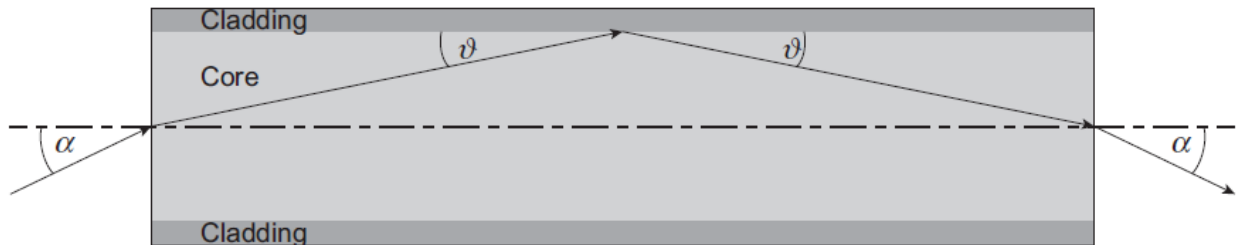


Figure 1-17. Light transmission in an optical fiber occurs by total internal reflection for which the transmitting fiber is coated with outer cladding material that has a lower refractive index than the inner core material. [100]  $\alpha$  is defined as incident angle,  $\theta$  is the refracted angle when light enters the optical fiber.



### 1.3.2 Materials and fabrication techniques of polymer optical fibers

#### 1.3.2.1 Industrial fabrication techniques of POFs

Plenty of industrial manufacturing techniques for the production of polymer optical fibers were developed and chosen depending on the products' requirements, such as production cost, planned production volume, acceptable attenuation, and whether step-index or graded-index POF. The production techniques can be divided into discontinuous and continuous processes listed in Figure 1-18.

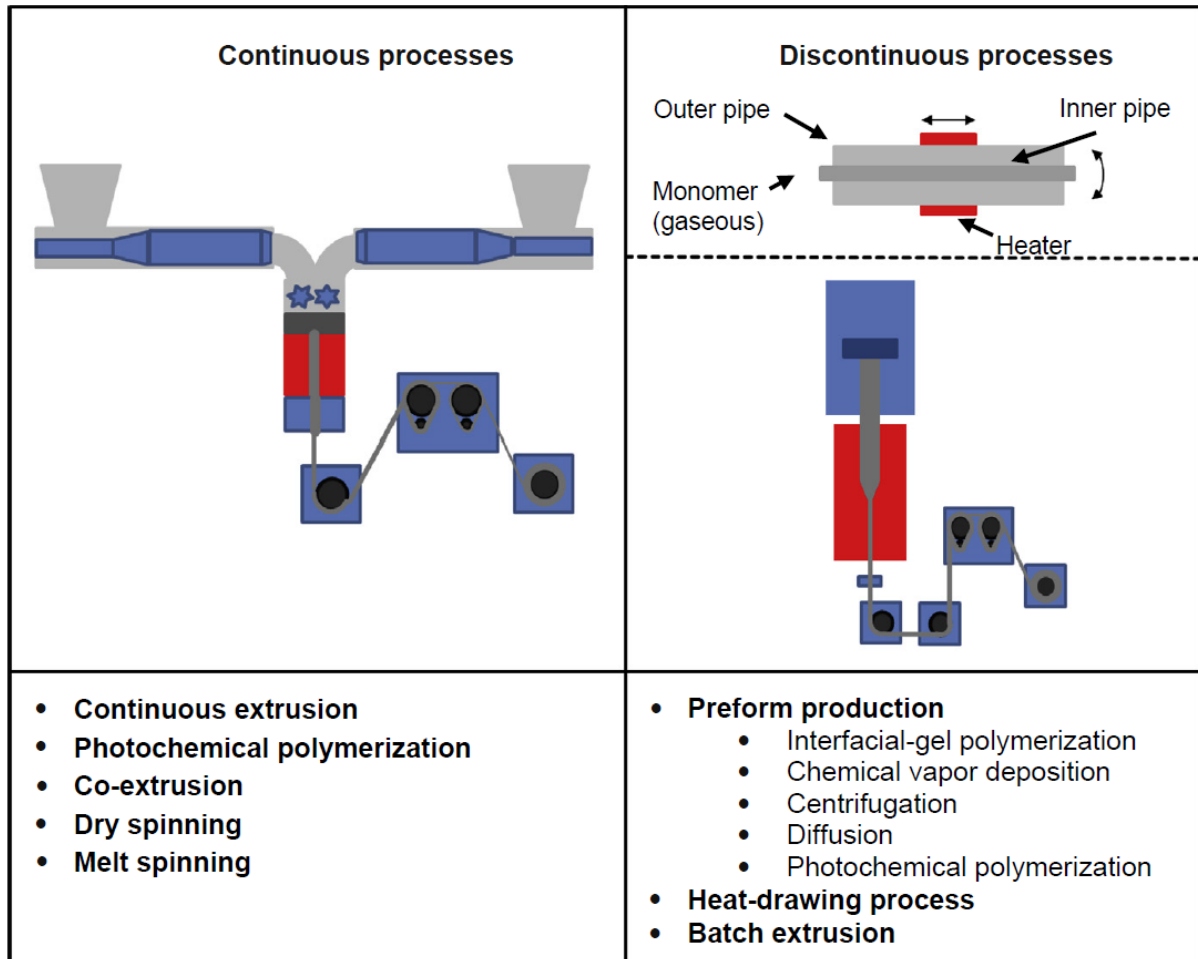


Figure 1-18. Overview about the different manufacturing techniques for POFs[100]

The most used discontinuous manufacturing process for optical fibers is the preform production with subsequently heat drawing.[101] The main differences between the methods lie in the production of the preform itself. The preform is an intermediate fabrication product and has the same optical properties as the later POF except for the diameter of the preform. It is drawn to a thin but long optical fiber with relatively the same geometric structure in a smaller dimension.

For the production of preforms for SI profiles, the structure can be achieved either by wet or dry processes. The wet process contains both a polymer and a monomer/prepolymer. The polymer, which will be the core or the cladding, is either surrounded or filled with the pre-polymer correspondingly before an in situ polymerization of the pre-polymer is started. The dry process is a further manufacturing step where the core and the cladding are joined. This is necessary because both the core and the cladding are formed in separated processes. For both wet and dry processes, it is essential to avoid any contamination on the boundary layer between core and cladding.[102]

For the production of the preform for GI profiles, the processing is slightly more complicated than that of SI profiles. Five methods can be applied, containing interfacial-gel polymerization, chemical vapor deposition, centrifugation, diffusion, and photochemical polymerization. The interfacial-gel polymerization method is introduced as an example. A tube made of PMMA is used and added

with two monomers with different molecular masses while the one with higher molecular weight has a higher refractive index. A rotation is applied to generate a symmetrical graded index (GI) profile. Due to the heating of the PMMA tube, a gel layer begins to grow on the inside of the tube surface. The monomers diffuse into this layer and get embedded. The diffusion rate of the monomer with a lower molecular weight is higher. This leads to a concentration gradient in the growing gel layer and therefore to the refractive-index profile. Finally, the refractive-index profile is fixed by polymerization.[103]

The heat-drawing process is conducted after the fabrication of the preform. The preform is fixed in a clamping system stably and is continuously fed into an oven where the preform is heated above the glass-transition temperature of the material. The polymer changes from a solid into a viscous state and then is drawn by the godet wheels. The diameter of the POF can be adjusted by the take-up speed and the feed rate of the clamping unit and is controlled by the diameter measuring unit.[104] Several parameters have an influence on the final optical and mechanical properties of the POFs, including mainly the purity of the preform, the molecular weight distribution of the polymer, the geometry and temperature of the oven, and the drawing speed.[102, 104, 105] This method is very simple and flexible with an outcome of POFs with outstanding optical quality but pitifully of low productivity and high production costs.

In comparison with the discontinuous approach, the continuous approach is suitable for the production of SI-POF and similar to the batch extrusion technique. Monomers, initiators, and additives are continuously added into a heated reaction chamber, where the polymerization reaction is running. The mixture of polymer and remaining monomer is then pumped into an extruder. The polymerization process continues in the tempered extruder to higher conversion until the mixture is conveyed through a degassing unit. The decrease in pressure in the degassing device leads to evaporation of the remaining monomers. These gaseous monomers are condensed and pumped back into the polymerization reactor while the polymer remains in the extruder. The extruder conveys the polymer through a spinning nozzle. The cladding material is deposited either there or in a separate spinning nozzle, which is provided by an additional extruder. After the core-cladding structure is formed, the fiber is cooled down, stretched, and wound up.[102, 104]

#### 1.3.2.2 *Novel materials and fabrication of POFs for biomedical use*

Except for the materials that have been used for industrial production, natural materials such as silk, chitosan, cellulose and synthetic polymers like hydrogels and elastomers have also been applied[106, 107], especially for biomedical purposes. To date, hydrogels and other polymers which offer biocompatibility and biodegradability features have earned lots of attention for fabricating optical fibers which are aimed to be employed in medical and health monitoring applications.

These materials can also be fabricated by similar approaches as those applied industrially like molding. 3D printing<sup>[108]</sup> has also attracted great attention as a new fabrication method as it can provide fast prototyping, great flexibility, cost-effectiveness, and without the need for complex steps such as oxidation at high temperature like in the conventional methods. It allows also to build easily complex structure as the materials are placed layer by layer according to the model design.<sup>[109]</sup>

### 1.3.3 Biomedical application of optical fibers

In this section, we have represented some recent applications of optical fibers for biomedical use, ranging from sensing, diagnosis to phototherapy and drug delivery.

#### 1.3.3.1 *POF-based sensor for sensing application*

Sensing and monitoring have been realized on optical fiber of different materials via distinguished mechanisms. Yetisen et al.[110] has reported a hydrogel optical fiber for continuous glucose sensing in real-time(Figure 1-19). The hydrogel fibers consist of poly(acrylamide-co-poly(ethylene glycol) diacrylate) cores functionalized with phenylboronic acid. The complexation of the phenylboronic acid and cis-diol groups of glucose enables reversible changes of the hydrogel fiber diameter. The analyses of light propagation loss allow for quantitative glucose measurements within the physiological range.



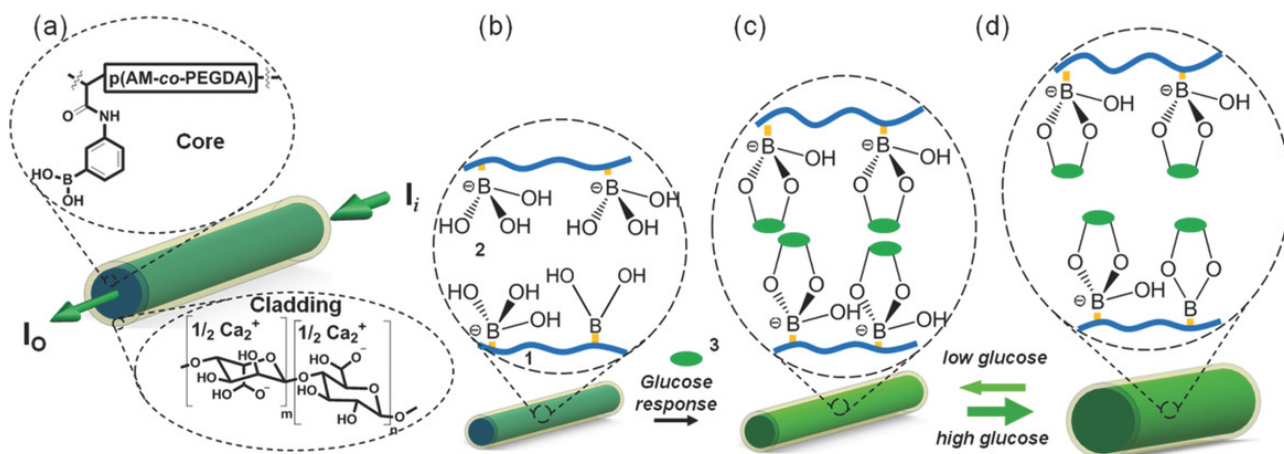


Figure 1-19. Design of the glucose-sensitive hydrogel optical fibers. a) Structural composition of the glucose-sensitive p(AM-co-PEGDA-co-3-APBA) fiber core cladded with Ca alginate. b) The hydrogel matrix is functionalized with 3-APBA. (1) PEG-crosslinked polyacrylamide hydrogel, (2) 3-APBA in charged tetrahedral state, (3) glucose. c) The PBA derivative binds cis diols of glucose molecules and changes the RI of the hydrogel fiber. d) The increase in the concentration of the glucose molecules can be quantified by measuring the variation in the intensity of the output light.[110]

Guo et al.[111] have demonstrated highly stretchable, elastic fibers made of alginate-polyacrylamide hydrogels in a step-index core-cladding structure as strain sensor that can be a useful building block for wearable device and implantable therapy-enabling devices. The sensor is with a large dynamic strain range of 120% and distributed strain sensing based on multiplexing different absorption materials.

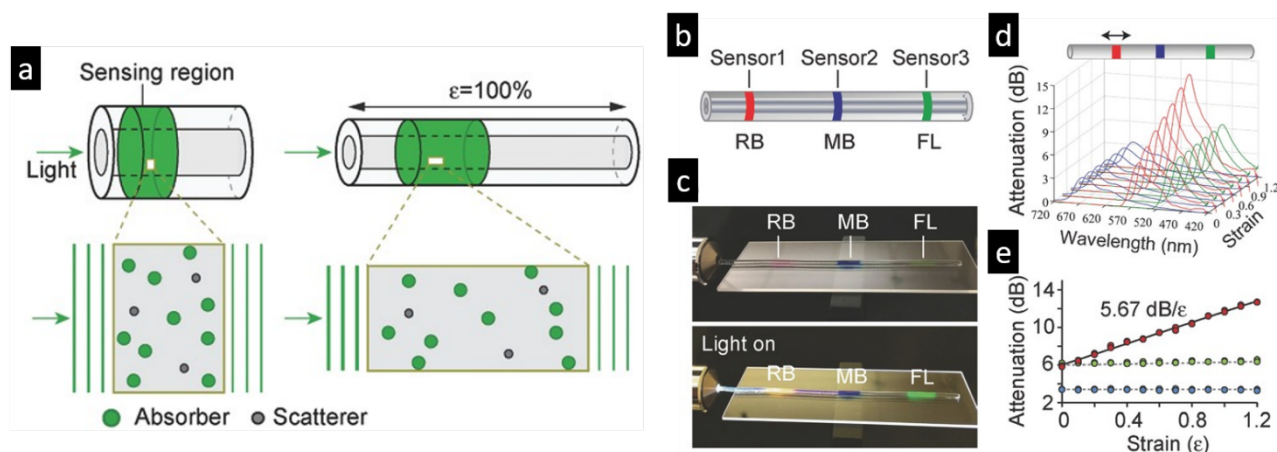


Figure 1-20. a) Illustration of the optical loss in a sensing region containing absorption and scattering elements. As the fiber is stretched, the distribution of the loss elements is altered, resulting in loss increasing exponentially with the length of the sensing region. This relation offers a simple technique for strain sensing. b) Schematic of a fiber with three sensor regions doped with different dyes, respectively: RB: rose Bengal, MB: methylene blue, FL: fluorescein. c) Photos showing a dye-doped fiber on a glass slide, without (top) and with (bottom) excitation broadband light. d) Extracted absorption spectra of the three sensors when local strain was applied to each sensor at a time (RB as an example). e) The dye absorption as a function of strain, showing linear readout in terms of dB/strain and negligible crosstalk between sensors (RB as an example).[111]

### 1.3.3.2 POF-based drug delivery systems

Optical fibers for drug delivery use are not as intensively studied as for sensing applications. Mainly, the optical fiber was used as a light trigger to actuate the release of drug molecules. Zamadar et al.[112] has developed an optical fiber for photodynamic therapy. An optical fiber with a maneuverable probe tip that sparges oxygen gas and photodetaches pheophorbide (sensitizer) molecules. Singlet oxygen is produced at the probe tip surface which reacts with an alkene spacer group releasing sensitizer upon fragmentation of a dioxetane intermediate. Optimal sensitizer photorelease occurred when the probe tip was loaded with 60nmol sensitizer, where crowding of the pheophorbide molecules and self-quenching were kept to a minimum. The fiber optic tip delivered pheophorbide molecules and singlet oxygen to discrete locations.

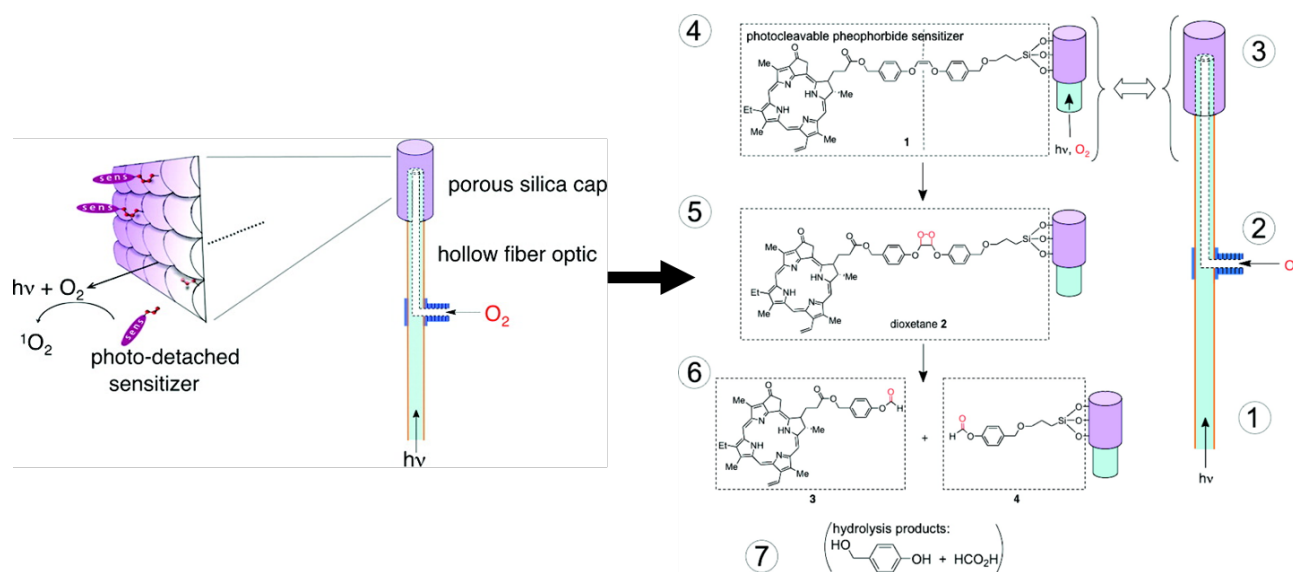


Figure 1-21. Concept of the singlet oxygen fiber optic: (1) illuminator-to-fiber coupling, (2) compressed oxygen-to-fiber coupling via a flare T-valve to a borosilicate fiber optic consisting of a Teflon gas flow tube, (3) porous Vycor glass (PVG) cap-to-fiber coupling, (4) photocleavable sensitizer solid, (5) internally flowing light and oxygen, externally produced  $^1O_2$ , [2 + 2] cycloaddition at the alkene site, (6) cleavage of sensitizer 3 free from the probe tip via the scission of dioxetane 2, and (7) production of cofragment 4 and hydrolysis byproduct.[112]

Another example of POFs as a matrix for light-triggered delivery has been demonstrated by Nazari and coworkers[113]. POFs integrated with light-responsive metal-organic frameworks (MOFs) have been produced, showing a good performance in chemotherapy. Optical fibers were coated with a thin layer of metal-organic-framework UiO-66 (synthesized by Universitetet i Oslo, is a metal organic framework made up of  $[Zr_6O_4(OH)_4]$  clusters with 1,4-benzodicarboxylic acid struts) and anticancer drug 5-Fluorouracil (5-FU) is deposited within the pores. Light with appropriate wavelength was used to trigger the release of drug at a high rate on demand.

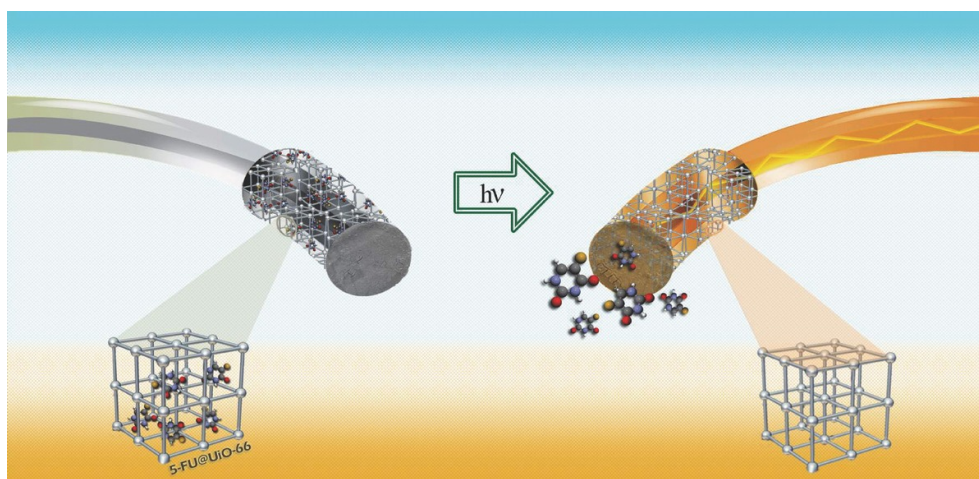


Figure 1-22. Schematic illustration describing the encapsulation of 5-FU into the UiO-66 thin film optical fiber and novel drug delivery system[113]

### 1.3.3.3 POF-based phototherapy

Optical fiber can be used for phototherapy by transmitting light into human tissues, but core-only fibers suffer from a huge loss of the light signal by scattering due to the inhomogeneous RI of the surrounding tissue. To tackle this issue, Applegate et al. [114] has proposed a SI core-cladding silk-based optical waveguide (Figure 1-23). The core is made of a silk film covered by silk hydrogel cladding. This fiber shows a smaller propagation loss compared to the core-only fiber and is less sensitive to the tissue environment. With its great softness, biocompatibility and degradability, it is of great potential to be applied as a light guide.

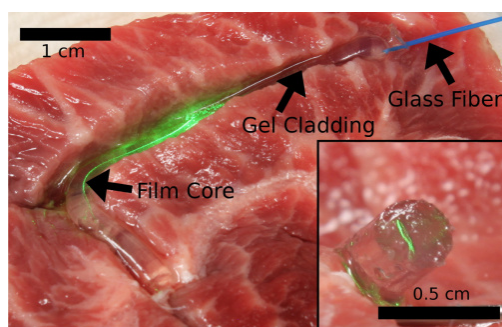


Figure 1-23. Silk waveguide guiding light in tissue. Light coupled from multimode glass fiber is confined within the silk film core of a 3.5 cm long waveguide. Inset shows the core of the waveguide glowing green after closure of the incisions.[114]

#### 1.3.3.4 Other potential biomedical applications of POFs

Optical fibers are especially suitable for sensing biochemical substances and monitoring of tissues as illustrated in Figure 1-24a and b. A variety of probes including antibody-conjugated organic dyes, pH-sensitive fluorophores, nucleic acids have been used in clinical to examine tissue slices, blood samples, and cells from tissues. These probes can be integrated into implantable, transparent light-guiding hydrogels and be fiber-optically accessed from outside the body. This allows continuous monitoring of biomarkers and chemical substances in vivo. In addition to the sensing of substances, the optical fibers can also be used to monitor physiological conditions, such as blood perfusion, oxygen consumption to name a few[115, 116]. The fluorescence probes can also be embedded in the waveguide to complement label-free sensing. Phototherapies such as blue light therapy to bigger and deeper tumors can be achieved by delivering light into deeper target tissues using an optical microneedle array (Figure 1-24c). Other potential applications[106] are summarized in Figure 1-24.

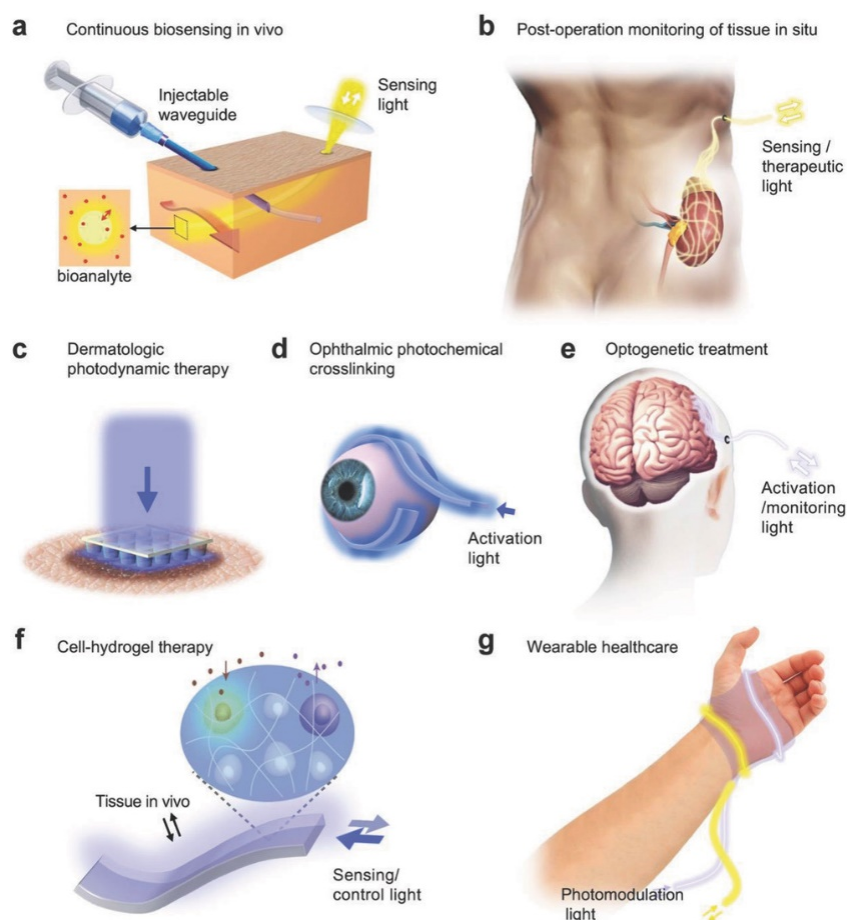


Figure 1-24. Potential medical applications of biomaterial waveguides. a) Continuous monitoring of biological analytes using an implanted optical fiber. b) Monitoring of the viability and function of a transplanted kidney using a mesh-type optical waveguide. c) Photodynamic therapy of skin tumors using an optical microneedle array. d) Minimally invasive photochemical crosslinking of the

sclera using a flexible waveguide. e) Long-term optogenetic treatment of brain disorders using implanted optical waveguides. f) On-demand synthesis of therapeutic substances from optogenetic cells encapsulated in a light-guiding hydrogel implant. g) Photo-modulation of wound healing using a wearable photonic bandage.[106]

## 1.4 Light-responsive drug release

Since the drug delivery process is one main factor that impacts the therapeutic effect, the development of novel delivery systems, improving the efficacy of old drugs besides the costly and time-consuming invention of new drugs, is gaining more interest. Massive efforts have been spent to administering the pharmaceutical compounds in multiple scales[117-119]. Versatile systems have been formulated over various materials (silica[6], gold[120], polymers[121], etc.), shapes (nanospheres, nanotubes[122], fibers[123], worm-like structure[124], etc.), and dimensions. The delivery has changed from the traditional passive less-effective approach to a controlled, targeted, and active process. More advanced delivery systems based on the responsive ability to many external stimuli including pH, temperature, redox potential, light, magnetic field, ultrasound, and mechanical forces are intensively studied[5], enabling the on-demand release. Light, as a stimulus, stands out as a fast, non-contact, controllable trigger towards a light-responsive delivery system. Further integration of these nanosystems to other matrices, particularly fibers, can expand significantly the application scenarios from conventional pharmaceutical use to medical devices, for example, wound patches[125], implants[126], and functional textiles[127].

The intelligent therapy has called for precise control of drug dosage as well as location and timing of administration. A variety of stimuli-triggered drug delivery systems have been reported and can be classified into two categories that work in either open or closed circuit[128-131]. Closed-loop systems are self-regulated and respond to changes in the physiological environment. Open-loop systems are independent of the physiological condition and release active molecules in response to external stimuli. The release profile of it depends on the intensity and duration of the stimulation. The accuracy of control and adaptability makes open-loop systems more attractive in personalized therapy. In particular, light-responsive drug delivery systems are advantageous for their noninvasive nature, high spatial resolution, temporal control and convenience, and ease of use. For the above-mentioned reasons, light has been applied in various biomedical applications including image-guided surgery, degradation of tissue engineering scaffolds, and photodynamic therapy for cancer. Beyond these applications, light has also been applied to trigger drug release mainly via three strategies: photoisomerization, where the excess energy causes structural changes; photocleavage, where the absorbed light energy is sufficient to break covalent bonds directly or by a photochemical reaction; and photothermal, where the absorbed photon energy is dissipated via vibrational motion.[132]

### 1.4.1 Controlled release via photoisomerization mechanism

A controlled release can be realized via further design[133-136] of nanocarriers with stimuli-responsive molecules. Stimuli-responsive delivery systems are built based on the property change of the corresponding molecules as a response to the stimuli. The change may either be an irreversible structure rupture, or a reversible conformation change.

Coumarin is one type of photo-responsive molecule. Mal et al. reported a UV light-induced reversible drug delivery system. 7-((3-triethoxysilyl) propoxy) coumarin was grafted to the silanol groups on the MSNPs[137]. The UV light with a wavelength of 310nm can induce photodimerization between two adjacent coumarin molecules to form cyclobutane rings that act as hinged double doors to block the drug molecules in the pores (Figure 1-25). When the system was irradiated with a light of 250nm, the dimer rings were photocleaved, yielding coumarin monomers to release the entrapped drug molecules. Based on this work, Guardado-Alvarez et al. introduced another coumarin-based delivery system coordinating with beta-cyclodextrin (beta-CD)[138]. The coumarin-based molecules were bounded to the surface of MSNP, and then bulky beta-CD molecules were non-covalently associated with the coumarin molecules, blocking the pores, and preventing the cargo diffusion. Upon the one-photon excitation at 376nm or two-photon excitation at 800nm, the bonds that connect the coumarin to the pores were cleaved, resulting in a fast release of both beta-CD caps and cargo molecules.



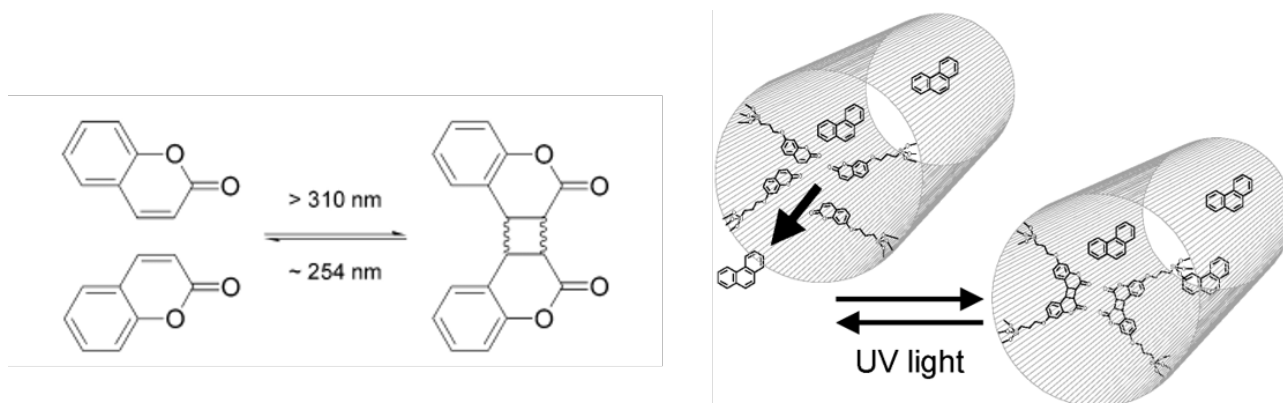


Figure 1-25. Photoisomerization of 7-((3-triethoxysilyl) propoxy)coumarin under UV irradiation[137]

This example has also provided some insights on the release from similar porous structures. The mechanism relies on the photo-induced conformational transition of the nanocarriers and the tuning of the pore outlet size as a response to stimuli determines the accessibility of the cargo molecules to the surrounding environment. Several points need to be fulfilled to generate capable steric crowding. First, a site-selective modification, particularly around the pore outlets with light-responsive molecules should be conducted to ensure an effective closing of the pores. Second, the size of the stimuli-responsive molecules should be chosen carefully according to the dimension of the pore outlets, avoiding the less-effective closing or the blocking of the pores with molecules of unfitting size to the pores.

Azobenzene (AB) is another type of light-sensitive molecule. When exposed to the UV-light at a wavelength of 350nm, AB can isomerize from the more stable *trans* to a less-stable *cis* configuration. Studies show the high binding affinity between beta-CD and *trans*-AB derivatives and a low binding affinity between the beta-CD and *cis*-AB derivatives in aqueous solutions. Thus, light-responsive delivery systems were designed based on this principle. Ferris et al.[139] have modified the MSNP with two different AB derivatives, 4-(3-triethoxysilylpropylureido) azobenzene and (E)-4-((4-(benzylcarbamoyl) phenyl) diazenyl) benzoic acid, which acts as stalks. Then, pyrene-modified beta-CD was threaded onto the stalks that bind to *trans*-AB units to cap the pores and seal the preloaded drugs. With irradiation of UV light at 350nm, the *trans*-AB form will isomerize to *cis* form, which leads to the dissociation of beta-CD rings, opening the pores and releasing the cargos (Figure 1-26).

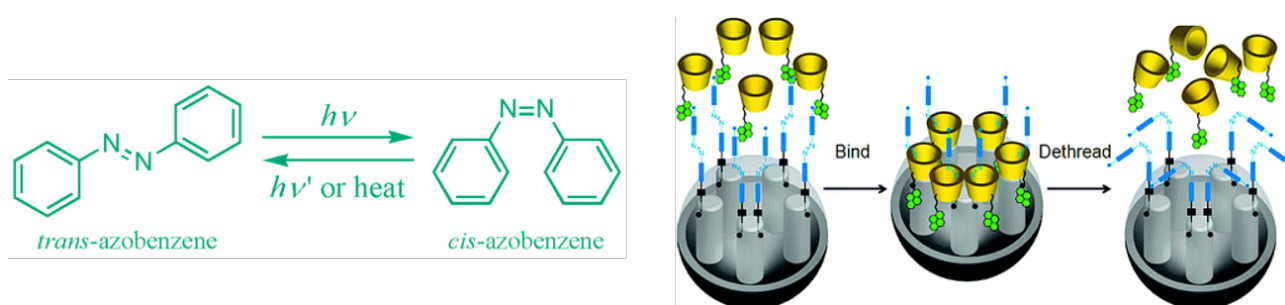


Figure 1-26. Drug release controlled by photoisomerization of AB derivatives[139]

Spiropyran (SP) has also been studied extensively for its relatively good photostability and can easily be functionalized with various groups that allow the attachment to various substrates. The isomerization and change of hydrophilicity and electrostatic state of spiropyran as a response to light endows itself the potential in the design of a controlled drug delivery system. Son. et al.[140] have prepared polymeric micelles using modified spiropyran. The light was induced to initiate the assembly and disassembly of micelles owing to the switch between hydrophobic SP state and hydrophilic merocyanine (MC) state. Drug delivery happens when the micelles break down under UV irradiation (Figure 1-27). Smirnov. et al. [141] have established a burst valve based on photosensitive membranes modified by the mixtures of photochromic spiropyran and hydrophobic molecules, making it possible to control the admission of water into the membrane using light. When the spiropyran is in the thermally stable, relatively hydrophobic closed form, the membrane is not wet by an aqueous solution. Upon exposure to UV light, the spiropyran photoisomerizes to the more polar merocyanine form, allowing water to enter the pores and cross the membrane. This research proves the potential of spiropyran as gatekeepers in delivery use based on the switch of wettability under UV irradiation.

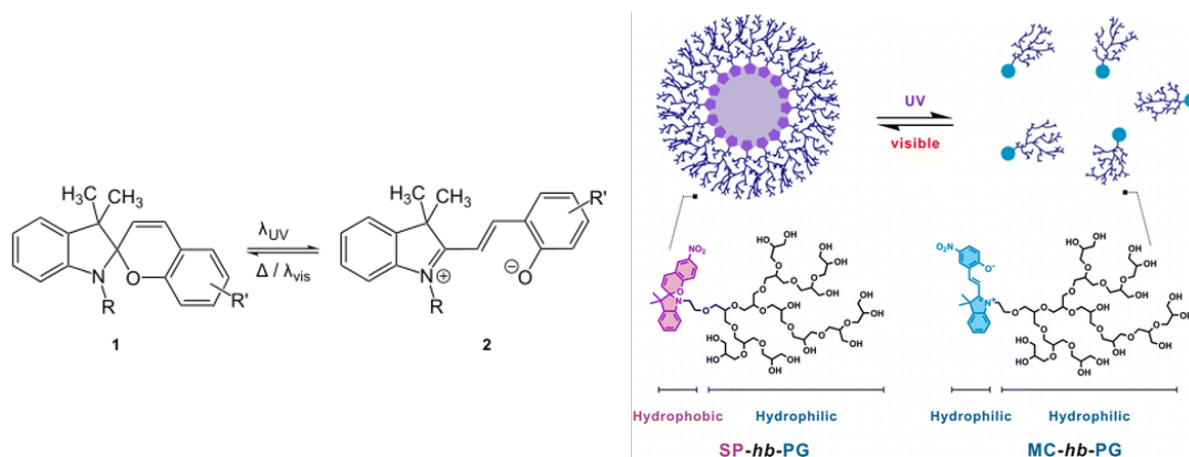


Figure 1-27. Illustration of light-responsive micelle assembly and disassembly of spiropyran-hyperbranched-polyglycerol (SP-hb-PG)[140]

The wavelength of light used to initiate the photochromism is an important factor, especially in *in-vivo* applications. The irradiation with UV light will be quite harmful to the nearby tissues. Consequently, a selection of photo-responsive molecules, which can be triggered with light at an appropriate wavelength range, is preferred.

Many different approaches are being taken to improve the photoisomerizable on-demand drug-delivery systems. However, a limited number of photoisomerizable molecules are being used currently, concerning their biocompatibility. For example, some azobenzene molecules will be irreversibly degraded with light irradiation[142] or by enzymes produced by bacteria in the GI tract[143]. Some of the degradation products, including nitrobenzene, are even considered toxic by the US FDA[128, 144]. As is the case with other categories of light-responsive drug-delivery systems, these systems have been limited to *in vitro* models due to biocompatibility issues not only with the photoresponsive moieties but also the light wavelength, intensity, and duration. More studies, especially *in vivo* studies, need to be conducted to better establish the safety and efficacy of these systems.

#### 1.4.2 Controlled release via the photocleavable mechanism

Drug delivery by photocleavable mechanism involves the covalent bond breakage of photoremovable conjugates under light irradiation (Figure 1-28). Such conjugates normally consist of the photoremovable protecting groups (PPGs) and the linked chemicals such as bioagents, acids, bases, oxidants, insecticides, pheromones, fragrances, etc. Commonly used photoresponsive moieties include ortho-nitrobenzyl(*o*-nitrobenzyl)-, coumarin- and pyrene-derivatives. The *o*-nitrobenzyl moiety cleaves irreversibly upon UV light to release a free carboxylic acid and *o*-nitrosobenzaldehyde[145] while coumarin- and pyrene-derivatives contain ester bonds that are readily cleaved upon UV irradiation[146, 147]. The systems required light that have sufficient energy per photons to break the covalent bonds like UV and high-energy visible light. Considering the harm of UV to human tissues[148], studies that replaced UV light with NIR light were reported following the strategies such as two-photon absorption[149, 150], triplet-triplet annihilation upconversion[151], second harmonic generation[152], and upconverting nanoparticles[153, 154], also achieving better tissue penetration than UV light.

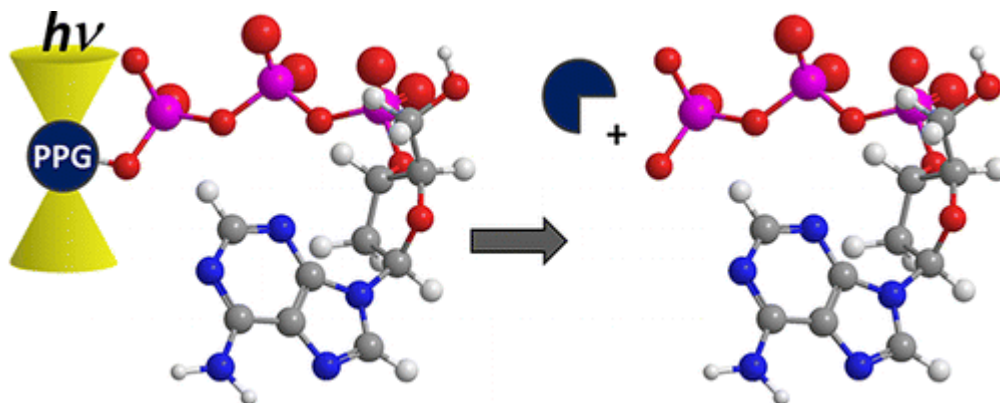


Figure 1-28. Illustration of the photocleavable release

The criteria for a good PPG depends on the application[155]. It should meet the following requirements but is not necessary to fulfill all of them at once. 1) PPGs should have strong absorption at wavelengths above 300nm, where irradiation is less likely to be absorbed by the biological entity. Also, the photoreaction should be clean and should occur with a high quantum yield or efficiency for release. 2) The PPGs must be pure, exhibit low intrinsic activity, and be stable in the media before and during photolysis. 3) The PPGs should be soluble in the targeted media. 4) The photochemical byproducts accompanying the released bioactive bioreagent should ideally be transparent at the irradiation wavelength to avoid competitive absorption of the excitation wavelengths.

The PPGs were used for light-triggered drug delivery by either releasing the drug from PPG prodrug molecules or breaking the structure of the carriers which is crosslinked by the PPGs. An example of drug release from PPG prodrug is given by Barman et al.[156] where they utilized the photoremovable pHP (p-Hydroxyphenacyl) protecting group as a delivery vehicle for a chemotherapeutic agent. The pHP protecting group was designed as an environment-sensitive fluorophore, and the excitation wavelength was extended to the visible wavelength region ( $\geq 410\text{nm}$ ). The excellent photoresponsive DDS ability of the molecule pHP-Benz-Cbl (p-Hydroxyphenacyl-Benzothiazole–Chlorambucil) was demonstrated by the dramatic fluorescence color change (green to blue) upon the efficient photorelease of the drug, enabling real-time monitoring.

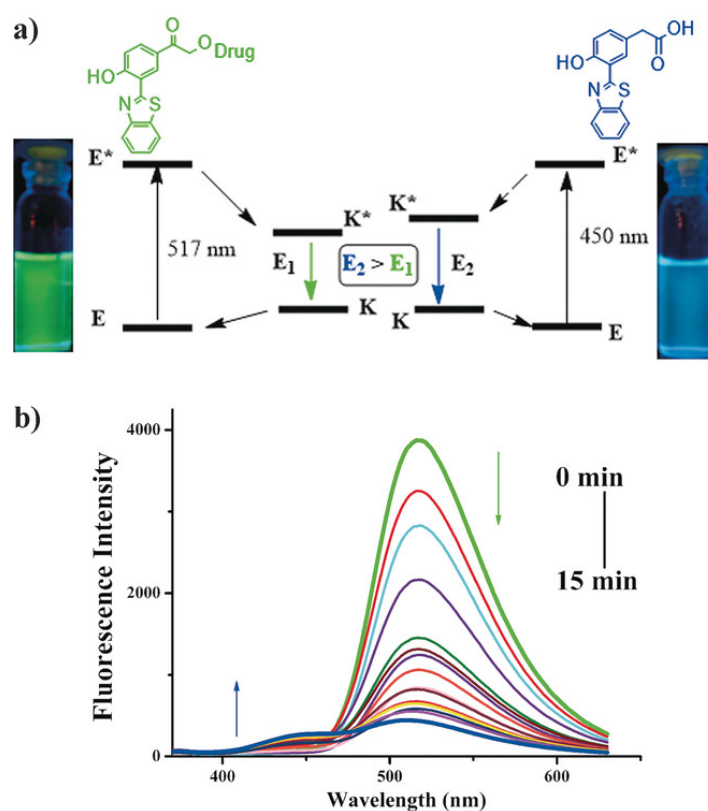


Figure 1-29. a) Jablonski diagram for the DDS pHP-Benz-Cbl and photoproduct pHP-Benz-COOH. b) Emission spectra of the DDS as the irradiation time is gradually increased (0–15min)

PPGs are also used to build drug carriers that can collapse upon the light irradiation and give a release of the hosted compounds. Yan et al.[157] have reported a NIR-triggered release system based on hydrogel. Crosslinks containing *o*-nitrobenzyl groups were used to hold together hydrogels made of PEG and PAM. To avoid using UV light, upconverting nanoparticles were loaded into the hydrogel and the *in vitro* release of large biomacromolecules was triggered with continuous-wave NIR light. The nanoparticles were able to convert the NIR light to UV light within the hydrogel and cause photo-oxidation of the *o*-nitrobenzyl moieties. This caused the hydrogel to break down and release the trapped biomacromolecules.

Although this approach gives little or even no release of the encapsulated drugs in the absence of stimulation, there are still challenges to overcome. First, photochemical triggering usually creates an irreversible change in the carrier, which means these systems are often ‘one-and-done’[158, 159], which could require multiple administrations of the drug carrier. Additionally, the same pool of photoresponsive moieties is being used to design these new photolabile groups, and there are concerns about their biocompatibility. Also, many of the photochemically triggered drug-delivery systems discussed in this section either require UV light or are more efficiently actuated by UV light. These wavelengths can damage biological molecules (e.g., DNA and growth factors) and

have poor tissue penetration, which has not only limited these systems to surface applications but also hindered their translation to the clinic.

### 1.4.3 Controlled release via the photothermal mechanism

Slightly different from the previous photoisomerization and photocleavable release, systems that involves materials that generate heat upon photoexcitation and thermally the sensitive components, which culminates with the drug, can also lead to a photothermal release. It requires two key components to successfully fabricate photothermally triggered drug-delivery systems: a chromophore that are able to convert light energy into thermal energy; and a thermally responsive material that rapidly responds to temperature changes, and leads to the release of a drug. Gold nanoparticles[160, 161], and NiPAAm hydrogels[162] are two of the most frequently applied materials for these delivery systems. Gold nanoparticles are inert and nontoxic depending on their size, shape, and surface chemistry[163]. Meanwhile, their optical and photothermal properties can be tailored at the nanoscale by playing with their size and shape to allow a strong absorbance in the NIR region [164]. NiPAAm is well-known for triggered drug-delivery systems for its reversible, temperature-induced change in hydrophobicity at its lower critical solution temperature. Above the lower critical solution temperature (LCST), NiPAAm goes from a swollen hydrogel to a globular state – expelling water and dissolved drugs from the dehydrated network. The temperature at which this transition occurs can be tuned to physiological temperatures by controlling the hydrophilic/hydrophobic ratio with the addition of co-monomers to the polymer network.[165] One example for the nanoparticle-temperature sensitive component system for drug delivery is as follows. Kim et al. has built a core-shell structure with gold nanoparticle as the core covered with thermally responsive hydrogel consisting of a mixture of N-isopropylacrylamide and acrylic acid. The drug-impregnated hydrogel coatings can be photothermally activated by exposure to light that can be absorbed by the plasmon resonance of the gold nanoparticle cores. Other chromophores, e.g. carbon nanotubes, have also been used for photothermal release. Carbon nanotubes (CNTs) can absorb NIR and generate local high temperature. This property not only makes it a good candidate for photodynamic therapy to kill cancer cells, but also allow it to combine with thermally responsive materials to realize photothermally triggered drug delivery. Zhou et al.[166] have developed a single wall carbon nanotube (SWNT) based thermo-sensitive hydrogel (SWNT-GEL) as an injectable drug delivery system as well as a medium for photothermal transduction. By incorporating hyperthermia therapy and controlled in situ doxorubicin (DOX) release, DOX-loaded SWNT-hydrogel with NIR radiation proves higher tumor suppression rate on mice xenograft gastric tumor models compared to free DOX without detectable organ toxicity.

## 1.5 Objective of the PhD work

Different stimuli can be applied to control the release of active molecules. Stimuli like pH, temperature have been investigated to generate a controlled release system. However, the applying and removing of the stimuli can be slow (for example in the temperature-responsive case) and environment-dependent (for example in the local pH-sensitive case), thus keep the systems from giving a fast and on-demand release. Therefore, the focus of this investigation will be set on light-responsive materials. Light can be applied rapidly and remotely. Additionally, light is a clean stimulus that can be focused easily on small and defined areas of the body.

Photo-responsive mesoporous silica particles have gained increased attention recently yet remained the problem of non-controllable biodistribution and circulation properties, which can lead to chronic toxicities. To overcome this problem, we propose to bind the mesoporous silicate particles directly onto the light source (optical fiber). Since optical fibers are already used invasively, they can be brought into the desired location of the body. The light-responsive mesoporous silicates will be coated onto the surface of the optical fiber. Several advantages are expected from such a system over free porous silicate particles combined with an external light source: Firstly, the light source is in close contact with the particles (via the optical fiber), so theoretically, light sources of lower intensity can be used. Secondly, the photo-responsive silica particles can be easily removed together with the optical fiber after the drug release has occurred and thus chronic toxicities can be avoided. Moreover, the drug release takes place exclusively in the desired region of the body.

Therefore, the main objective of this thesis is to build an optical fiber-based light-responsive delivery system. In this system, mesoporous silica nanoparticles will be decorated with photo-responsive prodrug moieties and coated onto the surface of optical fiber. The release of the drug is supposed to be triggered by the light field generated along optical fiber when light passes through.

Three sub-objectives are summarized as:

#### 1) *Synthesis of mesoporous silica nanoparticles (MSNPs) using non-surfactants as templating agents*



The synthesis of the MSNPs is based on the sol-gel method with non-surfactants, specifically, polyphenols (tannic acid, gallic acid, ethyl gallate, eudesmic acid, and quercetin), as templating agents. Silica precursors and polyphenols will be allowed to react in ethanol containing ammonium hydroxide to generate silica nanoparticles. After synthesis, the resulting particles will be washed with piranha solution to remove template residues and their morphology will be characterized.

*Deliverables:*

- a. Demonstrate the fabrication of MSNPs with tannic acid
- b. Relate the size growth of particles to pKa value of polyphenols
- c. Propose the pore formation mechanism of polyphenols

**2) *Development of a controlled strategy for the fabrication of particle-coated surfaces that applies to multiple genres of substrates***

The study will generate a fabrication method of particle-coated surfaces that applies to multiple genres of substrates and coating materials. We will start by employing a standard layer-by-layer (LbL) method: substrates (PMMA, PDMS) will be treated with air plasma to create a negatively charged surface. Then, the substrates will be immersed into positively charged polyelectrolytes and particle dispersion subsequently. The orthogonal experiments will be conducted to find the optimized condition to obtain a dense and homogeneous particle coating. A computer vision method will be developed to evaluate the coating. After having the particle coating, the substrates will be functionalized with silanes to obtain the amine groups on the surface that allow further attachment of drugs.

*Deliverables:*

- a. Establish an approach to generate a dense and homogenous monolayer coverage of particles on the substrates
- b. Develop particle recognition method to evaluate the particle coating by batch processing
- c. Modify the surface of substrates with silanes to allow further grafting of light-responsive prodrugs

**3) *Investigation of the light-responsive release of photolabile coumarin-chlorambucil conjugates from optical fibers***

In this step, we will study the triggered release of drug along the optical fiber axis by conducting visible light. The MSNPs will be incorporated onto PDMS optical fiber through the established LbL approach followed by the functionalization of silane to achieve an amine-covered surface. Coumarin-based photocleavable prodrugs will be selected as drug model and be grafted to amine groups. The outcoupled light and evanescent wave will cause the breakage of the prodrugs and release the drugs. The effectiveness of the system will be assessed by delivery studies from the free MSNPs in liquid media with/without the presence of light. Then, the release from optical fiber will be investigated. A simulation study will also be performed to reveal the interaction between particle coatings and light to understand better the triggering mechanism.

*Deliverables:*

- a. Fabricate the light-responsive optical fiber system
- b. Demonstrate the release ability from the free particles
- c. Demonstrate the active delivery control by light from optical fiber

# Chapter 2 Polyphenol as morphogenetic agents for the controlled synthesis of mesoporous silica nanoparticles

## 2.1 Introduction

Mesoporous silica nanoparticles (MSNPs) have been the subject of intense investigation for potential use in catalysis, separation, or biomedicine thanks to their large surface-area-to-volume ratios, tunable pore sizes as well as the variety of possible surface modification approaches that they allow. These properties make MSNPs highly attractive also for biomedical applications, especially for the development of multimodal imaging systems, controlled delivery[167], and sensing[168]. Surfactant-templating is the most widely used approach for the synthesis of mesoporous silica nanoparticles. In 1992 it was shown[169] that the self-assembly of surfactant molecules, when conducted in aqueous solutions of silica species, can result in spontaneous co-assembly of silica-surfactant mesophases. Removal of the surfactant leaves behind periodic mesoporous solids, the negative replica of the supramolecular assembly of the surfactant. Over the past years, a wide compositional range of mesoporous solids was produced[9, 170, 171], and the possibility to tune the pore sizes from one to tens of nanometers was demonstrated by using a variety of surfactants. In this regard, MCM-41 and SBA-15 (Mobil Composition of Matter no. 41 and Santa Barbara Amorphous no. 15, respectively) are excellent examples of the power of this approach.[172] However, the presence of residual surfactants in MSNPs constitutes one major drawback for their use in biomedical applications, as the most commonly used surfactants, including cetyltrimethylammonium bromide (CTAB), are cytotoxic. Therefore, extensive purification is necessary before the particles could be used for biological applications. The strong retention of surfactants makes their removal a difficult and time-consuming step, especially if performed by wet methods[173-175] or requires the calcination of the particles at high temperature, which in some cases can lead to the partial or total collapse of the internal porous structure[176].

In nature, the most striking examples of surfactant-templating strategy are provided by diatoms[177] and radiolarian[178], which show highly complex architectures carved in silica. These structures are formed by biomineralization, a templated self-assembly process in which preorganized organic surfaces regulate the nucleation, growth, morphology, and orientation of inorganic crystals. To date, a variety of synthetic pathways have been proposed to mimic biomineralization, started from the early report of Dickey[179], who used an azo-dye (methyl orange) for the synthesis of templated silica gels. The use of non-surfactants as templating agents was rediscovered decades later when Wei et al. showed how monolithic mesoporous silica could be produced using D-glucose, dibenzoyl-L-tartaric acid, and D-maltose.[180, 181] Subsequent studies indicated that other molecules, such as poly(propylene)imine dendrimers[182], organic hydroxy-carboxylic acids[14, 16, 183, 184] (including citric acid, lactic acid, malic acid, and tartaric acid),  $\beta$ -cyclodextrin-urea complexes[18], fatty alcohols[185] and sugars[186] (including sucrose and fructose) could be successfully used to generate mesoporous silica monoliths. Such an approach has then been successfully extended to the synthesis of nanoparticles. However, while the size of non-surfactant-templated MSNPs can be varied in a broad range without loss of monodispersity, the pore size is usually less than 4 nm due to the small size of the templating molecules.[186] Recently, Gao et al. proposed tannic acid[21] as an especially suitable non-surfactant for the synthesis of large-pore mesoporous silica nanoparticles.

Tannic acid (TA, decagalloyl glucose) is a type of water-soluble natural polyphenol derivative of glucose and the simplest tannin. TA is highly biocompatible and its medical uses are widespread thanks to its antibacterial and antioxidant properties.[21] Despite a growing interest[187-189] for tannic acid-templated MSNPs, however, the templating mechanism still remains unclear. It is generally hypothesized that the formation of the porous silica framework would be the result of hydrogen bonding interactions between TA (also in the form of supramolecular complexes) and silicate species originated from the hydrolysis of the organosilane precursor.[21] However, no systematic attempt has been reported to date to investigate this mechanism.

In the present work, we studied the influence of the chemical structure and properties of polyphenols on MSNP morphology. To elucidate the morphogenetic process, we studied the templating ability of TA and other polyphenols (gallic acid, ethyl gallate, eu-desmic acid, and quercetin). We demonstrated for the first time that the pKa values and supramolecular structure of templates are

responsible for the particle size and pore formation, respectively. Additionally, we used SAXS to gain a deeper knowledge of morphology, especially the porosity of the resulting MSNPs and their surface roughness.

## 2.2 Effect of tannic acid concentration on the morphology of MSNP

Synthesis of silica nanoparticles by the sol-gel Stöber method involves the controlled hydrolysis and condensation of tetraethoxysilane in alcohol-water mixtures in presence of ammonia as basic catalyst. This approach leads to non-porous nanoparticles unless suitable templating agents are used. Here, we resorted to a previously optimized protocol[190] for the synthesis of 100 nm-diameter non-porous silica nanoparticles to study the morphogenetic properties of TA and other related polyphenols.

The complete solubilization of all components is of great importance to achieve control of particle nucleation and growth. Solubility tests were performed to determine the upper limit concentration of TA, which, for our reaction system, was determined to be about 1.6 mg•mL<sup>-1</sup> (corresponding to 512 mg of TA in total). The total amount in mg of the templating agent used for each synthesis was used as reference to identify the samples.

Dynamic light scattering (DLS) and scanning electron microscopy (SEM) were employed for the determination of average diameter and polydispersity of the resulting particles. The results show that the addition of 64 mg of TA resulted in a slight increase in the particle diameter compared to non-mesoporous nanoparticles (blank) (Table 2-1 and Figure 2-1)

Table 2-1. Size information (obtained from DLS and SEM) of resulting particles templated with TA

Sample	Particle size, DLS (nm)	Pdl from DLS	Particle size, SEM (nm)
Blank SNP	157	0.027	122±20
TA64-MSNP	155	0.014	145±17
TA128-MSNP	170	0.026	146±18
TA256-MSNP	175	0.012	150±28
TA384-MSNP	167	0.033	152±23
TA512-MSNP	225	0.080	222±37 (long axis) 156±23 (short axis)

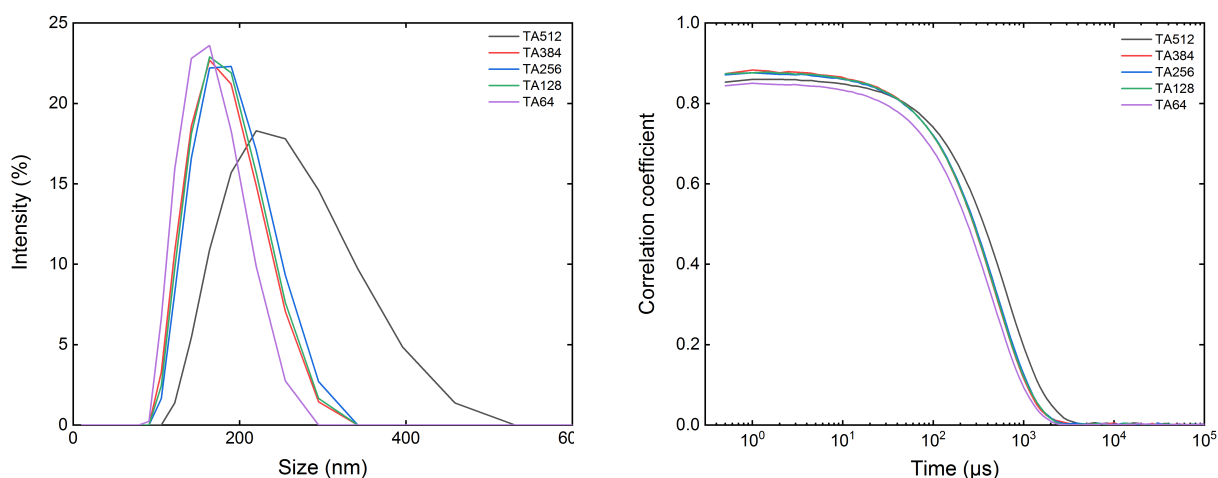


Figure 2-1. Size distribution (by intensity, left panel) and raw correlation data (right panel) of TA-templated MSNP samples

The size of TA512-MSNPs measured through SEM images in both long axis and short axis fur to the irregular morphology. The effective particle size should be located between the two values. Of note, the particle size determined by DLS is in this case equivalent to that of the long axis. Except for this case (TA512), we noticed that the particle size grows only slightly with the increase in the TA content. Moreover, all samples show a narrow, monodisperse distribution ( $PdI < 0.1$ ). The SEM provided also preliminary information about particle morphology, which experienced a change from spherical to irregular (cauliflower-like), visible for MSNPs prepared with 256mg or 512mg of TA (Figure 2-2, left column). This morphology is likely to originate from the aggregation of small sub-particles. TEM shows an increasingly porous structure in the particles for increasing amounts of TA (Figure 2-2, right column).

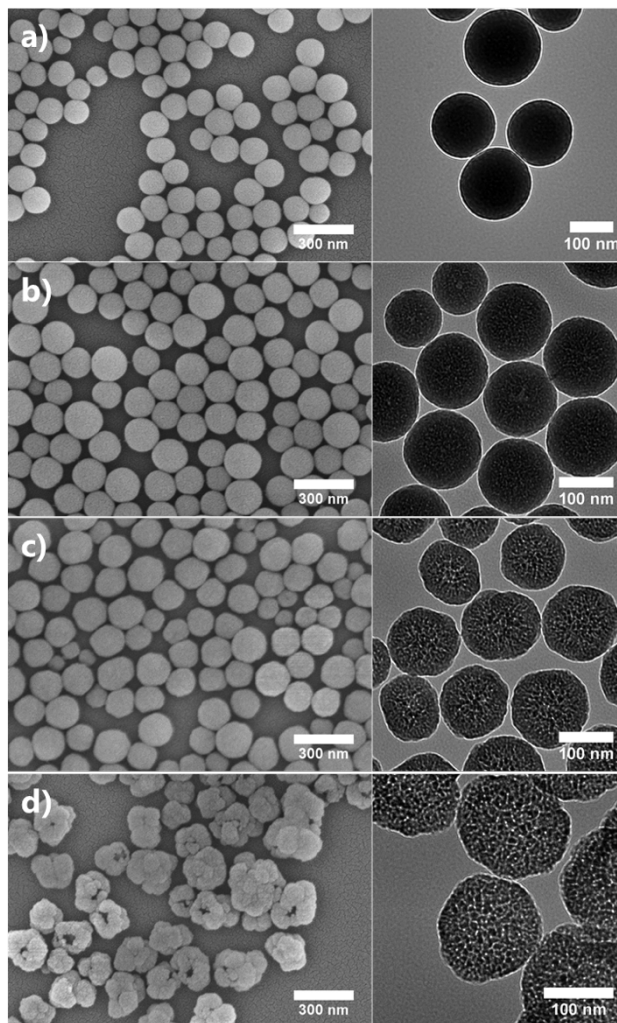


Figure 2-2. SEM (left column) and TEM (right column) images of TA-templated silica nanoparticles prepared with increasing amounts of templating agent: a) TA64-MSNPs, b) TA128-MSNPs, c) TA256-MSNPs, d) TA512-MSNPs

In contrast with previous literature reports[21, 189], we noticed that a certain amount of TA was retained inside the silica matrix even after several cycles of washing with ethanol and water, as the particles were of a light-brown color. The removal of residual templating agent ("detemplating") from mesoporous silica nanoparticles is usually accomplished by both dry and wet methods. The most conventional treatment is calcination, i.e. particles are subjected to high temperature (typically 500-600 °C) in an oxidizing atmosphere to burn the residues of organic templating agents. However, this approach can lead to particle sintering, with consequent worsening of colloidal stability, and damage of the porous structure (e.g. pore collapsing)[191]. Milder detemplation approaches are based on wet processes such as ion exchange (for ionic surfactants) or, chemical degradation by means of Fenton-like reactions and acid piranha solution (for non-ionic species)[192]. Here, we studied the removal of residual TA by means of calcination as well as of acid piranha treatment (refer to the experimental section for details). Both approaches resulted in white particles (Figure 2-3) and electron microscopy analysis (SEM and TEM) showed that the particle morphology was not affected by any of the treatments (Figure 2-4). However, from a qualitative point of view, calcination was found to affect more the colloidal stability of the particles compared to the piranha treatment, which produced stable suspensions.

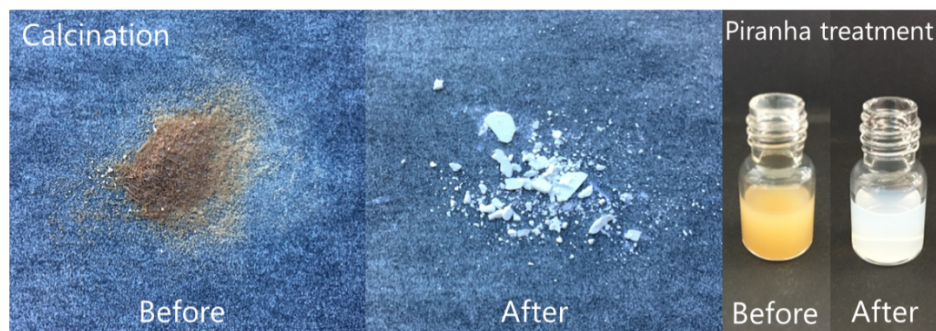


Figure 2-3. MSNP templated with TA before and after detemplation

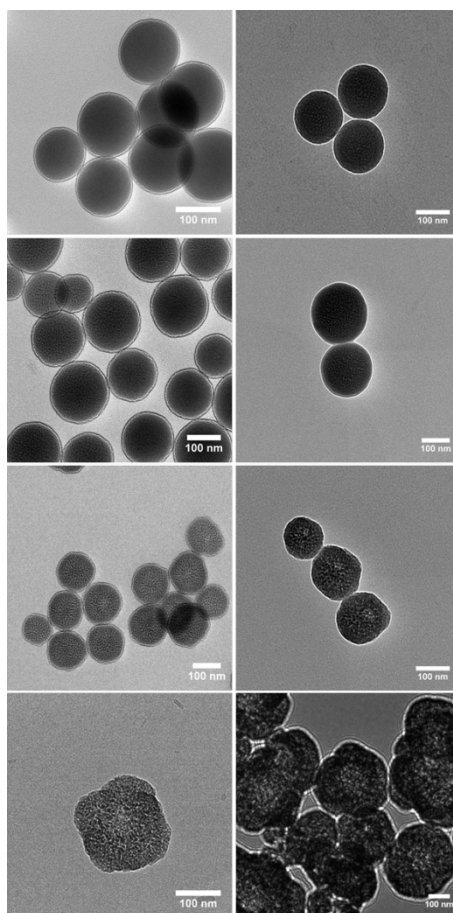


Figure 2-4. HRTEM images of tannic acid (TA) templated silica nanoparticles after removal of tannic acid. From up to down, the amount of tannic acid is 64mg, 128mg, 256mg, 512mg, respectively. Left column: MSNPs after piranha treatment, right column: MSNPs after TGA

To investigate more in detail the morphology and especially the porosity of the particles, SAXS measurements were performed on samples before and after detemplation with piranha treatment. In Figure 2-5a, the intensity versus scattering vector,  $q$ , from non-porous silica particles is shown. The 1D scattering profile has been obtained from azimuthal integration of the 2D pattern represented in the inset of Figure 2-5a. First of all, the Porod slope of  $-4.0$  reveals the existence of a smooth particle surface which is expected to be the case for non-porous particles. In addition, the nanoparticle size can usually be estimated using the Guinier approximation[193]. However, as the particles size ( $\sim 200$  nm) in this study went beyond the observation window of our SAXS setup, the Guinier region of the scattering curve was not accessible. Nevertheless, it is known that the oscillations (observation of minima/maxima) in the scattering form factor of spheres are an indication of system monodispersity. It is important to note that, the observed minima position in equidistant intervals, with the first minimum at  $4.5/R_g$  ( $R_g$  is the radius of gyration and, for a sphere and is related to nominal radius,  $r$ , of spherical particle by  $R_g = (\sqrt{3/5} \cdot r)$ ). As the size distribution of particles becomes broader

these oscillations are suppressed and for highly polydisperse samples, a smooth decay in the scattering intensity will be recorded. In our studied non-templated silica particles system, the maxima and minima could still be resolved in the scattering intensity (see the arrow around 0.085 nm<sup>-1</sup> in Figure 2-5a), though the order of this minimum could not be determined solely from SAXS data.[194] Here, we referred to primary knowledge on size estimation from DLS. For particles of radius around 100 nm, the first minimum position is approximated around ~0.045 nm<sup>-1</sup>. This would mean that the minimum observed around 0.085 nm<sup>-1</sup> must correspond to the second minima as indicated in Figure 2-5a. Having this in mind, we further implemented the indirect Fourier transformation (IFT)[195, 196], considering the  $r_{max}$  of 200 nm, to simulate the scattering pattern while precisely extrapolating the curve to ultra-small angles. The IFT calculation was implemented using the GIFT software (University of Graz, Austria). The simulated curve in reciprocal space corresponds to the pair-distance distribution function (also called  $p(r)$  function), in real space which reveals detailed information on the size and shape of the particles. The  $p(r)$ , shown in Figure 2-5b, corresponds to  $R_g$  value of 65.7 ± 2 nm and has a fairly symmetric shape which is normally associated with low polydispersity in spherical particles systems. However, a quantitative measure of polydispersity index requires high-resolution data at ultra-small angle regime for this system.

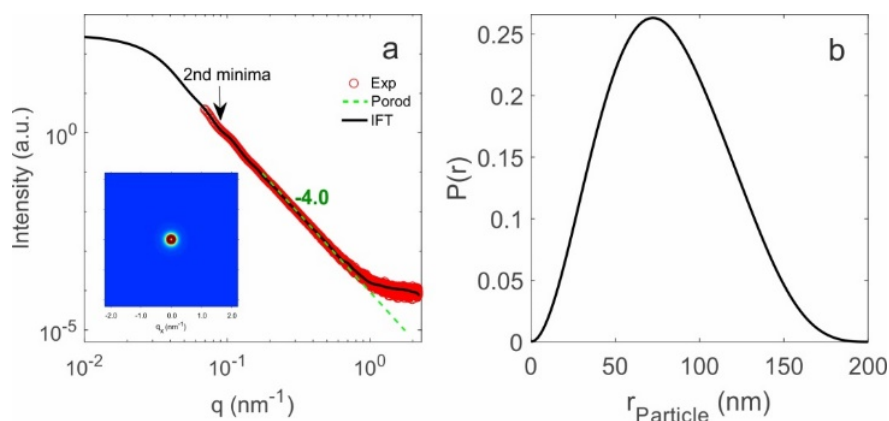


Figure 2-5. a) Experimental and simulated scattering intensities versus scattering vector from silica particles synthesized without templating agent. The inset represents the 2D scattering pattern. b) the corresponding  $p(r)$  obtained from IFT calculation.

We also performed the classical Porod analysis in order to evaluate the surface roughness of the synthesized particles. In this approach, the decay rate of the intensity versus  $q$  in log-log scale is calculated. The slope of -4, typically corresponds to scattering from particles of a smooth surface while deviation from that, indicates surface roughness. In our studied systems, the Porod values vary from -4 (non-templated nanoparticles) to -3.4 (for templated nanoparticles with the highest applied TA concentration). Therefore, the comparison of the Porod slope values for different particles shows that the latter displays higher surface roughness with respect to the former one (Figure 2-6a,c,e and Figure 2-7b), in agreement with the morphologies observed by electron microscopy[197]. This monotonous and systematic decrease in Porod slope with increasing amounts of TA indicates well-controlled surface roughness through this synthetic approach.

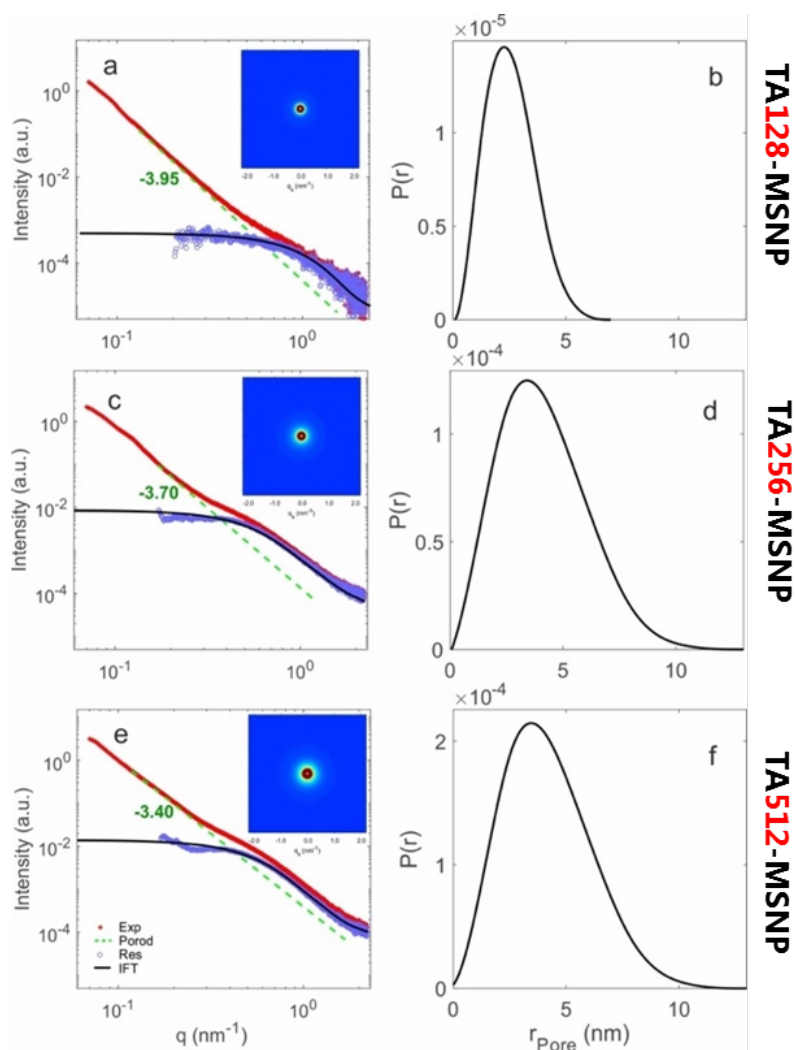


Figure 2-6. a, c and e) The experimental scattering patterns and their relevant residual scattering obtained from subtraction of Porod line are shown together with the IFT evaluation of residual scattering. The insets represent the 2D scattering patterns. b, d and f) the pair-distance distribution function,  $p(r)$ , obtained from IFT analysis of residual scattering from pores. The distribution reveals increase in pore size and pore volume by increasing templating agent concentration, in this case TA.



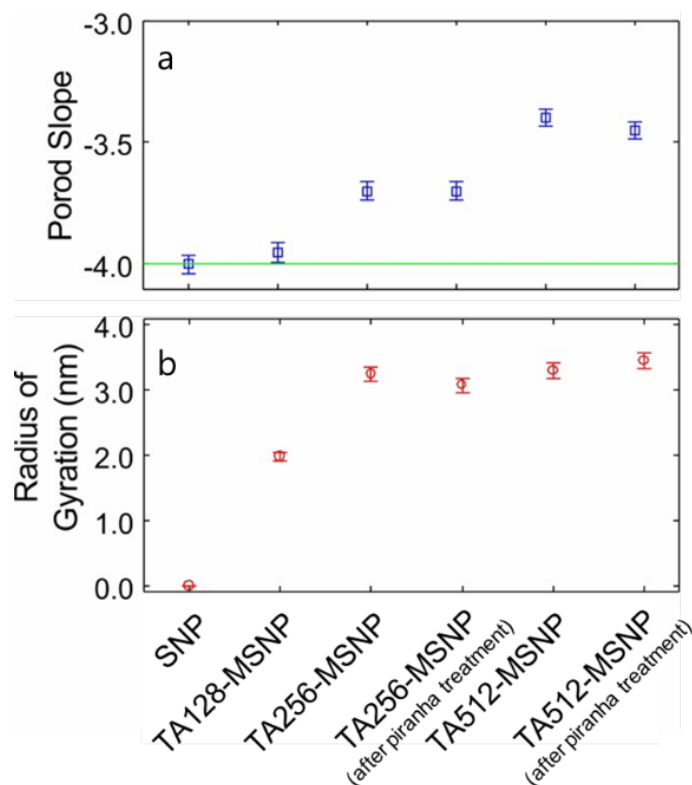


Figure 2-7. Radius of gyration ( $R_g$ ) of the pores and the Porod slope values obtained from TA-templated silica nanoparticles before and after piranha treatment.

The X-ray scattering from templated nanoparticles with varying amounts of TA demonstrates an additional feature; a hump at around 0.5 to 1  $\text{nm}^{-1}$ , depending on the templating agent concentration. The hump is a typical scattering feature from porous materials which originates from the electron density variations within the particles and its position and intensity is correlated with the pore size and the total number of pores[198]. In order to carefully analyze the pores within the particles, we subtracted the fitted Porod line from the experimental data within the  $q$ -range of observation of the hump. The resulting curve, so called residual scattering, was further considered as the new pattern, its IFT analysis revealed the  $P(r)$  function of the pores (see Figure 2-6b,d,f). The radius of gyration obtained from this approach shows an increase in the pore radius from about 2 nm in TA128-MSNP to about 3.5 nm in TA512-MSNP (Figure 2-7a). The evaluated pore sizes, similar to the particles' surface roughness, increase with the concentration of the templating agent. It is also interesting to figure out that nearly identical scattering profiles have been acquired from particles before and after removal of templates by piranha treatment; the calculated Porod slopes and the radii of gyration of the pores vary only within the margin of error (see Figure 2-7b), suggesting that piranha treatment has no effect on both pore size and roughness of the particles.

Complementary information about porosity was obtained by means of nitrogen sorption-desorption measurements, which were carried out on detemplated samples (Figure 2-8). The resulting BET surface area and pore volume values, summarized in Table 2-2, were found to increase with the amount of TA used. The particles obtained with the two lowest amounts of templating agent (TA64-MSNP and TA128-MSNP) displayed a very low nitrogen sorption, suggesting a non-porous structure. The nitrogen sorption is nearly zero in a pressure range lower than 0.8 P/P0, which may imply that the adsorption mainly happened on the particle surface. In contrast, the isotherms of TA256-MSNP were characterized by a type IV curve with a dominant type H2 hysteresis loop between 0.4 P/P0 and 0.8 P/P0, strongly indicating the presence of mesopores. The hysteresis loop at about 0.9 P/P0 can be attributed to interconnected pores. This latter feature is shared with the TA512-MSNP, of which the long hysteresis loop between 0.4 P/P0 and 0.9 P/P0 may suggest the presence of different populations of pores.

Table 2-2. Structural properties of TA-templated particles as determined by BET and SAXS

Particles	Surface area( $\text{m}^2/\text{g}$ )	Pore volume( $\text{cm}^3/\text{g}$ )	Pore size by SAXS (nm)
TA64-MSNP	26.0	0.27	-



TA128-MSN	27.4	0.24	5.2±0.2
TA256-MSN	255.2	0.52	8.4±0.2
TA512-MSN	362.9	1.10	8.6±0.2
GA64-MSN	25.5	0.14	-
GA128-MSN	11.2	0.03	-

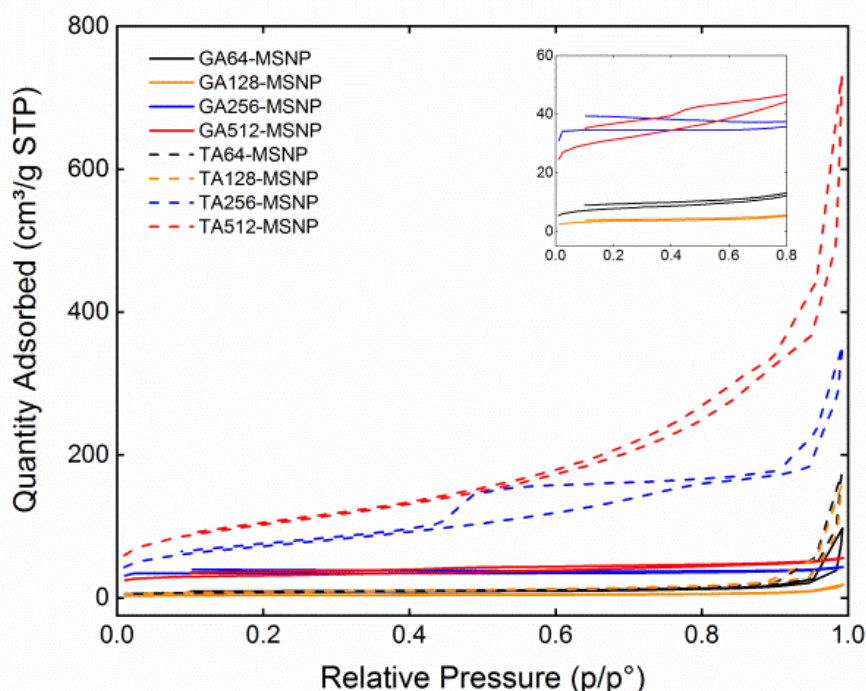


Figure 2-8. Nitrogen adsorption-desorption isotherms of templated MSNPs after detemplation

The molecular dimensions of a tannic acid molecule are  $1.85\text{ nm} \times 1.65\text{ nm} \times 1.01\text{ nm}$ [199], which would correspond to a volume of around  $3\text{ nm}^3$ . On the basis of SAXS and BET results, however, it is reasonable to conclude that the pore size in our TA-templated MSNPs is larger than the size of a single TA molecule. This is in accordance with the suggestion of Gao[21] that TA could self-assemble into supramolecular structures, most probably by means of hydrogen bonding, which would then direct the pore formation. However, our results suggest also that there could be a critical concentration of TA, below which a porous structure could not be achieved (e.g. because of an insufficient degree of self-assembly) or, conversely, above which would result in a morphological change (see TA256- and TA512-MSN).

EM images show the change in particle porosity and morphology under different concentrations of TA. Pore size increases with the content of TA, which is in agreement with SAXS results with an increase of radius of gyration from  $2\text{ nm}$  to  $3.5\text{ nm}$  corresponding to a pore size from  $5\text{ nm}$  to  $9\text{ nm}$ . However, comparing the SAXS and BET results of TA256- and TA512-MSN samples, it is clear that the surface area is not accompanied by an increase in pore size. This may imply that the increase of surface area does not come from the enlargement of single pores but is mainly due to the interconnection between pores or the presence of cracks in the particles, which are supported by the nitrogen adsorption and desorption isotherm of TA512-MSN. In addition, the morphology of the mesoporous nanoparticles changes: under higher concentrations of TA, particles with irregular shapes were formed. The particles showed no longer a particulate and smooth surface as at lower concentrations of TA, instead, irregular shape and rough surface were formed. This observation is consistent with the conclusion from SAXS, which points out that surface roughness gradually increased from TA128 to TA512. Moreover, it is also interesting to see that the TA512-MSN has a cauliflower shape, very likely to originate from the aggregation of small sub-particles (see discussion on SEM/TEM results). The morphology change could be interpreted according to the mechanism of particle formation. It is generally agreed that in a sol-gel process the silica precursors are

hydrolyzed and form small nuclei which are considered as primary particles. The primary particles will further aggregate to form the large particles.[200] When TA is used as template, the silica moieties can form hydrogen bonds with TA and associate around TA. But due to the irregular shape of TA itself and the TA supramolecular network, the primary particles formed are also irregular. Such primary particles can hardly pack as densely as spherical ones to form a uniform structure, but on the contrary, may result in cracks between connected primary particles and irregular morphology of the final particles. The information from EM images and BET as well as SAXS results all support this hypothesis.

## 2.3 Investigation of tannic acid-related polyphenols as morphogenetic agents

### 2.3.1 Comparison of chemical structure of four phenol derivatives

One possible explanation for the pore formation, as suggested by a previous study[21], is that the mesopores can be attributed to the formation of TA supramolecular network. However, no study has been carried out so far to verify this hypothesis. To further unravel the morphogenetic properties of TA, we focused on strictly related molecules, namely: gallic acid, ethyl gallate, eudesmic acid and quercetin with their chemical structure presented below (Figure 2-9).

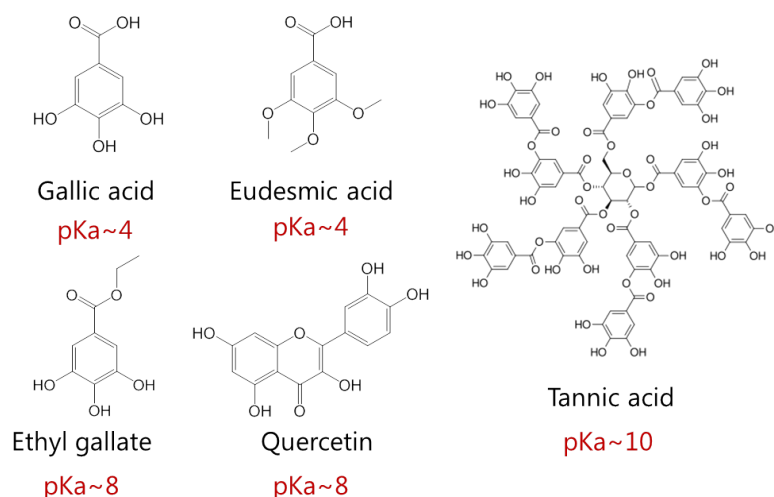


Figure 2-9. Chemical structure and respective acidity constants of polyphenols used as morphogenetic agents

### 2.3.2 Characterization of the phenol derivatives-templated silica nanoparticles

Tannic acid is decagalloyl glucose, thus GA can be considered as its monomer. When the synthesis of silica nanoparticles was carried out by substituting TA with GA, particle size increased (from about 240 nm to about 600 nm) as a function of the GA amount with other reaction conditions being constant (Figure 2-10 and Figure 2-11). Moreover, the resulting particles were of a dark-brown color, which was not altered after prolonged washings with ethanol and water. Even repeated treatments with piranha solution were only partially effective in bleaching the color, suggesting that a fraction of the templating agent was still buried in the particles. Colorless particles could be obtained only by means of calcination. This dark-brown color is hypothesized to be the result of a complex process including dissociation, radical formation and oxidation in alkaline environments in presence of air with the formation of brown-colored products.[201] EG and EA were also used under the same conditions, resulting in white particles with a similar trend in the increase of particle size upon increasing amounts of templating agents: 233 nm to 490 nm for EG and 240 nm to 731 nm for EA (Figure 2-10 and Figure 2-11). When QU was chosen as templating agents, particles were slightly yellow and the growth was similar to that obtained with EG. The results of DLS and SEM are summarized in Table 2-3 and the particle size evolution is compared in Figure 2-10.

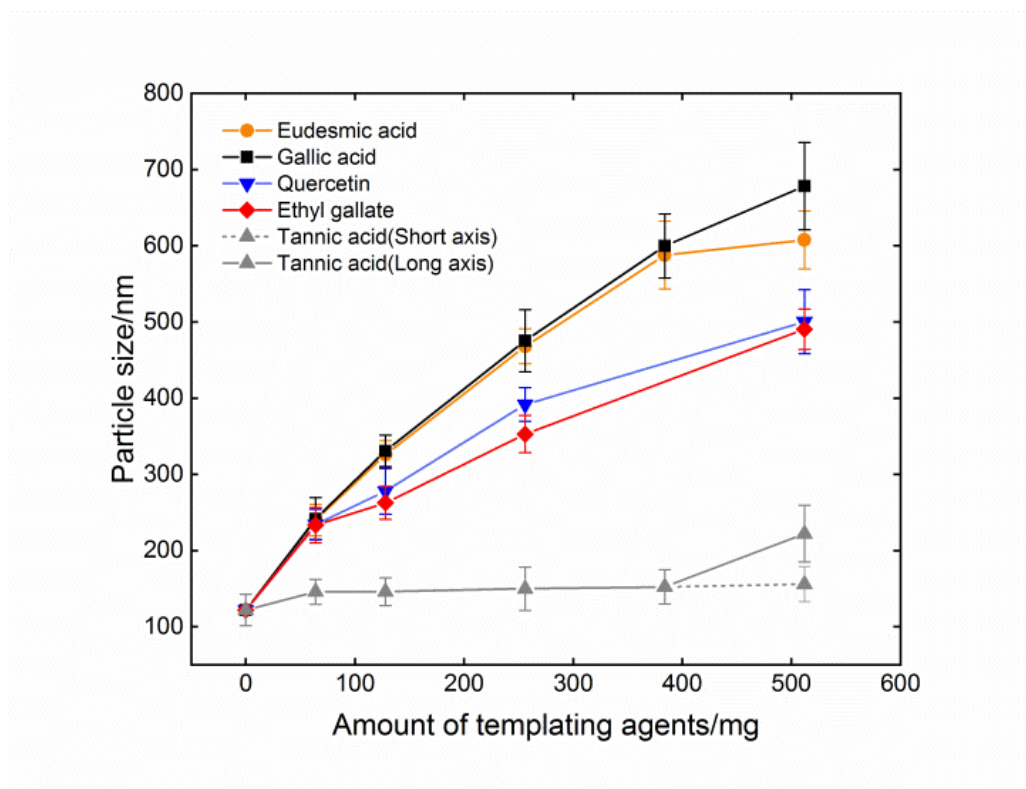


Figure 2-10. Size of particles out of various templating agents as a function of mass of templating agent

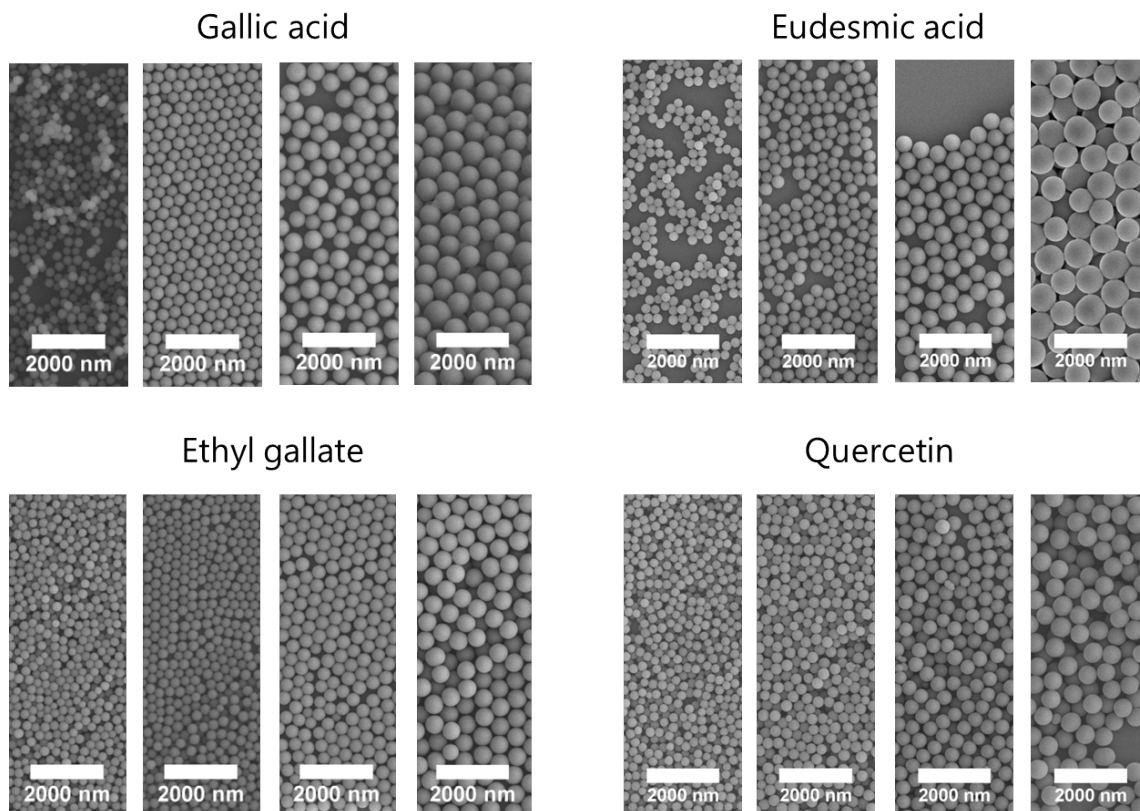


Figure 2-11. SEM images of particles synthesized by polyphenols as morphogenetic agents. For each morphogenetic agent, from left to right, the amount of morphogenetic agent is 64mg, 128mg, 256mg, and 512mg.

Table 2-3. DLS results of particles synthesized by different morphogenetic agents

Sample	DLS particle size/nm	SEM particle size/nm
SNP	156.6	122±20
GA64-SNP	272.5	242±28
GA128-SNP	365.0	331±20
GA256-SNP	601.2	476±41
GA512-SNP	715.6	667±53
EG64-SNP	250.6	233±23
EG128-SNP	281.0	263±22
EG256-SNP	377.4	353±24
EG512-SNP	538.2	491±26
QU64-SNP	242.6	234±20
QU128-SNP	307.4	278±30
QU256-SNP	424.4	392±22
QU512-SNP	558.5	500±42
EA64-SNP	258.8	240±20
EA128-SNP	346.5	326±18
EA256-SNP	585.6	468±23
EA512-SNP	635.6	586±37

### 2.3.3 Study of influencing factors for size growth

The presence of functional group moieties seems to play an important role in particle growth, as is apparent from comparing the results of Figure 2-10 with Figure 2-9. The pH of the reaction mixture may be a parameter that could explain the growth and the final size of Stöber silica particles. In a Stöber reaction, the base is added as a catalyst to facilitate hydrolysis. At a high pH, more hydroxide ions are present in the system that can directly attack the silica atoms in the silica source (e.g. TEOS) through a nucleophilic mechanism, which leads to a faster hydrolysis of the silica precursors, contributing to a larger particle size. However, if the hydrolysis is fast at the initial nucleation step, then more nuclei will be generated so that the final particle size may be smaller. In our case, the five templates exhibit a pKa value of ~4 for GA[202] and EA[203], ~8 for EG and QU[204], and ~10 for TA[21], which decreases the pH of the reaction mixture at different extents. When having the same weight dosage, templates with a lower pKa value will consume more base catalysts. The initial silica nucleation process is constrained, thus fewer nuclei are generated and result in bigger particles. This helps explain the bigger particle size in the case of template-induced particles comparing to the blank silica nanoparticles. Our results suggest that the nucleation process is more dominant for the final particle size compared to the particle's growth speed. Furthermore, as more templates are added, the amount of ammonium ions consumed through the reaction with templates will increase, hindering the hydrolysis of silica precursors to form fewer nuclei at the beginning. Thus, bigger particles are generated.

### 2.3.4 Study of mechanism of pore formation

In addition to the difference in size, there are differences in pore formation as well. Pores are only found in particles templated by GA and TA. We attributed this to the existing state of the templates in the mixture. To verify this hypothesis, we have performed

DLS measurements for the reaction mixture prepared using the same procedure but without silica precursors (Table 2-4). The results showed that only at the highest concentration (512mg) the TA and GA molecules assembled to stable aggregates or supramolecular structures. The size of TA aggregates remained almost constant with time while GA aggregates kept growing. On the contrary, EA, EG, and QU did not show any tendency to form stable aggregates. This may be due to the dissociation degree of the templating molecules. EA, EG, QU were deprotonated at the reaction pH and therefore lacked donor for hydrogen bonding, which explained why we failed to characterize them by DLS. Due to the same reason, they were not able to interact with silica precursors to play a role as templates. Further, the TA and GA frameworks were imaged by SEM (Figure 2-12). The size of TA aggregates by DLS and SEM roughly corresponds to the size of the TA particles, not to the pore sizes. According to this, we postulate that the mesoporous structure is a consequence of the crosslinking of silica precursors in the free space of the TA framework. TA contains enough phenol groups in one molecule which are able to serve as binding site for each other. The molecules are linked by hydrogen bonds and come out as a heavy supramolecular framework, especially compared to the silica precursors, which are in an original small dimension. Therefore, when silica precursors diffuse into the TA framework, they gather around the TA skeletons via hydrogen bonds, followed by the polymerization into primary particles that will further merge into the disordered MSNPs. The pores turned out to be big and interconnected, as demonstrated by BET, SAXS and TEM. Figure 2-13 shows a schema presenting the templating process of tannic acid. GA-particles have a different morphology, which comes from the nature of the formed framework. GA aggregates were growing in parallel with silica condensation. GA reacts with both GA and silica species via hydrogen bonds. When silica monomers are involved in the reaction, GA will undergo a competition with silica monomers that will lead to the break-down of the clusters as the intermolecular forces between GA and silica species and that between GA are similar. Therefore, instead of yielding large clusters, GA was present in smaller size and templated MSNPs with small isolated pores and gullies on the surface (Figure 2-14). In contrast, the force between TA molecules is much stronger owing to the high density of hydrogen bonds.

Table 2-4. DLS results of reaction mixture without silica precursors

Equilibrium time/min	Size of generated aggregates/nm							
	GA512	TA512	TA256	TA128	TA64	EA512	EG512	QU512
0	269	260						
10	300	251						
20	321	255			Not suitable for measurement.			
60	681	262			Poor data quality.			
70	678	254						
80	709	265						

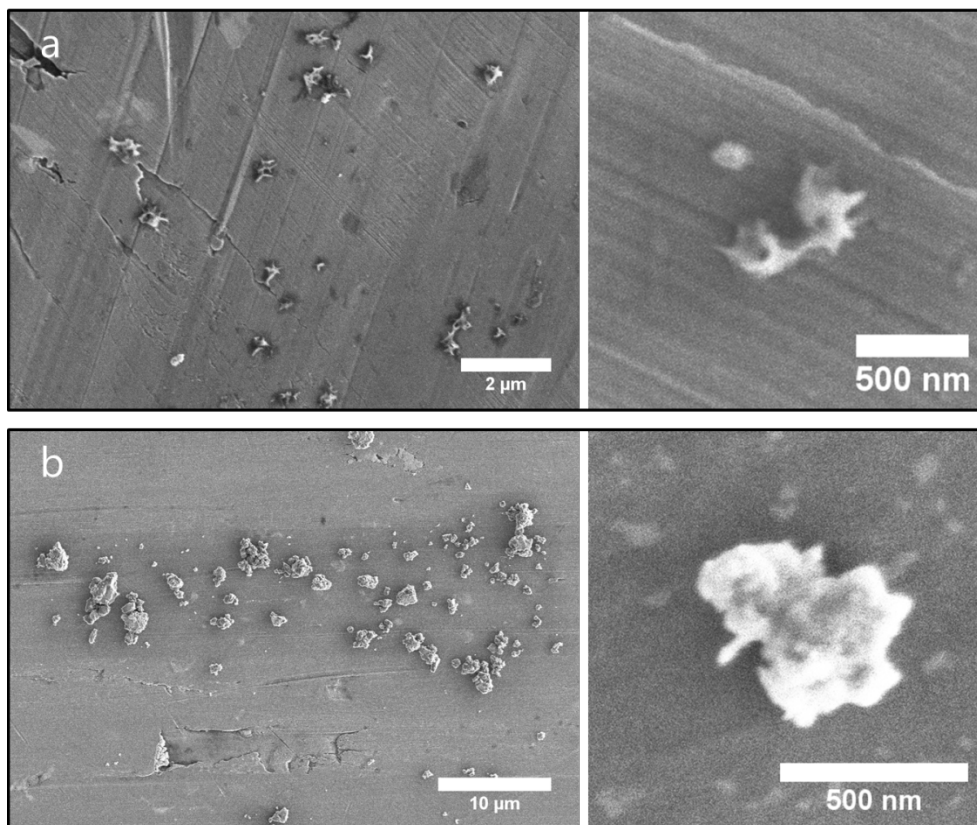


Figure 2-12. SEM images of TA and GA frameworks before TEOS addition. a) TA512 supramolecular structure; b) GA512 cluster. Specimens were taken from the reaction solutions 20min after the beginning of the reaction.

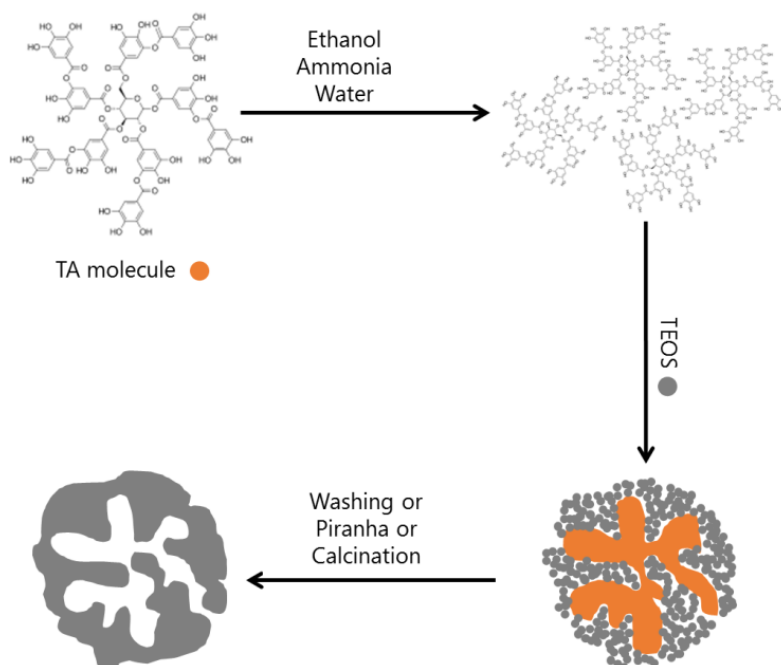


Figure 2-13. Schema of the formation mechanism of MSNPs using TA as templating agent



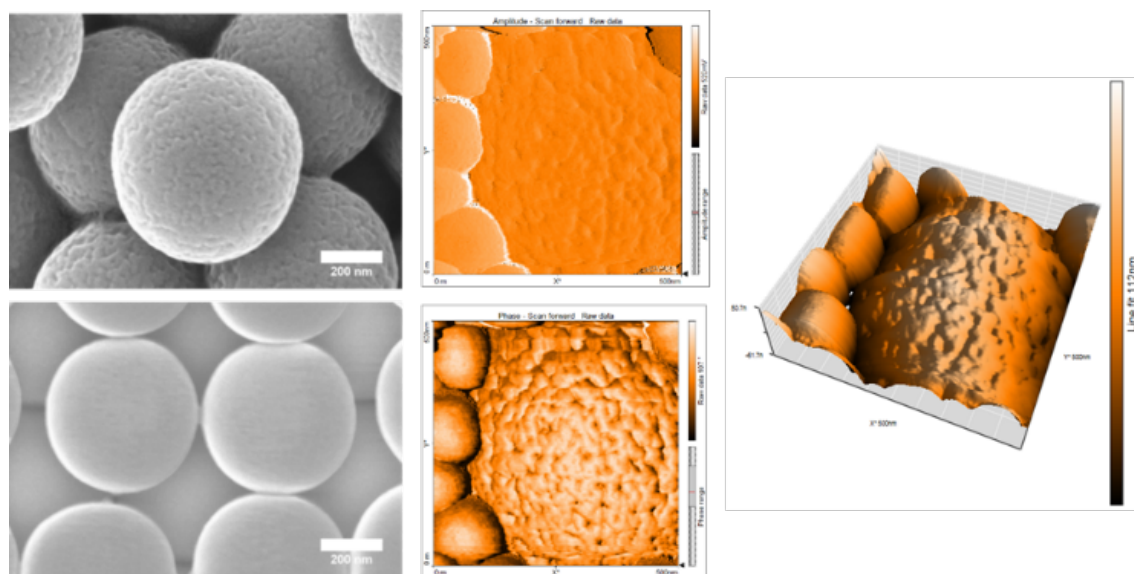


Figure 2-14. Comparison of particle surface. Left: SEM images of particles templated by GA (top) and EG (bottom). Center: AFM images of one GA512-MSN particle (rough) surrounded by smooth, non-templated SNP particles: amplitude scan (top), and phase scan (bottom). Right: AFM 3D representation of the same particles.

The AFM and SEM images indicate a very different morphology of the particles between the well-templated MSNPs (e.g. GA MSNPs) and the poorly-templated (e.g. EG particles) as well as non-templated ones. When GA was dissolved in the reaction mixture for a longer time before the addition of TEOS, bigger pores were obtained, mainly because GA clusters became bigger and collapsed to relatively larger aggregates which participate in the pore formation, further supporting our hypothesis (Figure 2-15).

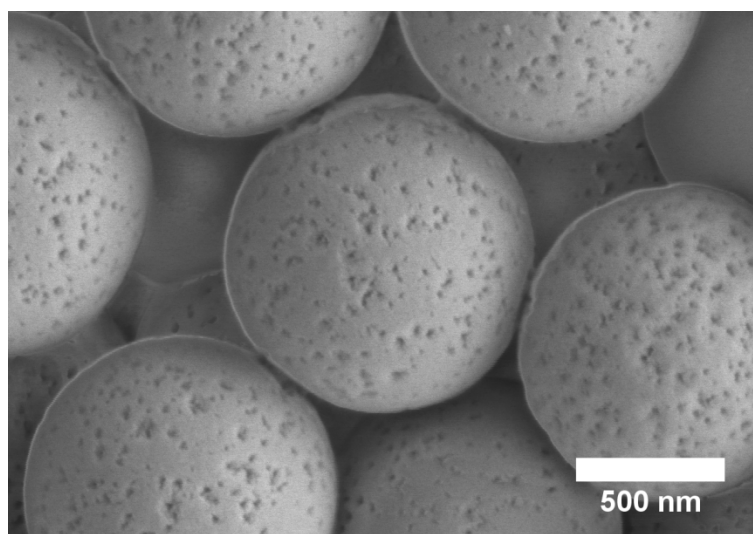


Figure 2-15. SEM image of particles templated by GA. TEOS was added 1h after the dissolution of GA.

To verify the decisive influence of supramolecular structure towards the pore formation, we quantified the mass loss of the particles after calcination resulting from all five templates at different concentrations (Table 2-5). The SNP samples, used as a contrast, were calcinated to measure the mass loss originated from the silica substance. Then, the mass loss of the templated ones was measured. The difference of the mass loss between the templated ones and the SNP samples was considered as the net weight of the templates contained in the particles.

The non-templated SNP samples showed a mass loss of 10.3% which could be attributed to the incomplete reactions and bounded water molecules on the surface. The mass loss of all detemplated samples fell within 2% of this value, indicating a relatively complete removal of templating agents, except for GA512. In this case, the mass loss was slightly higher, showing that GA was buried inside particles. This could suggest the formation of closed pores.



Regarding the as-synthesized samples, the TA and GA samples showed an increase of mass loss with the amount of templates, while the mass loss of the EA, EG, and QU samples remained relatively stable. It implies that, for EA, EG, and QU samples, the polyphenols were not surrounded by TEOS and had no templating effect for the pore formation. Thus, the introduction of EA, EG, and QU did not lead to porous structure but only slowed down the hydrolysis of the silica precursors to generate fewer nuclei and give a larger particle size. The extra mass loss compared to the blank SNPs contrast is attributed to the attached polyphenols on the surface. On the contrary, TA and GA are shown to be templates by the increase of remained weight with the initial concentration, demonstrating the participation of TA and GA in the pore formation. Moreover, a larger mass loss is associated with a higher porosity, in agreement with the BET results.

Table 2-5. Mass loss before and after calcination of particles prepared with different morphogenetic agents

Sample name	Mass loss (%), detemplated	Mass loss (%), as-synthesized
SNP	10.3	-
TA64-MSNP	9.0	10.5
TA128-MSNP	11.8±1.6	11.5±0.4
TA256-MSNP	8.5	20.5
TA512-MSNP	10.3±0.6	39.9±0.8
GA64-MSNP	9.8	10.8
GA128-MSNP	12.2±1.8	11.9±0.08
GA256-MSNP	10.2	14.2
GA512-MSNP	12.5±2.1	19.0±0.2
EG64-MSNP	9.3	11.4
EG128-MSNP	9.7	11.3
EG256-MSNP	8.1	11.5
EG512-MSNP	11.6±2.4	11.5±0.4
EA64-MSNP	9.3	10.8
EA128-MSNP	9.4	11.3
EA256-MSNP	9.4	11.4
EA512-MSNP	11.9±2.4	11.0±0.8
QU64-MSNP	9.6	11.0
QU128-MSNP	9.8	10.8
QU256-MSNP	9.8	11.1
QU512-MSNP	9.8	11.6

## 2.4 Conclusion

The morphogenetic mechanism of mesoporous silica nanoparticles by polyphenols was thoroughly studied by using tannic acid and four related molecules (GA, EG, EA, QU). The resulting particles were characterized by SEM, TEM, DLS, SAXS, BET, and TGA. The results showed that TA and GA lead to a porous structure following different mechanisms. The TA supramolecular structure served as skeleton for the silica precursors to polymerize around and generate pores. GA, in presence of silica precursors, formed small aggregates acting as templates to yield different particle morphology than the TA ones. TGA and DLS measurements indicated that the aggregates are responsible for the porous morphology. The involved polyphenols have a different impact on the size of final particles: this was determined by the pKa of the polyphenols, with lower pKa leading to a larger size. Our work unraveled the morphogenetic mechanism of mesoporous silica nanoparticles by polyphenols, contributing to the design of porous nanomaterials for drug delivery and bio-related applications.

# Chapter 3 A robust and controlled strategy for surface modification with particles

## 3.1 Introduction

Nanoparticle thin films are gaining more interest for use in the area of photonics, catalysis, sensors, and biomaterials, to name a few.[205] The fabrication of these types of applications usually required a very good control of particle alignment, density, and film thickness so as to achieve ideal performance and efficiency. Many techniques for the fabrication of particle-based films have been developed that are categorized into two genres: the direct deposition of particles and the in-situ growth of particles. For direct deposition, the most commonly used approaches include Langmuir-Blodgett (LB) deposition[206, 207], transfer printing[208], spraying[209], and dipping[210]. Each of them is of great advantages in certain cases but less preferable in another case. For example, LB deposition allows precise control of the particle alignment on a monolayer level but could also be very time-consuming. Transfer printing can be used to fabricate complicated pattern but always in a need of printing templates which is not as flexible and easy as dipping or spraying methods, for which the materials and templates can be switched flexibly and the operation is quite simple. The criteria of the selection of technique for each application should fulfill the requirements of both quality and ease of use. Besides that, in-situ growth of particles is also a useful method to generate particle coating.[211-213]

In the present study, we work to fabricate monolayer silica nanoparticle films with functional groups for further grafting of light-responsive drug delivery. We have considered the coating and surface modification process as a whole, first coating the silica nanoparticles and adding silanes to react with particles to obtain nearly a full coverage with silanes over the surface. In this way, we successfully fabricated a particle-coated film of a high surface functionalization that can result in a high drug loading as well as a low structural complexity for better understanding the triggering mechanism. Layer-by-Layer (LbL) assembly was applied because it shows special advantages like fast and easy preparation and adaptivity to various substrates and materials. We have successfully coated silica nanoparticles of different morphology onto optical substrates such as PDMS and PMMA. An image recognition method was developed to quantitatively assess the homogeneity of the particle coating. The coating and silanization processes were controlled to generate an approximately complete coverage of silica species. SEM, contact angle measurement, fluorescence labeling, XPS were performed to characterize the morphology and chemical properties of the substrates. Our strategy suggests a robust and controlled strategy for surface modification with particles.

## 3.2 Layer-by-layer approach for surface modification

### 3.2.1 Selection of coating approach

To successfully assemble the particle-optical fiber structure for drug release, we should have a surface that contains particles with amine functional groups to allow the anchoring of the photo-triggered prodrug. To achieve this, we should create a particle coating plus an amino-silane functionalized surface. There can be various assembly strategies as illustrated in Figure 3-1. Option 1 will be generating a layer of particles followed by functionalization with silanes. The conventional layer-by-layer assembly is based on electrostatic interaction and is very suitable for build particle layers to absorb the charged building materials to the substrate, the substrate should be treated to generate charges on the surface. One easy way is to expose the substrate to plasma, and the resulting surface will be negatively charged and be ready to absorb positively charged compounds. Silica nanoparticles are negatively charged. To construct a particle layer on the substrate, we have first introduced PDDA to form a positively charged layer on the substrate first and then attached silica nanoparticles on the top. Option 2 is to functionalize the silica nanoparticles with silanes and then assemble the amine-functionalized particle to the substrates. The amine-functionalized silica nanoparticles have a positively charged surface and can be directly assembled to the surface, however, we have used PEI as the first layer because it is proven to be able to work as a scaffold, making multilayer more stable.[214] PSS was then absorbed, allowing the sequential assembly of amine-functionalized particles. Option 3 is to chemically bond the particles with the substrate after silanization of the particles. Chemically bonding is also considered a possible route to attach the particle to the substrate. The surface was first plasma-treated to generate hydroxy groups on the surface and then modified with amino-silane. The obtained substrate was treated further with

glutaraldehyde and then used to react with amine-silica. We have investigated the three options and we have found that for option 3, showed the chemically bonded particle coating before and after sonication. Although the particle coating remained stable even after sonication, the particles self-aggregated as shown in Figure 3-2. The same aggregation was observed when coated the amine-functionalized silica nanoparticles. It is because the silanization will lead to a lower zeta potential, which is not enough to keep a homogeneous particle dispersion. Therefore, we decided to go with option 1, first coating the particle and then following with surface modification.

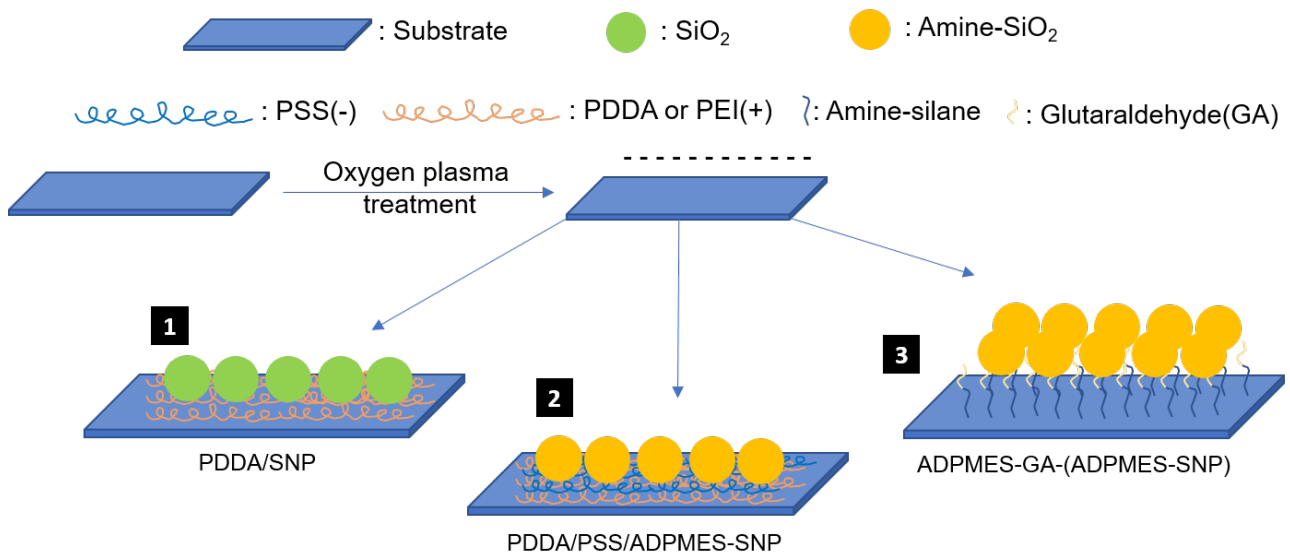


Figure 3-1. Strategies to build amine-functionalized silica nanoparticle coating

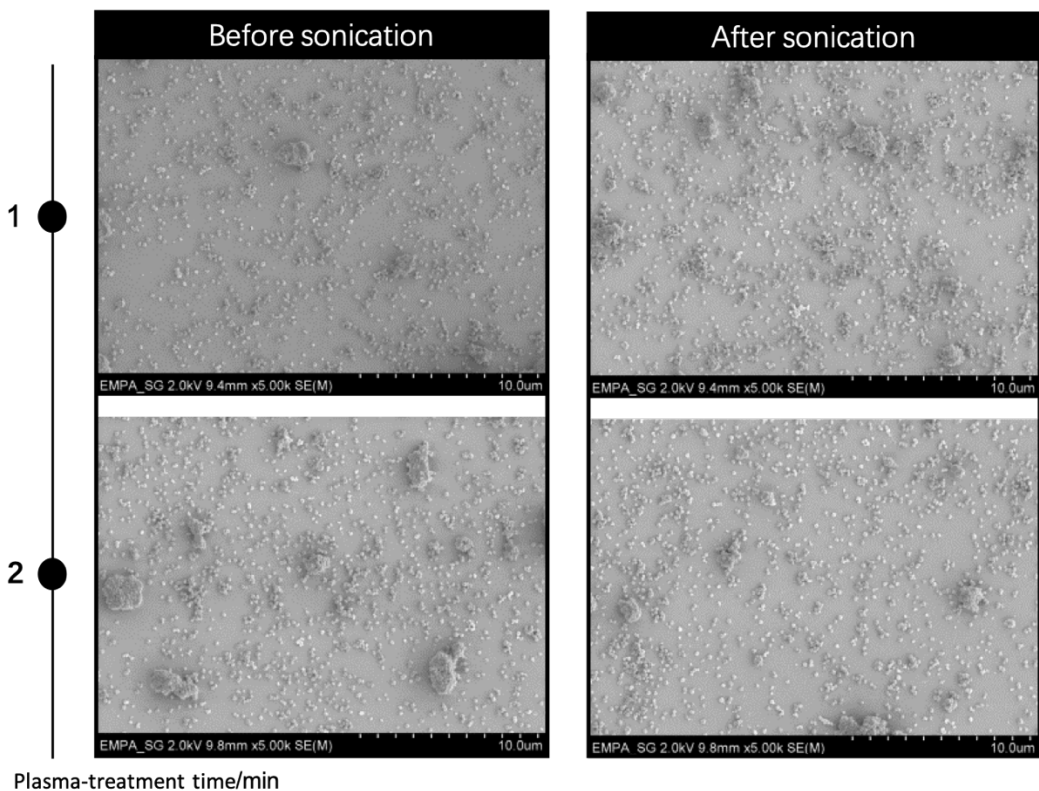


Figure 3-2. Chemically bonded particle coating via glutaraldehyde

### 3.2.2 Plasma-assisted approach for surface treatment

A typical layer-by-layer approach starts with the treatment of the substrate surface. The plasma-assisted approach is a rapid, clean, and substrate-independent method and is mostly used to generate hydrophilic surfaces on different matrices. In a plasma treatment process, the surface is placed in a chamber under a vacuum and bombarded with ionized gas, changing the surface energy of the substrate. We have treated PMMA and PDMS wafers and successfully assembled silica nanoparticles on the top. Interestingly, we have found different morphology of the coating on these two polymer substrates (Figure 3-3). The particles stand on the PMMA surface while in the case of PDMS, it seemed that the particles were partially buried in the matrix. The possible explanation for this will be hydrophobic recovery. One common problem with plasma hydrophilization is that it is not stable. A partial or complete hydrophobic recovery will take place which is caused by a reorientation of the surface layer. When it happened, the particles could be dragged into the PDMS network. It is somehow not the case for rigid matrices like PMMA, on which the particles still stay completely on the surface. Also, because of the hydrophobic recovery, the coating process should be done within a short time (within 30min for PMMA and 10min for PDMS) on a freshly treated surface.

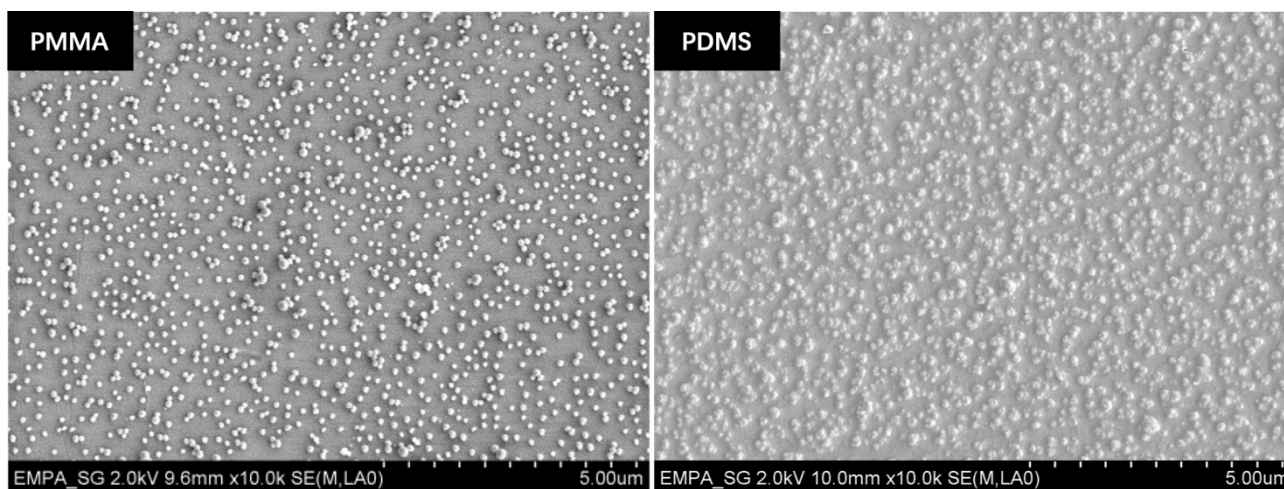


Figure 3-3. Morphology of particle coating on PMMA and PDMS surface

The further increase of time for the plasma treatment seemed to have not contributed to a higher coating density after 2 minutes (Figure 3-4). Therefore, the plasma irradiation lasted for 2 minutes for all samples under consideration of time efficiency and particle packing density. The density was evaluated quantitatively by Matlab as described in the next section.

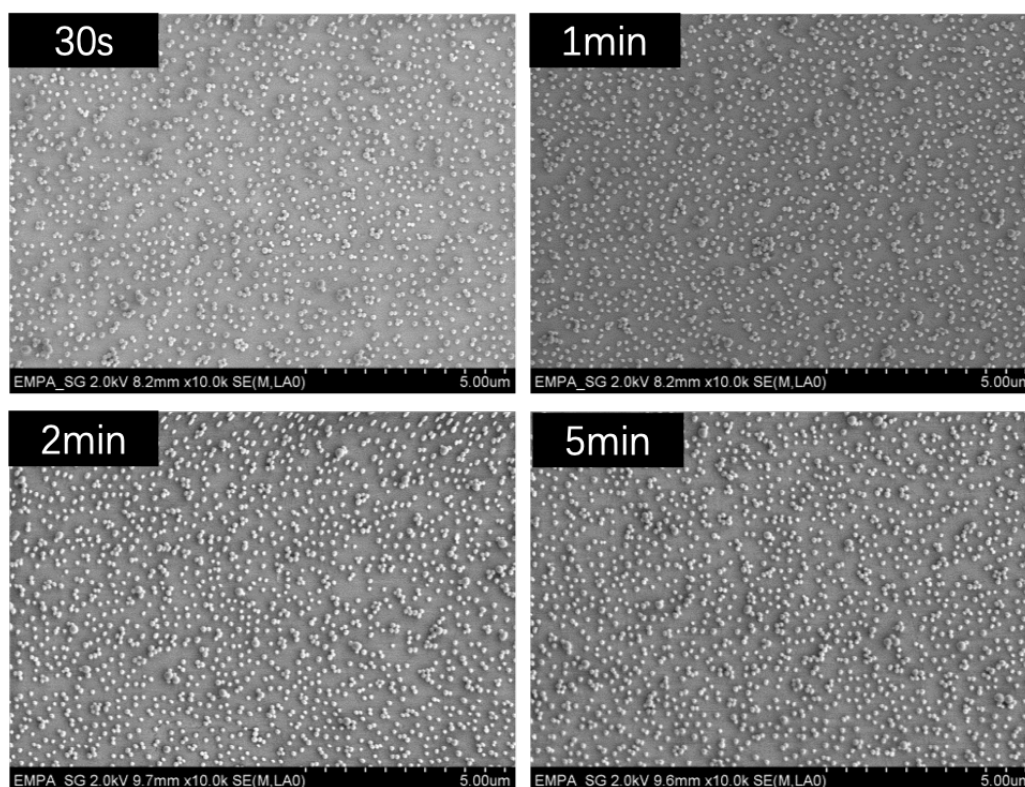


Figure 3-4. The density of particle coating when plasma-treated for different durations

### 3.2.3 Optimization of the layer-by-layer assembly via DoE

Generally speaking, the coating needed for our application or in most cases is supposed to be uniform, stable, and reproducible with a high packing density, which arouses the demand towards a robust, highly efficient standard coating method. It is important to optimize the coating condition in respect of production quality, time, and cost. Here, we have applied the orthogonal experimental design to screen the conditions that lead to the most homogeneous and dense particle monolayers. This methodology is widely used in industrial production to reduce the experiment counts. Silica nanoparticle and PDDA solution were selected as the negatively and positively charged polyelectrolytes, respectively, to be coated on PMMA substrates. As a complicated multicomponent system, both the concentration of deposition materials and the dipping time can significantly influence the density and homogeneity of the particle coating. Thus, experiments concerning 3 factors (Concentration of silica nanoparticles, concentration of PDDA solution, and dipping time) with 3 levels were arranged with the L9 orthogonal array table (Table 3-1).

Table 3-1. L9 orthogonal array table

Factor	A	B	C
Level	PDDA Conc.(mg/mL)	Particle Conc.(mg/mL)	Dipping Time/min
1	2	2	2
	2	8	5
	2	16	10
2	8	2	5
	8	8	10
	8	16	2
3	16	2	10
	16	8	2
	16	16	5



In order to evaluate the distribution of particles on substrates and compare quantitatively the density and homogeneity of the LbL films, we have represented them with the average distance between adjacent particles and its standard deviation, respectively. In the beginning, we have selected manually the particles with ImageJ and run the calculation based on the built-in adds of ImageJ. However, we found that the recognition of particles by ImageJ depended greatly on the nature of images and individual software operation. For example, the change of brightness of images and the dense packing of particles can lead to a failed recognition (Figure 3-5). Thus, all distances were measured from SEM images with MatLab codes that allowed precise recognition of particles regardless of the image brightness, particle shapes, and packing state.

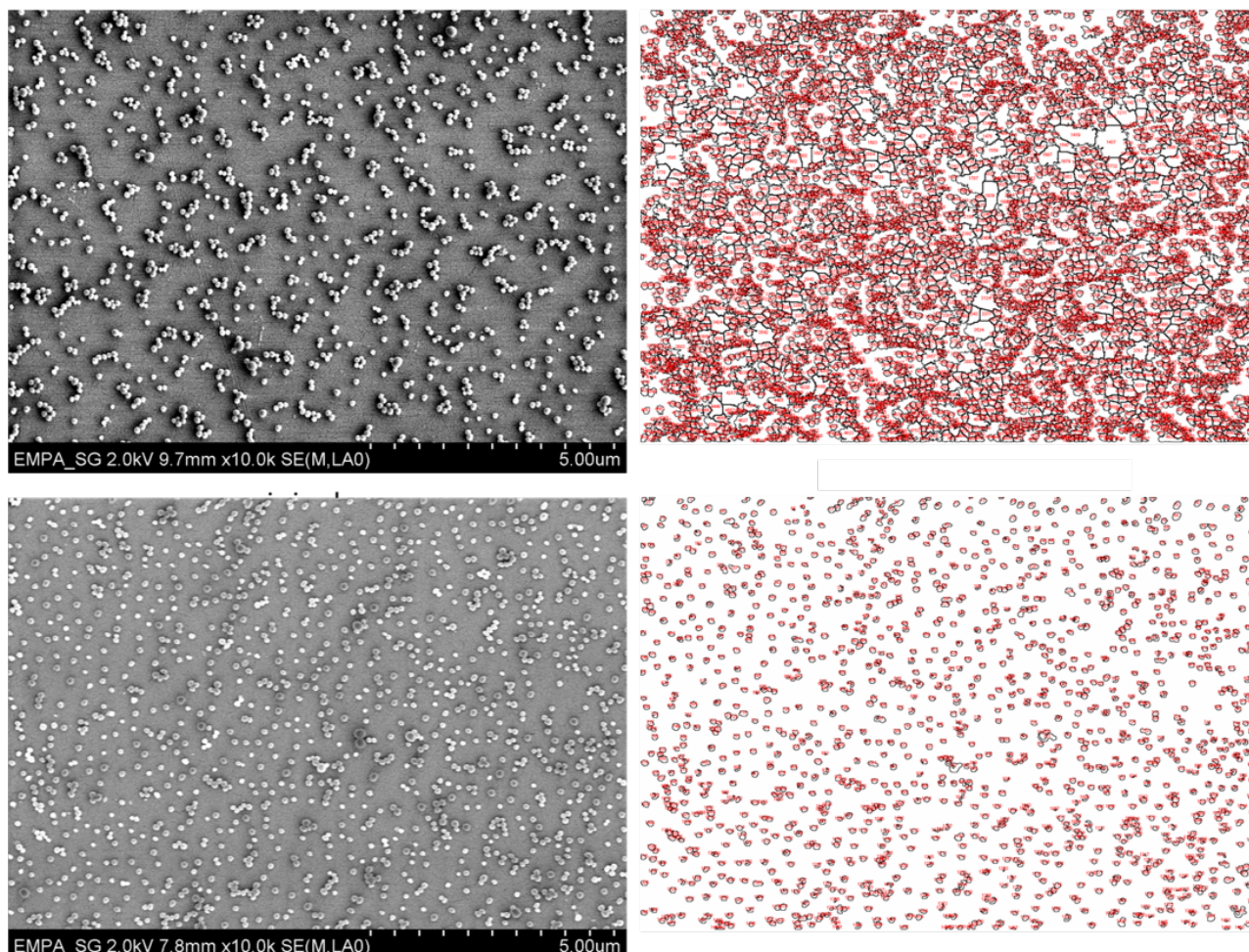
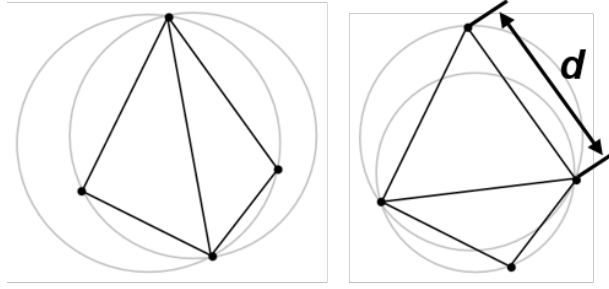


Figure 3-5. Recognition of particles from images with distinguished brightness by Image J

First, circle hough transform was used to select all the particles that are employed within the image area. Delaunay triangulation (Figure 3-6) algorithms were then applied to link two adjacent particles in the most optimized manner followed by removing the connecting lines on the edge area in order to avoid a bias of distance in between two particles towards a higher value (Figure 3-7). It can be seen that each particle was selected accurately, which is huge progress compared to that treated with ImageJ.



## Delaunay Triangulation



- Density  $\propto \frac{1}{d}$
- Homogeneity  $\propto \frac{1}{St.dev\ of\ d}$

Figure 3-6. Illustration of Delaunay triangulation

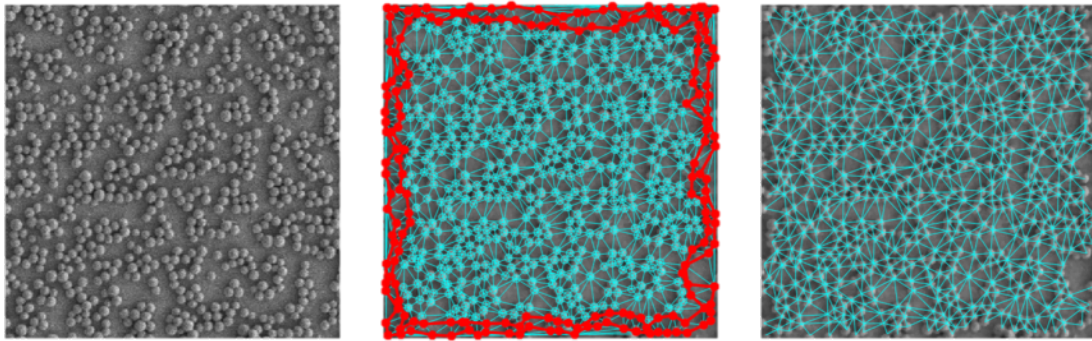


Figure 3-7. Particle recognition by Matlab. Left: original SEM image; Middle: particle recognition on the SEM image, identified red part will not be selected for the calculation of the adjacent distance to avoid a bias towards a higher value; Right: the network for calculation of the adjacent distance after removal of red part

Even though it works quite well for homogeneously distributed particles, the image recognition may fail and give an overread of the image information in the case where particles exhibited an aggregation or stayed exact next to each other. Thus, Matlab parameters in terms of [centers, radii] (refer to code summarized in section 5.4) need to be adjusted manually to make sure of precise particle recognition (Figure 3-8).

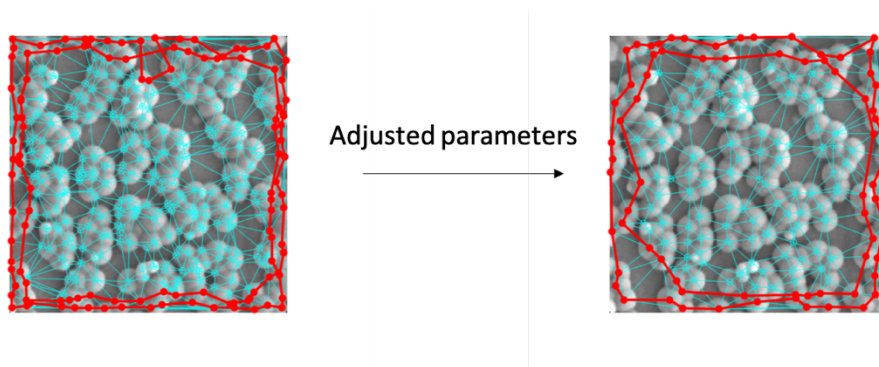


Figure 3-8. Comparison of the particle recognition result for adherent particles

The codes were then used to treat the SEM images obtained for the experiment series listed in the above-mentioned L9 orthogonal array table. For each experiment, we have repeated three specimens and three SEM images were captured for each specimen. The output distance(**d**) information was summarized as below (Table 3-2).

Table 3-2. Distance between adjacent particles obtained by Matlab

PDDA Conc./mg/mL	Particle Conc./mg/mL	Dipping time/min	Average distance( <b>d</b> )		St.Dev of <b>d</b>		<i>St. dev of d</i> <b>d</b>
			pixel	nm	pixel	nm	
2	2	2	23	460	9.9	198	0.430
2	8	5	14	280	5.6	112	0.400
2	16	19	13	260	5.0	100	0.385
8	2	5	16	320	6.4	128	0.400
8	8	10	13	260	5.0	100	0.385
8	16	2	13	260	4.7	94	0.362
10	2	10	14	280	5.4	108	0.386
10	8	2	13	260	4.6	92	0.354
10	16	5	12	240	4.1	82	0.342

The coating density and homogeneity are negatively associated with the distance and standard deviation, respectively (Figure 3-6). In order to figure out the condition that contributes to the highest density and best homogeneity, we have categorized the data based on factor A, B, and C. For each factor, we have taken the average of the particle distance and standard deviation of all three levels and plotted the value as a function of the corresponding parameter (Figure 3-9). When the concentration of the dipping solution and dipping time went up, the average distance between particles and its standard deviation decreased, implying an improvement of density and homogeneity of the particle coating. However, the growth trend slowed down gradually with the increase of concentration and dipping time. Considering the time efficiency and cost-effectiveness, the intermediate level for all three factors was selected as the optimal condition.

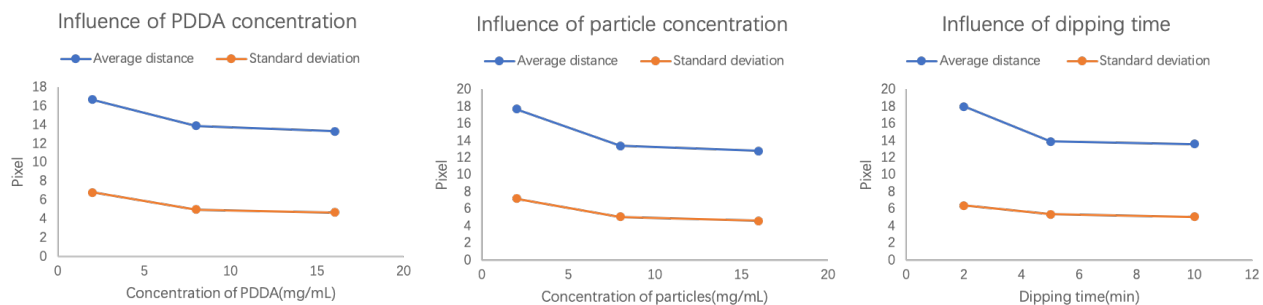


Figure 3-9. Analysis of the influence of each parameter on the density and homogeneity of the particle coating. Calculation was done based on the data in Table 3-2.

We have also conducted the factorial analysis to figure out which is the prominent influencing factor for coating density and homogeneity, respectively. The average value at each level of the three factors was calculated and the difference between the highest and lowest value ( $R_A$ ) is used to assess the effect of the corresponding factor. The larger the difference is, the more effective the factor is (Figure 3-10). It is clear that particle concentration has the most significant influence on both density and homogeneity. Dipping time is the second dominant factor for coating density while for homogeneity is the PDDA concentration.

Our founding may suggest that for particle coating, the particle concentration will be the most impactful factor for the process and the density and homogeneity can be controlled by tuning the particle concentration. Moreover, we have calculated the ratio of the standard deviation of **d** and **d**. A high ratio indicates a relatively denser but less homogeneous coating while for a low ratio it is opposite. Based on this ratio, the conditions can be chosen strategically for different application scenarios.

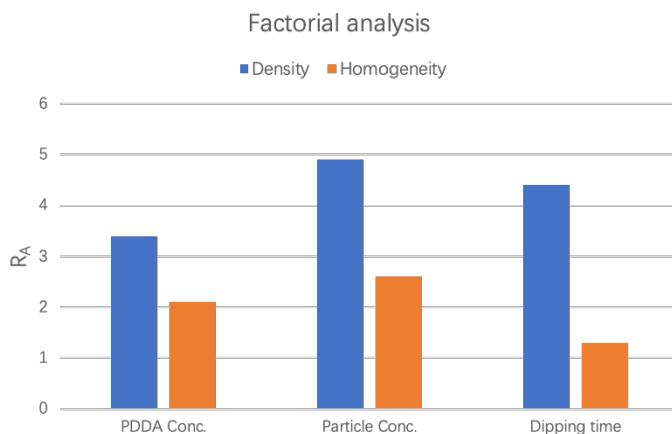


Figure 3-10. Determination of the prominent influencing factor

The repetition of the coating cycles can improve effectively the number of particles deposited on the substrates yet improve the complexity of the system (Figure 3-11). For our light-triggered release study from the optical fiber side, we prefer to have a simple model for a better understanding of the triggering mechanism. Moreover, to ensure that the triggered release occurs for all deposited particles, the coating should be within a certain thickness smaller than the penetration thickness of light. Thus, we stuck to a monolayer coating and continued with the silanization step. With trialkyloxysilane, we are able to cover nearly the whole surface as we discussed in the following section.

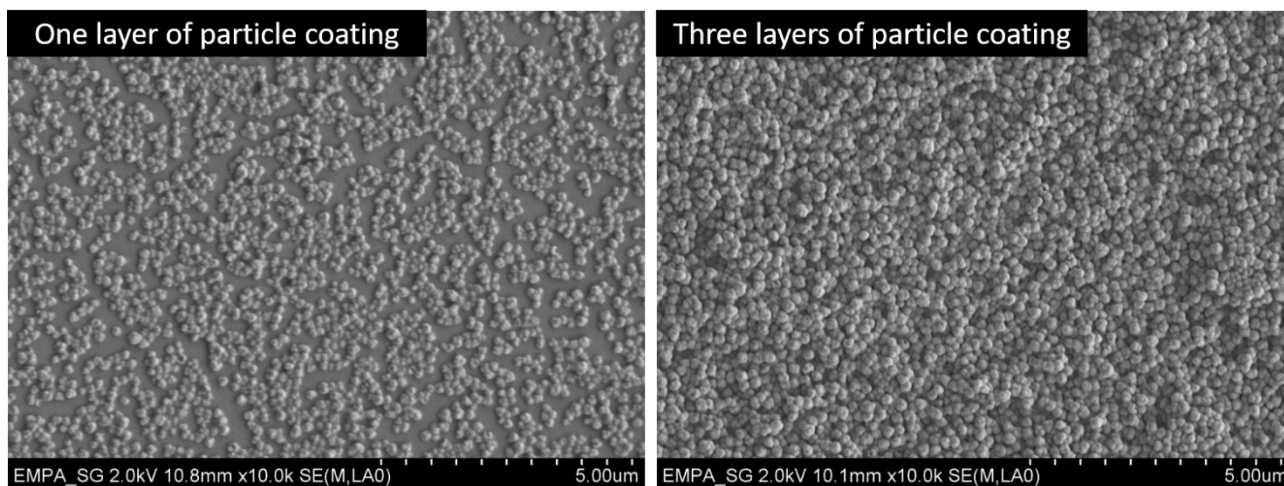


Figure 3-11. Surface morphology of PDMS substrate after one coating cycle(left) and three coating cycles(right)

### 3.3 Study of the silanization approach

#### 3.3.1 Selection of silanes

Silanization is a simple way to introduce functional groups to the surface of silica nanoparticles.[215, 216] Amine-silanes are the most frequently used because they can act as an anchor and react with many functional groups, eg. the carboxylic acid group to have a further surface modification. However, the varied binding branches of silanes will have a different effect on the surface modification. Aminopropyltriethoxysilane (APTES) and aminopropyltrimethylethoxysilane (APDMES) (Figure 3-12) can both bring in amine groups on silica nanoparticles but with a difference in coverage. APTES can self-crosslink while binding with the silanol groups on the surface of the particles owing to three ethoxy groups on one molecule. The crosslinking between APTES molecules can lead to a thick multilayer coverage and a high degree of amine addition on the particles. On the contrary, APDMES molecule possesses only one ethoxy group. It can either react with surface silanol groups or with another APDMES molecule. Therefore, it can only lead to a monolayer coverage of the silica nanoparticles and a relatively low degree of amine.

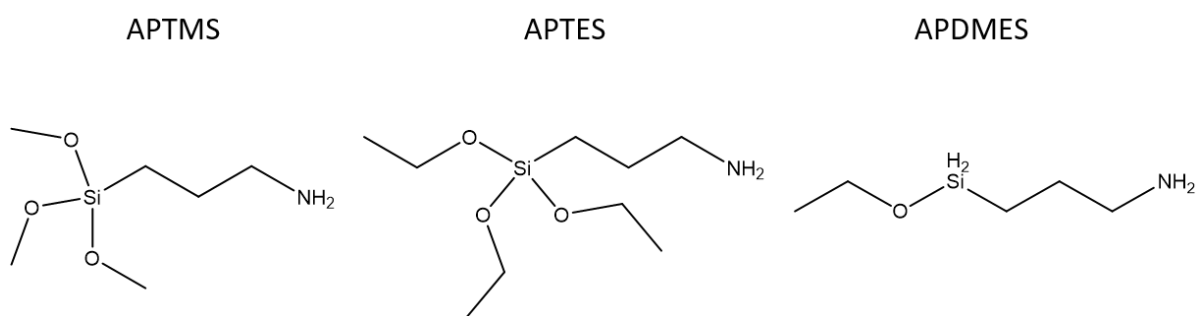


Figure 3-12. Chemical structure of APTMS, APTES and APDMES

This is clearly elucidated by the zeta potential measurement after 4 hours of surface modification with excess amount of silane (Table 3-3), from which we see a bigger change in zeta potential brought by APTES due to a higher modification degree when keeping the same amount of silanes. If we prolongate the reaction time, the zeta potential of the APDMES-MSNPs continuously changed from -24.5mV after 4h to 9.9mV after 24h, demonstrating a more sufficient modification. The APTES-MSNPs also exhibited a larger DLS size compared to the APDMES-MSNPs because of the self-aggregation attributed to a smaller surface potential. APDMES, as it can give a monolayer of coating, can greatly simplify the structure of the system. However, APDMES can only bring a very limited number of amines for the attachment of coumarin-chlorambucil conjugates, which may result in very few amount of drug release. Thus, silanes like APTES/APTMS were selected for the release purpose. Another reason to select APTES/APTMS instead of APDMES is that they promote the growth of the particles, which can contribute to the maximum drug loading owing to a high density of amines on the particles and the full coverage of particles on the substrates as we will discuss below.

Table 3-3. Zeta potential of different species of silica nanoparticles (after 4h of silanization)

Samples	Zeta-potential/mV	DLS size/nm
MSNP	-35.1±0.3	220
APTES-MSNP	16.6±0.8	2830
APDMES-MSNP	-24.5±0.7	1070

### 3.3.2 Characterization of the silanization on the substrate surface

APTMS has a similar structure as APTES and also forms multilayer coating on the particle surface, thus, it should give a similar modification outcome. To understand how the silanization goes on the particles on the substrate, we have first coated PMMA substrate with spherical silica nanoparticles (diameter around 160nm, almost the same dimension as the MSNPs) based on the optimal parameters we obtained for the coating process and then let the plate react with APTMS at room temperature in a nitrogen atmosphere for 24h. As shown in Figure 3-13, the particles have experienced a growth in diameter and aggregation with each other. Interestingly, this results in a nearly full monolayer coverage of silica nanoparticles on PDMS. Here, for the condition for surface modification, we did not seek for the best conditions for particle coating and silanization independently, but we are trying to make a compromise in between to endow the coating with a high drug loading and low structural complexity.

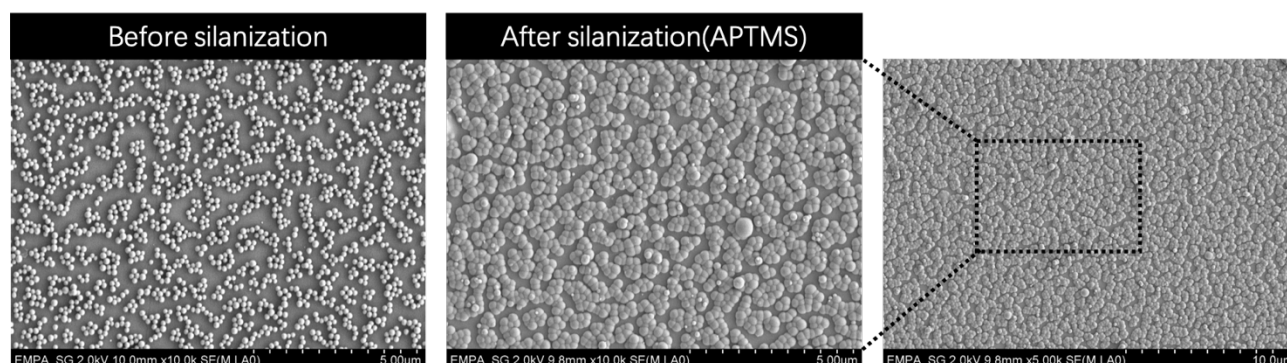


Figure 3-13. SEM images of particles before and after silanization on PMMA substrates

To provide direct evidence of the presence of nitrogen introduced by silanization, we have conducted an element scan survey by XPS. Compared to MSNPs without any modification, both APTMS-MSN and APDMES-MSN showed a signal peak at around 400 eV. This binding energy is attributed to nitrogen, which suggests the successful attachment of amine-silanes on the particle surface. Moreover, the APTMS-functionalized one gives a stronger signal than the APDMES one, indicating a larger amount of amine groups thanks to the self-crosslinking of APTMS.

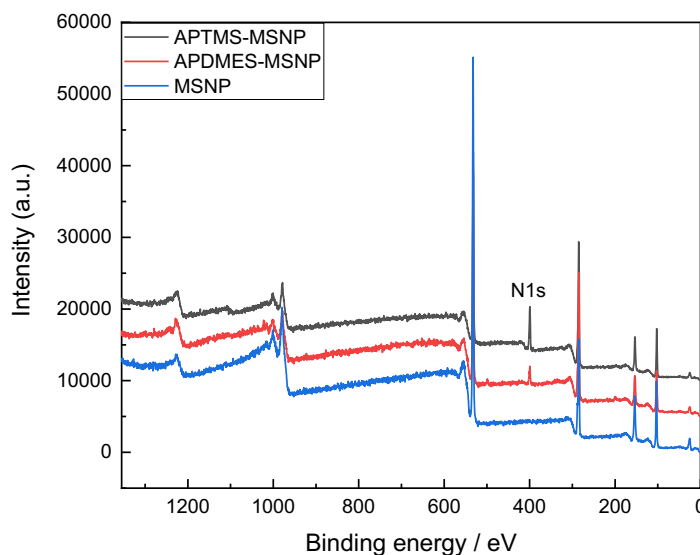


Figure 3-14. XPS spectra of the particles with and without silane

Besides the XPS method, fluorescein isothiocyanate (FITC) was applied as a fluorescent label to visualize the amine attachment. The fluorescence of the FITC-attached PMMA substrates (without particles, before silanization, and after silanization) was collected by Tecan microarray scanner (excited at 488 nm) and was then plotted in Figure 3-15c. Before silanization, the fluorescence intensity was quite weak. However, it increased after silanization with APDMES because the FITC molecules were linked with the amine groups of the silane, which also manifested the attachment of silane molecules. It should be noticed that the green color shown in Figure 3-15b is not the real fluorescence, but an artificial treatment for better visualization.

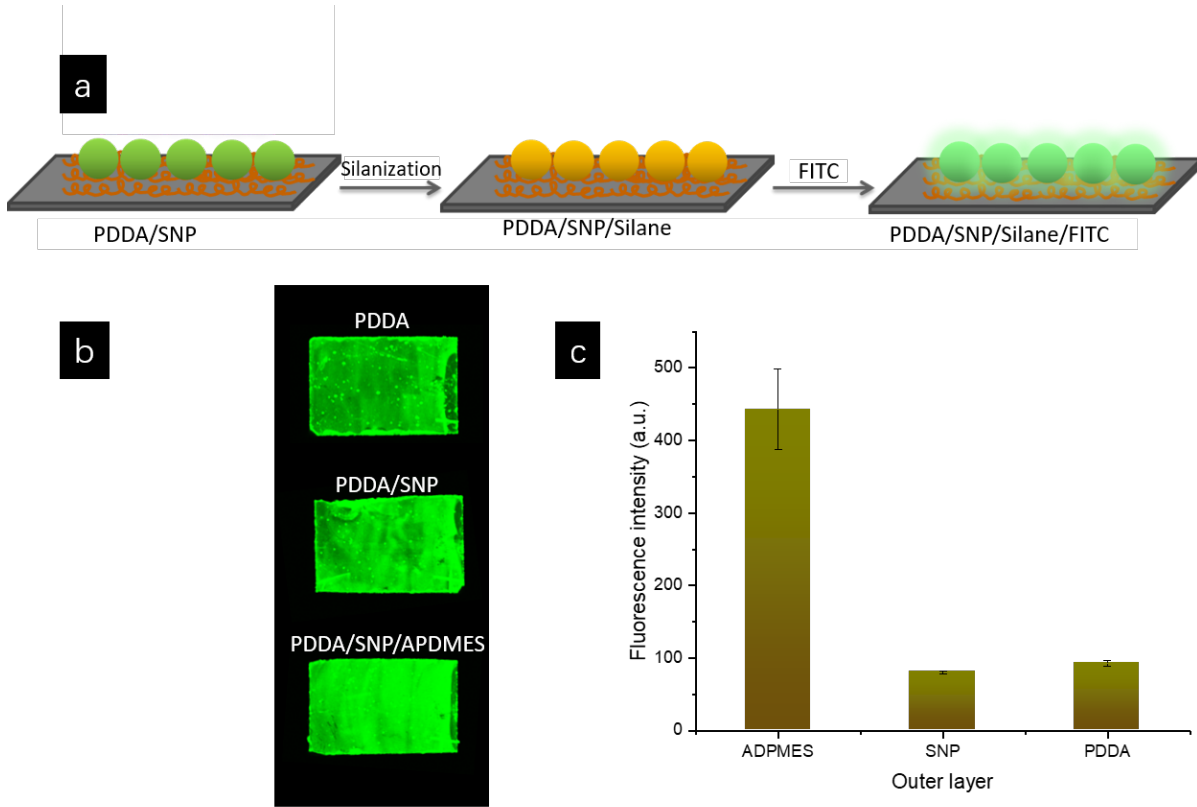


Figure 3-15. a) Step to label the particle-coated substrates with FITC; b) The visualized FITC signal on the PDDA-coated PMMA substrate and particle-coated substrates with and without silanization (false colors, not real fluorescence); c) The fluorescence intensity of substrates with different coatings (Signal was calculated by ImageJ with saturated pixels fixed at 0.4% for contrast enhancement)

Contact angle measurement is also quite a common method to verify surface modification. Chemical modification can vary the hydrophilicity of the surface, which is able to be detected by contact angle measurement. We have measured on both particle-coated PMMA and PDMS substrates (Figure 3-16). In the case of PMMA, the silanization of silica nanoparticles has caused a sharp increase of contact angle from 35° to 74° due to the decrease of hydrophilicity. When it comes to PDMS, the increase of contact angle is quite moderate, from 132° to 140°. The most interesting part is that the contact angle of the PDMS and PMMA substrates has changed oppositely after the introduction of silica nanoparticles to these two substrates. The same particles were employed but for PMMA, the contact angle dropped from 63° to 35° while for PDMS, the surface became more hydrophobic and the contact angle grew from 114° to 132°. As we know, hydrophobicity can be achieved by chemical functionalization and structural design. As the same functional groups were added to the particles, the reason for the difference in the change of contact angle should be ascribed to the surface morphology. This phenomenon can be explained by the Wenzel model[217]. Wenzel model is built on the basis of Young's equation and used to quantitatively calculate the contact angle on a rough surface. The Wenzel equation is described as

$$\cos \theta_w = \frac{r(\gamma_{SA} - \gamma_{SL})}{\gamma_{LA}} = r \cos \theta_0$$

Equation 3-1. Wenzel equation

where  $\theta_0$  is intrinsic contact angle,  $\theta_w$  is Wenzel contact angle and  $r$  represents the roughness of a surface, equal to the ratio between real surface area and projected area. As the particle-coated surface is rough,  $r$  is always bigger than 1. When  $\theta_0 < 90^\circ$ ,  $\theta_w < \theta_0$ . When  $\theta_0 > 90^\circ$ ,  $\theta_w > \theta_0$ . This means that surface roughness can amplify the hydrophilic properties of the surface. For hydrophilic surfaces, whose contact angle is smaller than 90°, the introduction of surface roughness will lead to a more hydrophilic surface as we observed for the PMMA substrate. For the PDMS substrate, whose contact angle is bigger than 90°, the surface became more hydrophobic after particle coating.

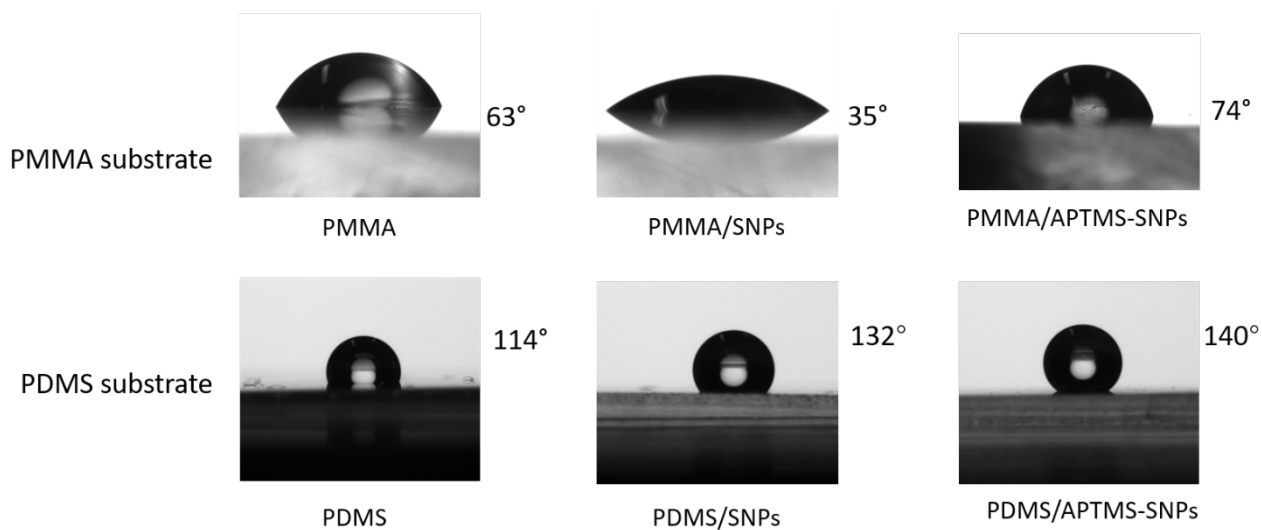


Figure 3-16. Contact angle measurement for PMMA and PDMS substrate

### 3.4 Conclusion

This chapter is to explore the optimal condition for surface modification process that can be applied in the next chapter for surface modification of optical fibers for the release study. We have successfully established an easy layer-by-layer approach to create a monolayer of particle coating on both PMMA and PDMS substrates. The approach enables a low structural complexity and a dense and homogenous coverage with particles on the substrates. The computer vision method was employed to quantitatively evaluate the particle coating, increasing dramatically the efficiency and accuracy of the coating evaluation. We have then functionalized the particles with different silanes. SEM, XPS, DLS, fluorescence labeling, and contact angle measurement were used to characterize the silanization. Our work offers a robust and controlled strategy for the fabrication of particle-coated surfaces that is applicable to multiple genres of substrates and coating materials.



# Chapter 4 Light-responsive drug release from flexible polymer optical fiber

## 4.1 Introduction

Chemotherapy has experienced a great revolution since first applied to tumor treatment and remains one of the most effective routes to release patients from cancer.[218] Cytotoxicity of the anticancer compounds, limiting the proliferation of cancer tissue, yet brings up severe side effects to healthy cells. Drugs and delivery strategies have been upgraded in terms of drug efficiency and specificity to minimize this issue by reducing the applied drug dosage as well as enabling release on site.[219, 220] An extensively applied route is to host drugs within a carrier such as nanoparticles[221-223], polymer networks[224-226], liposomes[227, 228] decorated with targeting groups for automatic targeting or stimulus-responsive molecules followed by locating and triggering release with the corresponding stimulus such as pH[229], temperature[230], magnetism[231, 232]. However, the controlled release based on environment-dependent factors such as pH or temperature is passive and hard for external manipulation while in contrast, light, as an active trigger, can be switched on-and-off and enables an instant on-demand and zero-premature release. Light-responsive molecules like coumarin[233, 234], spiropyran[235, 236], azobenzene[237, 238] have been employed to build various systems to release drugs via different strategies. The photocleavable release is one approach where drug molecules were decorated with photolabile protecting groups(PPG) which can be excited with particular light can cause the breakage of the bond between the drug and light-responsive component, leading to the diffusion of hosted compounds.[239] A modification to the photolabile group can enable the excitation of bond breakage with light from visible to even near-infrared (NIR) range[240, 241].

Further integration of these nanosystems to other matrices, particularly fibers, can expand significantly the application scenarios from conventional pharmaceutical use to medical devices, for example, wound patches[242, 243], implants[244, 245], and functional textiles[246, 247]. Even though it is a promising trend to follow, the integration process needs to be adjusted individually due to the particular material profiles. Silica nanoparticles have a long history to be used as drug carriers for their chemical stability, large surface area, tunable pore sizes, as well as surface diversity owing to a variety of well-established modification approaches.[248] Here, we have combined MSNPs with PDMS optical fibers to build a novel light-responsive system that can be used to release diverse species of compounds via photolabile release from the optical fiber side (Figure 4-1) as a proof-of-concept.

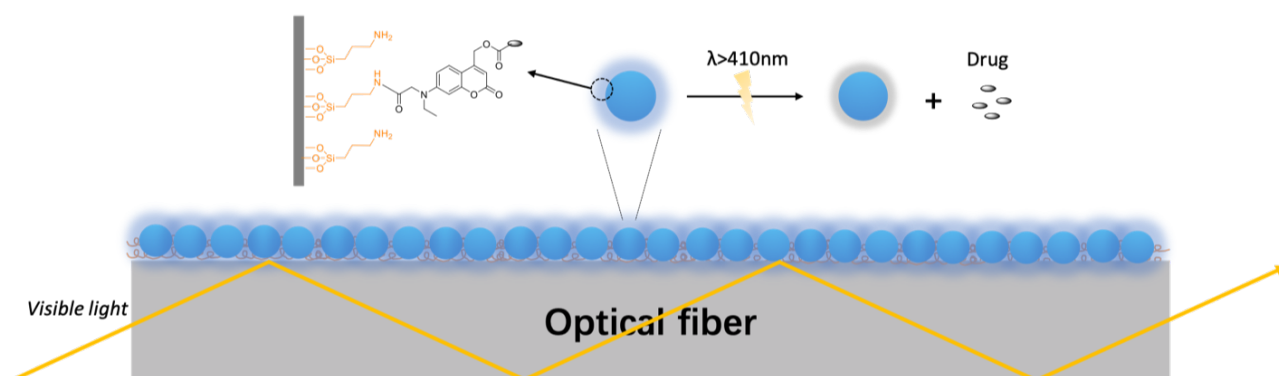


Figure 4-1. Illustration of photo-triggered release from optical fibers

The particles served as hosts for coumarin-based chlorambucil prodrugs (CCDs) (Figure 4-2, structure 2) and coated along PDMS fibers. Transmission of visible light ( $>400\text{nm}$ ) through the fibers can trigger the photolabile breakage of coumarin-chlorambucil bonds and result in the diffusion of chlorambucil. Our system gives an easy approach to fabricate functional fibers with releasing properties for chemotherapy. PDMS endows flexibility and comfortability compared to glass optical fiber. Instead of the well-known targeted release introduced by specific recognition or triggered by the unusual chemo-physio environment of tumors, it is possible to realize on-site release of drugs to the cancer lesions by physical approach. Moreover, the use of modified coumarin

allows the release with visible light, avoiding harm to body tissue by UV light. Both the evanescent wave and outcoupled light were responsible for activating the light-responsive molecules to trigger the release. Even though there have already several studies on the drug release from the tips of optical fibers have been reported[112, 113], but to the best of our knowledge, it is the first time that the drug release occurs on the optical fiber side. Also, it is worthy to mention that, as optical fibers are widely used as sensors, it is very promising to combine both sensing and releasing functions to fulfill the demands towards the development of an advanced theranostic device or personalized release platform, either for in-vivo or in-vitro applications.

## 4.2 Release of chlorambucil anticancer drug from isolated MSNPs and PDMS-nanoparticle hybrid films

### 4.2.1 Photolabile protecting groups (PPG) for controlled release

Photolabile protecting groups are increasingly used as a versatile tool allowing for the temporally and spatially controlled release of various bioagents[239]. Attractive features of coumarin-derived PPGs are their strong absorption extending to the visible range, which is very promising for in vivo release to avoid UV harm to living tissues. Original coumarin molecule has a fluorescence absorbance at 356nm, but the addition of electron-donating group (e.g. alkyl group) was proven to enable an absorbance shift to a higher wavelength. Following this principle, we have been inspired by a coumarin-derivative (Figure 4-2, structure 1) with N-diethyl functional decoration at position 7 which enables an absorbance of visible light. One branch of the N-ethyl group was substituted with N-carboxymethyl group (Figure 4-2, structure 2) in order to bond with silanized MSNP. Meanwhile, chlorambucil was connected to position 4 via a carboxylic group that will hydrolyze under irradiation of visible light in presence of water.

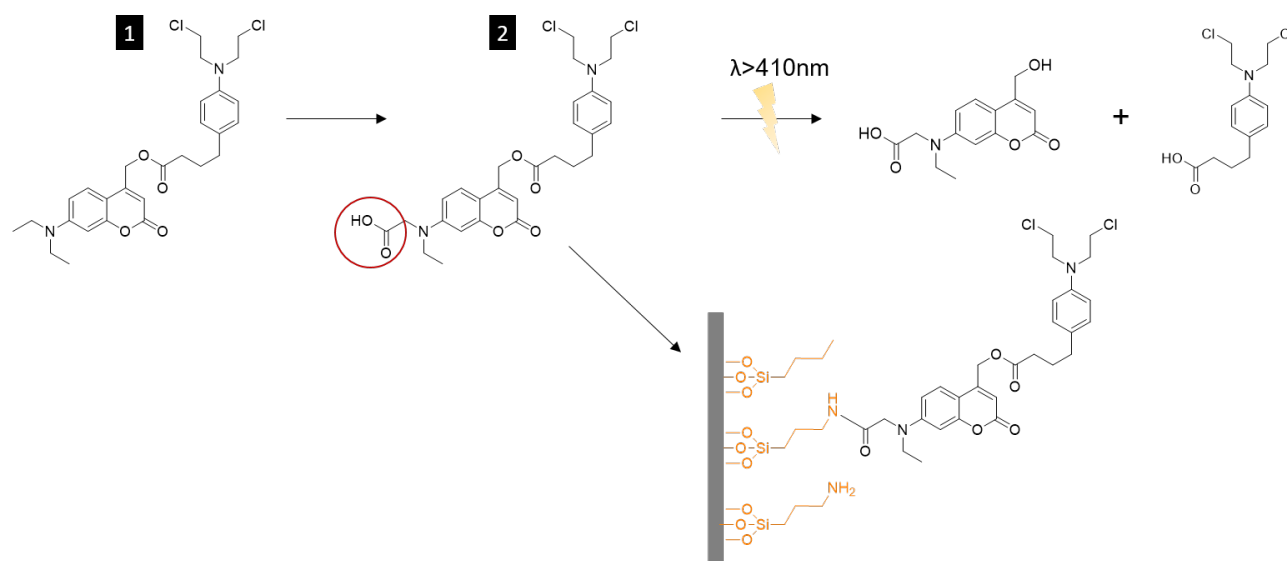


Figure 4-2. The structure of coumarin-chlorambucil-prodrug and the releasing principle

A release experiment from the isolated coumarin-chlorambucil conjugates was performed to verify the photolysis-induced bond breakage. A dose of the conjugates was dissolved in a water acetonitrile mixture (v/v 10:90) and irradiated with Volpi intraLed 3 (>400nm) as a light source and products were detected by UPLC.

### 4.2.2 Characterization of coumarin-chlorambucil-anchored nanoparticles and films

The cauliflower MSNP carriers were prepared according to our previously established method described in chapter 2[249]. The resulting cauliflower-like particles have a diameter around 220nm in the long axis and an average pore size of 7nm confirmed by EM, nitrogen absorption method, and SAXS analysis. The particles were then silanized by APTMS to create amine groups for the further attachment of coumarin-chlorambucil conjugates. The morphology of MSNPs (Figure 4-3) has experienced an change after silanization with more aggregation in agreement with the previous literature[250]. The resulting APTMS-functionalized MSNPs (AP-MSNPs) were then functionalized with the coumarin-chlorambucil conjugates.

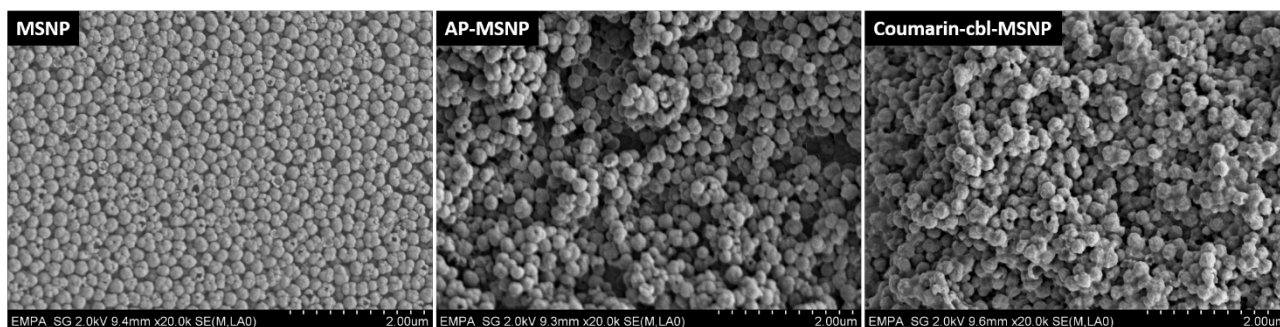


Figure 4-3. Morphology of the MSNPs, AP-MSNPs, and coumarin-clb-MSNPs

The synthesized particles were then coated onto PDMS fiber by a layer-by-layer approach (Figure 4-4). The quality of coating was evaluated quantitatively using the particle recognition method we built in chapter 3 in terms of coating density and homogeneity demonstrated by the distance between two adjacent nanoparticles and its standard deviation, respectively. The analysis of the SEM images by Matlab stated that an average distance between particles is  $170 \pm 90$  nm. The coating process showed good reproducibility and consistency on PDMS fibers. Notably, the coating of particles remained a single layer to have a low structural complexity and the employment of APTMS induced a high density of amines for the prodrugs grafting (Figure 4-5). The obtained result can then be compared with the simulation results.

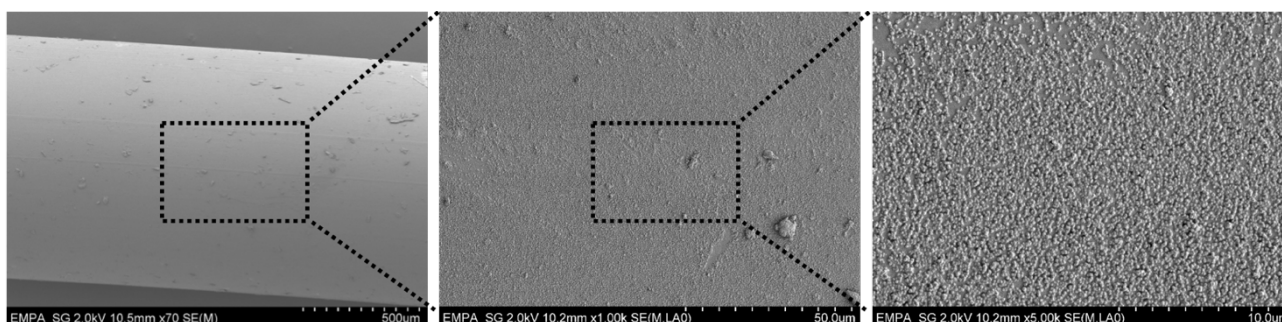


Figure 4-4. SEM images of particle coating on PDMS fibers

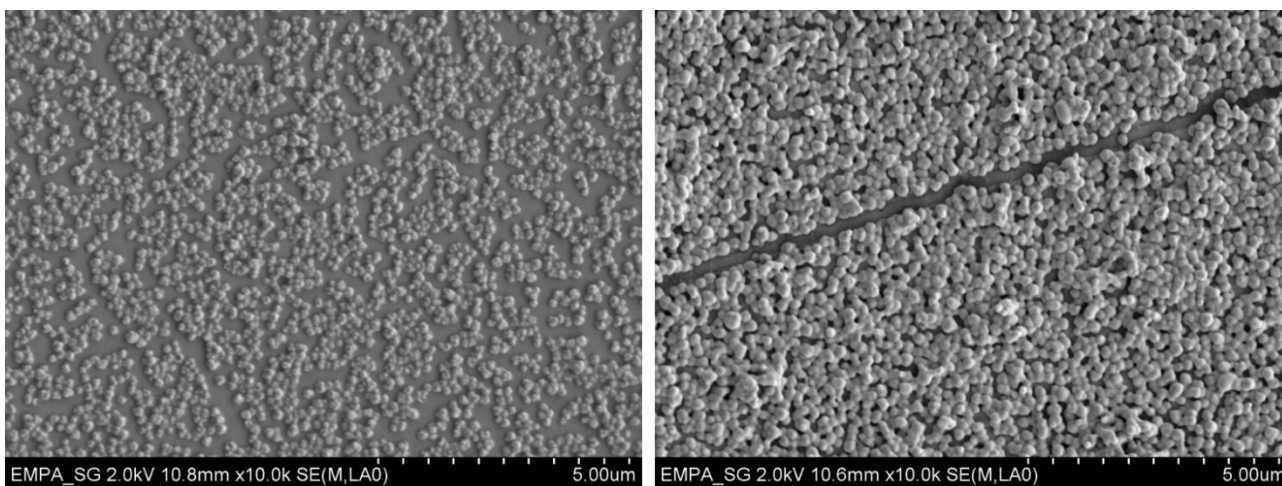


Figure 4-5. SEM images of particle-PDMS substrates before and after the attachment of coumarin-chlorambucil conjugates

Meanwhile, the CCDs were designed to be activated with visible light ( $>400$  nm). The existence of amine groups from APTMS and prodrugs were confirmed by XPS, indicating a successful attachment (Table 4-1). Nitrogen and chlorine were attributed to the APTMS and CCD, respectively. Fluorine was detected for particle samples due to the scratching on the PTFE tube surface in the drying process. More structural details were revealed by the high-resolution scan of the element of interest (Table 4-2). The APTMS-CCD components seemed quite stable with only a slight reduction of chlorine in the order of 10% for 1h measurement duration suggested by the increased chlorine amount. Interestingly, the functionalized MSNPs were observed with 2 types of bind-

ing energy for nitrogen and chlorine, indicating two types of chemical structures of the functionalized moieties. The  $N^+$  amount equaled roughly to  $Cl^-$ , implying the existence of an ionic state.

Table 4-1. XPS element survey results (surface atomic%)

	C	O	Si	N	Cl	F
PDMS-MSNP	39.5	37.3	23.2	-	-	-
PDMS-APTMS	45.9	28.9	21.0	4.2	-	-
PDMS-APTMS-CCD	45.6	28.2	21.7	2.9	1.6	-
MSNP-APTMS-CCD	26.9	40.8	20.4	4.7	1.7	5.5

Table 4-2. High resolution scan for nitrogen and chlorine elements (surface atomic%)

	Cl(start)	Cl(finish)	%N-C	$N^+$	Cl-C	$Cl^-$
PDMS-APTMS	-	-	3.7	0.5	-	-
PDMS-APTMS-CCD	26.1	28.5	1.3	1.6	0.3	1.3
MSNP-APTMS-CCD	14.4	15.8	2.6	2.0	0.3	1.4

Figure 4-6 has showed the fluorescence of the particles and MSNP-coated PMDS fibers. It can be seen that both fibers and MSNPs have blue fluorescence compared to pure PDMS fiber, indicating the attachment of coumarin-chlorambucil conjugates. The commercial 7-(diethylamino)coumarin-3-carboxylic acid was also chemically bonded to the particles on the fiber as control. The fluorescence of the commercial coumarin-decorated fiber turned out to be slightly bluer than that of the coumarin-clb conjugates because the existence of electron-donating groups has contributed to the absorbance of the light with a higher wavelength. The intensity of the fluorescence was also stronger for the commercial coumarin, as the absorbed energy was all emitted as fluorescence while in the case of coumarin-cbl conjugates, part of the absorbed light will trigger the breakage of the carboxylic bond to release chlorambucil, leading to a weaker fluorescent intensity.

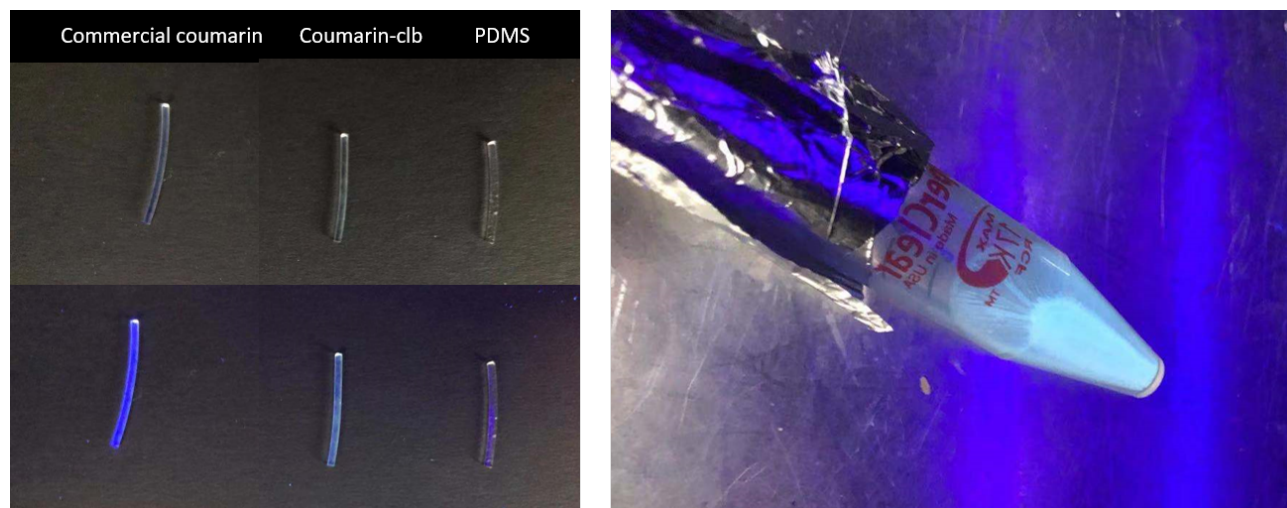


Figure 4-6. Fluorescence images of the MSNP-PDMS fibers (top left: before UV irradiation, bottom left: under UV irradiation) and MSNPs(right) decorated with coumarin-cbl-conjugates.

### 4.2.3 Pre-release studies

#### 4.2.3.1 Distribution of coumarin-chlorambucil conjugates on PDMS fiber

The concept of our study is to build a particle-fiber release system where the particles serve as drug carriers and fiber as the light source to activate the breakage of the photolabile prodrug bond. Thus, the distribution of coumarin-chlorambucil conjugates needs to be confirmed. Several factors will influence the distribution of the drug by influencing the diffusion process, including the solvent effect and reaction activity between each layer coating and prodrug. In terms of solvent effect, PDMS show different swelling behavior when exposed to various solvents (Figure 4-7). In solvents (for example, toluene) that can lead to a big swelling of the cross-linked network may result in the penetration of prodrugs into PDMS fiber instead of only chemically bonded to MSNPs. Thus, we

have chosen DMF as the reaction solvent throughout the whole experiment as it is a good solvent for the prodrugs and cause limited swelling of PDMS. To verify that the prodrug will mainly present on MSNPs, we have applied FITC as a label and visualized its location using CLSM (confocal laser scanning microscopy) (Figure 4-8).

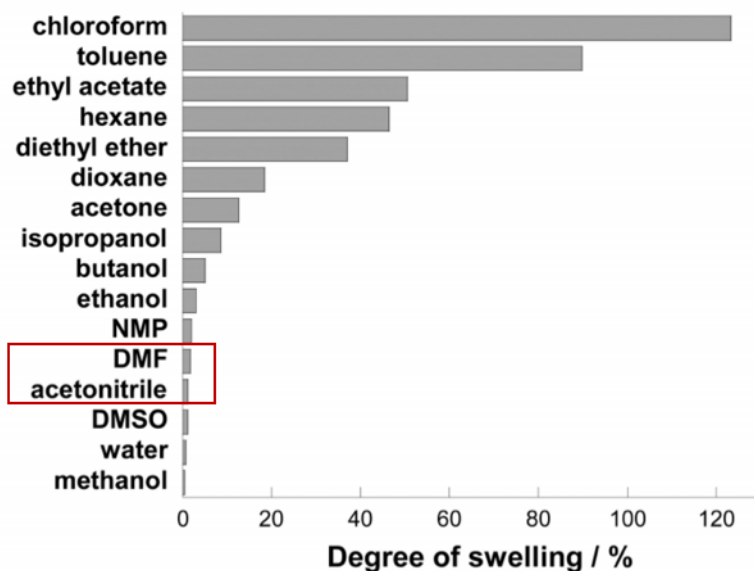


Figure 4-7. Degree of swelling of PDMS in different solvents.[251]

Except for the AP-MSN-coated PDMS fibers, we have immersed PDMS fibers in selected solvents including N,N-dimethylformamide (DMF) and acetonitrile (ACN) because they have different evaporation temperatures for 24 hours, and half of them were dried in the oven at 90°C to evaporate the solvents. All these fibers were then immersed in FITC solution for another 24 hours, washed to remove physically absorbed FITC, and observed under CLSM. AP-MSN-coated fiber exhibited a strong fluorescence comparing to other samples, indicating FITC molecules are exclusively from MSNPs. Fiber that was immersed in acetonitrile has shown a slight diffusion of FITC into PDMS due to the swelling of the crosslinked network. When the fiber was dried before reacting with FITC, the fluorescence is negligible compared to the one without the drying process. DMF is hard to remove at 90°C, leading to almost the same fluorescence despite being dried. Our study suggested solvent will influence the loading of molecules of interest into our particle-fiber system and must be carefully selected.

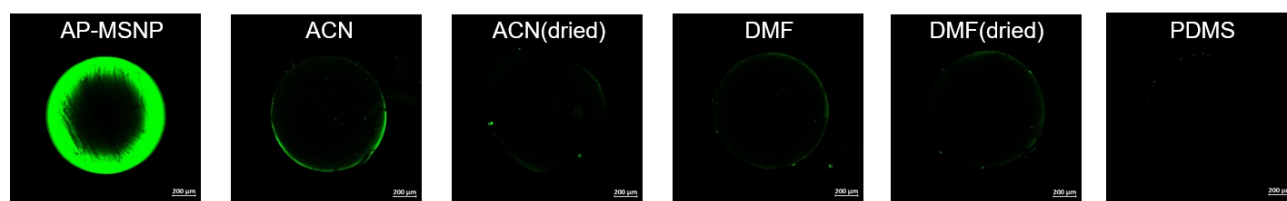


Figure 4-8. Solvent influence on the distribution of FITC molecule.

Besides the solvent effect, our particle-fiber system has a complex composition with multiple layers and ingredients. To prove the silanization took place only on the coated MSNPs, we have allowed the PDMS fibers (MSN-coated fibers, PDMA-coated fibers, and plasma-treated fibers, fibers without any treatment) to react with silanes and then visualize the silanes with FITC (Figure 4-9). PDMS fibers without any treatment, as control, showed no fluorescence at all. MSN-coated PDMS fibers had a strong fluorescent signal compared to the PDMA-coated and plasma-treated one on which the fluorescence is ignorable, indicating that, the further grafting of prodrugs will occur on particles.



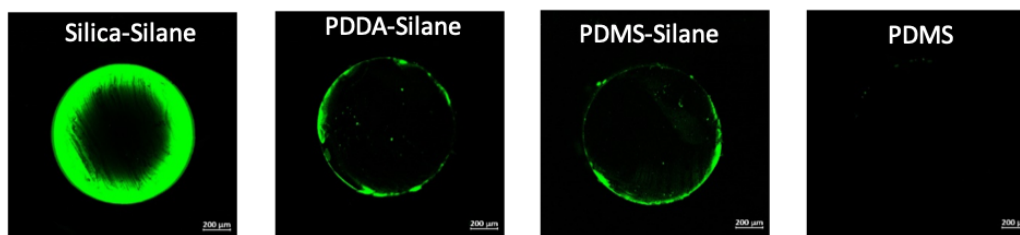


Figure 4-9. Influence of each layer of coating on the distribution of FITC

#### 4.2.3.2 Proof of existence of out-coupled light along PDMS fiber

The photolysis of the coumarin-chlorambucil conjugates on the PDMS fiber surface should be attributed to the outcoupled scattered light and evanescent wave. In our work, the release is not triggered by direct irradiation, thus it is essential to have a proof-of-concept before the release experiment. The AP-MSNPs-coated PDMS fiber was allowed to react with FITC for 24h to have sufficient bonding of FITC molecules with amine. Then, the fiber was coupled with an internal light source of a fluorometer on one end and an optical fiber which is connected with the fluorometer detector was used to collect the fluorescent emission as illustrated in Figure 4-10. Light ( $\lambda=490\text{nm}$ ) propagated through the PDMS fiber and the fluorescent signal of FITC was recorded in Figure 4-11. PDMS fiber without any surface modification gave no fluorescence while that with FITC-particles had emission peak at around 520nm, suggesting a successful excitation of FITC. As a control, a PDMS fiber without particle coating was immersed in FITC solution for 24 hours and measured. The result shows no emission peak at 520nm, demonstrating FITC were mainly anchored on the MSNPs, in agreement with the CLSM images.

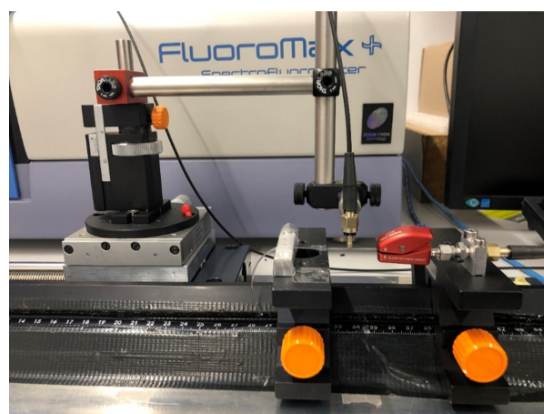
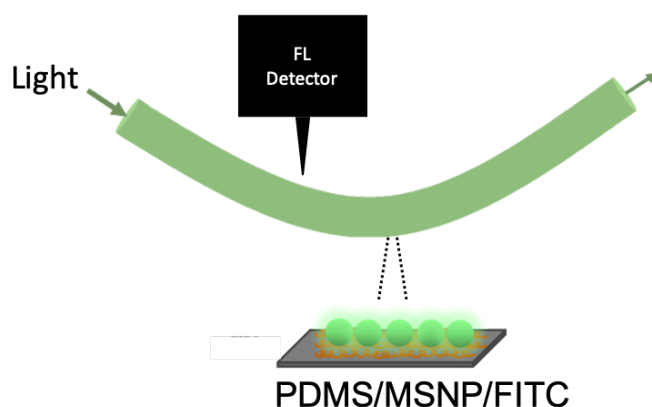


Figure 4-10. Setup for measurement of fluorescence excitation from the side of fiber

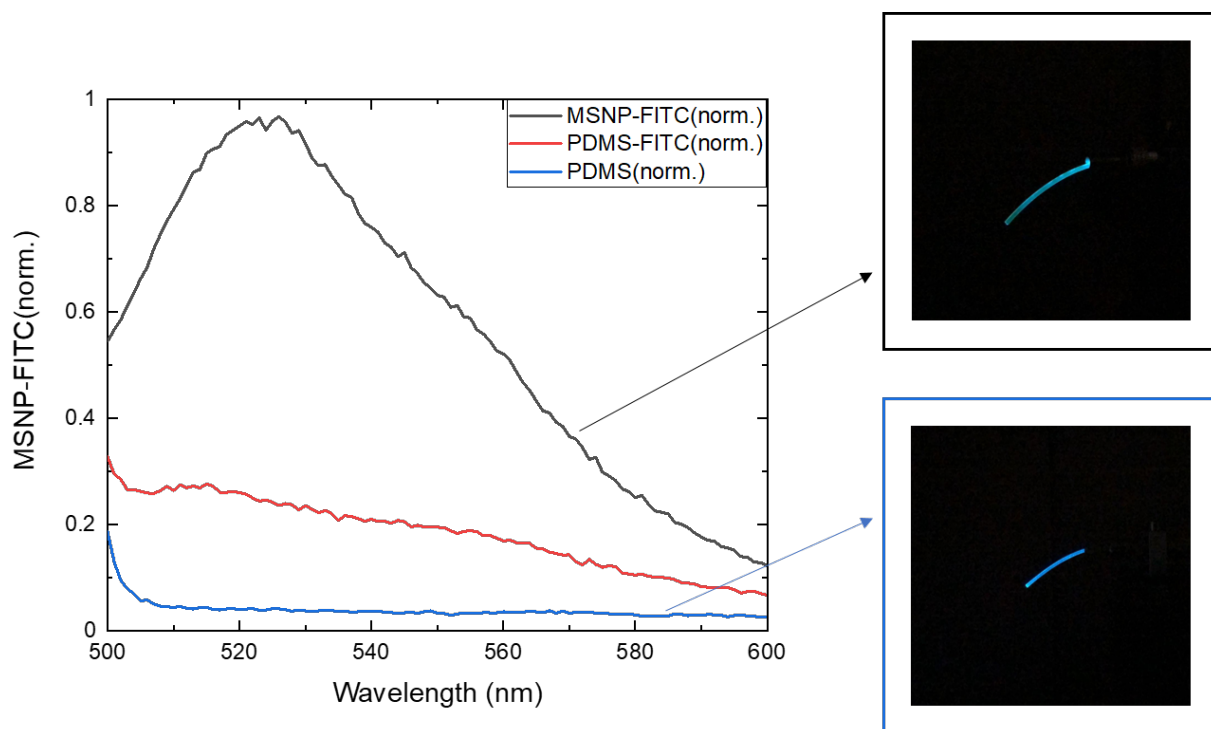


Figure 4-11. Fluorescent emission along PDMS fiber

#### 4.2.3.3 Release study(on-going)

The release studies were carried out from both particles and PDMS-particle optical fibers independently. As a control, the release under dark condition was checked for light-induced release. Then, the particles and fibers were directly irradiated with a light source. In parallel, the PDMS optical fiber was attached to the light source on one end as illustrated in Figure 4-12. All release experiments were conducted in an acetonitrile-water mixture (v/v 90:10).

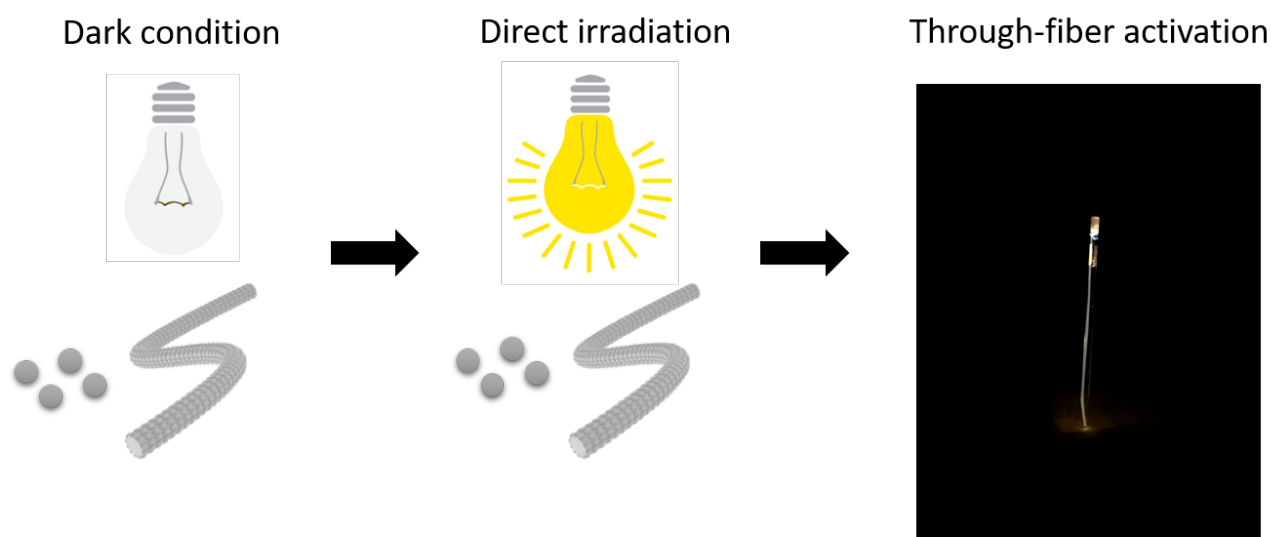


Figure 4-12. Illustration of the steps for release study

Before the release study, commercial chlorambucil was detected by liquid chromatography-mass spectrometry (LC-MS) as a control for that released from substrates. LC-MS in scan acquisition mode was used. A peak appeared at  $t=5.67\text{min}$  in chromatogram and further identified as chlorambucil by MS, showing a molecular ion at  $m/z$  304.2  $[M+H]^+$  after subtraction of the solvent background.



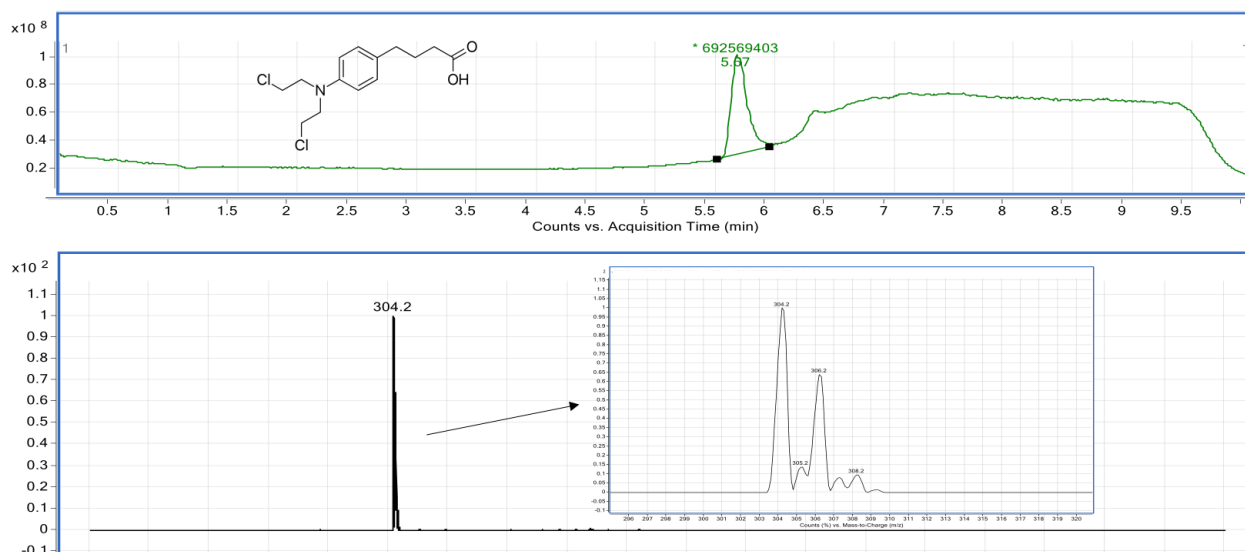


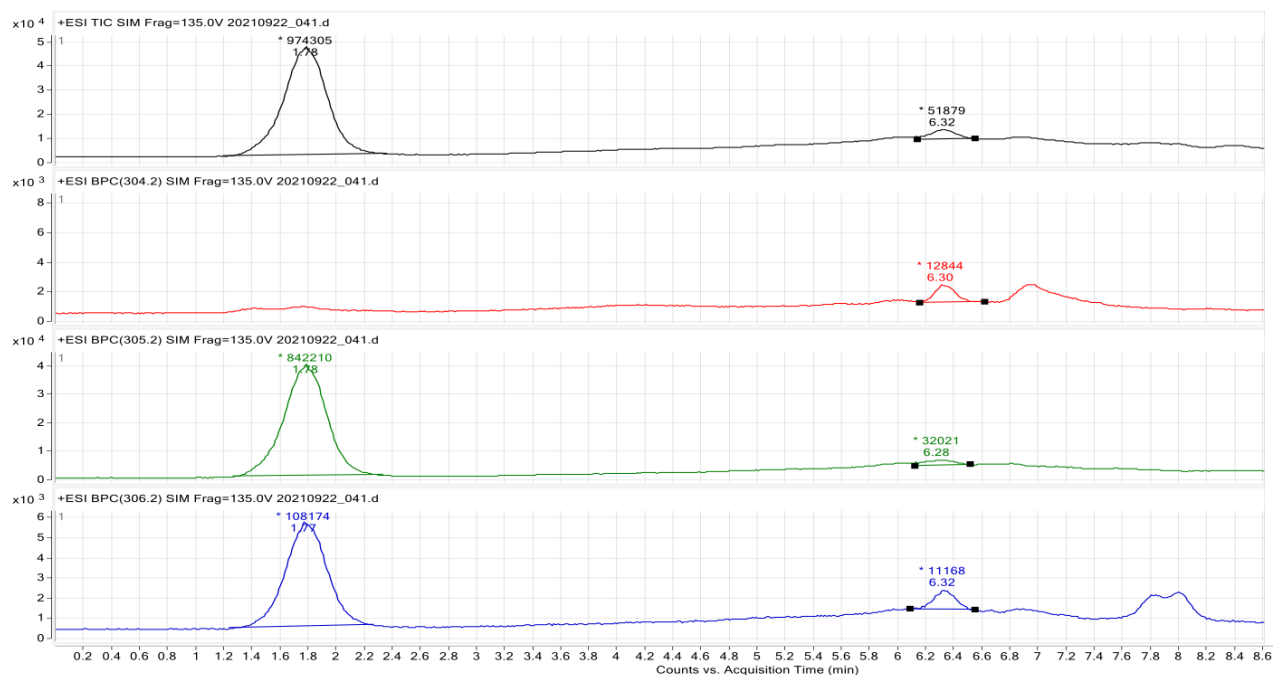
Figure 4-13. LC-MS chromatogram & mass spectra of chlorambucil standard at 26.4 ng/ $\mu$ L

#### 4.2.3.4 Release of chlorambucil from PDMS fiber

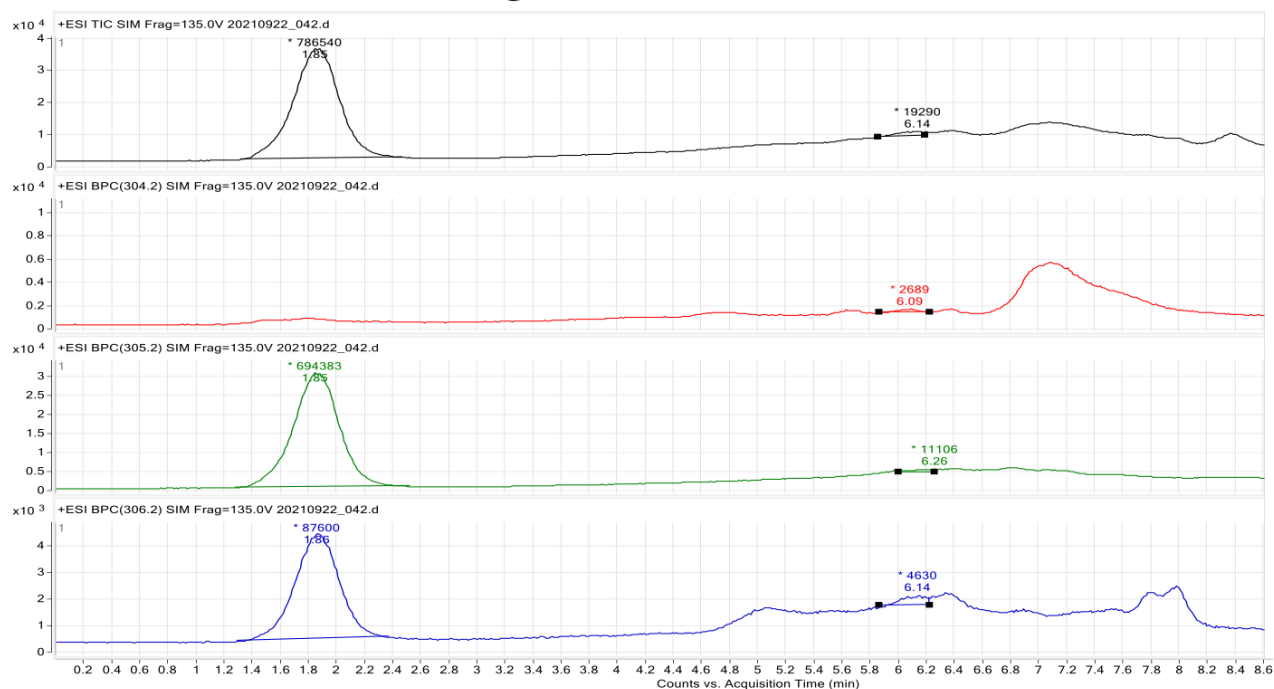
Three release experiments of chlorambucil from optical fiber were conducted in parallel. For each experiment, one 20cm-long prodrug-coated fiber was applied. The activation with light (direct irradiation and through-fiber activation) were let run for 90min and the control was kept in dark for the same time. The after-released liquid medium of the three experiments was dried and dissolved in 100 $\mu$ L methanol and detected by LC-MS (Figure 4-14). In all three experiments no peak of  $m/z$  304.2 appeared at  $t \approx 5.7$ min as suggested by the standard, but a very weak signal appeared at  $t \approx 6.3$ min, indicating no or very slight amount of chlorambucil was released. However, we have observed the peak at  $t \approx 1.4$ min for all three experiments. We have further analyzed spectra and very interestingly, molecular ion at  $m/z$  305.2 was identified as the main peak. The integral ratio of the peak  $m/z$  305.2 and  $m/z$  306.2 is very similar to the peak  $m/z$  304.2 and  $m/z$  305.2 for the standard chlorambucil, likely suggesting the protonation of chlorambucil. The nitrogen site of nitrogen mustards (including chlorambucil) has strong affinities for proton, which may account for the increase of molecular mass by 1. Also, the protonation will lead to the formation of polar ion-complex, which will not be able to stay in a reverse-phase column for long and will be washed out in a shorter time compared to the non-polar molecules, in agreement with the results obtained. Our finding suggested a release of derivative of chlorambucil from the PDMS fiber.

The released amount was compared for three experiments based on the peak  $m/z$  305.2. For dark condition, we supposed that no signal will be obtained, yet we have observed signal of  $m/z$  305.02, which should be identified as the derivative of chlorambucil as we proposed above. It could be because that the fiber was temporarily exposed to light when handled manually. The signal of the mass peak  $m/z$  305.2 in dark condition and through-fiber irradiation were very close, implying nearly no release from the fiber in this irradiation manner. It could be attributed to an insufficient activation time as the low light intensity along the fiber requires longer time to release detectable amount. The direct irradiation has led to a higher mass signal, demonstrating the successful triggering of the bond breakage of the coumarin-chlorambucil prodrugs.

## a Dark condition



## b Through-fiber irradiation



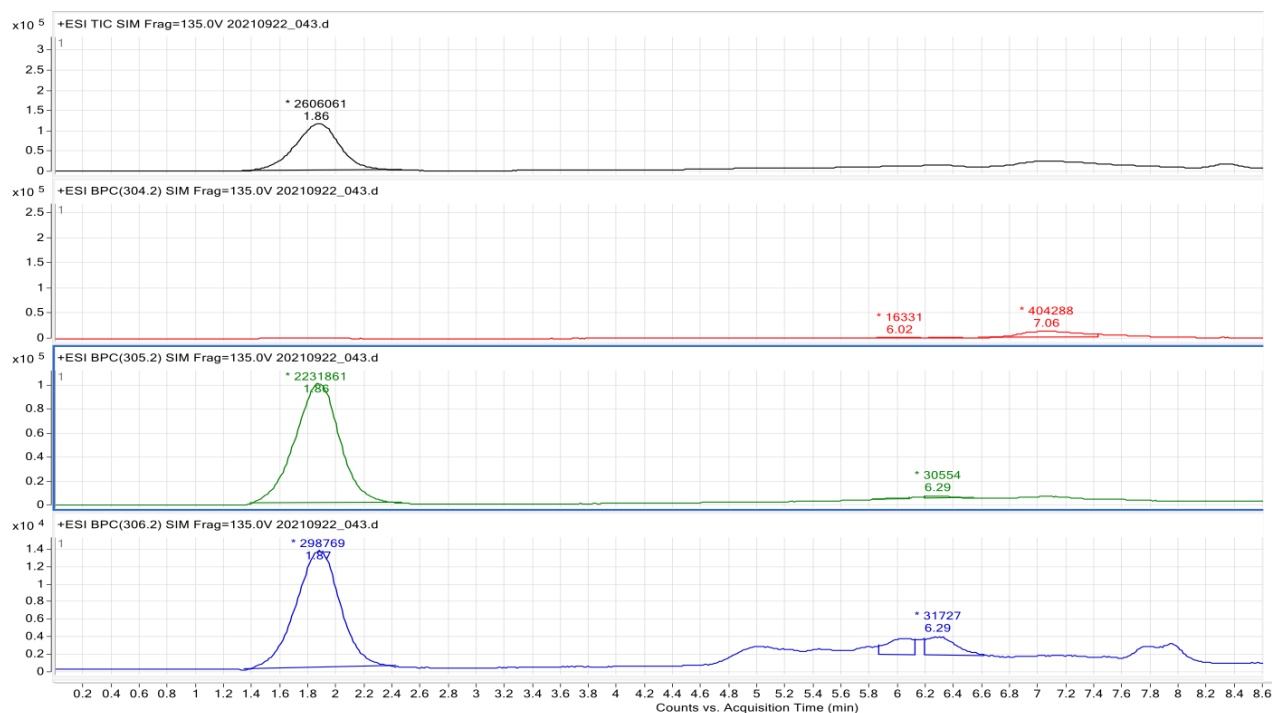
**c** Direct irradiation

Figure 4-14. Mass spectra of released substances in dark condition, under direction irradiation and by through-fiber activation

## 4.3 Conclusion

In this chapter, we investigated the light-responsive release of photolabile coumarin-chlorambucil conjugates from optical fibers. To the best of our knowledge, it is the first study to explore the release of drugs from the side of optical fibers. So far, we have shown that chlorambucil derivatives were released out as a response to light. However, more studies need to be done to have a holistic understanding of the releasing process and some of them are ongoing. Firstly, the release from coumarin-chlorambucil conjugates should be conducted 1) to confirm whether the chlorambucil derivatives will be released instead of chlorambucil; 2) to compare with the released substances from particles and from our final particle-fiber matrix to figure out whether the attachment of the prodrugs will have impacts on the release behaviors. Secondly, the release from particles should also be conducted in comparison to the release from the fiber matrix. The chlorambucil derivative was proposed as a hypothesis and it will be appealing to sketch its chemical structure. Characterization approaches including UV and FT-IR could be applied to provide hints. To have a complete release study, the time dependence of release should be investigated and the amount of release should be calculated according to calibration curve.

# Chapter 5 Experimental

## 5.1 Materials

Concentrated (28%) ammonium hydroxide, tetraethoxysilane (TEOS), ethanol (absolute), tannic acid (TA), gallic acid (GA), ethyl gallate (EG), eudesmic acid (EA), quercetin (QU), concentrated (98%) sulfuric acid and concentrated (30%) hydrogen peroxide were purchased from Sigma-Aldrich and used as received.

All polyelectrolytes, Glutaraldehyde, Sylgard 184 silicone elastomer kit, aminopropyltrimethoxysilane (APTMS), and aminopropyltriethoxysilane (APTES) were purchased from Sigma-Aldrich and used as received. Aminopropyltrimethoxysilane was purchased from abcr GmbH. PMMA sheets were ordered from Merck and cut into 1.5cm x 1cm pieces for coating.

Chlorambucil, m-aminophenol and ethylacetoacetate,  $K_2CO_3$ , Tetrabutylammonium bromide (TBAB), KI, ethyl bromide, bromoacetic acid tert-butyl ester, N, N-Diisopropylethylamine (DIPEA), selenium dioxide, and trimethylamine were ordered from Sigma Aldrich and used as received. SYLGARD®184 was purchased from Dows. All solvents were obtained commercially and used without any further purification.

MilliQ water (resistivity  $\geq 18 M\Omega cm^{-1}$ ) was thoroughly used.

## 5.2 Fabrication of PDMS fiber-based release system

### 5.2.1 Particle synthesis

#### 5.2.1.1 Synthesis of non-porous silica nanoparticles

In a typical synthesis, 8 mL of concentrated ammonium hydroxide were diluted with 33 mL of water; ethanol was then added to a final volume of 320 mL. The solution's temperature was stabilized at 30°C under stirring; afterwards 2 mL of TEOS were added at once. Six hours after the addition of TEOS, the suspension was centrifuged (7800 rpm, 10 min) and the pellet was redispersed in ethanol to remove excess reactants. This cycle was repeated three times. Eventually, the particles were dispersed in ethanol.

#### 5.2.1.2 Synthesis of porous silica nanoparticles

For the synthesis of porous silica nanoparticles, the selected templating agent was dissolved in 150 mL of ethanol and then added to the ammonia-water mixture. The procedure was then carried out as described for the synthesis of non-porous silica nanoparticles. Five different templating agents (TA, GA, EG, EA, QU) were used with different amounts (512 mg, 384mg, 256 mg, 128 mg and 64 mg in total). After synthesis, the particles were collected by centrifugation and were thoroughly washed by several cycles of centrifugation and redispersion in ethanol and water. Removal of organic residues by means of acid piranha treatment was performed for all particles. About 0.1g of particles were dispersed in water three times to exchange all the ethanol and the resulting aqueous suspension was treated with a diluted acid piranha solution (2 M  $H_2SO_4$  and 10%  $H_2O_2$ ) at 60°C for 2 h under stirring. The suspension was then centrifuged (7800 rpm, 10 min) and the procedure repeated. Eventually the particles were washed three times with water to get rid of acid residues and were redispersed in water.

### 5.2.2 Processing of PDMS fibers and PMMA substrates

Polydimethylsiloxane (PDMS) substrates were prepared as follows. The base (Sylgard 184 Silicone Elastomer) and curing agent were mixed at a weight ratio of 10 to 1 and degassed for 5 min by centrifugation at 5000rpm. The mixture was then pulled into a glass well plate and cured at 120°C for 2h. The obtained PDMS films were cut into 1.5cm x 1cm for particle coating of MSNPs after being cleaned with isopropanol. PMMA substrates were obtained commercially and cleaned with hexane and water before use.

## 5.2.3 Layer-by-Layer coating of nanoparticles to PDMS fibers and PMMA substrates

### 5.2.3.1 Coating of MSNPs to PMMA substrates

Option 1 (refer to 3.2.1): Silica nanoparticles were deposited onto substrates by the layer-by-layer process. PDMS and PMMA substrates were treated with air plasma with Harrick Plasma basic plasma cleaner for 2min to generate a negatively charged surface. Then, they were immediately immersed into 8mg/mL aqueous PDDA solution and 8mg/mL MSNP dispersion for 5 minutes sequentially with a 1min rinsing with Milli-Q water after each dipping. The substrates were dried carefully with an airgun and used for silanization. The resulting substrate were treated similarly. For PMMA, silanization was allowed to happen in hexane instead of DMF. Both substrates were incubated in 5mL APTMS solution (10% v/v) for 24 hours in incubator shaker (KS 4000 I control, IKA) with 80rpm shaking speed. The modified substrates were washed to remove the unbound silanes. PDMS substrates were rinsed with ethanol and PMMA substrates were rinsed with hexane. Then the modified substrates were stabilized at 90°C for 1 hour.

Option 2 (refer to 3.2.1): PMMA substrates were treated with air plasma for 2min and sequentially immersed into 2mg/mL aqueous PEI solution, 2mg/mL aqueous PSS solution, 2mg/mL aqueous PDDA solution and, 2mg/mL APTMS-MSNP dispersion for 5 minutes with a 1min rinsing with Milli-Q water after each dipping.

Option 3 (refer to 3.2.1): PMMA substrates were modified by APTMS to get amino group terminated surface. They were first plasma-activated for 2min and then incubated with 10% v/v APTMS prepared in hexane at 30°C for 24h in incubator shaker with 80rpm shaking speed. The modified substrates washed with hexane and stabilized at 90°C for 1 hour. Then the silanized substrates were immersed into 2% v/v glutaraldehyde solution in pH=6 PBS solution (1x) for 30min at room temperature. Then the surface was washed by Milli-Q water to remove the unbound glutaraldehyde. The resulting substrates were immersed into 2mg/mL APTMS-particle dispersion for 24h at room temperature in incubator shaker with 80rpm shaking speed. After that, the substrates were cleaned with Milli-Q water.

### 5.2.3.2 Coating of MSNPs to PDMS fibers

MSNPs were deposited onto PDMS fibers by layer-by-layer process. PDMS fibers were treated with air plasma with Harrick Plasma basic plasma cleaner for 2min to generate a negatively charged surface. The fibers were immediately immersed into aqueous 8mg/mL PDDA solution and 8mg/mL MSNP dispersion for 5 minutes sequentially with a 1min rinsing with Milli-Q water after each dipping.

## 5.2.4 Silanization of particles

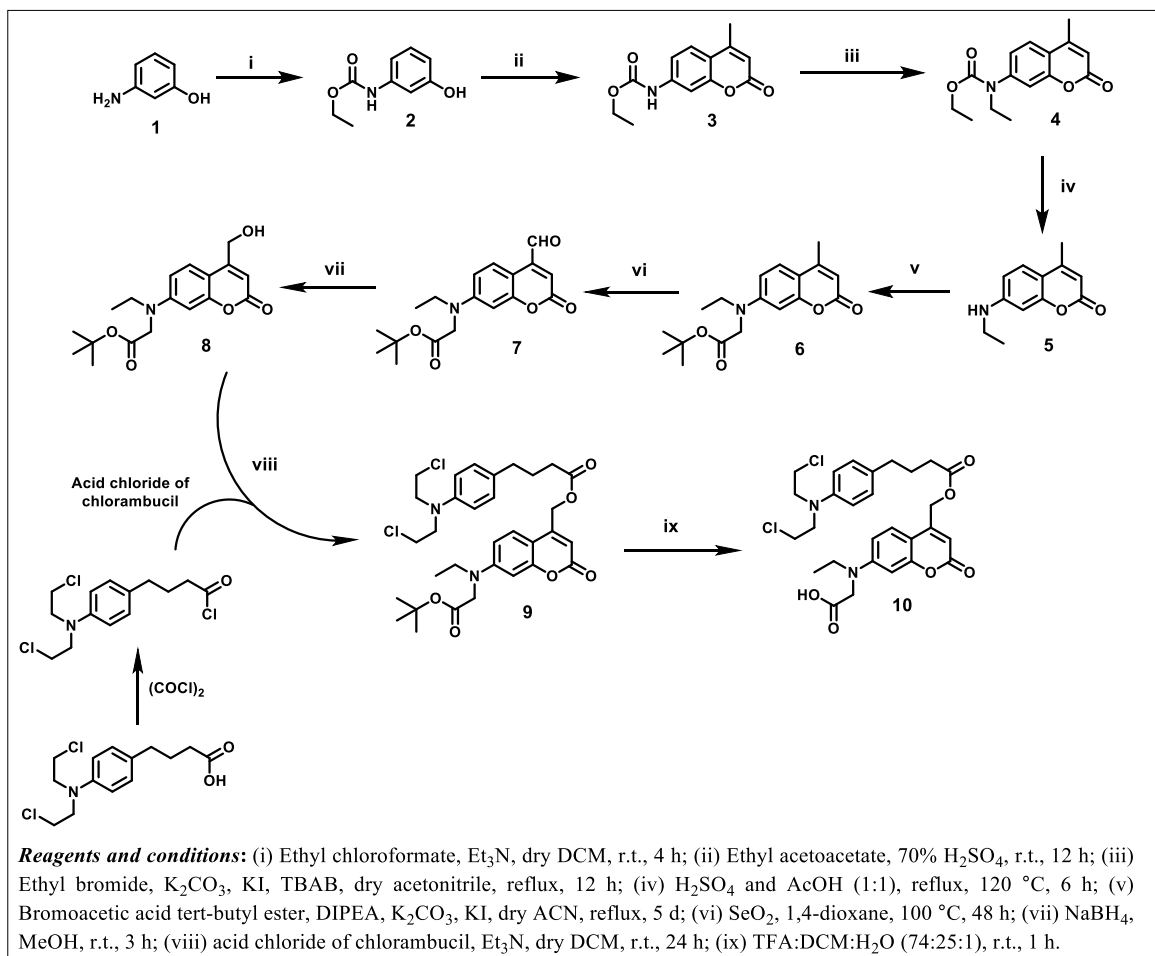
20mg of MSNPs were placed in a reaction flask flushed with nitrogen. 10mL of anhydrous DMF was added to the flask followed by the injection of 50μL of Silanes. The reactions were kept for 24 hours. Then, the particles were centrifuged and the pellet was re-dispersed in ethanol to remove excess silanes for 3 times followed by stabilization at 90°C for 1 hour.

## 5.2.5 DoE and particle recognition

A L9 orthogonal array table was applied to study the influence of PDDA concentration, particle concentration and dipping time on the quality of the particle coating. The layer-by-layer process were conducted as described in section 5.2.3.1 with corresponding levels and checked with SEM. The obtained SEM images were then treated in a batch with Matlab code for assessment of the coating density and homogeneity.

## 5.2.6 Synthesis of coumarin-chlorambucil conjugate

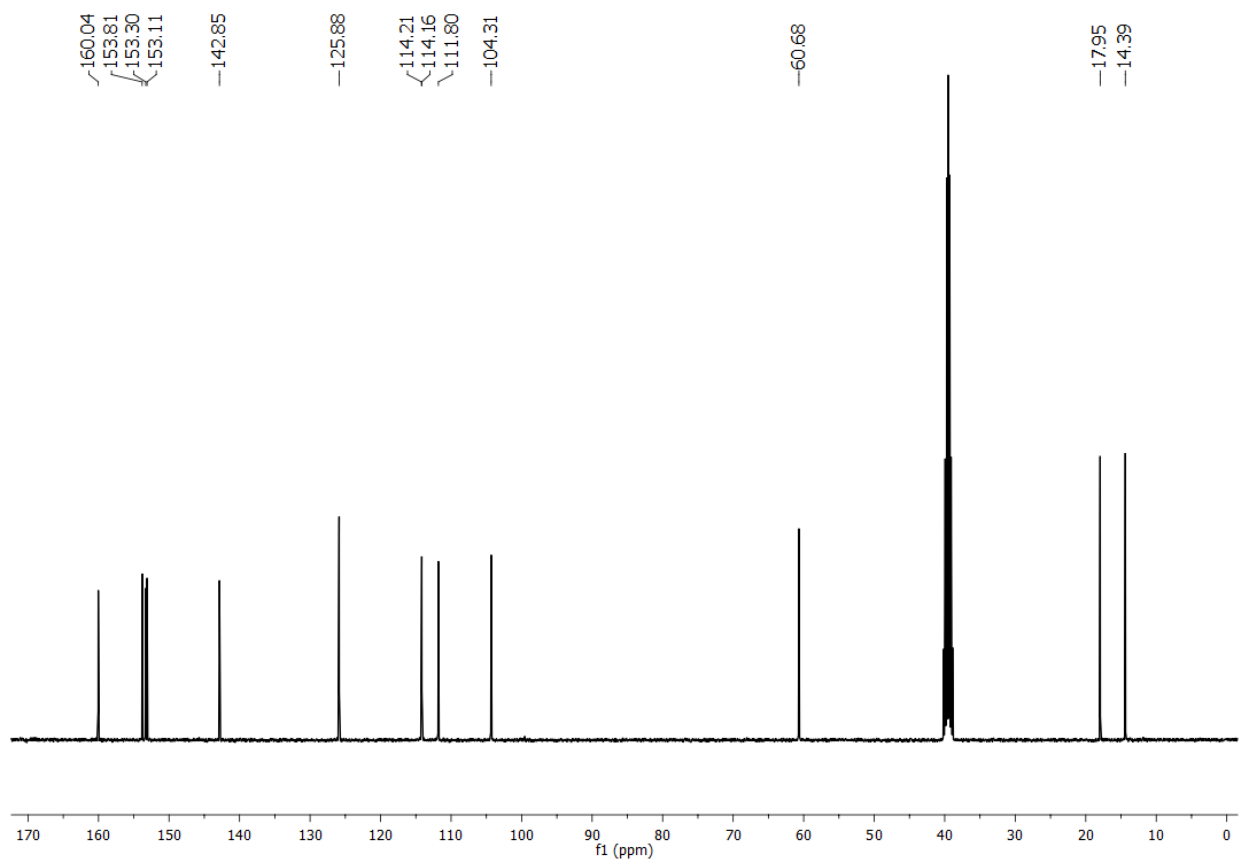
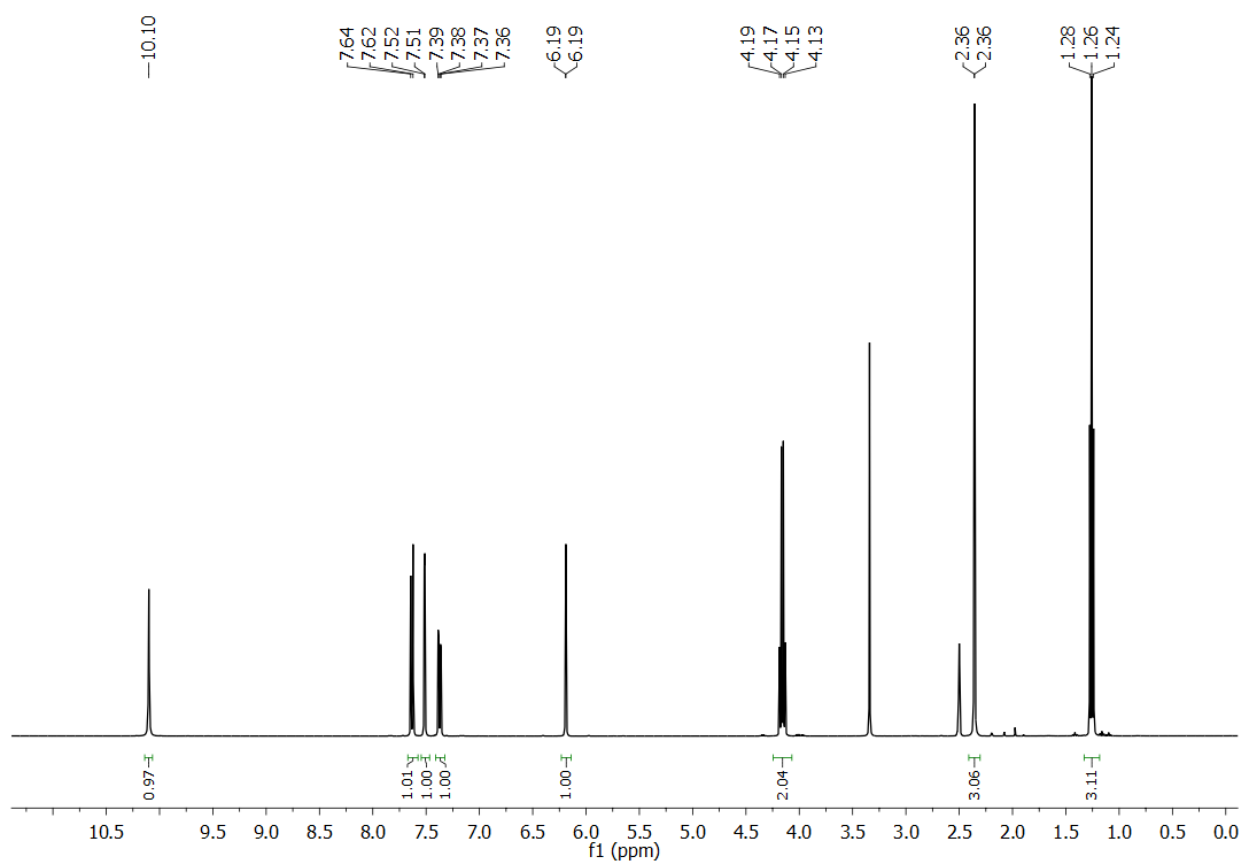
*\*The synthesis part was done by Dr. Sandipan Biswas*



Scheme 5-1. Synthesis of Coumarin-Chlorambucil conjugate (10).

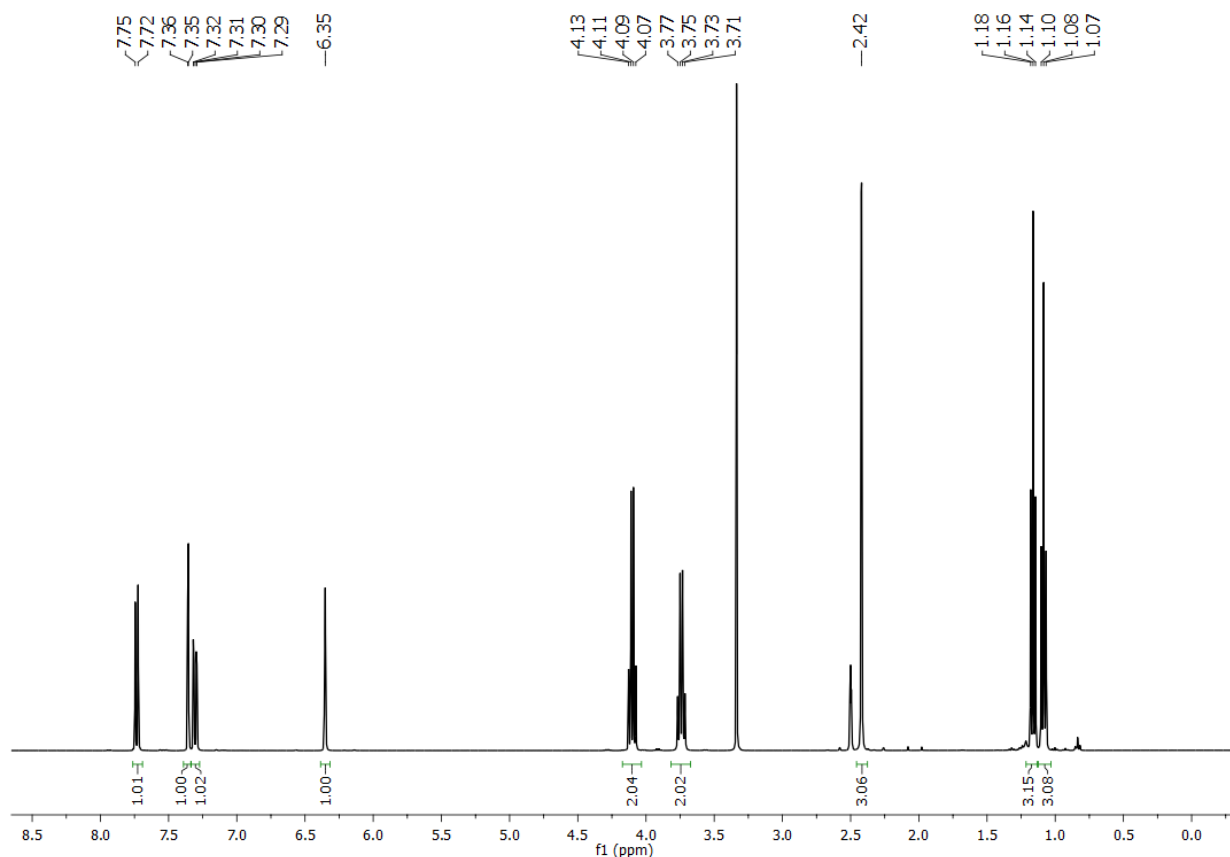
**Step 1: Synthesis of 7-carbethoxyamino-4-methylcoumarin (3):** 7-carbethoxyamino-4-methylcoumarin (**3**) was initially synthesized from *m*-aminophenol and ethylacetoacetate following a known procedure (classical Pechmann condensation) from literature, as shown in Scheme 5-1. <sup>1</sup>H NMR (400 MHz, DMSO) δ 10.10 (s, 1H), 7.63 (d, *J* = 8.7 Hz, 1H), 7.51 (d, *J* = 2.0 Hz, 1H), 7.37 (dd, *J* = 8.7, 2.1 Hz, 1H), 6.19 (d, *J* = 1.2 Hz, 1H), 4.16 (q, *J* = 7.1 Hz, 2H), 2.36 (d, *J* = 1.1 Hz, 3H), 1.26 (t, *J* = 7.1 Hz, 3H). <sup>13</sup>C NMR (101 MHz, DMSO) δ 160.04, 153.81, 153.30, 153.11, 142.85, 125.88, 114.21, 114.16, 111.80, 104.31, 60.68, 17.95, 14.39.

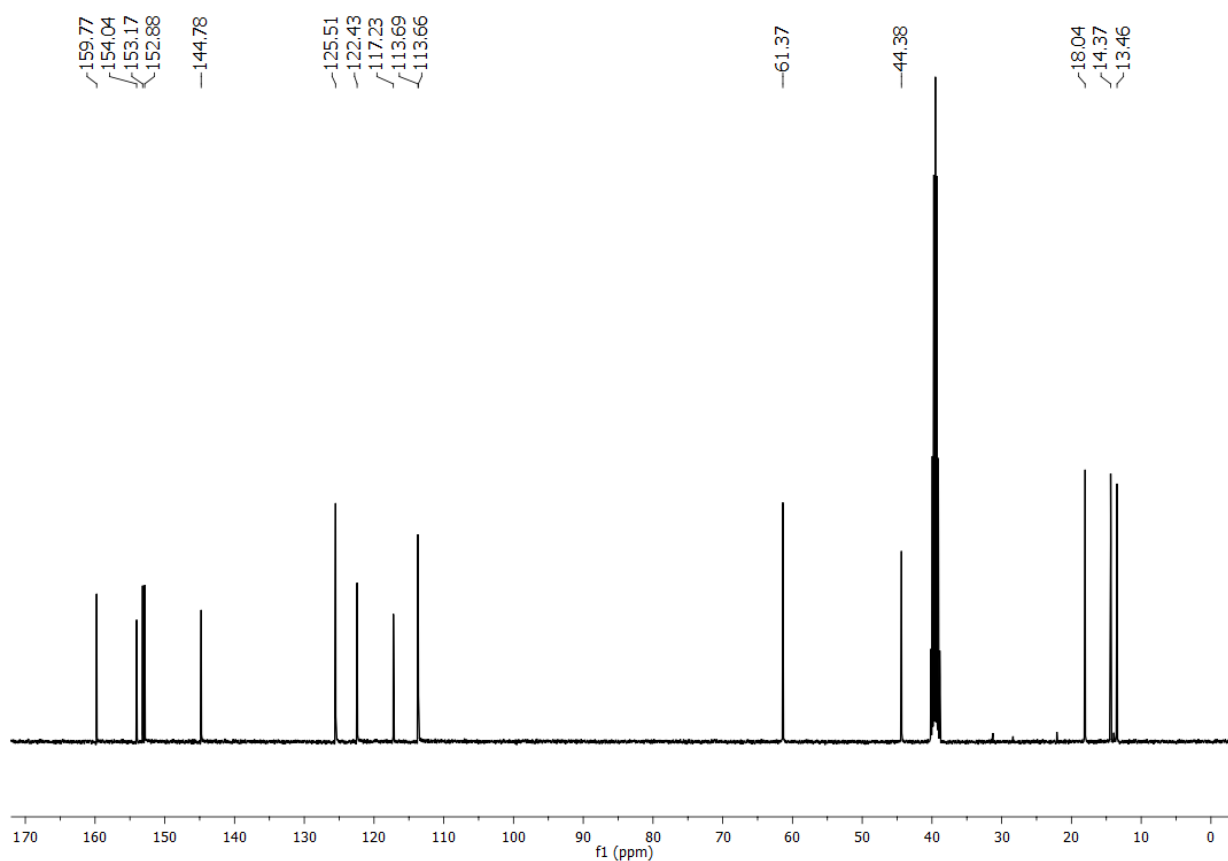
# Experimental





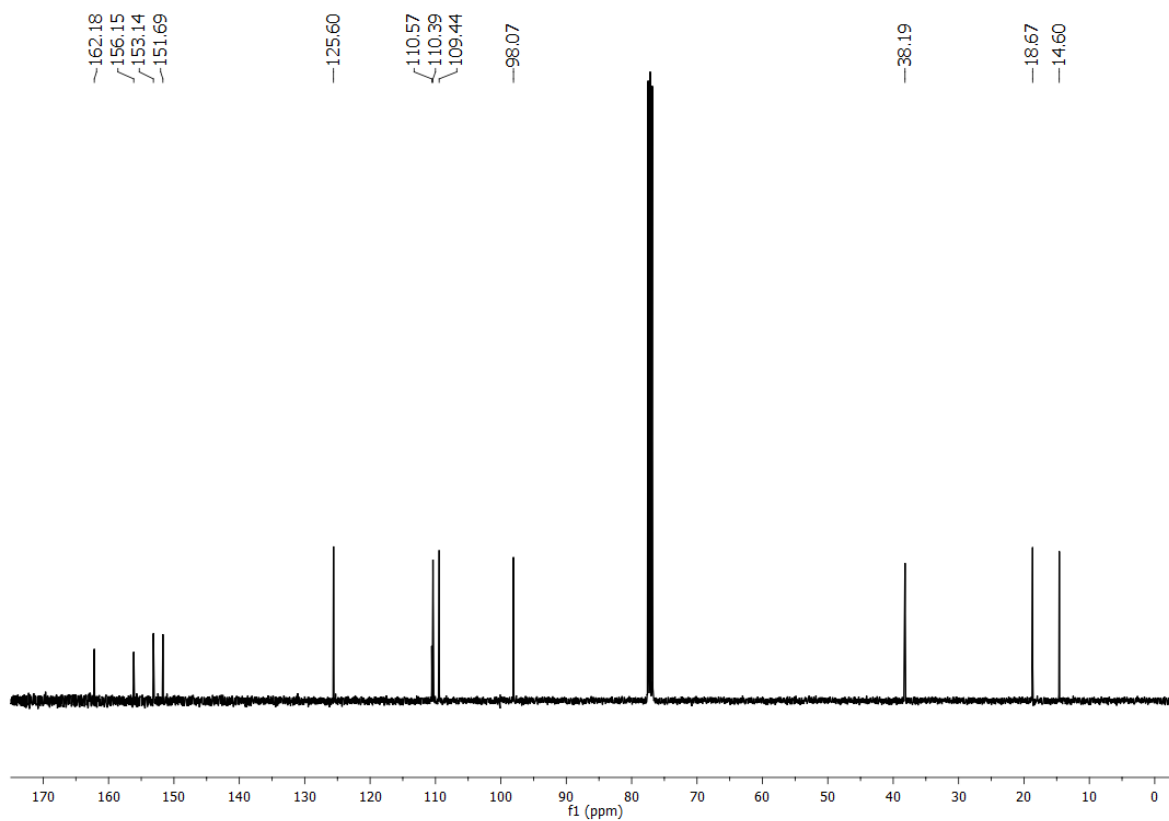
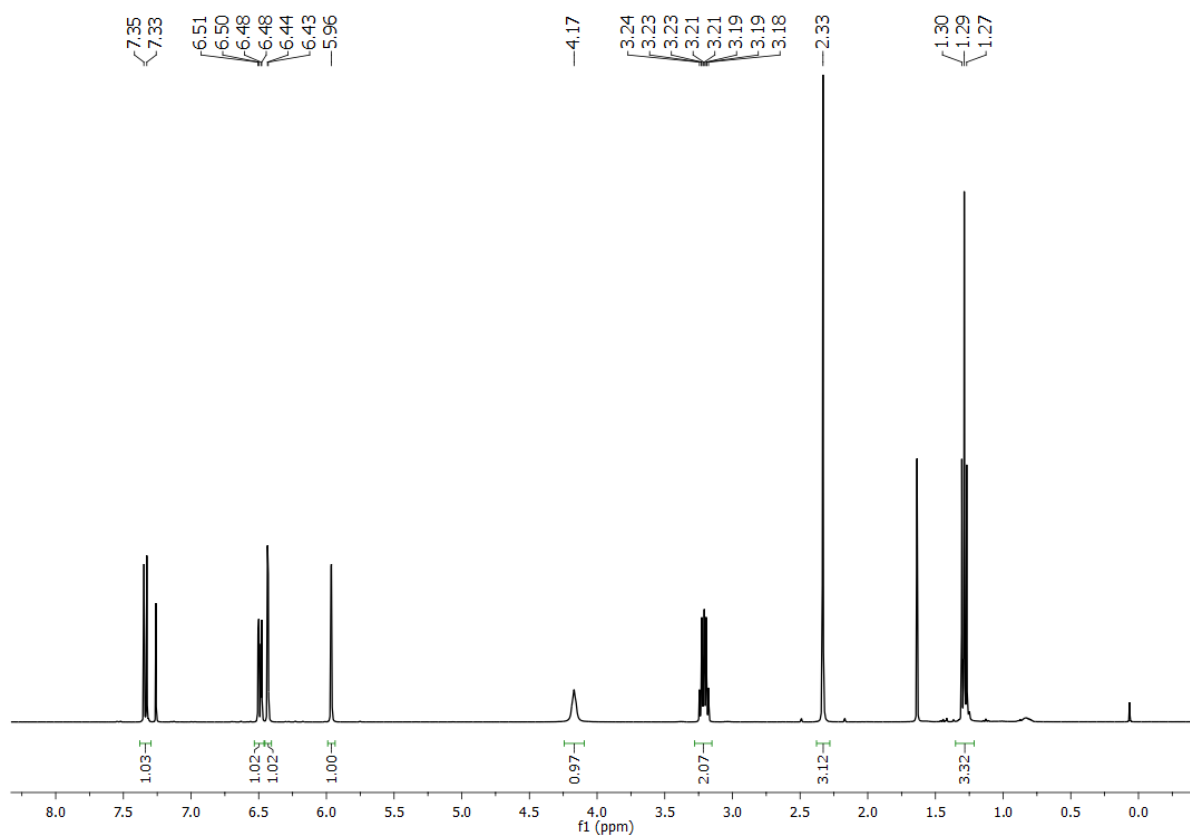
**Step 2: Synthesis of 7-[N-ethyl,N-carbethoxy]-4-methylcoumarin (4):** To a solution of 7-carbethoxyamino-4-methylcoumarin (**3**) (500 mg, 2.022 mmol) in dry acetonitrile, 1.5 eqv of  $K_2CO_3$  (420 mg, 3.03 mmol), 0.5 eqv of TBAB (325.91 mg, 1.01 mmol) was added. The mixture was stirred for 30 min at 80 °C. After 30 min 0.5 eqv of KI (170 mg, 1.02 mmol) and 20 eqv. of ethyl bromide (2.997 ml, 40.44 mmol) were added to the reaction mixture and refluxed for 12 h. After the reaction was completed, the reaction mixture was cooled to room temperature and filtered. The filtrate was then concentrated under reduced pressure and the residue was washed with ethyl acetate and brine water. The organic layer was collected, dried over  $Na_2SO_4$  and evaporated to concentrate the product. The product was purified via flash chromatography ( $SiO_2$ , 15-45% EtOAc in hexane) to afford **4** as white solid in 85 % yield.  $^1H$  NMR (400 MHz, DMSO)  $\delta$  7.73 (d,  $J$  = 8.5 Hz, 1H), 7.36 (d,  $J$  = 2.1 Hz, 1H), 7.31 (dd,  $J$  = 8.5, 2.1 Hz, 1H), 6.35 (s, 1H), 4.10 (q,  $J$  = 7.1 Hz, 2H), 3.74 (q,  $J$  = 7.1 Hz, 2H), 2.42 (s, 3H), 1.16 (t,  $J$  = 7.1 Hz, 3H), 1.08 (t,  $J$  = 7.1 Hz, 3H).  $^{13}C$  NMR (101 MHz, DMSO)  $\delta$  159.77, 154.04, 153.17, 152.88, 144.78, 125.51, 122.43, 117.23, 113.69, 113.66, 61.37, 44.38, 18.04, 14.37, 13.46.





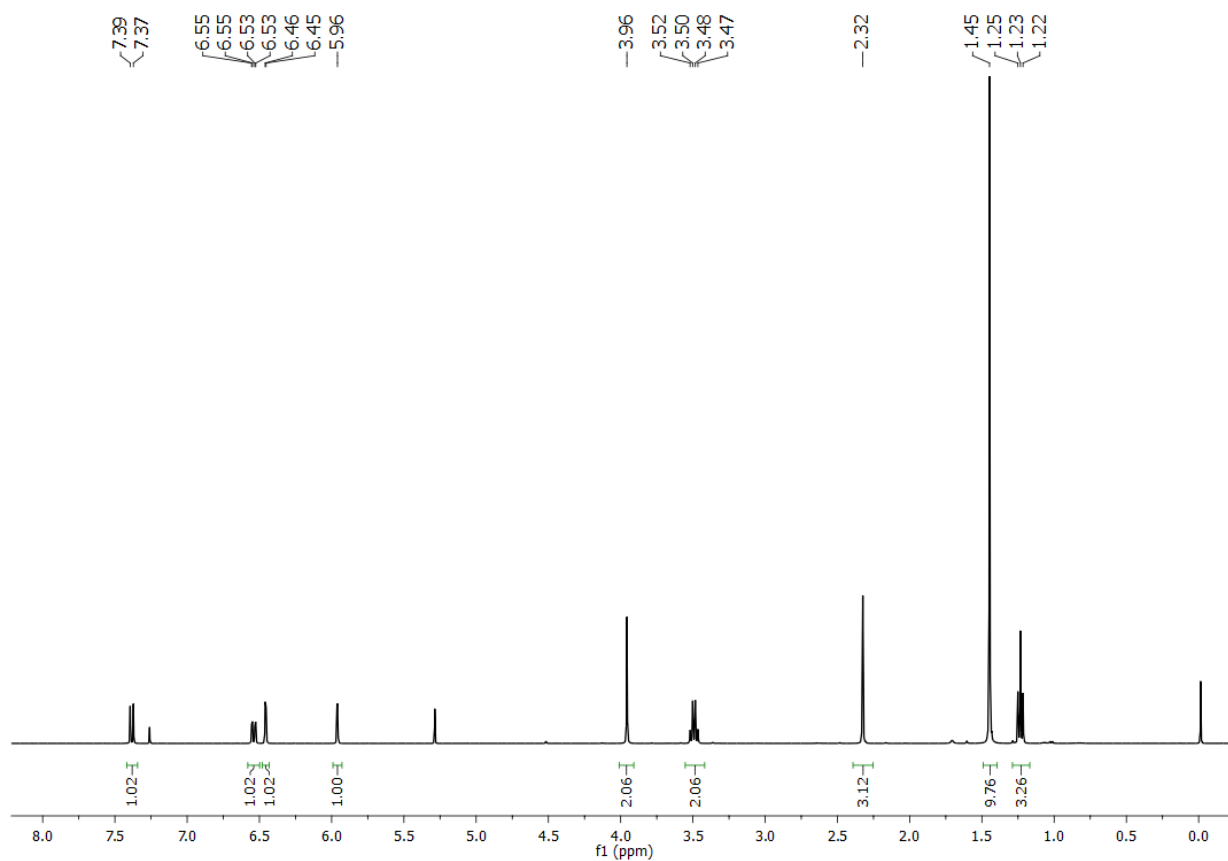
**Step 3: Synthesis of 7-ethylamino-4-methylcoumarin (5):** Compound **4** (490 mg, 1.779 mmol) was suspended in 1:1 mixture of conc. H<sub>2</sub>SO<sub>4</sub> and glacial acetic acid (3 ml + 3ml). The mixture was refluxed at 120 °C for 6 h to give an orange solution. After completion of the reaction the reaction mixture was cooled to room temperature and poured into ice cold water and kept overnight for complete precipitation of an off-white solid. The suspension was brought to pH ~7 with 20% NaOH solution. The precipitate was then filtered under suction and dried to obtain the desired product **5** as a greenish powder in ~ 95% yield. <sup>1</sup>H NMR (400 MHz, CDCl<sub>3</sub>) δ 7.34 (d, *J* = 8.7 Hz, 1H), 6.49 (dd, *J* = 8.7, 2.3 Hz, 1H), 6.43 (d, *J* = 2.3 Hz, 1H), 5.96 (s, 1H), 4.17 (s, 1H), 3.21 (qd, *J* = 7.2, 5.4 Hz, 2H), 2.33 (s, 3H), 1.29 (t, *J* = 7.2 Hz, 3H). <sup>13</sup>C NMR (101 MHz, CDCl<sub>3</sub>) δ 162.18, 156.15, 153.14, 151.69, 125.60, 110.57, 110.39, 109.44, 98.07, 38.19, 18.67, 14.60.

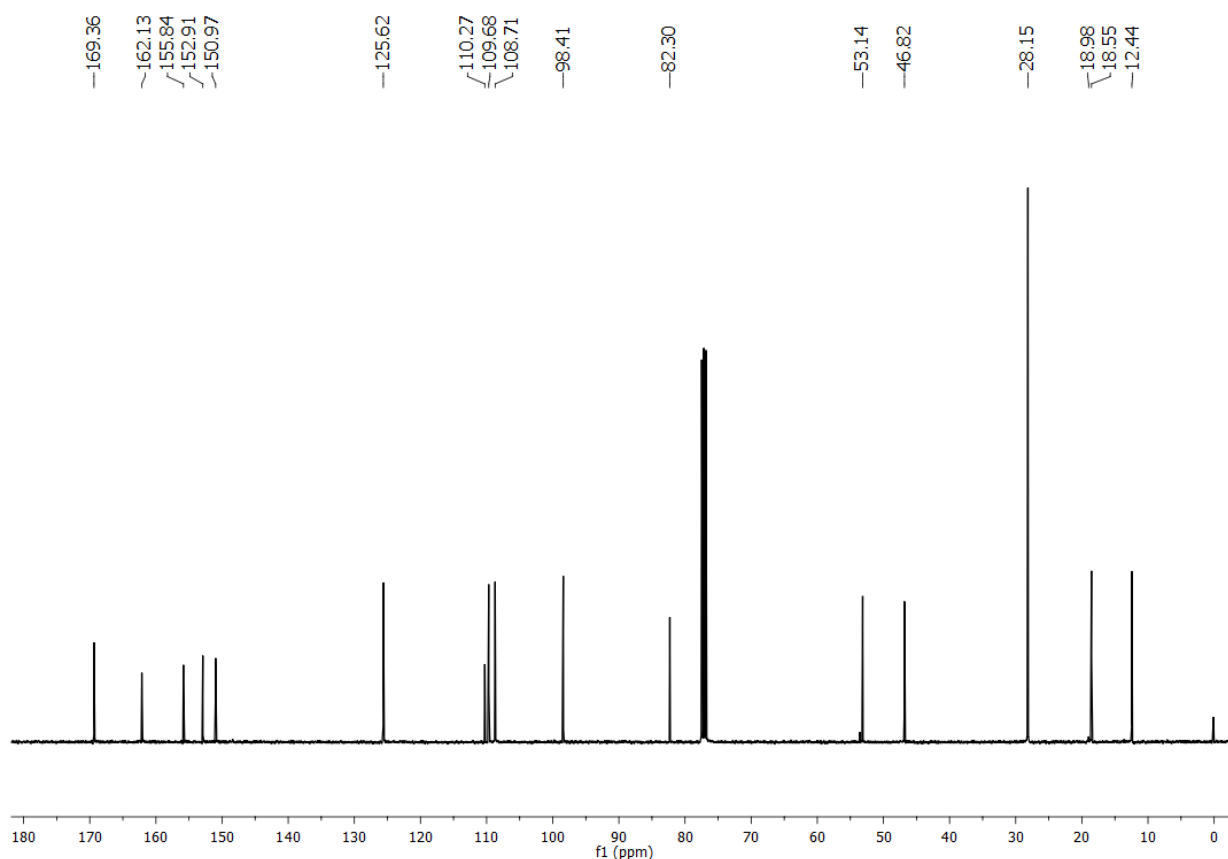
# Experimental



**Step 4: Synthesis of 7-[N-ethyl,N-tert-Butoxycarbonylmethyl]-4-methylcoumarin (6):** Compound 5 (350 mg, 1.72 mmol), bromoacetic acid tert-butyl ester (1.78 ml, 12.04 mmol), DIPEA (1.2 ml, 6.88 mmol), and KI (285.5 mg, 1.72 mmol) in 20 mL CH<sub>3</sub>CN were

refluxed for 5 days. The mixture was cooled to room temperature, filtered, and the solvent evaporated in vacuo. The residue was dissolved in 250 mL EtOAc, washed with 350 mL brine, dried over Na<sub>2</sub>SO<sub>4</sub>, and concentrated in vacuo to afford a brown oil. The oil purified via flash chromatography (SiO<sub>2</sub>, 15-45% EtOAc in hexane) to afford 6 in 76% yield. <sup>1</sup>H NMR (400 MHz, CDCl<sub>3</sub>) δ 7.38 (d, J = 8.9 Hz, 1H), 6.54 (dd, J = 8.9, 2.6 Hz, 1H), 6.46 (d, J = 2.6 Hz, 1H), 5.96 (s, 1H), 3.96 (s, 2H), 3.49 (q, J = 7.2 Hz, 2H), 2.32 (s, 3H), 1.45 (s, 9H), 1.23 (t, J = 7.2 Hz, 3H). <sup>13</sup>C NMR (101 MHz, CDCl<sub>3</sub>) δ 169.36, 162.13, 155.84, 152.91, 150.97, 125.62, 110.27, 109.68, 108.71, 98.41, 82.30, 53.14, 46.82, 28.15, 18.98, 18.55, 12.44.





**Step 5: Synthesis of 7-[N-ethyl,N-*tert*-Butoxycarbonylmethyl]-4-formylcoumarin (7):** Compound **6** (400 mg, 1.26 mmol) was dissolved in 20 mL dioxane by heating at 80 °C, then 2 eqv. of selenium dioxide (280 mg, 2.52 mmol) was added to the reaction mixture. The mixture was refluxed for 48 h with stirring under Ar atmosphere. The reaction mixture was filtered hot through celite bed to remove black selenium, and the filtrate was concentrated under reduced pressure. The resulting orange-red precipitate was used for the next steps without further purification.

**Step 6: Synthesis of 7-[N-ethyl,N-*tert*-Butoxycarbonylmethyl]-4-(hydroxymethyl)-coumarin (8):** NaBH<sub>4</sub> (210 mg, 5.55 mmol) was added to compound **7** in 50 mL moist methanol, and the mixture was stirred at room temperature for 3 h. The reaction mixture was diluted with H<sub>2</sub>O (20 mL), acidified (pH 5) with 0.1 N HCl and extracted three times with CH<sub>2</sub>Cl<sub>2</sub> (30 mL each). The organic phase was washed with H<sub>2</sub>O and brine, dried over Na<sub>2</sub>SO<sub>4</sub>, and concentrated in vacuo. The crude product was purified by flash chromatography (50-70 % EtOAc in hexane) to afford **8** in 72% yield.

**Step 7: Synthesis of 7-[N-ethyl, N-*tert*-Butoxycarbonylmethyl]-4-(hydroxymethyl)-coumarin-chlorambucil caged ester (9):** Chlorambucil (91.250 mg, 0.299 mmol) was dissolved in 1 mL oxalyl chloride and was stirred for 1 h at 60 °C under N<sub>2</sub> atmosphere. Then the oxalyl chloride was removed under vacuum to afford the acid chloride of chlorambucil as brown oil. Then the acid chloride was dissolved in dry DCM (5 mL) and the esterification reaction was carried out without further purification. The solution of the acid chloride in CH<sub>2</sub>Cl<sub>2</sub> was added to the solution of **8** (100 mg, .0299 mmol) trimethylamine (1.5 eqv. 0.062 ml, 0.449 mmol) and in dry DCM (10 ml). The mixture was stirred at room temperature for 48 h, and then the solvent was removed under reduced pressure. The crude reaction mixture was purified by column chromatography using 60 % EtOAc in pet ether to give the compound **9** in 68 % yield.

**Step 8: Synthesis of 7-[N-ethyl, N-carboxymethyl]-4-(hydroxymethyl)-coumarin-chlorambucil caged ester (10):** Compound **9** (40 mg, 0.064 mmol) was stirred in a mixture (2 mL) of TFA/CH<sub>2</sub>Cl<sub>2</sub>/ H<sub>2</sub>O (74:25:1) at room temperature for 1h. The solvents were evaporated, and the residue was co-evaporated three times with ether to give 0.090 (90%) of the pure active ester **10**.

#### 5.2.6.1 Attachment of coumarin prodrugs to MSNPs

The crosslinked MSNP-coated PDMS fibers were modified with silanes to introduce amine groups onto MSNPs as anchors for the following attachment of coumarin-chlorambucil prodrugs. 20cm fibers were placed in a reaction flask flushed with nitrogen. 10mL

of anhydrous DMF was added to the flask followed by the injection of 50  $\mu$ L of APTMS. The reactions were kept for 24 hours. Then, the fibers were taken out and rinsed with ethanol and water. After that, the fibers were stabilized at 90°C for 1 hour.

The loading of the coumarin-based prodrugs on AP-MSNPs was achieved by amide coupling reaction according to the reported literature[252]. For isolated MSNPs, 10mg AP-MSNPs was dispersed in 2mL anhydrous DMF. N-hydroxysuccinimide (NHS)(0.021 mmol) and 1-ethyl-3-(3-dimethylaminopropyl) carbodiimide hydrochloride (EDC)( 0.021 mmol) was dissolved in 3mL anhydrous DMF and added to coumarin-chlorambucil conjugate ( 0.018 mmol). The mixture was stirred for 15min under room temperature before being added to the particle suspension. The reaction was run in dark condition for 24h followed by centrifugation at 13400r/min for 3min. The resulting particles were washed DMF and acetone respectively and dried with air. The reaction procedure was kept the same for particle-coated fibers with a reduced usage of reagent (NHS, EDC and Coumarin-chlorambucil conjugates in 2.5mL anhydrous DMF)

### 5.2.6.2 Photolysis of the coumarin-chlorambucil

#### 1. Photolytic drug release from particles

The photolytic release of chlorambucil from CDD-MSNPs was conducted by irradiating the particle dispersion (5mg/mL in the acetonitrile-water mixture (v/v, 90:10) with Volpi intraLED 3 (>400nm) at a distance of 2 cm from the light source. A small aliquot (100  $\mu$ L) of the suspension was taken and centrifuged (13400rpm/min) for 3min each 20min. The obtained supernatant was analyzed by reversed-phase LC-MS using a BEH C18 1.7mm column at 40°C. After injection of 10  $\mu$ L, the separation was conducted by applying a gradient wash with methanol (0.1% acetic acid, solvent A) and Milli-Q water (0.1% acetic acid, solvent B) at a flow rate of 0.3mL/min. The chromatogram was recorded by using the integral of absorbance peak of chlorambucil.

#### 2. Photolytic drug release from particle-embedded fibers

The release from fiber was conducted by direct irradiation and through-fiber irradiation. For through-fiber irradiation, the release of chlorambucil was conducted in an NMR tube to allow complete immersion of the PDMS fiber in a small volume of releasing medium(2.5mL). One end of the PDMS fiber was connected to the light source (HAMAMATSU L10290, Figure 5-1) and the rest part was immersed in the acetonitrile-water mixture (9:1, v/v). The analysis of chlorambucil was conducted following the same procedure for particles above.



Figure 5-1. HAMAMATSU L10290 light source

For release by direct irradiation, a 20cm-long fiber was cut into pieces of 2cm, immersed in the same releasing medium(1mL) and exposed to Volpi intraLED 3 (>400nm) at a distance of 2 cm from the light source. The analysis of chlorambucil was conducted following the same procedure.

#### 3. Control experiment

For photolytic release from both particles and fibers, control experiments were performed under dark to evaluate the release from physically attached coumarin-chlorambucil conjugates.

### 5.3 Characterization

Scanning electron microscopy (SEM) was performed using a JEOL Hitachi S-4800. For imaging particles, a small drop of dilute ethanolic particle suspension was allowed to evaporate on a piranha-cleaned silicon substrate mounted on conductive tape and was then sputter-coated with 5 nm of Au-Pd alloy. Besides the characterization of silica particles, SEM was also used to observe the TA and GA aggregates (TA512 and GA512). A small drop was taken from the reaction solution before TEOS addition, diluted to 1/16 of the original concentration, and directly deposited on a clean aluminum support for imaging. For imaging particle-coated PDMS and PMMA surface, the substrates were mounted on conductive tape and were then sputter-coated with 5 nm of Au-Pd alloy for SEM observation.

Transmission electron microscopy (TEM) was performed using a JEOL JEM 2200fs. The samples were mounted on carbon-coated grids by evaporating a dilute particle suspension in ethanol.

Dynamic light scattering (DLS) was performed to measure the hydrodynamic size as well as the polydispersity index (Pdl) of the resulting particles using a Malvern Zetasizer Nano. All solutions were prepared in MilliQ water.

Zeta-potential measurement was also carried out using a Malvern Zetasizer Nano. Particles were dispersed in Milli-Q water with 0.1% PBS.

Thermogravimetric analysis (TGA) was performed with as-prepared particles. The particles were directly centrifuged out and dried at 50°C overnight without washing step. About 10 mg of the resulting samples were then filled into an Al<sub>2</sub>O<sub>3</sub> pan and heated from 25°C to 900°C with an increasing rate of 20°C min<sup>-1</sup> under oxidant conditions (50 mL min<sup>-1</sup> of synthetic air made of 80% nitrogen and 20% oxygen).

Nitrogen sorption measurements were used to determine the surface area and pore volume of the silica particles. The particles were dried first at 50°C overnight and then at 80°C for 1200 minutes before the introduction of N<sub>2</sub> gas. The nitrogen adsorption/desorption cycles were measured at 77 K using a Micromeritics Triflex. Brunauer–Emmet–Teller (BET) method was used to calculate the specific surface area. The pore volume was obtained from analysis of the adsorption branch using the Barrett–Joyner–Halenda (BJH) method.

Atomic force microscopy (AFM) analysis was carried out using a scanning probe microscope Nanosurf FlexAFM V5 equipped with a C3000 controller. The ethanolic dispersion of non-templated silica nanoparticles and GA-templated MSNPs was deposited on clean glass wafer and dried in ambient condition. The dry sample was scanned in tapping mode with a silicon probe (Tap SHR300, a high-resolution cantilever with a sharp diamond-like carbon tip having a precise radius of 1 nm, Budget Sensor) with a resonance frequency of 300 kHz and a force constant of 40 N/m. The image analysis was processed with Gwyddion software (version 2.51).

Small-angle X-ray scattering (SAXS) studies were further performed in order to evaluate the particles pore sizes and their surface roughness. A Nanostar SAXS instrument (Bruker GmbH, Karlsruhe, Germany), with a microfocused X-ray source (Incoatec GmbH, Geesthacht, Germany), generating Cu K $\alpha$  radiation with a wavelength of 0.154 nm, has been used. The system is equipped with MONTEL optics (two Göbel mirrors arranged perpendicular to each other) and two pinholes of 300  $\mu$ m to focus the X-ray beam and a VÅNTEC-2000, Xe-based gas avalanche detector capable of photon counting with 0.5 seconds temporal resolution. By applying a sample-detector distance of  $\sim 107$  cm, a  $q_{\min}$  of 0.06 nm<sup>-1</sup> could be accessible where  $q = \frac{4\pi}{\lambda} \sin(\theta)$  and  $2\theta$  is the scattering angle. This corresponds to a maximum spatial resolution of 52.4 nm. All the experiments were carried out in a vacuum chamber (0.01 mbar) and at the room temperature over 2 hours of exposure time. Although the electron density contrast of the analyzed particles (silica) with respect to solvent (water) is quite high, a long exposure time was still needed in order to reveal scattering features from pores within the particles. The samples were transferred into quartz capillaries of 1.5 mm in outer diameter (Hilgenberg GmbH, Malsfeld, Germany). The capillaries were vacuum tightened using sealing wax. The scattering profiles of empty and water filled capillaries were obtained under the same conditions and a semi-transparent beam stop enabled to perform normalization of the curves and then background noise subtraction.

Fluorescent scanning was performed with a Tecan microarray scanner. FITC solution was prepared by adding 0.2 mL 0.5 mg/mL ethanolic stock solution into 4.8 mL Milli-Q water. The silanized substrates were immersed into the solution for 24 hours and then washed with Milli-Q water. For the fluorescence scanning, the substrates were placed inside the detection chamber and excited with 488 nm. The obtained images were imported into ImageJ for reading the fluorescence intensity. All parameters were kept the same to allow the comparison between samples.



Contact angle measurement was done as described. A 4  $\mu$ L droplet of super pure water was injected and stayed on the needle tip. The position of the sample holder was carefully adjusted upwards until the droplet touched the sample surface. The holder was then moved down to separate the droplet from the needle tip. The focus of the camera was adjusted to obtain a clear view of the droplet and the contact angle was captured by the program automatically.

XPS measurements were performed with a scanning XPS microprobe spectrometer (PHI VersaProbe II, Physical Electronics, Minnesota, U.S.) using monochromatic Al K $\alpha$  radiation (1486.6 eV). The operating pressure of the XPS analysis chamber was below  $10^{-6}$  Pa for all data presented here. Survey scan spectra and higher resolution narrow region spectra were acquired with a photoemission take-off angle of 45 degrees (with respect to the surface plane). Survey scan spectra (0 – 1100 eV) were acquired with an energy step of 0.8 eV, an acquisition time of 160 ms per data point and an analyzer pass energy of 187.85 eV. Detail spectra were acquired of C 1s (278 eV to 298 eV), O 1s (523 eV to 543 eV), Si 2p (94 eV to 114 eV), N 1s (391 eV to 411 eV) and Cl 2p (190 eV to 210 eV) using an energy step of 0.125 eV and acquisition times of 1.9 s per data point at an analyzer pass energy of 29.35 eV. The energy resolution (FWHM, full width at half-maximum height) measured on the silver Ag 3d5/2 photoemission line is 2.2 eV (for a pass energy of 187.85 eV) and 0.7 eV (for a pass energy of 29.35 eV). The specimens were adhered to a stainless-steel holder via double-sided adhesive tape, whereas the majority of each specimen was placed over a hole to rule out any background signal. Randomly chosen measurement surface positions were analyzed using a micro-focused X-ray beam of diameter 100  $\mu$ m (operated at a power of 25 W at 15 kV). The 180 degrees spherical capacitor energy analyzer was operated in the fixed analyzer transmission mode. Sample charging was compensated using dual beam charge neutralization with a flux of low energy electrons ( $\sim$  1 eV) combined with very low energy positive Ar ions (10 eV). The binding energy is referenced to the C-C, C-H hydrocarbon moiety signal (aliphatic C 1s peak at 285.0 eV). Intensity determination and curve fitting was carried out with CasaXPS software version 2.3.16 (Casa Software Ltd, Teignmouth, UK) using a fixed 70% Gaussian – 30% Lorentzian product function to fit the XPS spectra. Atomic concentrations were calculated from XPS peak areas after subtracting a Shirley type background.

Confocal laser scanning spectroscopy (CLSM) was performed with LSM 780 (Carl Zeiss, Germany) to visualize the distribution of coumarin-chlorambucil conjugates on the PDMS fiber. Fluorescein isothiocyanate (FITC) was used in substitution of coumarin-chlorambucil conjugates to react with AP-MSNPs on PDMS fiber. A small length of resulting fiber was placed on a glass substrate with the cross-section to the top. An excitation wavelength of 488nm was applied for the fluorescence imaging process.

Fluorescence spectroscopy was conducted with a Horiba FluoroMax from PDMS fiber surface.

## 5.4 Matlab code for qualitative analysis of particle coating

\*Parameters should be adjusted for each specific situation to have the best particle recognition.

```
clc;
clear all
close all

%% Setup
figshow = false; % true: display figures; false: do not display
figsave = true; % true: save figures; false: do not save
figwidth = 300; %pixels
figheight = 300; %pixels
filename = 'after-silane optimization.csv'; % Output filename
warning('off'); % Switch off the warning from triangulation when radii is small

% Directory of the images folder
img_dir = 'C:\Users\luj\Documents\MATLAB\APTMS-parameter\test-original\';

% Input the files names
img_file = '*.tif'; % all files with TIFF format
%img_file = 'IMG_4473.TIFF'; % to check single file

Images=dir([img_dir, img_file]);
```

```

for img_id = 1:length(Images)

    img_name = Images(img_id).name;
    fprintf(['=====',img_name,'=====\n']);
    fprintf("Computing the image %s \n", img_name);

    t = Tiff(fullfile(img_dir, img_name), 'r');
    O = read(t);
    close(t);

    %% If the input is a 3D array
    %   O = O(:,:,1:3);
    %   O = rgb2gray(O);

    %% If the input is a 2D Matrix
    O = O(:,:);

    %% Choose smaller size for experiments
    [min_val, min_pos] = min(O(:,1));
    %O = O(1:min_pos-1,:); % Cut the metadata from SEM
    O = O(1:figwidth,1:figheight);

    %% Original image
    %   if figsave == true
    %       fig(1) = figure;
    %       if figshow == false; set(fig(1), 'Visible', 'off'); end
    %       imshow(O); title("Raw Image")
    %   end

    %% Find circles
    % Check here for a list of filter
    %https://www.mathworks.com/help/images/linear-filtering.html
    O=medfilt2(O); %Deal with salt and pepper noise

    % We don't need to see the filtered images
    % if figshow == true
    %     figure(); imshow(O)
    % end

    [centers,radii,~] = imfindcircles(O,[10 20],'ObjectPolarity','bright','Sensitivity',0.99);
    x = centers(:,1);
    y = centers(:,2);

    %% Triangulation
    TR = delaunayTriangulation(x,y);
    % Highlight the free boundaries
    %plot(x(F),y(F),'-r*','LineWidth',2)
    %plot(x1(k2),y1(k2),'-r*','LineWidth',2);
    %plot(x(k1),y(k1),'-r*','LineWidth',2);

    %% Boundary searching
    % Free boundary
    F = freeBoundary(TR);
    % First layer of poly boundary
    k1 = boundary(x,y);
    x1 = x(setdiff(1:end,k1));
    y1 = y(setdiff(1:end,k1));
    % Second layer of poly boundary
    k2 = boundary(x1,y1);

```

```

x2 = x1(setdiff(1:end,k2));
y2= y1(setdiff(1:end,k2));

%% Show raw figureF-triangulized figure free boundary and first layer of poly boundary k1
% if figsave == true
    fig(2) = figure;
    if figshow == false; set(fig(2), 'Visible', 'off'); end
    imshow(O); hold on
    plot(imgca, x, y, 'o', 'MarkerSize',5, 'Color', 'c')
    hold on
    triplot(TR, 'Color', 'c'), hold on
    plot(x1(k2), y1(k2), '-r*', 'LineWidth', 2);
    plot(x(k1), y(k1), '-r*', 'LineWidth', 2);
% end

%% Remove boundary
% We can remove:
% 1. Free boundary,
% 2. First layer of poly boundary k1
% 3. Second layer of poly boundary k2
% !!!Here we remove free boundary and k1 only.

% Removing Free boundary
% bonds = setdiff(TR.edges, sort(F, 2), 'rows');

% Removing k1 and F
k1F = unique([k1; F(:,1)]); % Remove repeat vertices
[p, q] = meshgrid(k1F, k1F);
k1_pairs = [p(:) q(:)];
bonds_inter = intersect(TR.edges, sort(k1_pairs, 2), 'rows'); % Find possible bonds that contains the cross connection at k1 level
bonds = setdiff(TR.edges, bonds_inter, 'rows'); % Remove cross bonds at k1 level

% Removing k1
[p, q] = meshgrid(k2, k2);
k2_pairs = [p(:) q(:)];
bonds_inter = intersect(bonds, sort(k2_pairs, 2), 'rows');
bonds = setdiff(bonds, bonds_inter, 'rows');

%% Show the bonds after removing the boundaries
% if figsave == true
    fig(3) = figure;
    if figshow == false; set(fig(3), 'visible', 'off'); end
    imshow(O); hold on
    for i = 1:length(bonds)
        plot(x(bonds(i,:)), y(bonds(i,:)), 'c')
        hold on;
    end
% end

%% Computing bond statistics
bond_length = zeros(1, length(bonds));
for i = 1:length(bonds)
    bond_length(i) = sqrt(diff(x(bonds(i,:)))^2 + diff(y(bonds(i,:)))^2);
end

mean_length = mean(bond_length);
std_length = std(bond_length);
median_length = median(bond_length);
fprintf('Mean: %f \n', mean_length);
fprintf('Std: %f \n', std_length);
fprintf('Median: %f \n', median_length);

```

```
%% Save figures
if figsave == true
    [imgpath,name,ext] = fileparts(img_name);
    %savefig(fig, [name,'.fig'])
    saveas(fig(1),[name,'Raw.png'])
    saveas(fig(2),[name,'Boundary.png'])
    saveas(fig(3),[name,'Bonds.png'])
end

%% Output to files
fout=fopen(filename,'a');
fprintf(fout,'%s,%f,%f,%f\n',img_name, mean_length, std_length,median_length);
fclose(fout);

end
```



# Chapter 6 Conclusion and outlook

## 6.1 Achieved results and future work

Different stimuli, such as pH, temperature, redox, etc., can be applied to control the release of active molecules. Yet they have been used to generate a controlled release system, the applying and removing of the stimuli can be slow (e.g. temperature-responsive) and environment-dependent (e.g. local pH-sensitive system), keeping the systems from giving a fast and on-demand release. Therefore, the focus of this investigation will be set on light-responsive materials. Light can be applied rapidly and remotely. Additionally, light is a clean stimulus that can be focused easily on small and defined areas of the body. Even though photo-responsive mesoporous silica particles have been intensively investigated, the non-controllable biodistribution and circulation properties of the particles remain a problem, which can lead to chronic toxicities. To overcome this problem, we propose to bind the mesoporous silicate particles directly onto the light source (optical fiber) in this dissertation. Since optical fibers are already used invasively, they can be brought into the desired location of the body. The light-responsive mesoporous silicates will be coated onto the surface of the optical fiber. There are several advantages of our system. Firstly, the light source is in close contact with the particles (via the optical fiber), so theoretically, light sources of lower intensity can be used. Secondly, the photo-responsive silica particles can be easily removed together with the optical fiber after the drug release has occurred and thus chronic toxicities can be avoided. Moreover, the drug release takes place exclusively in the desired region of the body.

The synthesis of mesoporous silica nanoparticles employing non-surfactants as templating agents was discussed in the first part of this thesis (chapter 2). For the first time, a systematic investigation of the morphogenetic mechanism of mesoporous silica nanoparticles by polyphenols has been carried out. According to our findings, the pKa value of polyphenols influences the nucleation and particle growth processes, and the establishment of the supramolecular network adds to the porous structure by acting as a skeleton for the silica precursors to polymerize. Further research into tailoring the supramolecular network of tannic acid, such as by injecting iron ions to produce a tannic acid-iron complex, will be of considerable interest since it might lead to the generation of MSNPs with the desired size and porosity. Also, tannic acid was only used for the synthesis of silica nanoparticles in our current work, however, it is worthwhile to explore whether it can be used as the template for other chemical species.

The second element of the project (chapter 3) is to develop a method for creating a complicated matrix of particle-polymer optical fibers (POF). Based on layer-by-layer (LbL) assembly, we devised a robust and controlled strategy for the fabrication of particle-coated surfaces that is applicable to a wide variety of substrates and coating materials. Due to a dense and homogeneous monolayer covering of particles on the substrates, significant drug loading and low structural complexity can be accomplished at the same time. The computer vision method was used to quantitatively analyze the particle coating, greatly boosting the efficiency and accuracy of the coating evaluation. According to the factorial analysis, particle concentration was the most important influence factor on coating uniformity and density. For future prospects, the established particle-fiber system is supposed to have the potential as implants to deliver active molecules, thus, it is necessary to enhance the stability of the particle coating in order to completely avoid the chronic toxicity of the de-attached particles due to non-controllable biodistribution and circulation in human body. It can be achieved in three ways. One possible approach will be to post-crosslink the layers with appropriate linkers, another way is to functionalize the particles with groups that can bond with the surface, like our attempt of using glutaraldehyde, but the aggregation of particles should be avoided. Another interesting method will be the in-situ growth of particles on the surface. This approach will allow control of the particle morphology as well as ensure a stable coating in one single step. Another consideration will be how to improve the degree of silanization so that more prodrugs can be grafted.

The final part of the work (chapter 4) focused on the light-responsive release of photolabile coumarin-chlorambucil conjugates from optical fibers. To our knowledge, this is the first study to look into drug release from the side of optical fibers. We've already established that chlorambucil derivatives are released in reaction to light. However, more research is needed to gain a comprehensive understanding of the releasing process, and some of these studies are currently underway. First, coumarin-chlorambucil conjugate release should be carried out for two reasons: 1) to see if chlorambucil derivatives will be released instead of chlorambucil; 2) to compare the released substances from particles and our final particle-fiber matrix to see if the prodrugs' attachment will have an effect on the release behaviors. Second, the release of particles from the fiber matrix should be compared to the release from the fiber matrix. The chlorambucil derivative was brought up as a hypothesis, and sketching its chemical structure will be appealing.

Characterization techniques including UV, FT-IR could be used to provide insights. The temporal dependence of release should be explored in order to get a thorough release study. We also did a simulation research to show how the interaction between light and the coating on the optical fiber surface can result in the release.

Our light-responsive delivery system has many possibilities to be modified or improved in terms of the strategy of controlled release and the species of compounds that can be released. We could stick to the photocleavable mechanism and alternate the species of PPGs to expand the species of molecules that can be integrated with PPGs. Also, we can design the chemical structure of PPGs to enable the release with the light of expected wavelength or release of multiple drugs under irradiation of different light. Moreover, we have a curiosity to know whether we can apply the fluorescence resonance energy transfer (FRET) concept for the photocleavable release. Other controlled release mechanisms can also be selected, for example, instead of the photocleavable mechanism, we can encapsulate the drugs in a nanoparticle reservoir and gate the pores with light-responsive molecules that experience a configuration transformation. In this way, we can control the release of drugs by changing the size, hydrophilicity, or ionic state of the gate molecules. We have also proposed some potential application that is derived from our system in section 6.3.

## 6.2 Simulation

In this section, I outline some preliminary simulation results.

### 6.2.1 3D simulation model

To understand better the theory of the triggering process, we have run a COMSOL simulation. Assuming the MSNP coating is a monolayer, the computational unit was built onto one single particle and repeated periodically at a distance of 250nm according to the MatLab analysis as illustrated in Figure 6-1. To further simplify the model, we have set the particle as a non-porous sphere. A silica nanoparticle (180nm,  $n=1.469$ ) was placed on PDMS layer ( $n=1.426$ ) with a PDDA layer (thickness=5nm,  $n=1.375$ ) in between. A liquid layer (ACN water mixture v/v 9:1,  $n=1.34$ ) was added on the top. A bunch of plain waves (polarized in the y-direction) was let through from the bottom to the top. The incident angle is defined as the angle between light and z-axis. On both sides, a perfectly matched layer (PML) was set to prevent the plain wave from reflecting to the interior area.

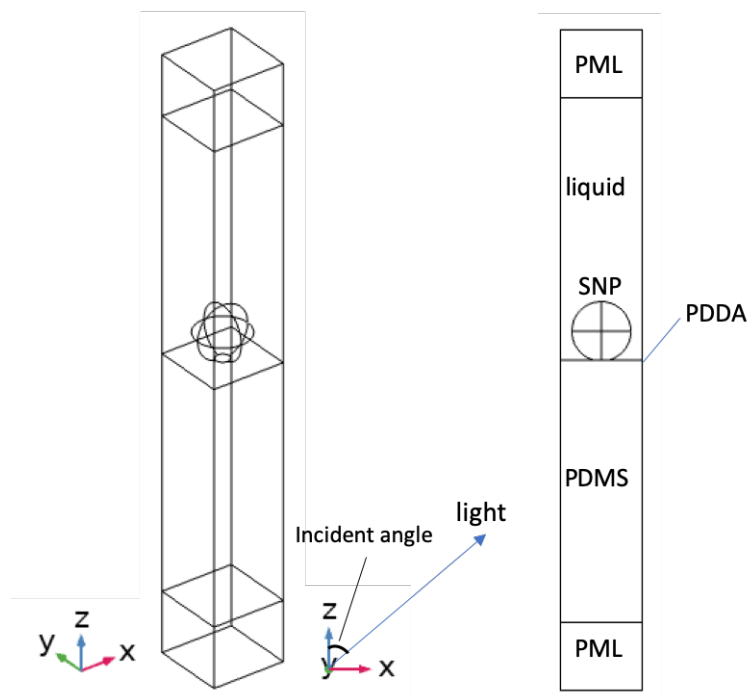


Figure 6-1. 3D simulation model of the particle-fiber delivery system

### 6.2.2 Light transmission and intensity simulation of the built-up model

We started by defining the computational region with pure PDMS. Figure 6-2 showed the light transmission at different incident angles. The light traveled smoothly within the region and no scattering was observed as expected. It is because the region has a



homogeneous density thus no scattering can happen. However, when defining PDMS, PDDA and liquid medium for the model, the light behavior changed. Instead of smooth transmission in the region, the light started to show a partially scattering effect when the incident angle reaches  $60^\circ$ . When the incident angle is  $70^\circ$ , the transmission pattern represents the total internal reflection at the interface, in agreement with the theoretical critical angle ( $69.9^\circ$ , calculated from refractive indices of PDMS and liquid medium) between the liquid layer and the PDMS layer. To figure out the interaction between particle and light, a particle was introduced to the previously defined model. Compared to the situation without particles, the light transmission behavior has changed dramatically. First, a disturbance at  $10^\circ$  was recorded, which should be attributed to the light scattering caused by particles. However, if this is the case, we should see similar disturbance to the light transmission at all angles. At  $60^\circ$ , the light has a strong interference pattern. It is likely to be the sum-up of the light-particle interaction and light-PDDA interaction. Currently, we are still looking for a good explanation for this.

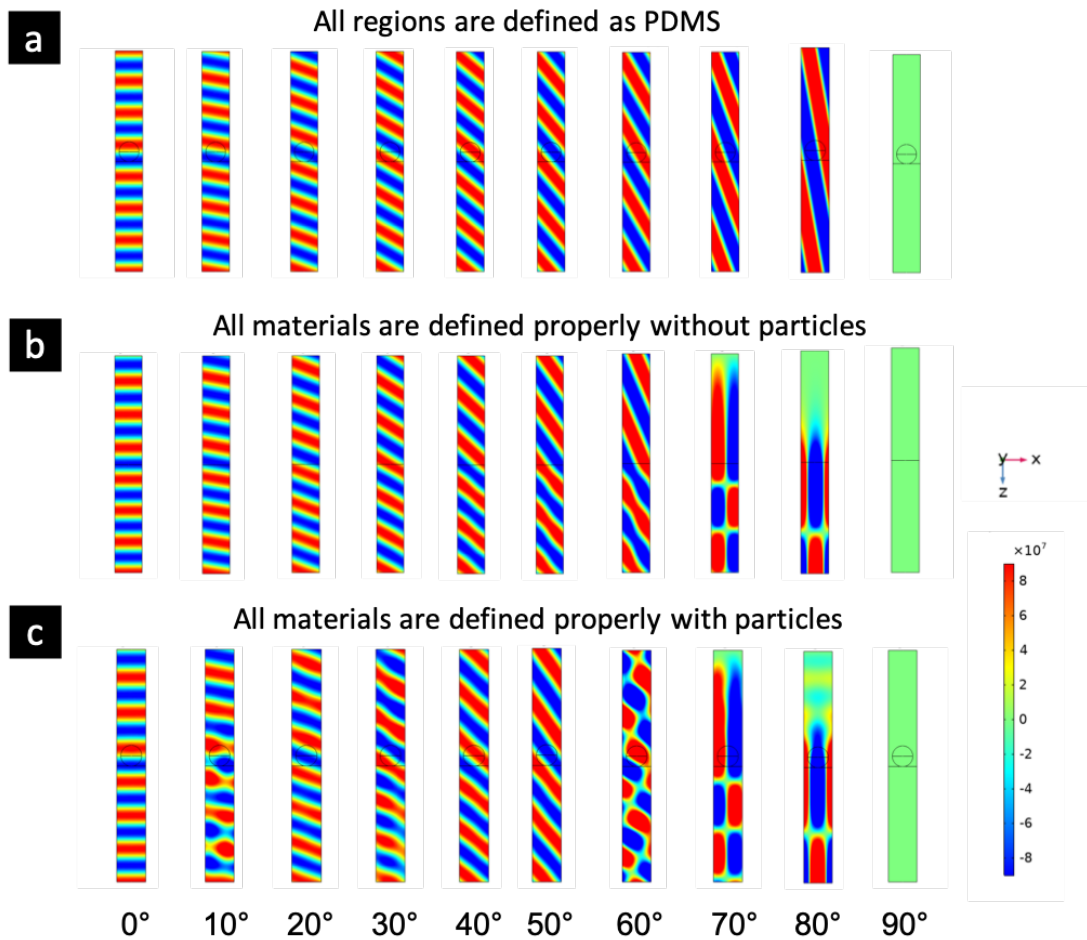


Figure 6-2.a) light transmission through the defined material (PDMS) with the incident angle changing from  $0^\circ$  to  $90^\circ$ ; b) light transmission through the region when PDMS, PDDA, and solvent were properly defined with the incident angle changing from  $0^\circ$  to  $90^\circ$ ; c) light transmission through the region when all materials were properly defined with the incident angle changing from  $0^\circ$  to  $90^\circ$ . Color bar:  $[-9E7, 9E7]$ .

Besides, the light transmission behavior, we also compared the light intensity on the PDMS surface with and without particle coating by integration of the light intensity at different incident angles, from  $70^\circ$  to  $90^\circ$  at a step of  $2.5^\circ$ . Without particles, the light intensity was homogeneous at the same altitude and gradually decreased along the z-axis, while particle coating has aroused a heterogeneous light intensity distribution. Also, the light intensity is of a smaller scale when the particle was placed. That is due to light loss caused by the light scattering.

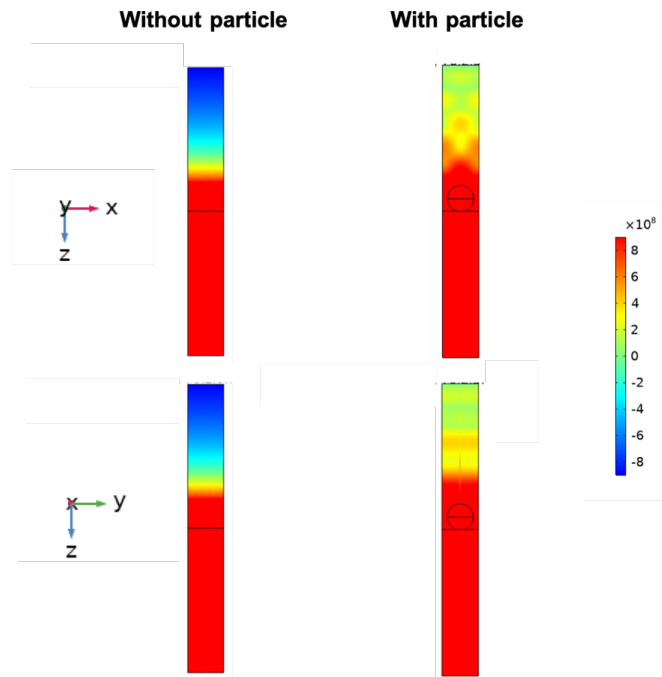


Figure 6-3. Light intensity on PDMS fiber surface by simulation, color bar:  $[-9E8, 9E8]$

### 6.2.3 Influence of PDDA layer on the light behavior

The PDMS surface was coated with PDPA and silica nanoparticles. This could lead to the complexity in light behavior at the interface. Based on the refractive index of the coated material, there could be total internal reflection between PDPA/ PDMS, liquid/PDPA, liquid/PDMS. Thus, it is interesting to study the light behavior with and without the PDPA layer. Compared with PDPA-coated one, the uncoated one has shown an obvious different pattern especially at an incident angle of  $60^\circ$  (Figure 6-3), suggesting PDPA does have an influence on the light transmission on the surface. In Figure 6-5, we have showed the reflectance and transmittance of the light on the surface of optical fiber when PDPA and particles were introduced or missing and we are trying to understand the factors that causes the difference.

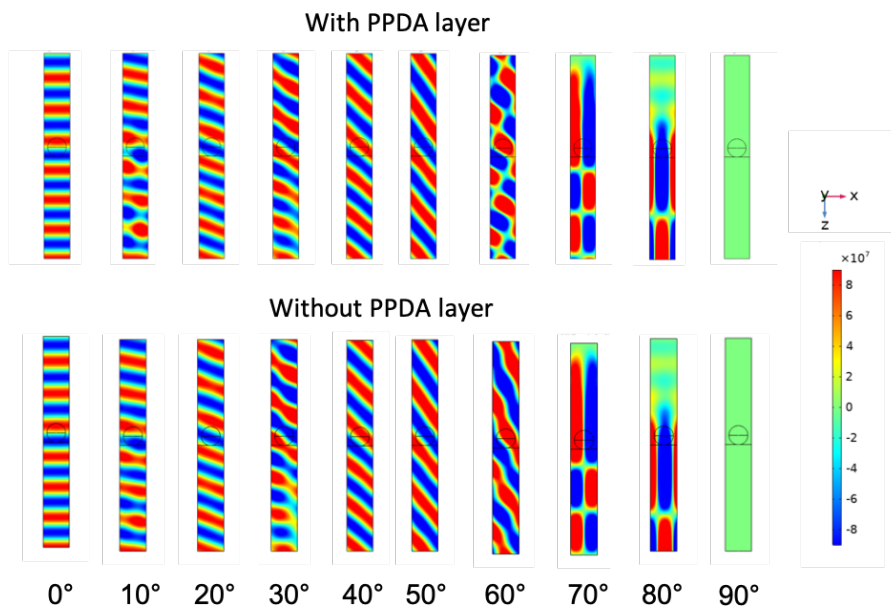


Figure 6-4. Comparison of the light transmission on the side of optical fiber with (the same as Figure 6-2c) and without PDPA coating

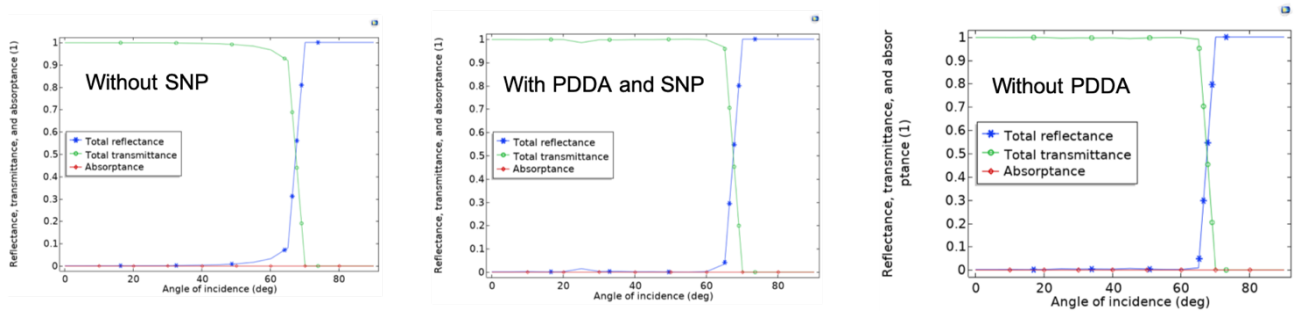


Figure 6-5. Reflectance and transmittance of the light on the surface of optical fiber when PDDA and particles were introduced or missing

### 6.2.4 Influence of refractive index of medium on the light behavior

The change of refractive index can cause a change in the total internal reflection. Therefore, the alternation of solvent will result in different light behavior and thus influence the release process. We have applied three different refractive indices (one smaller than PDMS, one roughly the same as PDMS, one bigger than PDMS) for the liquid medium and see whether it will give a difference. When the refractive index of liquid increased, the total internal reflection disappeared gradually, letting out the light. This is confirmed by the simulation result, showing the light intensity is growing with the refractive index of liquid (Figure 6-6). The releasing behavior in different solvents would also be different. In a releasing medium with a higher refractive index, the release should be faster when other conditions remaining the same and that is due to the higher intensity of the outcoupled light.

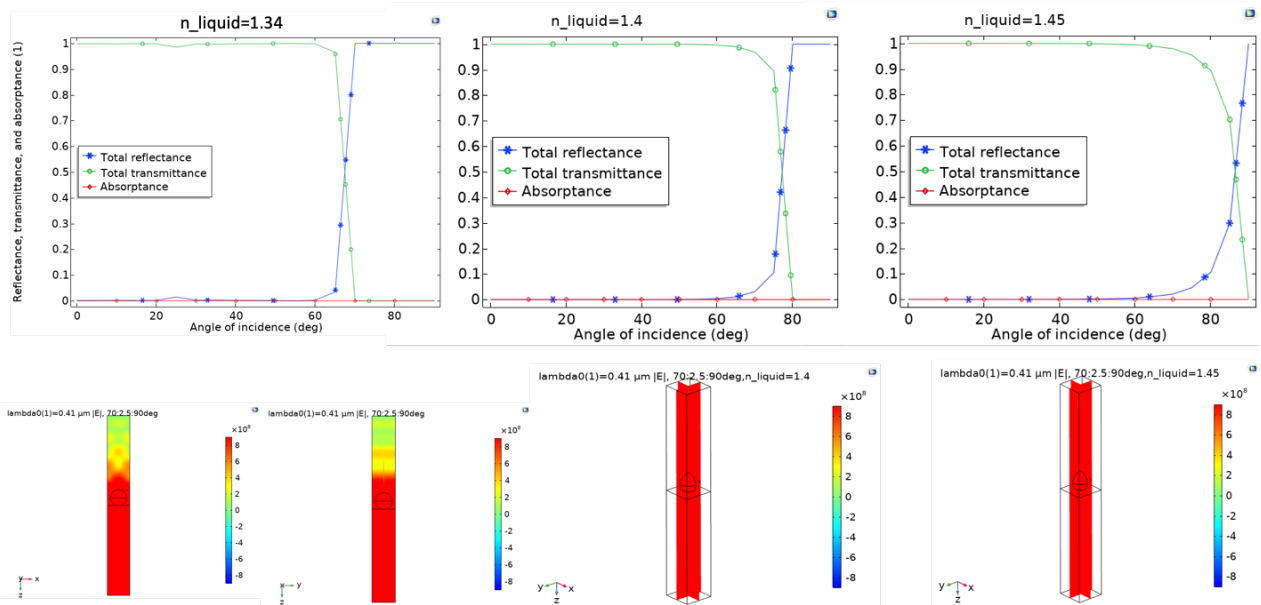


Figure 6-6. Reflectance and transmittance of the light on the surface of optical fiber in different releasing medium

To summarize, the preliminary simulation results are not completed, more studies should be done to explain properly the simulation results.

## 6.3 Outlook: Some potential applications of the complex delivery system

The fabrication of this delivery system will enable potential use in various practical applications in collaboration with other functional components. Here, as an example, propose a few possible applications that are regarded of great commercial value.

### Skincare and healthcare textiles

For skincare purposes, a large variety of functional substances release can be stored into either the textile fibers or the fibers with controlled-release abilities for continuous or on-demand care. For example, cosmetics-loaded clothing can be a new category of

fashion textiles. Pharmaceutical compounds-loaded fibers can be woven to a wearable textile as an aiding platform of transdermal drug delivery.

#### **Personalized dosage-adapted drug delivery system**

Therapeutic time window and therapeutic dose play a dominant role in affecting the effectiveness of drug therapy. A constant appropriate drug-releasing dose can guarantee the safety as well as a high efficacy of the treatment. However, the therapeutic dose varies from person to person. It can be anticipated that there is a potential demand for personalized precise drug delivery. Despite the immaturity of our optical-fiber-based drug delivery system, it should be possible, in the future, to build an integrated device that possesses both monitoring and releasing components. The device can enable real-time detection of the concentration of the released drug in the human circulatory system and automatically adjusting the releasing rate to maintain a constant release within the therapeutical window. This system shows a dramatic advantage, especially for chronic diseases.

#### **Continuous glucose monitoring system**

The level of human blood glucose is a dynamic value that changes every second. Conventional blood glucose monitoring conducted only at some time points has thus a restriction to represent the real-time glucose level. It is very attractive to have a device that can give continuous monitoring of the blood glucose, bringing great benefits to diabetes patients. For those who need to inject insulin regularly to control the blood glucose level, a substitution of needle injection with continuous insulin pump/ implants can improve the treatment experience steeply, reducing the pain and freeing patients from the routine injection. It is quite meaningful to monitor the glucose and triggered automatically the release of insulin once the glucose reaches a high level. As we know, it has been widely reported that optical fiber has been used to detect glucose. There is a way to combine the monitoring of blood glucose and releasing of insulin on one optical fiber. With the assistance of data science, electronic engineering and mechanical engineering, the designed prototype can be used for smart diabetes therapy.

#### **Urgent AMI (acute myocardial infarction) aiding implants**

Cardiovascular diseases (CVD) remain the number one killer disease in a worldwide range according to the WHO annual report 2015. Within all the subtypes, acute myocardial infarction (AMI) is considered highly threatened as the attack occurs without sign which, as a consequence, will lead to an extremely high risk of death because of the low probability to acquire the first aid in time. Therefore, an early diagnosis is one of the key means to lower the death rate. Based on this knowledge, we propose here a long-term monitoring and urgent aiding system. This system will be thus composed of two parts--- the optical fiber-based monitoring section and the light-triggered on-demand release section. For the release part, our fibrous releasing system will be directly induced and serve as an AMI drug reservoir. As long as the monitoring component senses the abnormal behavior of the heart, the signal will be instantly transmitted to the light-controlling component. The LED will be activated immediately and trigger the urgent release of AMI drugs like aspirin. To ensure precise monitoring, enzyme-linked immunosorbent assay (ELISA) can be applied with the choice of cardiac troponin I (cTnI) as it is currently regarded as the gold standard biomarker for AMI. Its high sensitivity and specificity are very helpful in the stratification of patients with AMI. In our design, the cTnI antibody assay will be planted on the end of our fibrous photo-triggered delivery platform. When AMI occurs, the cTnI antigens will be released and meet the antibody assay on the fiber. The bonding will lead to a change in the optical signal that will be captured by the platform. As feedback, the light will be triggered on and allows the rapid release of AMI drugs. In a time-counting situation like AMI, this design can be very helpful to save more time for accessing treatment.

## References

1. Popat, A., et al., *Mesoporous silica nanoparticles for bioadsorption, enzyme immobilisation, and delivery carriers*. Nanoscale, 2011. **3**(7): p. 2801-2818.
2. Manzano, M. and M. Vallet-Regí, *Mesoporous Silica Nanoparticles for Drug Delivery*. Advanced Functional Materials, 2020. **30**(2): p. 1902634.
3. Zhou, Y., et al., *Mesoporous silica nanoparticles for drug and gene delivery*. Acta Pharmaceutica Sinica B, 2018. **8**(2): p. 165-177.
4. Mitchell, M.J., et al., *Engineering precision nanoparticles for drug delivery*. Nature Reviews Drug Discovery, 2021. **20**(2): p. 101-124.
5. Yang, P., S. Gai, and J. Lin, *Functionalized mesoporous silica materials for controlled drug delivery*. Chemical Society Reviews, 2012. **41**(9): p. 3679-3698.
6. Slowing, I.I., et al., *Mesoporous silica nanoparticles as controlled release drug delivery and gene transfection carriers*. Advanced Drug Delivery Reviews, 2008. **60**(11): p. 1278-1288.
7. Li, Y. and L. Yang, *Driving forces for drug loading in drug carriers*. Journal of Microencapsulation, 2015. **32**(3): p. 255-272.
8. Kresge, C., et al., *Ordered mesoporous molecular sieves synthesized by a liquid-crystal template mechanism*. nature, 1992. **359**(6397): p. 710.
9. Zhao, D., et al., *Triblock copolymer syntheses of mesoporous silica with periodic 50 to 300 angstrom pores*. Science, 1998. **279**(5350): p. 548-552.
10. Kleitz, F., S.H. Choi, and R. Ryoo, *Cubic Ia 3 d large mesoporous silica: synthesis and replication to platinum nanowires, carbon nanorods and carbon nanotubes*. Chemical Communications, 2003(17): p. 2136-2137.
11. Wei, Y., et al., *A Non - surfactant Templating Route to Mesoporous Silica Materials*. Advanced Materials, 1998. **10**(4): p. 313-316.
12. Wei, Y., et al., *Preparation and physisorption characterization of D-glucose-templated mesoporous silica sol- gel materials*. Chemistry of Materials, 1999. **11**(8): p. 2023-2029.
13. Larsen, G., E. Lotero, and M. Marquez, *Facile sol-gel synthesis of porous silicas using poly (propylene) imine dendrimers as templates*. Journal of Materials Research, 2000. **15**(8): p. 1842-1848.
14. Pang, J.-B., et al., *A facile preparation of transparent and monolithic mesoporous silica materials*. Chemical Communications, 2000(6): p. 477-478.
15. Pang, J.-B., K.-Y. Qiu, and Y. Wei, *Preparation of mesoporous silica materials with non-surfactant hydroxy-carboxylic acid compounds as templates via sol-gel process*. Journal of non-crystalline solids, 2001. **283**(1-3): p. 101-108.
16. Pang, J.-B., K.-Y. Qiu, and Y. Wei, *A new nonsurfactant pathway to mesoporous silica materials based on tartaric acid in conjunction with metallic chloride*. Chemistry of materials, 2001. **13**(7): p. 2361-2365.
17. Cheng, S., et al., *Facile Synthesis of Mesoporous Gold- Silica Nanocomposite Materials via Sol- Gel Process with Nonsurfactant Templates*. Chemistry of materials, 2003. **15**(7): p. 1560-1566.
18. Zheng, J.-Y., et al., *Synthesis of mesoporous silica materials via nonsurfactant templated sol-gel route by using mixture of organic compounds as template*. Journal of sol-gel science and technology, 2002. **24**(1): p. 81-88.
19. Misran, H., R. Singh, and M.A. Yarmo, *Nonsurfactant route of fatty alcohols decomposition for templating of mesoporous silica*. Microporous and Mesoporous Materials, 2008. **112**(1-3): p. 243-253.
20. Mukherjee, I., et al., *Effect of nonsurfactant template content on the particle size and surface area of monodisperse mesoporous silica nanospheres*. Microporous and Mesoporous Materials, 2009. **122**(1-3): p. 168-174.
21. Gao, Z. and I. Zharov, *Large pore mesoporous silica nanoparticles by templating with a nonsurfactant molecule, tannic acid*. Chemistry of Materials, 2014. **26**(6): p. 2030-2037.
22. Nam, L., et al., *Drug Delivery Nanosystems for the Localized Treatment of Glioblastoma Multiforme*. Materials, 2018. **11**(5): p. 779.
23. Brühwiler, D., *Postsynthetic functionalization of mesoporous silica*. Nanoscale, 2010. **2**(6): p. 887-892.
24. Bass, J.D. and A. Katz, *Bifunctional Surface Imprinting of Silica: Thermolytic Synthesis and Characterization of Discrete Thiol-Amine Functional Group Pairs*. Chemistry of Materials, 2006. **18**(6): p. 1611-1620.
25. Dai, S., et al., *Imprint coating: a novel synthesis of selective functionalized ordered mesoporous sorbents*. Angewandte chemie international edition, 1999. **38**(9): p. 1235-1239.
26. Shin, Y., et al., *Ordered Hierarchical Porous Materials: Towards Tunable Size - and Shape - Selective Microcavities in Nanoporous Channels*. Angewandte Chemie, 2000. **112**(15): p. 2814-2819.
27. Yang, C.-M., et al., *Stepwise Removal of the Copolymer Template from Mesopores and Micropores in SBA-15*. Chemistry of Materials, 2004. **16**(15): p. 2918-2925.
28. Kecht, J., A. Schlossbauer, and T. Bein, *Selective Functionalization of the Outer and Inner Surfaces in Mesoporous Silica Nanoparticles*. Chemistry of Materials, 2008. **20**(23): p. 7207-7214.
29. Gartmann, N. and D. Brühwiler, *Controlling and Imaging the Functional - Group Distribution on Mesoporous Silica*. Angewandte Chemie International Edition, 2009. **48**(34): p. 6354-6356.
30. Iler, R., *Multilayers of colloidal particles*. Journal of colloid and interface science, 1966. **21**(6): p. 569-594.
31. Decher, G., J.D. Hong, and J. Schmitt, *Buildup of ultrathin multilayer films by a self-assembly process: III. Consecutively alternating adsorption of anionic and cationic polyelectrolytes on charged surfaces*. Thin solid films, 1992. **210**: p. 831-835.
32. Richardson, J.J., M. Björnalm, and F. Caruso, *Technology-driven layer-by-layer assembly of nanofilms*. Science, 2015. **348**(6233).
33. Schlenoff, J.B., S.T. Dubas, and T. Farhat, *Sprayed polyelectrolyte multilayers*. Langmuir, 2000. **16**(26): p. 9968-9969.
34. Stockton, W. and M. Rubner, *Molecular-level processing of conjugated polymers. 4. Layer-by-layer manipulation of polyaniline via hydrogen-bonding interactions*. Macromolecules, 1997. **30**(9): p. 2717-2725.

35. Liang, Z. and Q. Wang, *Multilayer Assembly and Patterning of Poly(p-phenylenevinylene)s via Covalent Coupling Reactions*. Langmuir, 2004. **20**(22): p. 9600-9606.
36. Anzai, J.-i., et al., *Layer-by-layer construction of multilayer thin films composed of avidin and biotin-labeled poly (amine) s*. Langmuir, 1999. **15**(1): p. 221-226.
37. Muller, W., et al., *Attempts to mimic docking processes of the immune system: recognition-induced formation of protein multilayers*. Science, 1993. **262**(5140): p. 1706-1708.
38. Lojou, É. and P. Bianco, *Buildup of polyelectrolyte- protein multilayer assemblies on gold electrodes. Role of the hydrophobic effect*. Langmuir, 2004. **20**(3): p. 748-755.
39. Itano, K., J. Choi, and M.F. Rubner, *Mechanism of the pH-Induced Discontinuous Swelling/Deswelling Transitions of Poly(allylamine hydrochloride)-Containing Polyelectrolyte Multilayer Films*. Macromolecules, 2005. **38**(8): p. 3450-3460.
40. Choi, J. and M.F. Rubner, *Influence of the Degree of Ionization on Weak Polyelectrolyte Multilayer Assembly*. Macromolecules, 2005. **38**(1): p. 116-124.
41. Bieker, P. and M. Schönhoff, *Linear and Exponential Growth Regimes of Multilayers of Weak Polyelectrolytes in Dependence on pH*. Macromolecules, 2010. **43**(11): p. 5052-5059.
42. Yoo, D., S.S. Shiratori, and M.F. Rubner, *Controlling Bilayer Composition and Surface Wettability of Sequentially Adsorbed Multilayers of Weak Polyelectrolytes*. Macromolecules, 1998. **31**(13): p. 4309-4318.
43. Shiratori, S.S. and M.F. Rubner, *pH-Dependent Thickness Behavior of Sequentially Adsorbed Layers of Weak Polyelectrolytes*. Macromolecules, 2000. **33**(11): p. 4213-4219.
44. Burke, S.E. and C.J. Barrett, *pH-Responsive Properties of Multilayered Poly(l-lysine)/Hyaluronic Acid Surfaces*. Biomacromolecules, 2003. **4**(6): p. 1773-1783.
45. Salomäki, M., I.A. Vinokurov, and J. Kankare, *Effect of Temperature on the Buildup of Polyelectrolyte Multilayers*. Langmuir, 2005. **21**(24): p. 11232-11240.
46. Lvov, Y., G. Decher, and H. Moehwald, *Assembly, structural characterization, and thermal behavior of layer-by-layer deposited ultrathin films of poly(vinyl sulfate) and poly(allylamine)*. Langmuir, 1993. **9**(2): p. 481-486.
47. Tan, H.L., et al., *Temperature Dependence of Polyelectrolyte Multilayer Assembly*. Langmuir, 2003. **19**(22): p. 9311-9314.
48. Dubas, S.T., T.R. Farhat, and J.B. Schlenoff, *Multiple Membranes from "True" Polyelectrolyte Multilayers*. Journal of the American Chemical Society, 2001. **123**(22): p. 5368-5369.
49. Dubas, S.T. and J.B. Schlenoff, *Polyelectrolyte Multilayers Containing a Weak Polyacid: Construction and Deconstruction*. Macromolecules, 2001. **34**(11): p. 3736-3740.
50. Salomäki, M., et al., *The Hofmeister Anion Effect and the Growth of Polyelectrolyte Multilayers*. Langmuir, 2004. **20**(9): p. 3679-3683.
51. Salomäki, M. and J. Kankare, *Specific Anion Effect in Swelling of Polyelectrolyte Multilayers*. Macromolecules, 2008. **41**(12): p. 4423-4428.
52. Salomäki, M., T. Laiho, and J. Kankare, *Counteranion-Controlled Properties of Polyelectrolyte Multilayers*. Macromolecules, 2004. **37**(25): p. 9585-9590.
53. Poptoshev, E., B. Schoeler, and F. Caruso, *Influence of Solvent Quality on the Growth of Polyelectrolyte Multilayers*. Langmuir, 2004. **20**(3): p. 829-834.
54. Koetse, M., et al., *Influence of Charge Density and Distribution on the Internal Structure of Electrostatically Self-assembled Polyelectrolyte Films*. Langmuir, 2002. **18**(5): p. 1655-1660.
55. Soltwedel, O., et al., *Influence of Polycation (PDADMAC) Weight on Vertical Diffusion within Polyelectrolyte Multilayers during Film Formation and Postpreparation Treatment*. Macromolecules, 2012. **45**(19): p. 7995-8004.
56. Kujawa, P., et al., *Effect of Molecular Weight on the Exponential Growth and Morphology of Hyaluronan/Chitosan Multilayers: A Surface Plasmon Resonance Spectroscopy and Atomic Force Microscopy Investigation*. Journal of the American Chemical Society, 2005. **127**(25): p. 9224-9234.
57. Jang, Y., et al., *Molecular Weight Dependence on the Disintegration of Spin-Assisted Weak Polyelectrolyte Multilayer Films*. Macromolecules, 2013. **46**(11): p. 4580-4588.
58. Nestler, P., M. Paßvogel, and C.A. Helm, *Influence of Polymer Molecular Weight on the Parabolic and Linear Growth Regime of PDADMAC/PSS Multilayers*. Macromolecules, 2013. **46**(14): p. 5622-5629.
59. Liu, G., et al., *Role of Chain Interpenetration in Layer-by-Layer Deposition of Polyelectrolytes*. The Journal of Physical Chemistry B, 2008. **112**(11): p. 3333-3338.
60. Liu, G., et al., *Roles of Chain Conformation and Interpenetration in the Growth of a Polyelectrolyte Multilayer*. The Journal of Physical Chemistry B, 2008. **112**(14): p. 4167-4171.
61. Wu, B., et al., *Formation of Polyelectrolyte Multilayers by Flexible and Semiflexible Chains*. The Journal of Physical Chemistry B, 2012. **116**(10): p. 3106-3114.
62. Pichon, B.P., et al., *Magnetotunable hybrid films of stratified iron oxide nanoparticles assembled by the layer-by-layer technique*. Chemistry of Materials, 2011. **23**(16): p. 3668-3675.
63. Dontsova, D., et al., *Photocatalytic layer-by-layer polyelectrolyte/TiO<sub>2</sub> nanoparticle films on model and reactor surfaces*.
64. Schneider, G. and G. Decher, *From functional core/shell nanoparticles prepared via layer-by-layer deposition to empty nanospheres*. Nano Letters, 2004. **4**(10): p. 1833-1839.
65. Wang, Y., et al., *Mirror-Like Photoconductive Layer-by-Layer Thin Films of Te Nanowires: The Fusion of Semiconductor, Metal, and Insulator Properties*. Advanced Materials, 2006. **18**(4): p. 518-522.
66. Mwaura, J.K., et al., *Photovoltaic Cells Based on Sequentially Adsorbed Multilayers of Conjugated Poly(p-phenylene ethynylene)s and a Water-Soluble Fullerene Derivative*. Langmuir, 2005. **21**(22): p. 10119-10126.
67. Liang, Z., et al., *Covalent Layer-by-Layer Assembly of Conjugated Polymers and CdSe Nanoparticles: Multilayer Structure and Photovoltaic Properties*. Advanced Functional Materials, 2006. **16**(4): p. 542-548.
68. Agrios, A.G., et al., *Nanostructured Composite Films for Dye-Sensitized Solar Cells by Electrostatic Layer-by-Layer Deposition*. Chemistry of Materials, 2006. **18**(23): p. 5395-5397.
69. Nolte, A.J., M.F. Rubner, and R.E. Cohen, *Creating Effective Refractive Index Gradients within Polyelectrolyte Multilayer Films: Molecularly Assembled Rugate Filters*. Langmuir, 2004. **20**(8): p. 3304-3310.
70. Han, J.T., et al., *Stable Superhydrophobic Organic-Inorganic Hybrid Films by Electrostatic Self-Assembly*. The Journal of Physical Chemistry B, 2005. **109**(44): p. 20773-20778.
71. Zhai, L., et al., *Patterned Superhydrophobic Surfaces: Toward a Synthetic Mimic of the Namib Desert Beetle*. Nano Letters, 2006. **6**(6): p. 1213-1217.

72. Lee, D., M.F. Rubner, and R.E. Cohen, *All-Nanoparticle Thin-Film Coatings*. Nano Letters, 2006. **6**(10): p. 2305-2312.
73. Hollman, A.M. and D. Bhattacharyya, *Pore Assembled Multilayers of Charged Polypeptides in Microporous Membranes for Ion Separation*. Langmuir, 2004. **20**(13): p. 5418-5424.
74. Shiratori, S., Y. Inami, and M. Kikuchi, *Removal of toxic gas by hybrid chemical filter fabricated by the sequential adsorption of polymers*. Thin Solid Films, 2001. **393**(1): p. 243-248.
75. Lee, D., et al., *pH-Induced Hysteretic Gating of Track-Etched Polycarbonate Membranes: Swelling/Deswelling Behavior of Polyelectrolyte Multilayers in Confined Geometry*. Journal of the American Chemical Society, 2006. **128**(26): p. 8521-8529.
76. Zhang, J., L.S. Chua, and D.M. Lynn, *Multilayered Thin Films that Sustain the Release of Functional DNA under Physiological Conditions*. Langmuir, 2004. **20**(19): p. 8015-8021.
77. Wang, Y. and F. Caruso, *Template Synthesis of Stimuli-Responsive Nanoporous Polymer-Based Spheres via Sequential Assembly*. Chemistry of Materials, 2006. **18**(17): p. 4089-4100.
78. Onda, M., et al., *Sequential actions of glucose oxidase and peroxidase in molecular films assembled by layer-by-layer alternate adsorption*. Biotechnology and Bioengineering, 1996. **51**(2): p. 163-167.
79. Dotzauer, D.M., et al., *Catalytic Membranes Prepared Using Layer-by-Layer Adsorption of Polyelectrolyte/Metal Nanoparticle Films in Porous Supports*. Nano Letters, 2006. **6**(10): p. 2268-2272.
80. Shchukin, D.G. and H. Möhwald, *Urea Photosynthesis inside Polyelectrolyte Capsules: Effect of Confined Media*. Langmuir, 2005. **21**(12): p. 5582-5587.
81. Podsiadlo, P., et al., *Layer-by-Layer Assembly of Nacre-like Nanostructured Composites with Antimicrobial Properties*. Langmuir, 2005. **21**(25): p. 11915-11921.
82. Ai, H., et al., *Nano-encapsulation of furosemide microcrystals for controlled drug release*. Journal of Controlled Release, 2003. **86**(1): p. 59-68.
83. Shutava, T., et al., *Microcapsule Modification with Peroxidase-Catalyzed Phenol Polymerization*. Biomacromolecules, 2004. **5**(3): p. 914-921.
84. Pargaonkar, N., et al., *Controlled Release of Dexamethasone from Microcapsules Produced by Polyelectrolyte Layer-by-Layer Nanoassembly*. Pharmaceutical Research, 2005. **22**(5): p. 826-835.
85. Barnoski, M., *Fundamentals of optical fiber communications*. 2012: Elsevier.
86. Willner, A., *Optical fiber telecommunications*. Vol. 11. 2019: Academic Press.
87. Kumar, S., et al., *A comprehensive review on fiber bragg grating and photodetector in optical communication networks*. Journal of Optical Communications, 2019.
88. Talataisong, W., et al., *Suspended-Core Microstructured Polymer Optical Fibers and Potential Applications in Sensing*. Sensors, 2019. **19**(16): p. 3449.
89. Roriz, P., et al., *Optical Fiber Temperature Sensors and Their Biomedical Applications*. Sensors, 2020. **20**(7): p. 2113.
90. Herman, O., et al., *Time multiplexed super resolution of multicore fiber endoscope using multimode fiber illumination patterns*. Optical Fiber Technology, 2020. **54**: p. 102122.
91. Zhang, Y., Y. Cao, and J.-X. Cheng, *High-resolution photoacoustic endoscope through beam self-cleaning in a graded index fiber*. Optics Letters, 2019. **44**(15): p. 3841-3844.
92. Villatoro, J., *Phase-shifted modal interferometers for high-accuracy optical fiber sensing*. Optics Letters, 2020. **45**(1): p. 21-24.
93. Li, C., et al., *A knotted shape core cladding optical fiber interferometer for simultaneous measurement of displacement and temperature*. Photonics and Nanostructures - Fundamentals and Applications, 2020. **39**: p. 100778.
94. Kumari, C.R.U., et al., *Fiber optic sensors in ocean observation: A comprehensive review*. Optik, 2019. **179**: p. 351-360.
95. Scott, R.H., et al., *Development of low cost packaged fibre optic sensors for use in reinforced concrete structures*. Measurement, 2019. **135**: p. 617-624.
96. Gong, H., et al., *Advances in fibre optic based geotechnical monitoring systems for underground excavations*. International Journal of Mining Science and Technology, 2019. **29**(2): p. 229-238.
97. Addanki, S., I.S. Amiri, and P. Yupapin, *Review of optical fibers-introduction and applications in fiber lasers*. Results in Physics, 2018. **10**: p. 743-750.
98. Nazempour, R., et al., *Biocompatible and Implantable Optical Fibers and Waveguides for Biomedicine*. Materials, 2018. **11**(8): p. 1283.
99. Mowbray, S.E. and A.M. Amiri, *A Brief Overview of Medical Fiber Optic Biosensors and Techniques in the Modification for Enhanced Sensing Ability*. Diagnostics, 2019. **9**(1): p. 23.
100. Bunge, C.A., M. Beckers, and B. Lustermann, *3 - Basic principles of optical fibres*, in *Polymer Optical Fibres*, C.-A. Bunge, T. Gries, and M. Beckers, Editors. 2017, Woodhead Publishing. p. 47-118.
101. Harmon, J.P. and G.K. Noren, *Optical polymers : fibers and waveguides*. ACS symposium series, 795. 2001, Washington, DC: American Chemical Society.
102. Kuzyk, M.G., *Polymer Fiber Optics: materials, physics, and applications*. 2018: CRC press.
103. Nihei, E., T. Ishigure, and Y. Koike, *High-bandwidth, graded-index polymer optical fiber for near-infrared use*. Applied Optics, 1996. **35**(36): p. 7085-7090.
104. Marcou, J., M. Robiette, and J. Bulabois, *Plastic optical fibres : practical applications*. 1997: New York (N.Y.) : Wiley.
105. Nalwa, H.S., H. S. Nalwa, Ed., *Polymer Optical Fibers*, American Scientific Publishers, Los Angeles (2004). 2004.
106. Shabahang, S., S. Kim, and S.-H. Yun, *Light-Guiding Biomaterials for Biomedical Applications*. Advanced Functional Materials, 2018. **28**(24): p. 1706635.
107. Guo, J., et al., *Soft and Stretchable Polymeric Optical Waveguide-Based Sensors for Wearable and Biomedical Applications*. Sensors, 2019. **19**(17): p. 3771.
108. Luo, Y., et al., *Toward optical fibre fabrication using 3D printing technology*. Optical Fiber Technology, 2020. **58**: p. 102299.
109. Yenilmez, B., et al., *Label-Free Sickle Cell Disease Diagnosis using a Low-Cost, Handheld Platform*. Advanced Materials Technologies, 2016. **1**(5): p. 1600100.
110. Yetisen, A.K., et al., *Glucose-Sensitive Hydrogel Optical Fibers Functionalized with Phenylboronic Acid*. Advanced Materials, 2017. **29**(15): p. 1606380.
111. Guo, J., et al., *Highly Stretchable, Strain Sensing Hydrogel Optical Fibers*. Advanced Materials, 2016. **28**(46): p. 10244-10249.
112. Zamadar, M., et al., *Photosensitizer drug delivery via an optical fiber*. Journal of the American Chemical Society, 2011. **133**(20): p. 7882-7891.

113. Nazari, M., et al., *Metal-Organic-Framework-Coated Optical Fibers as Light-Triggered Drug Delivery Vehicles*. Advanced Functional Materials, 2016. **26**(19): p. 3244-3249.
114. Applegate, M.B., et al., *Biocompatible silk step-index optical waveguides*. Biomedical Optics Express, 2015. **6**(11): p. 4221-4227.
115. Nizamoglu, S., et al., *Bioabsorbable polymer optical waveguides for deep-tissue photomedicine*. Nature Communications, 2016. **7**(1): p. 10374.
116. Nizamoglu, S., M.C. Gather, and S.H. Yun, *All - Biomaterial Laser Using Vitamin and Biopolymers*. Advanced Materials, 2013. **25**(41): p. 5943-5947.
117. Maulvi, F.A., et al., *In vitro and in vivo evaluation of novel implantation technology in hydrogel contact lenses for controlled drug delivery*. Journal of Controlled Release, 2016. **226**: p. 47-56.
118. Zhang, S., et al., *A pH-responsive supramolecular polymer gel as an enteric elastomer for use in gastric devices*. Nature materials, 2015. **14**(10): p. 1065.
119. Ranger, M., et al., *From well - defined diblock copolymers prepared by a versatile atom transfer radical polymerization method to supramolecular assemblies*. Journal of Polymer Science Part A: Polymer Chemistry, 2001. **39**(22): p. 3861-3874.
120. Ghosh, P., et al., *Gold nanoparticles in delivery applications*. Advanced drug delivery reviews, 2008. **60**(11): p. 1307-1315.
121. Hoare, T.R. and D.S. Kohane, *Hydrogels in drug delivery: Progress and challenges*. Polymer, 2008. **49**(8): p. 1993-2007.
122. Liu, Z., et al., *Drug delivery with carbon nanotubes for in vivo cancer treatment*. Cancer research, 2008. **68**(16): p. 6652-6660.
123. Zeng, J., et al., *Biodegradable electrospun fibers for drug delivery*. Journal of Controlled Release, 2003. **92**(3): p. 227-231.
124. Won, Y.-Y., H.T. Davis, and F.S. Bates, *Giant wormlike rubber micelles*. Science, 1999. **283**(5404): p. 960-963.
125. Kalantari, K., et al., *Wound dressings functionalized with silver nanoparticles: promises and pitfalls*. Nanoscale, 2020. **12**(4): p. 2268-2291.
126. Basova, T.V., et al., *The use of noble metal coatings and nanoparticles for the modification of medical implant materials*. Materials & Design, 2021. **204**: p. 109672.
127. Vigneshwaran, N., *Modification of textile surfaces using nanoparticles*. Surface Modification of Textiles, 2009: p. 164-184.
128. Alvarez - Lorenzo, C., L. Bromberg, and A. Concheiro, *Light - sensitive intelligent drug delivery systems*. Photochemistry and photobiology, 2009. **85**(4): p. 848-860.
129. Lavan, D.A., T. McGuire, and R. Langer, *Small-scale systems for in vivo drug delivery*. Nature biotechnology, 2003. **21**(10): p. 1184-1191.
130. Kost, J. and R. Langer, *Responsive polymeric delivery systems*. Advanced drug delivery reviews, 2012. **64**: p. 327-341.
131. Sershen, S. and J. West, *Implantable, polymeric systems for modulated drug delivery*. Advanced drug delivery reviews, 2002. **54**(9): p. 1225-1235.
132. Linsley, C.S. and B.M. Wu, *Recent advances in light-responsive on-demand drug-delivery systems*. Therapeutic delivery, 2017. **8**(2): p. 89-107.
133. Mura, S., J. Nicolas, and P. Couvreur, *Stimuli-responsive nanocarriers for drug delivery*. Nature Materials, 2013. **12**(11): p. 991-1003.
134. Wang, Y., et al., *Metal-organic frameworks for stimuli-responsive drug delivery*. Biomaterials, 2020. **230**: p. 119619.
135. Gulzar, A., et al., *Stimuli responsive drug delivery application of polymer and silica in biomedicine*. Journal of Materials Chemistry B, 2015. **3**(44): p. 8599-8622.
136. Li, Z., N. Song, and Y.-W. Yang, *Stimuli-Responsive Drug-Delivery Systems Based on Supramolecular Nanovalves*. Matter, 2019. **1**(2): p. 345-368.
137. Mal, N.K., M. Fujiwara, and Y. Tanaka, *Photocontrolled reversible release of guest molecules from coumarin-modified mesoporous silica*. Nature, 2003. **421**: p. 350.
138. Guardado-Alvarez, T.M., et al., *Activation of Snap-Top Capped Mesoporous Silica Nanocontainers Using Two Near-Infrared Photons*. Journal of the American Chemical Society, 2013. **135**(38): p. 14000-14003.
139. Ferris, D.P., et al., *Light-Operated Mechanized Nanoparticles*. Journal of the American Chemical Society, 2009. **131**(5): p. 1686-1688.
140. Son, S., E. Shin, and B.-S. Kim, *Light-responsive micelles of spiropyran initiated hyperbranched polyglycerol for smart drug delivery*. Biomacromolecules, 2014. **15**(2): p. 628-634.
141. Vlassioui, I., et al., *Control of Nanopore Wetting by a Photochromic Spiropyran: A Light-Controlled Valve and Electrical Switch*. Nano Letters, 2006. **6**(5): p. 1013-1017.
142. Galvan-Gonzalez, A., et al., *Photodegradation of azobenzene nonlinear optical chromophores: the influence of structure and environment*. JOSA B, 2000. **17**(12): p. 1992-2000.
143. Rao, J. and A. Khan, *Enzyme sensitive synthetic polymer micelles based on the azobenzene motif*. Journal of the American Chemical Society, 2013. **135**(38): p. 14056-14059.
144. Joseph, J.M., et al., *The sonochemical degradation of azobenzene and related azo dyes: rate enhancements via Fenton's reactions*. The Journal of Physical Chemistry A, 2000. **104**(2): p. 301-307.
145. Zhao, H., et al., *o-Nitrobenzyl alcohol derivatives: opportunities in polymer and materials science*. Macromolecules, 2012. **45**(4): p. 1723-1736.
146. Pelliccioli, A.P. and J. Wirz, *Photoremovable protecting groups: reaction mechanisms and applications*. Photochemical & photobiological sciences, 2002. **1**(7): p. 441-458.
147. Wang, H., W. Zhang, and C. Gao, *Shape transformation of light-responsive pyrene-containing micelles and their influence on cytotoxicity*. Biomacromolecules, 2015. **16**(8): p. 2276-2281.
148. Barhoumi, A., Q. Liu, and D.S. Kohane, *Ultraviolet light-mediated drug delivery: Principles, applications, and challenges*. Journal of Controlled Release, 2015. **219**: p. 31-42.
149. Croissant, J., et al., *Two-Photon-Triggered Drug Delivery via Fluorescent Nanovalves*. Small, 2014. **10**(9): p. 1752-1755.
150. Goodwin, A.P., et al., *Synthetic Micelle Sensitive to IR Light via a Two-Photon Process*. Journal of the American Chemical Society, 2005. **127**(28): p. 9952-9953.
151. Wang, W., et al., *Efficient triplet-triplet annihilation-based upconversion for nanoparticle phototargeting*. Nano letters, 2015. **15**(10): p. 6332-6338.
152. Barhoumi, A., B. Salvador-Culla, and D.S. Kohane, *NIR-Triggered Drug Delivery by Collagen-Mediated Second Harmonic Generation*. Advanced Healthcare Materials, 2015. **4**(8): p. 1159-1163.
153. Fedoryshin, L.L., et al., *Near-Infrared-Triggered Anticancer Drug Release from Upconverting Nanoparticles*. ACS Applied Materials & Interfaces, 2014. **6**(16): p. 13600-13606.
154. Liu, J., et al., *NIR-Triggered Anticancer Drug Delivery by Upconverting Nanoparticles with Integrated Azobenzene-Modified Mesoporous Silica*. Angewandte Chemie International Edition, 2013. **52**(16): p. 4375-4379.



155. Klán, P., et al., *Photoremovable Protecting Groups in Chemistry and Biology: Reaction Mechanisms and Efficacy*. Chemical Reviews, 2013. **113**(1): p. 119-191.
156. Barman, S., et al., *A p-Hydroxyphenacyl–Benzothiazole–Chlorambucil Conjugate as a Real-Time-Monitoring Drug-Delivery System Assisted by Excited-State Intramolecular Proton Transfer*. Angewandte Chemie International Edition, 2016. **55**(13): p. 4194-4198.
157. Yan, B., et al., *Near infrared light triggered release of biomacromolecules from hydrogels loaded with upconversion nanoparticles*. Journal of the American Chemical Society, 2012. **134**(40): p. 16558-16561.
158. Eeman, M. and M. Deleu, *From biological membranes to biomimetic model membranes*. Biotechnologie, Agronomie, Société et Environnement, 2010. **14**(4): p. 719-736.
159. Cao, J., et al., *Multifunctional near-infrared light-triggered biodegradable micelles for chemo-and photo-thermal combination therapy*. Oncotarget, 2016. **7**(50): p. 82170.
160. Alkilany, A.M., et al., *Gold nanorods: their potential for photothermal therapeutics and drug delivery, tempered by the complexity of their biological interactions*. Advanced drug delivery reviews, 2012. **64**(2): p. 190-199.
161. Kumar, A., X. Zhang, and X.-J. Liang, *Gold nanoparticles: emerging paradigm for targeted drug delivery system*. Biotechnology advances, 2013. **31**(5): p. 593-606.
162. Gandhi, A., et al., *Studies on thermoresponsive polymers: Phase behaviour, drug delivery and biomedical applications*. asian journal of pharmaceutical sciences, 2015. **10**(2): p. 99-107.
163. Alkilany, A.M. and C.J. Murphy, *Toxicity and cellular uptake of gold nanoparticles: what we have learned so far?* Journal of nanoparticle research, 2010. **12**(7): p. 2313-2333.
164. Link, S. and M.A. El-Sayed, *Shape and size dependence of radiative, non-radiative and photothermal properties of gold nanocrystals*. International reviews in physical chemistry, 2000. **19**(3): p. 409-453.
165. Feil, H., et al., *Effect of comonomer hydrophilicity and ionization on the lower critical solution temperature of N-isopropylacrylamide copolymers*. Macromolecules, 1993. **26**(10): p. 2496-2500.
166. Zhou, M., et al., *Doxorubicin-Loaded Single Wall Nanotube Thermo-Sensitive Hydrogel for Gastric Cancer Chemo-Photothermal Therapy*. Advanced Functional Materials, 2015. **25**(29): p. 4730-4739.
167. Zhang, Q., et al., *Multifunctional Mesoporous Silica Nanoparticles for Cancer-Targeted and Controlled Drug Delivery*. Advanced Functional Materials, 2012. **22**(24): p. 5144-5156.
168. Widmer, S., et al., *Incorporation of a FRET dye pair into mesoporous materials: a comparison of fluorescence spectra, FRET activity and dye accessibility*. Analyst, 2015. **140**(15): p. 5324-5334.
169. Kresge, C.T., et al., *Ordered mesoporous molecular sieves synthesized by a liquid-crystal template mechanism*. Nature, 1992. **359**(6397): p. 710-712.
170. Stevens, W.J.J., et al., *Investigation of the Morphology of the Mesoporous SBA-16 and SBA-15 Materials*. The Journal of Physical Chemistry B, 2006. **110**(18): p. 9183-9187.
171. Fröba, M., et al., *Fe<sub>2</sub>O<sub>3</sub> nanoparticles within mesoporous MCM-48 silica: In situ formation and characterization*. Chemistry of Materials, 1999. **11**(10): p. 2858-2865.
172. Knežević, N.Ž. and J.-O. Durand, *Large pore mesoporous silica nanomaterials for application in delivery of biomolecules*. Nanoscale, 2015. **7**: p. 2199-2209.
173. Benjelloun, M., et al., *Reproducible synthesis of high quality MCM-48 by extraction and recuperation of the gemini surfactant*. Physical Chemistry Chemical Physics, 2001. **3**(1): p. 127-131.
174. Hitz, S. and R. Prins, *Influence of Template Extraction on Structure, Activity, and Stability of MCM-41 Catalysts*. Journal of Catalysis, 1997. **168**(2): p. 194-206.
175. Perez, L.L., et al., *Detemplation of soft mesoporous silica nanoparticles with structural preservation*. Journal of Materials Chemistry A, 2013. **1**(15): p. 4747-4753.
176. Chen, C.-Y., H.-X. Li, and M.E. Davis, *Studies on mesoporous materials: I. Synthesis and characterization of MCM-41*. Microporous Materials, 1993. **2**(1): p. 17-26.
177. Sumper, M., *Biomimetic Patterning of Silica by Long -Chain Polyamines*. Angewandte Chemie International Edition, 2004. **43**(17): p. 2251-2254.
178. Mann, S., *Biomimetalization: principles and concepts in bioinorganic materials chemistry*. Vol. 5. 2001: Oxford University Press on Demand.
179. Dickey, F.H., *The Preparation of Specific Adsorbents*. Proceedings of the National Academy of Sciences of the United States of America, 1949. **35**(5): p. 227-229.
180. Wei, Y., et al., *A Non-surfactant Templating Route to Mesoporous Silica Materials*. Advanced Materials, 1998. **10**(4): p. 313-316.
181. Wei, Y., et al., *Preparation and Physisorption Characterization of D-Glucose-Templated Mesoporous Silica Sol–Gel Materials*. Chemistry of Materials, 1999. **11**(8): p. 2023-2029.
182. Larsen, G., E. Lotero, and M. Marquez, *Facile Sol-gel Synthesis of Porous Silicas Using Poly(propylene)imine Dendrimers as Templates*. Journal of Materials Research, 2011. **15**(8): p. 1842-1848.
183. Pang, J.B., K.Y. Qiu, and Y. Wei, *Preparation of mesoporous silica materials with non-surfactant hydroxy-carboxylic acid compounds as templates via sol–gel process*. Journal of Non-Crystalline Solids, 2001. **283**(1): p. 101-108.
184. Cheng, S., et al., *Facile Synthesis of Mesoporous Gold–Silica Nanocomposite Materials via Sol–Gel Process with Nonsurfactant Templates*. Chemistry of Materials, 2003. **15**(7): p. 1560-1566.
185. Misran, H., R. Singh, and M.A. Yarmo, *Nonsurfactant route of fatty alcohols decomposition for templating of mesoporous silica*. Microporous and Mesoporous Materials, 2008. **112**(1): p. 243-253.
186. Mukherjee, I., et al., *Effect of nonsurfactant template content on the particle size and surface area of monodisperse mesoporous silica nanospheres*. Microporous and Mesoporous Materials, 2009. **122**(1): p. 168-174.
187. Guo, J., et al., *Highly Stretchable, Strain Sensing Hydrogel Optical Fibers*. Advanced Materials, 2016: p. n/a-n/a.
188. Gao, J., et al., *Dopamine functionalized tannic-acid-templated mesoporous silica nanoparticles as a new sorbent for the efficient removal of Cu<sup>2+</sup> from aqueous solution*. Scientific Reports, 2017. **7**: p. 45215.
189. Sahiner, N., S. Sagbas, and N. Aktas, *Preparation and characterization of monodisperse, mesoporous natural poly(tannic acid)–silica nanoparticle composites with antioxidant properties*. Microporous and Mesoporous Materials, 2016. **226**: p. 316-324.
190. Grojo, D., et al., *Size scaling of mesoporous silica membranes produced by nanosphere mediated laser ablation*. Nanotechnology, 2012. **23**(48): p. 485305.

191. Silencieux, F., et al., *Mesoporous Silica Nanoparticles under Sintering Conditions: A Quantitative Study*. Langmuir, 2015. **31**(47): p. 13011-13021.
192. Ruggiero, I., et al., *Piranha treatment-Diatomite silica nanoparticles for drug delivery*. Nanoscale Research Letters, 2014. **9**(1): p. 329-329.
193. Guinier, A., *X-ray Diffraction in Crystals, Imperfect Crystals, and Amorphous Bodies*. 1994: Dover Publications.
194. Feigin, L.A. and D.I. Svergun, *Structure analysis by small-angle X-ray and neutron scattering*. 1987, New York: Springer Science.
195. Glatter, O., *A new method for the evaluation of small-angle scattering data*. Journal of Applied Crystallography, 1977. **10**(5): p. 415-421.
196. Fritz, G., A. Bergmann, and O. Glatter, *Evaluation of small-angle scattering data of charged particles using the generalized indirect Fourier transformation technique*. Journal of Chemical Physics, 2000. **113**(21): p. 9733-9740.
197. Cherny, A.Y., et al., *Scattering from surface fractals in terms of composing mass fractals*. Journal of Applied Crystallography, 2017. **50**: p. 919-931.
198. Nishikawa, K., *Pore Structure Analyses of Carbons by Small-Angle X-ray Scattering*, in *Carbon Alloys*, E.-i. YASUDA, et al., Editors. 2003, Elsevier Science: Oxford. p. 175-188.
199. Shutava, T., et al., *pH Responsive Decomposable Layer-by-Layer Nanofilms and Capsules on the Basis of Tannic Acid*. Macromolecules, 2005. **38**(7): p. 2850-2858.
200. Carcouët, C.C.M.C., et al., *Nucleation and Growth of Monodisperse Silica Nanoparticles*. Nano Letters, 2014. **14**(3): p. 1433-1438.
201. Toth, I.Y., et al., *Mechanism of in situ surface polymerization of gallic acid in an environmental-inspired preparation of carboxylated core-shell magnetite nanoparticles*. Langmuir, 2014. **30**(51): p. 15451-61.
202. Erdemgil, F.Z., et al., *Determination of pKa values of some hydroxylated benzoic acids in methanol-water binary mixtures by LC methodology and potentiometry*. Talanta, 2007. **72**(2): p. 489-496.
203. National Center for Biotechnology Information. PubChem Compound Database; CID=8357, <https://pubchem.ncbi.nlm.nih.gov/compound/8357> (accessed Oct. 29, 2018).
204. Erdogan, G. and R. Karadag, *Quercetin (3, 3', 4', 5, 7-pentahydroxyflavone) Complexes with Calcium (II) and Magnesium (II), Its Potentiometric and Spectrophotometric studies*. Reviews in Analytical Chemistry, 2005. **24**: p. 9-24.
205. Fox, D.W., et al., *Uniform Deposition of Silver Nanowires and Graphene Oxide by Superhydrophilicity for Transparent Conductive Films*. ACS Applied Nano Materials, 2021. **4**(8): p. 7628-7639.
206. Sun, H., et al., *Enhanced Transmission from Visible to Terahertz in ZnTe Crystals with Scalable Subwavelength Structures*. ACS Applied Materials & Interfaces, 2021. **13**(14): p. 16997-17005.
207. Haghani, S., A.J. Galante, and P.W. Leu, *Challenges and Prospects of Bio-Inspired and Multifunctional Transparent Substrates and Barrier Layers for Optoelectronics*. ACS Nano, 2020. **14**(12): p. 16241-16265.
208. Song, L., et al., *Transfer printing of graphene using gold film*. ACS nano, 2009. **3**(6): p. 1353-1356.
209. Lefort, M., et al., *Spray - on organic/inorganic films: a general method for the formation of functional nano - to microscale coatings*. Angewandte Chemie International Edition, 2010. **49**(52): p. 10110-10113.
210. Gan, X., et al., *ZnO nanowire/TiO2 nanoparticle photoanodes prepared by the ultrasonic irradiation assisted dip-coating method*. Thin Solid Films, 2010. **518**(17): p. 4809-4812.
211. Choi, Y., et al., *Methods and Applications of Biomolecular Surface Coatings on Individual Cells*. ACS Applied Bio Materials, 2020. **3**(10): p. 6556-6570.
212. Ghoshdastidar, S., et al., *Plate-Adherent Nanosubstrate for Improved ELISA of Small Molecules: A Proof of Concept Study*. Analytical Chemistry, 2020. **92**(16): p. 10952-10956.
213. Kim, K.J., et al., *Facet-dependent in situ growth of nanoparticles in epitaxial thin films: the role of interfacial energy*. Journal of the American Chemical Society, 2019. **141**(18): p. 7509-7517.
214. Kolasińska, M., R. Krastev, and P. Warszyński, *Characteristics of polyelectrolyte multilayers: Effect of PEI anchoring layer and posttreatment after deposition*. Journal of Colloid and Interface Science, 2007. **305**(1): p. 46-56.
215. Krasnoslobodtsev, A.V. and S.N. Smirnov, *Effect of water on silanization of silica by trimethoxysilanes*. Langmuir, 2002. **18**(8): p. 3181-3184.
216. Howarter, J.A. and J.P. Youngblood, *Optimization of silica silanization by 3-aminopropyltriethoxysilane*. Langmuir, 2006. **22**(26): p. 11142-11147.
217. Wenzel, R.N., *Surface roughness and contact angle*. The Journal of Physical Chemistry, 1949. **53**(9): p. 1466-1467.
218. Wagner, A.D., et al., *Chemotherapy in advanced gastric cancer: a systematic review and meta-analysis based on aggregate data*. Journal of clinical oncology, 2006. **24**(18): p. 2903-2909.
219. Jabir, N.R., et al., *Nanotechnology-based approaches in anticancer research*. International journal of nanomedicine, 2012. **7**: p. 4391.
220. Mai, X., et al., *Designing intelligent nano-bomb with on-demand site-specific drug burst release to synergize with high-intensity focused ultrasound cancer ablation*. Journal of Controlled Release, 2021. **331**: p. 270-281.
221. Slowing, I.I., et al., *Mesoporous silica nanoparticles as controlled release drug delivery and gene transfection carriers*. Advanced drug delivery reviews, 2008. **60**(11): p. 1278-1288.
222. zur Mühlen, A., C. Schwarz, and W. Mehnert, *Solid lipid nanoparticles (SLN) for controlled drug delivery—drug release and release mechanism*. European journal of pharmaceuticals and biopharmaceutics, 1998. **45**(2): p. 149-155.
223. Lee, J.H., et al., *On -demand drug release system for in vivo cancer treatment through self -assembled magnetic nanoparticles*. Angewandte Chemie, 2013. **125**(16): p. 4480-4484.
224. Wang, Y., et al., *A novel controlled release drug delivery system for multiple drugs based on electrospun nanofibers containing nanoparticles*. Journal of pharmaceutical sciences, 2010. **99**(12): p. 4805-4811.
225. Neffe, A.T., et al., *Polymer networks combining controlled drug release, biodegradation, and shape memory capability*. Advanced Materials, 2009. **21**(32 - 33): p. 3394-3398.
226. Lohani, A., et al., *Interpenetrating polymer networks as innovative drug delivery systems*. Journal of drug delivery, 2014. **2014**.
227. Blume, G. and G. Cevc, *Liposomes for the sustained drug release in vivo*. Biochimica et Biophysica Acta (BBA)-Biomembranes, 1990. **1029**(1): p. 91-97.
228. An, X., et al., *Photoinduced drug release from thermosensitive AuNPs-liposome using a AuNPs-switch*. Chemical communications, 2010. **46**(38): p. 7202-7204.
229. Meng, H., et al., *Autonomous in vitro anticancer drug release from mesoporous silica nanoparticles by pH-sensitive nanovalves*. Journal of the American Chemical Society, 2010. **132**(36): p. 12690-12697.

230. Choi, S.W., Y. Zhang, and Y. Xia, *A temperature - sensitive drug release system based on phase - change materials*. Angewandte Chemie International Edition, 2010. **49**(43): p. 7904-7908.
231. Liu, T.-Y., et al., *Magnetic-sensitive behavior of intelligent ferrogels for controlled release of drug*. Langmuir, 2006. **22**(14): p. 5974-5978.
232. Hu, S.-H., et al., *Nano-ferrosporges for controlled drug release*. Journal of Controlled Release, 2007. **121**(3): p. 181-189.
233. Mal, N.K., M. Fujiwara, and Y. Tanaka, *Photocontrolled reversible release of guest molecules from coumarin-modified mesoporous silica*. Nature, 2003. **421**(6921): p. 350-353.
234. Ji, W., et al., *Coumarin-containing photo-responsive nanocomposites for NIR light-triggered controlled drug release via a two-photon process*. Journal of Materials Chemistry B, 2013. **1**(43): p. 5942-5949.
235. Yuan, W., et al., *Light-and pH-dually responsive dendrimer-star copolymer containing spiropyran groups: Synthesis, self-assembly and controlled drug release*. Polymer Chemistry, 2018. **9**(26): p. 3651-3661.
236. Chen, S., et al., *Nanocomposites of spiropyran-functionalized polymers and upconversion nanoparticles for controlled release stimulated by near-infrared light and pH*. Macromolecules, 2016. **49**(19): p. 7490-7496.
237. Zhang, Y., et al., *A DNA-azobenzene nanopump fueled by upconversion luminescence for controllable intracellular drug release*. Angewandte Chemie, 2019. **131**(50): p. 18375-18379.
238. Yuan, Q., et al., *Photon-manipulated drug release from a mesoporous nanocontainer controlled by azobenzene-modified nucleic acid*. ACS nano, 2012. **6**(7): p. 6337-6344.
239. Klán, P., et al., *Photoremovable protecting groups in chemistry and biology: reaction mechanisms and efficacy*. Chemical reviews, 2013. **113**(1): p. 119-191.
240. Feeney, M.J., et al., *UV and NIR-Responsive Layer-by-Layer Films Containing 6-Bromo-7-hydroxycoumarin Photolabile Groups*. Langmuir, 2017. **33**(41): p. 10877-10885.
241. Shrestha, P., et al., *Efficient Far-Red/Near-IR Absorbing BODIPY Photocages by Blocking Unproductive Conical Intersections*. Journal of the American Chemical Society, 2020. **142**(36): p. 15505-15512.
242. Sofokleous, P., E. Stride, and M. Edirisinghe, *Preparation, characterization, and release of amoxicillin from electrospun fibrous wound dressing patches*. Pharmaceutical research, 2013. **30**(7): p. 1926-1938.
243. Wang, Y., et al., *Intelligent Patches for Wound Management: In Situ Sensing and Treatment*. 2021, ACS Publications.
244. Zilberman, M., *Novel composite fiber structures to provide drug/protein delivery for medical implants and tissue regeneration*. Acta biomaterialia, 2007. **3**(1): p. 51-57.
245. Ranganath, S.H. and C.-H. Wang, *Biodegradable microfiber implants delivering paclitaxel for post-surgical chemotherapy against malignant glioma*. Biomaterials, 2008. **29**(20): p. 2996-3003.
246. Rose, M., et al., *MOF processing by electrospinning for functional textiles*. Advanced Engineering Materials, 2011. **13**(4): p. 356-360.
247. Qiu, Q., et al., *Functional nanofibers embedded into textiles for durable antibacterial properties*. Chemical Engineering Journal, 2020. **384**: p. 123241.
248. Wen, J., et al., *Diverse gatekeepers for mesoporous silica nanoparticle based drug delivery systems*. Chemical Society Reviews, 2017. **46**(19): p. 6024-6045.
249. Luo, J., et al., *Polyphenols as Morphogenetic Agents for the Controlled Synthesis of Mesoporous Silica Nanoparticles*. Chemistry of Materials, 2019. **31**(9): p. 3192-3200.
250. Bagwe, R.P., L.R. Hilliard, and W. Tan, *Surface Modification of Silica Nanoparticles to Reduce Aggregation and Nonspecific Binding*. Langmuir, 2006. **22**(9): p. 4357-4362.
251. Honda, T., et al. *Controllable polymerization of biopolymers in a microreaction system*. in *World Congress of Medical Physics and Biomedical Engineering*. 2006.
252. Lin, Q., et al., *Anticancer drug release from a mesoporous silica based nanophotocage regulated by either a one-or two-photon process*. Journal of the American Chemical Society, 2010. **132**(31): p. 10645-10647.

# Curriculum Vitae

## JIALUO LUO

Felsenstrasse 101, 9000 St.Gallen, Switzerland – +41 796082076 – jialuo.luo@hotmail.com

### EDUCATION

#### **EPFL (Swiss Federal Institute of Technology Lausanne)**

Lausanne, Switzerland

##### *PhD in Material Science*

2017 -Present

- GPA 5.1/6 (Courses were completed at ETH Zurich); Conducted in-depth and novel research for nanotechnology and light-responsive drug delivery system; Finished courses in drug delivery, microfluidics, advanced optics, etc.
- Winner of Chinese National Innovation & Entrepreneurship Competition for students overseas 2020; Built and led the entrepreneurship team and organized a PhD club to offer PhDs extracurricular working opportunities
- Achieved 1<sup>st</sup> prize in case study session in Asian day workshop of HSG; Accomplished courses and workshops in IP management (HSG and IGE Bern), entrepreneurship(HSG) and scientific transfer(Tsinghua University)
- Active badminton player (3<sup>rd</sup> in female single in ETH badminton match, 2<sup>nd</sup> in mix double in Basel-Bern Chinese badminton match; Finished 2018 Marathon Zurich (team run)

#### **UNIVERSITY OF FREIBURG | UNIVERSITY OF STRASBOURG**

Freiburg, Germany | Strasbourg, France

##### *Dual master in Polymer Science*

2014 - 2016

- GPA 14.1/20 (bien), obtained University(DFH-UFA) awards mobility grants; First in class to finish master study
- Extensive traveler, completed tourism visit to over 25 countries during master study

#### **SUN YAT-SEN UNIVERSITY**

Guangzhou, China

##### *Bachelor in Polymeric Materials and Engineering*

2010 - 2014

- GPA 86/100, achieved yearly excellent student scholarship of Sun Yat-sen University 2011
- Editor of school journal; Developed a revenue-gaining resource for the department by selling record tapes of school activities to students

### EXPERIENCE

#### **GCC Bridge project (with Mirai Food)**

Zurich, Switzerland

##### *Student consultant*

2021

- Conducted research on Singapore cell-cultivated meat market with multiple business models (PESTEL, SWOT, Porter's five force, Perceptual map, etc) followed by providing regular written and oral reports
- Assisted with the establishment of market entry strategy for APAC region (specially Singapore)

#### **CICCB (Joint Venture of CICC and CCB Trust)**

Beijing, China

##### *Intern healthcare industry analyst*

2019

- Conducted feasibility analysis in product (technology and pipeline) and market research (status-quo, trend, competitor) followed by providing preliminary investment suggestions

- Delivered 6 reports for pharmaceutical, diagnosis, medical devices, medical services, and health insurance companies

**EMPA (Swiss Federal Institute for Material Science)**

St. Gallen, Switzerland

**PhD Researcher**

2016-Present

- Proposed a new hypothesis of pore formation mechanism in non-surfactant synthesis of porous nanoparticles
- Designed a standard approach for surface modification and a quality-evaluation method of particle coatings
- Fabricated a novel optical fiber-based light-responsive release system and revealed the triggering mechanism
- Screened and selected a series of appropriate FRET pairs for wound monitoring pH sensor for a start-up company

**CNRS (French National Center for Scientific Research)**

Strasbourg, France

**Research assistant**

2015 – 2016

- Assembled a metallic thin film system with special optical behaviors by grazing incidence spraying
- Developed flame-retardant textiles via layer-by-layer techniques

**SUN YAT-SEN UNIVERSITY**

Guangzhou, China

**Research assistant**

2013 – 2014

- Constructed a polymer brush based on click chemistry for high-efficient DNA and drug release

**PERSONAL INFORMATION**

- Language: Chinese (native), English (advanced), German (intermediate), French (intermediate), Japanese (intermediate), Cantonese (advanced)
- Interests: Soft-brush calligraphy, Handcraft, Design, Guqin, Piano, Ninjutsu

**PUBLICATION**

- Luo, et al. "Polyphenols as morphogenetic agents for the controlled synthesis of mesoporous silica nanoparticles". *Chemistry of Materials* (2019)
- Luo, et al. "A robust and controllable strategy for surface modification with particles" (In preparation for *Chemical Engineering Journal*)
- Luo, et al. "Evanescence wave-responsive anticancer drug release from flexible complex plastic optical fiber system" (In preparation for *Advanced Materials*)
- Yang, Luo, et al. "Characterization of nanoplastics release during washing and abrasion of polymer textiles". *Environmental science & technology* (2021)